REPORT NO. DOT-TSC-OST-74-6.II

BASIC UNDERSTANDING OF EARTH TUNNELING BY MELTING

Volume II -- Earth Structure and Design Solutions

D. L. Black et al

JULY 1974
FINAL REPORT

DOCUMENT IS AVAILABLE TO THE PUBLIC THROUGH THE NATIONAL TECHNICAL INFORMATION SERVICE, SPRINGFIELD, VIRGINIA 22151.

Prepared for
U.S. DEPARTMENT OF TRANSPORTATION
OFFICE OF THE SECRETARY
Office of the Assistant Secretary for
Systems Development and Technology
Office of Systems Engineering
Washington DC 20590

The contents of this report reflect the views of the Westinghouse Astronuclear Laboratory which is responsible for the facts and the accuracy of the data presented herein. The contents do not necessarily reflect the official views or policy of the Department of Transportation. This report does not constitute a standard, specification or regulation.

Technical Report Documentation Page

1. Report No.	2. Government Accession No.	3. Recipient's Catalog No.
)OT-TSC-OST-74-6.II		

4. Title and Subtitle	5. Report Date
\SIC UNDERSTANDING OF EARTH TUNNELING BY MELTING)lume II -- Earth Structure and Design Solutions	July 1974
	6. Performing Organization Code
7. Author(s)	8. Performing Organization Report No.
D. L. Black et al *	DOT-TSC-OST-74-6.II
9. Performing Organization Name and Address Jestinghouse Electric Corporation \stronuclear Laboratory 'ost Office Box 10864 'ittsburgh PA 15236	10. Work Unit No. (TRAIS)
	11. Contract or Grant No. DOT-TSC-591
12. Sponsoring Agency Name and Address I.S. Department of Transportation)ffice of the Secretary)ffice of the Assistant Secretary for Systems Develop- ıent and Technology; Office of Systems Engineering /ashington DC 20590	13. Type of Report and Period Covered Final Report April - September 1973
	14. Sponsoring Agency Code

15. Supplementary Notes *Under contract to: U.S. Department of Transportation
Transportation Systems Center
Kendall Square
Cambridge MA 02142

16. Abstract A novel technique, which employs the melting of rocks and soils as a means : excavating or tunneling while simultaneous generating a glass tunnel lining and/or 'imary support, was studied. The object of the study was to produce a good basic ıderstanding of the fundamental process, its limits and capabilities, as applied to ırge scale (∿10 m diameter) transportation tunnels.

A description of process is developed through the use of functional flow dia- 'ams, from which five modes of thermal tunneling are defined, ranging from complete :bris consolidation into the liner to complete extrusion and removal of the debris.

For calculation purposes, five geologic modes of the near-surface continental 'ust are presented representative of approximately 95% of the total land area, from ıconsolidated sediments to igeneous rocks. Thermophysical properties are synthesized 'om the composition of the components.

Basic physical principles are used to derive functional equations governing the 'imary process variables in five separate areas: thermal power and penetrator tem- :rature (end of Volume I), thrusting force, earth structural, glass liner structural, ıd melt cooldown. These were related to independent variables of penetration vel- :ity and tunnel geometry and to the geologic model properties.

Some potential design solutions are proposed to obviate some problems and limit- :ions. A comparison with small scale test data indicates that the process is pre- ctable but that thermal stress cracking of the glass liner would minimize its con- deration for the primary tunnel support.

17. Key Words		18. Distribution Statement
ıbterrene	Hydrofracture	DOCUMENT IS AVAILABLE TO THE PUBLIC THROUGH THE NATIONAL TECHNICAL INFORMATION SERVICE, SPRINGFIELD, VIRGINIA 22151.
ıermal Tunneling	Tunnel Lining	
)ckmelt		
ass		

19. Security Classif. (of this report)	20. Security Classif. (of this page)	21. No. of Pages	22. Price
Unclassified	Unclassified	274	

)rm DOT F 1700.7 (8-72) Reproduction of completed page authorized

PREFACE

This report on a "Basic Understanding of Earth Tunneling by Melting" was prepared for the Transportation Systems Center of the Department of Transportation, Cambridge, Massachusetts. All the requirements of Contract DOT-TSC-591 are fulfilled by this report which contains the details of the technical work performed from April 2, 1973 to October 2, 1973. The contract was performed under the technical direction of the Power and Propulsion Branch of TSC/DOT, Mr. John Putukian, Technical Monitor.

This study was conducted by the Westinghouse Astronuclear Laboratory, Pittsburgh, Pennsylvania. The Project Manager was Dr. D. L. Black; principal investigators were Dr. J. W. H. Chi, Dr. R. A. Smith, and Mr. D. B. Roberts of Westinghouse Georesearch Laboratory; technical advisors were Mr. R. R. Holman and Mr. R. Flaherty.

The guidance, reviews and comments of Dr. E. Foster and Mr. R. McFarland at DOT are most gratefully appreciated.

TABLE OF CONTENTS

VOLUME II

TABLE OF CONTENTS
(Continued)

TABLE OF CONTENTS
(Continued)

TABLE OF CONTENTS
(Continued)

TABLE OF CONTENTS
(Continued)

LIST OF ILLUSTRATIONS

VOLUME II

LIST OF ILLUSTRATIONS
(Continued)

LIST OF ILLUSTRATIONS
(Continued)

LIST OF ILLUSTRATIONS

(Continued)

LIST OF ILLUSTRATIONS
(Continued)

LIST OF TABLES

VOLUME II

7.0 APPLIED THRUST LOADS

The applied thrust load required for tunneling is an important factor in penetrator design, for it determines the stresses on the penetrator surface and the thrust load on the glass wall. The first establishes another potential operating limit, while the second determines the required strength and thickness of the glass liner and the size of the grip pads needed for propulsion.

This section presents the development of functional relations of controlling variables that govern applied thrust loads. Thrust load equations were developed for all five modes of penetration. Because of the lack of appropriate data, only the equation for conical penetrators was verified through correlation with experimental data. Numerical illustrations are provided through scoping calculations.

A number of forces contribute to the total applied thrust load (F_T) needed to advance the penetrator. These are the stem drag (F_s), the "adhesion" forces (F_a), the pressure forces or form drag (F_p) and the frictional drag forces (F_f).

$$F_T = F_s + F_a + F_f + F_p \qquad (7\text{-}1)$$

The location where each force originates is illustrated in Figure 7-1 for two typical penetrator designs. Stem drag (F_s) is due to the afterbody dragging along the solidified glass liner, which may be caused by eccentric motion of the stem relative to the glass lined hole/tunnel. The stem is defined here as any portion of the penetrator afterbody behind the point where the molten glass has resolidified and pulled away from the afterbody (see the figure below). The separation of the glass liner from the melt cooldown portion of the stem may be due to the natural non-adherency between materials such as graphite and glass (if a graphite afterbody were used) or to the presence of gaseous coolant flow between the glass liner and the stem. The stem is not considered a part of the melt cooldown section. Stem drag is expected to depend on the surface conditions of the glass and the stem, i.e., whether the glass is smooth or not. Chill-wrinkles in the glass liner are expected to cause appreciable stem drag.

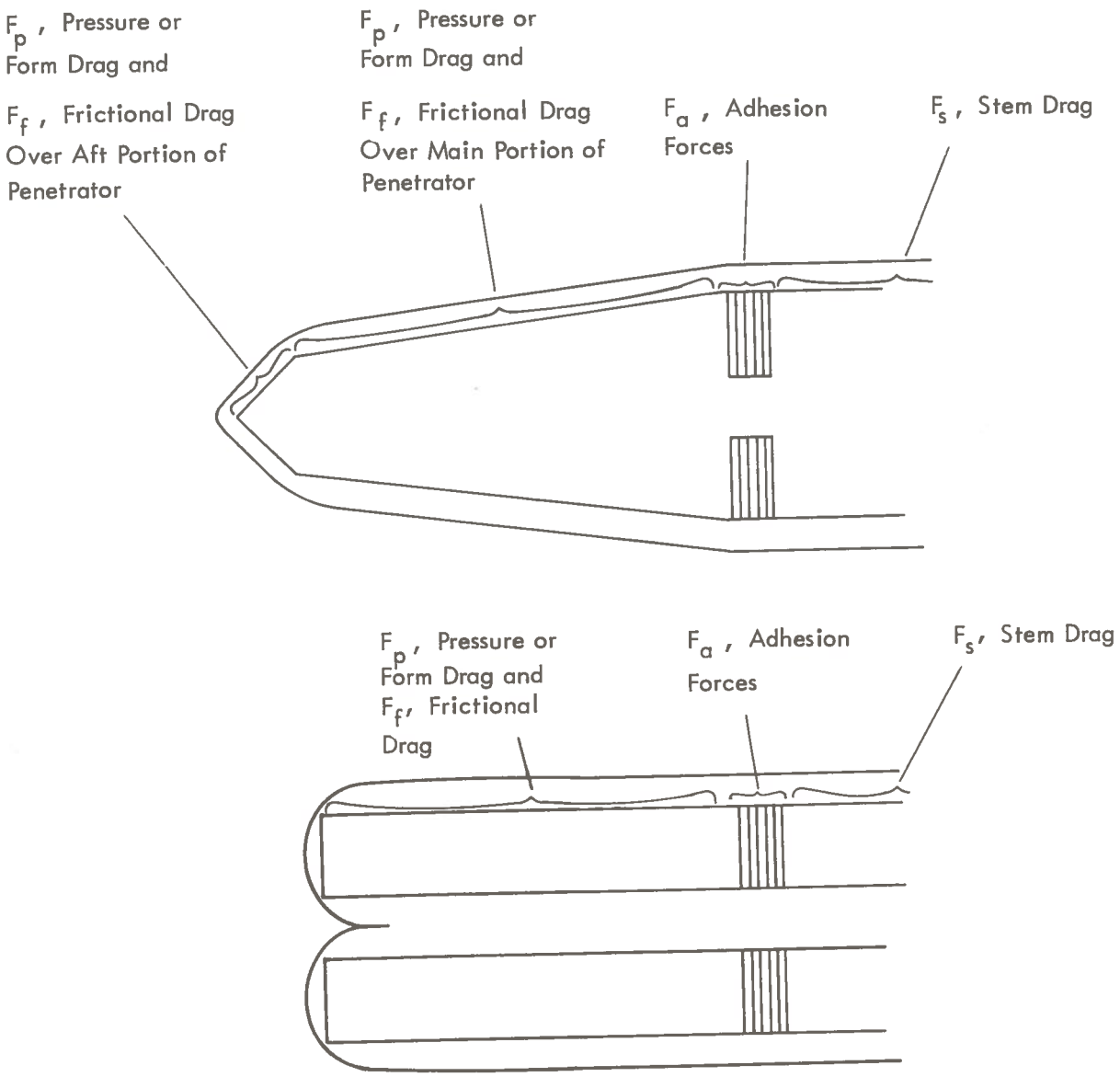

Figure 7-1. Schematic Diagrams of Typical Penetrators Showing Origins of Various Forces

Adhesion force (F_a) is defined here as the force necessary to overcome frictional drag as the melt flows over the melt cooldown section. In practically all of the LASL penetrator designs, layers of pyrographite separate the penetrator heated portion from the main stem to reduce stem losses (conduction losses). As a result of the relatively low thermal conductivity of pyrographite in the axial direction, there is a significant temperature drop and the molten glass is usually resolidified while flowing over this "melt cooldown" section. It is known that the viscosity of molten glasses increases significantly with decreasing temperatures. Consequently, the frictional drag forces occurring herein are termed "adhesion" forces.

Pressure forces (F_p) are also known as form drag. This occurs as a mass of fluid flows past a submerged object. This force is dependent on the pressure distribution along the surface of the body and on the dimensions and geometry of the body.

Frictional drag (F_f) is caused by skin friction from the flow of molten earth/rock over the heated portion of the penetrator. At the melting point of the earth/rock and higher temperatures, the viscosity of the melt is expected to be low compared to that over the melt cooldown section. The melt serves as a lubricant to effect the advance of the penetrator through the surrounding solid earth/rock.

7.1 DERIVATION OF FUNCTIONAL RELATIONS

Functional relations for the various forces have been derived. These are based on physical models and specific assumptions.

7.1.1 Stem Drag

$$F_s = fN \qquad (7\text{-}2)$$

where f is the coefficient of sliding friction. At the rates of penetrator advance considered here, f can be considered to be a constant and it can be readily approximated by the coefficient of static friction. N is the force normal to the surfaces in contact.

7.1.2 Adhesion Forces

Cylindrical Model

The adhesion forces can be determined from a solution of the equations of motion. Since by definition these forces occur over the cylindrical melt cooldown section, the equations of motion in cylindrical coordinates can be used. For this model, the following assumptions can be made:

- Momentum changes are negligible because of creeping flow (maximum Reynolds Number calculated is only ~ 0.3 for a 10 meter penetrator)
- Axisymmetric flow field
- Constant density of the melt around heated penetrator
- Constant effective viscosity
- No gravitational effects
- Quasi steady state

With these assumptions, the equations of motion and the equation of continuity (7-1) reduce to the following:

Equation of Motion:

$$\frac{\partial P}{\partial r} = \mu_{eff}\left[\frac{\partial}{\partial r}\left(\frac{1}{r}\frac{\partial}{\partial r}(rv)\right) + \frac{\partial^2 v}{\partial z^2}\right] \tag{7-3}$$

$$\frac{\partial P}{\partial z} = \mu_{eff}\left[\frac{1}{r}\frac{\partial}{\partial r}\left(r\frac{\partial u}{\partial r}\right) + \frac{\partial^2 u}{\partial z^2}\right] \tag{7-4}$$

Equation of Continuity:

$$\frac{1}{r}\frac{\partial rv}{\partial r} + \frac{\partial u}{\partial z} = 0 \qquad (7\text{-}5)$$

Because of the higly viscous nature of the melt and the slow laminar motion, velocities normal to the surface are negligible ($v \tilde{=} 0$). Then from Equation (7-5), $\partial u / \partial z = 0$. Equations (7-3 and 7-4) reduce to

$$\frac{\partial P}{\partial r} = 0 \qquad (7\text{-}6)$$

and

$$\frac{\partial P}{\partial z} = \frac{\mu_{eff}}{r}\frac{\partial}{\partial r}\left(r\frac{\partial u}{\partial r}\right) \qquad (7\text{-}7)$$

Equation (7-6) implies that the pressure is a function of z alone; therefore one can set

$$\frac{\partial p}{\partial z} = \frac{\Delta P}{L} = \text{constant} \qquad (7\text{-}8)$$

or

$$\frac{d}{dr} r \mu \frac{du}{dr} = \frac{\Delta P}{L} r \qquad (7\text{-}9)$$

Equation (7-9) can be integrated directly with the following boundary conditions:

$$\frac{du}{dr} = 0 \quad \text{at} \quad r = r_p + \delta \qquad (7\text{-}10)$$

$$u = 0 \quad \text{at} \quad r = r_p \qquad (7\text{-}11)$$

$$u = U_\infty \quad \text{at} \quad r = r_p + \delta \qquad (7\text{-}12)$$

It is also assumed that there is a mean, effective, constant viscosity (μ_{eff}) independent of the radial position r. With this assumption, the solution to Equation (7-9) is:

$$F_a = \frac{4 \pi \mu_{eff} L_c U_\infty \left[(r_p + \delta)^2 - r_p^2 \right]}{g_c \left[(r_p + \delta)^2 - r_p^2 + 2 (r_p + \delta)^2 \ln \frac{r_p}{r_p + \delta} \right]} \qquad (7\text{-}13)$$

Equation (7-13) is not only applicable to the calculation of adhesion forces, but is also valid for frictional drag forces due to melt flow over any heated cylindrical surface. In the latter case μ_{eff} should be replaced by μ_m.

Flat Plate Model

For relatively large tunnels and relatively thin glass liners, the effect of radius on the frictional drag becomes negligible and a simple one dimensional "flat plate" model may be assumed to calculate either frictional drag due to melt flow over heated surfaces or frictional drag due to melt flow over cooldown sections. Thus, when δ / D_p is on the order of 0.1 or less, the equations of motion in rectangular coordinates can be simplified with the following assumptions:

- Momentum changes are negligible
- Constant density of the melt
- No gravitational effects
- Quasi steady state
- Velocity components in the y and z directions are negligible.
- Constant melt thickness
- Constant viscosity

The equation of continuity then reduces to

$$\frac{\partial u}{\partial x} = 0$$

The equations of motion then reduce to a single equation.

$$\frac{\partial p}{\partial x} = \mu \frac{\partial^2 u}{\partial y^2} \tag{7-14}$$

The pressure is a function of x only; therefore it can be assumed that

$$\frac{\partial p}{\partial x} = \frac{\Delta P}{L} = \text{constant} \tag{7-15}$$

Combining (7-14) and (7-15),

$$\frac{\Delta P}{L} = \mu \frac{d^2 u}{d y^2} \tag{7-16}$$

The boundary conditions of this problem are the following:

$$\frac{du}{dy} = 0 \quad \text{when} \quad y = r_p + \delta \tag{7-17}$$

$$u = 0 \quad \text{at} \quad y = r_p \tag{7-18}$$

$$u = 0 \quad \text{at} \quad y = r_p + \delta \tag{7-19}$$

By integrating Equation (7-16) twice and by making use of the two boundary conditions, the following functional relations for pressure drop and frictional drag can be derived:

$$\Delta P = - \frac{2 \mu U_\infty L}{\delta 2 g_c} \tag{7-20}$$

$$F_f \text{ or } F_a = \frac{2 \pi D_p \mu U_\infty L}{\delta g_c} \tag{7-21}$$

where $L = L_H$, $\mu = \mu_m$ for frictional forces over heated portions of the penetrator, yielding F_f, or $L = L_c$ and $\mu = \mu_{eff}$ for frictional drag over melt cooldown section, yielding "adhesion" forces, F_a.

7.1.3 Pressure Drag Forces

The pressure and frictional drag forces are directly dependent on the geometry and shape of the penetrator; consequently, different physical and mathematical models are needed for different penetrator designs. Two primary models are considered here, a conical model to simulate consolidating conical penetrators,and a concentric annular cylindrical model to simulate extruders.

These two models are discussed separately.

Conical Model

For conical penetrators of the type designed and tested at the Los Alamos Scientific Laboratory, three distinct sections of the penetrator can be identified, (1) the conical tip, (2) the main portion of the penetrator, and (3) the melt cooldown section. These are shown in Figure 7-1.

For this model, the following assumptions are made:

1. Total pressure drop is equal to the sum of the pressure drops of the three regions.
2. Total frictional drag is the sum of the frictional drag of the three regions.
3. Axisymmetry

The assumption of axisymmetry is necessary to permit a closed form analytical solution of the problem. The effect of gravity on horizontal tunneling will be discussed in Section

For the conical model, orthogonal coordinates are proposed. These are shown in the schematic diagram below:

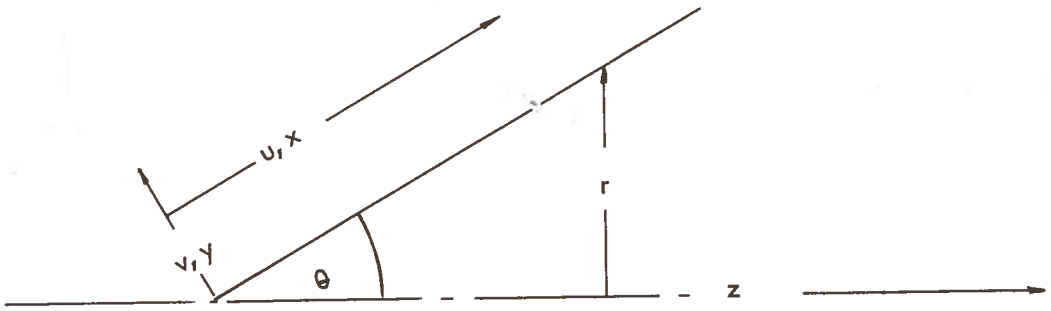

In terms of the orthogonal coordinates, the equations of momentum are the following:

Equations of Motion:

$$\frac{\partial P}{\partial y} = \frac{2}{\partial y}\left(\frac{\mu \partial v}{\partial y}\right) + \frac{1}{x}\frac{\partial}{\partial x}\left(x \mu \frac{\partial u}{\partial y}\right) \qquad (7\text{-}22)$$

$$\frac{\partial P}{\partial x} = \frac{\partial}{\partial y}\left(\mu \frac{\partial u}{\partial y}\right) \qquad (7\text{-}23)$$

Equation of Continuity:

$$\frac{1}{x}\frac{\partial (u x)}{\partial x} + \frac{\partial v}{\partial y} = 0 \qquad (7\text{-}24)$$

To solve this set of equations, it was assumed that there is no velocity component in the direction normal to the surface (i.e., $v = 0$). This is an excellent assumption for the creeping motion encountered here. With this assumption, Equation (7-24) yields

$$\frac{\partial (u x)}{\partial x} = 0$$

Based on this, it is assumed that $\partial \left(x \mu \frac{\partial u}{\partial y} \right) / \partial x = 0$, and Equation (7-22) reduces to

$$\frac{\partial P}{\partial y} = 0 \tag{7-25}$$

This implies that P is a function of x only; therefore, $\partial P / \partial x$ is a constant, independent of y and it can be given by

$$\frac{\partial P}{\partial x} = \frac{\Delta P}{L} = \frac{\partial}{\partial y} \left(\frac{\mu \partial u}{\partial y} \right) \tag{7-26}$$

The boundary conditions are the following:

$$u = 0 \quad \text{at} \quad y = 0, \text{ all } x \tag{7-27}$$

$$u = 0 \quad \text{at} \quad x = 0 \tag{7-28}$$

$$\frac{du}{dy} = 0 \quad \text{at} \quad y = \delta \tag{7-29}$$

$$u = U_{max} = U_{\infty} \cos \theta \quad \text{at} \quad y = \delta \tag{7-30}$$

The assumptions used in arriving at a closed form analytic solution are the following:

tuff, the melt thickness (calculated for a 7.5 cm penetrator) at the end of the conical tip is 0.75 centimeters, while the fully developed final liner thickness is 1.87 centimeters. The difference between the two thicknesses is not too great so that an average constant thickness may be assumed for the main portion of the penetrator. Solution to Equation (7-26) with the boundary conditions (7-27 to 7-30) yields the following equations for the forces due to pressure drag and frictional drag:

$$F_p = S_p \left[P_\infty + \frac{3}{2} \frac{\mu U_\infty r_p^2}{\delta^3 \sin\theta g_c} \right] \qquad (7\text{-}31)$$

$$F_f = \frac{2 S_p \mu U_\infty r_p \cot\theta}{g_c \delta^2} \qquad (7\text{-}32)$$

Derivation of these solutions is found in Reference(7-2).

Cylindrical Model

(7-3)

This model was proposed by Armstrong, et al., to estimate the pressure drag associated with extruders. The model is shown schematically below

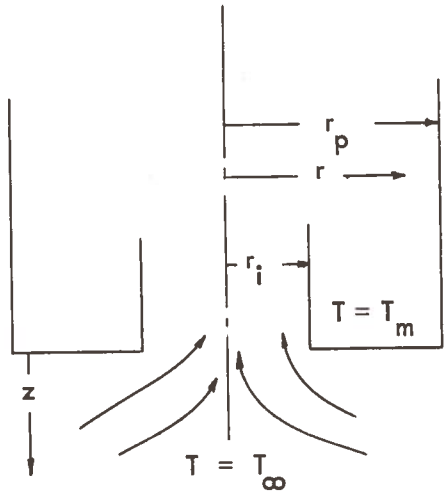

This model assumes that the viscosity is a function of the distance z, away from the face of the penetrator

$$\mu = \mu_o e^{Bz} \tag{7-33}$$

where

$$B = \frac{E}{RT_m} \left(\frac{T_m - T_\infty}{T_m} \right) \frac{\rho C_p U_\infty}{\lambda} \tag{7-34}$$

Another assumption is that there is no melt flow around the side of the penetrator; melt flows through the center hole only.

The equations of motion in terms of cylindrical coordinates to be used are the following:

$$\frac{\partial P}{\partial r} = \frac{Z}{r} \frac{\partial}{\partial r} r \mu \frac{\partial u}{\partial r} - 2\mu \frac{\partial u}{r^2} + \frac{\partial}{\partial z} \mu \left(\frac{\partial u}{\partial z} + \frac{\partial v}{\partial r} \right) \tag{7-35}$$

and

$$\frac{\partial P}{\partial z} = \frac{1}{r} \frac{\partial}{\partial r} r \mu \left(\frac{\partial u}{\partial z} + \frac{\partial v}{\partial r} \right) + 2 \frac{\partial}{\partial z} \mu \frac{\partial v}{\partial z} \tag{7-36}$$

This model was solved by Armstrong, et al.[7-3] by using the assumption that v is a function of z only.

The results yield the following equation for the pressure drag force:

$$F_p = \frac{\pi}{8} \mu_o U_\infty B^3 \left[4 r_p^4 \ln \left(\frac{r_p}{r_c} \right) - (3 r_p^2 - r_c^2) (r_p^2 - r_c^2) \right] \tag{7-37}$$

Real penetrator designs of the extruder type, however, do not have a flat, planar surface; consequently, it is expected that the pressure drag calculated by the above functional relation would be conservative.

7.1.4 Total Applied Thrust Load

The total applied thrust load for each mode of tunneling can now be established.

Mode 1

For Mode 1 tunneling using a conical penetrator, the total applied thrust load is the sum of forces needed to overcome pressure drag, frictional drag due to flow over the heated portion of the penetrator, frictional drag due to melt flow over the cooldown section (adhesion forces), and stem drag. The sum of these forces yield the equation

$$F_T = S_p \left[P_\infty + \frac{3}{2} \frac{\mu U_\infty r_p^2}{g_c \delta^3 \sin\theta} \right] + \frac{2 S_p \mu U_\infty r_p \cot\theta}{g_c \delta^2} + \frac{4\pi \mu_{eff} U_\infty \left[(r_p + \delta)^2 - r_p^2 \right] L_c}{g_c \left[(r_p + \delta)^2 - r_p^2 + 2 (r_p + \delta)^2 \ln \left(\frac{r_p}{r_p + \delta} \right) \right]} + f N \qquad (7\text{-}38)$$

Mode 2

Mode 2 tunneling has basically the same geometry as Mode 1 with the addition of extrusion. For this mode of tunneling, the pressure drag force can be determined by combining the solutions for the conical and cylindrical penetrators. An idealized model of actual extruder designs is assumed as shown below:

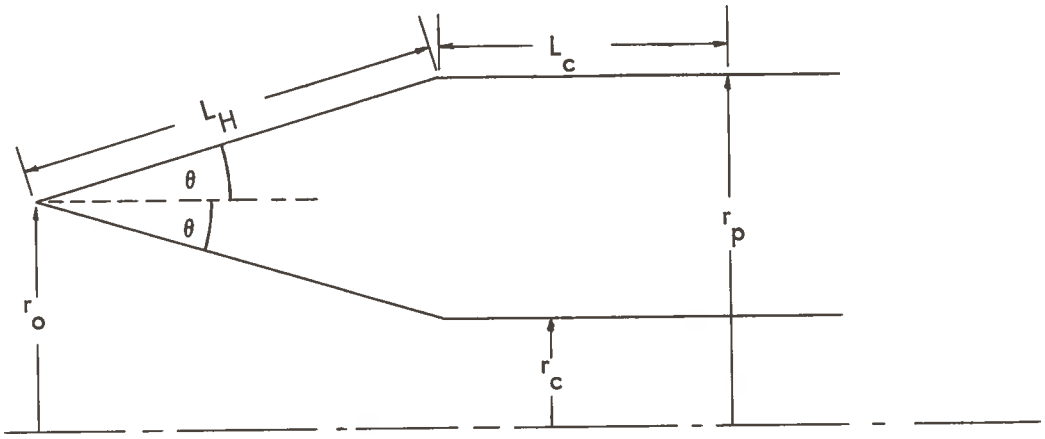

The thrust load equation for this mode of tunneling may be approximated by the equation

$$F_T = \pi (r_p^2 - r_o^2) \left\{ \left[P_\infty + \frac{3}{2} \frac{\mu_m U_\infty r_p^2}{2 g_c \delta^3 \sin\theta} \right] + \frac{\mu_m U_\infty D_p \cot\theta}{g_c \delta^2} \right\}$$

$$+ \frac{\pi}{8} \mu_o U_\infty B^3 \left[4 r_o^4 \ln \frac{r_o}{r_c} - (3 r_o^2 - r_c^2)(r_o^2 - r_c^2) \right]$$

$$+ \frac{4 \pi \mu_c U_\infty \left[(r_p + \delta)^2 - r_p^2 \right] L_c}{g_c \left[(r_p + \delta)^2 - r_p^2 + 2 (r_p + \delta)^2 \ln \left(\frac{r_p}{r_p + \delta} \right) \right]} + f N \qquad (7\text{-}39)$$

where μ_m denotes the viscosity in the heated portion of the penetrator, while μ_c denotes the viscosity in the melt cooldown section.

Mode 3

The applied thrust load equation for Mode 3 tunneling is identical to that for Mode 2. The only difference is that the melt layer along the outer surface of the penetrator is relatively thin. It exists not for the purpose of forming a self-supporting liner, rather it is developed to reduce "stem drag", for if a melt layer does not exist, "stem" drag would be extended to the penetrator tip section also.

Mode 4

For this mode of operation, the frictional drag over the melt cooldown section can be calculated from the flat plate model because δ / D_p is expected to be small. Also there is no extrusion in this mode of tunneling. Hence,

$$F_T = \pi (r_p^2 - r_o^2) \left\{ \left[P_\infty + \frac{3}{2} \frac{\mu_m U_\infty r_p^2}{g_c \delta^3 \sin\theta} \right] + \frac{D_p \mu_m \cot\theta U_\infty}{\delta^2 g_c} \right\}$$

$$+ \frac{2 \pi D_p \mu_c U_\infty L_c}{\delta g_c} + f N \qquad (7\text{-}40)$$

Mode 5

This mode of operation is basically the same as Mode 4, the addition of extrusion being the only difference. Hence the thrust load equation can be estimated from the following equation:

$$F_T = \pi (r_p^2 - r_o^2) \left\{ \left[P_\infty + \frac{3}{2} \frac{\mu_m U_\infty r_p^2}{g_c \delta^2 \sin\theta} \right] + \frac{D_p \mu_m U_\infty \cot\theta}{g_c \delta^2} \right\}$$

$$+ \frac{\pi}{8} \mu_o U_\infty B^3 \left[4 r_o^4 \ln\left(\frac{r_o}{r_c}\right) - (3 r_o^2 - r_c^2)(r_o^2 - r_c^2) \right] + \frac{2\pi D_p \mu_c U_\infty L_c}{\delta g_c} + fN \quad (7\text{-}41)$$

It should be pointed out that the functional relations presented are based on idealized penetrator geometries, while actual penetrator designs are considerably more complex. The use of these equations may require empirical adjustments and careful definition of geometric parameters.

7.2 VERIFICATION OF FUNCTIONAL RELATIONS

7.2.1 Analysis of Data

Experimental data on the total applied thrust loads have been obtained at the Los Alamos Scientific Laboratory for every test drilling made. However, most of the experiments were carried out for the purpose of feasibility and developmental testing or demonstrations only; they were not carefully controlled, and most of the data are of little use as far as verification of the functional relations are concerned. At the request of WANL, one set of experimental measurements was made to provide more useful thrust load data. This set of data was obtained with a 75 mm conical consolidating penetrator through dried tuff. The

experiments were carried out by holding the total thermal power constant while varying the applied thrust load to study its effect on the rate of penetration. Power levels were held at nominal values of 3 kW, 4 Kw, 6 kW and 8 kW. Typical thermal power, thrust load, and rate of penetration traces are reproduced in Figure 7-2, while a typical relation between the thrust load and the rate of penetration at constant thermal power is shown in Figure 7-3. This figure illustrates the gross effect of thrust loads on the rate of penetration. The following characteristics may be noted.

For a given thermal power level, there is a minimum thrust load below which the penetrator cannot advance. This is shown as point 1 on the figure. Above this minimum thrust load, the rate of penetration increases rapidly with slight increases in the thrust load until a critical velocity, U_c, is reached (curve 1-2). Thereafter, further increases in the rate of penetration can be accomplished only by increasing appreciably the thrust load (curve 2-3). As the thrust load is increased, there is a critical value (point 3) at which the rate of penetration again can be increased dramatically with no apparent further increase in the applied thrust load (curve 3-4). These phenomena were observed for every set of data taken at constant total thermal power.

The minimum thrust load is that needed to overcome ambient pressure. The incremental thrust load needed to attain the critical rate of penetration is that amount required to overcome frictional drag of melt flow over the heated penetrator section. With increasing thrust load beyond this point, the rate of penetration increases only slightly. This is due to the fact that thrust loads over and above the critical value result in compression of the melt thickness just ahead of the conical penetration. This results in lower melt superheat in this

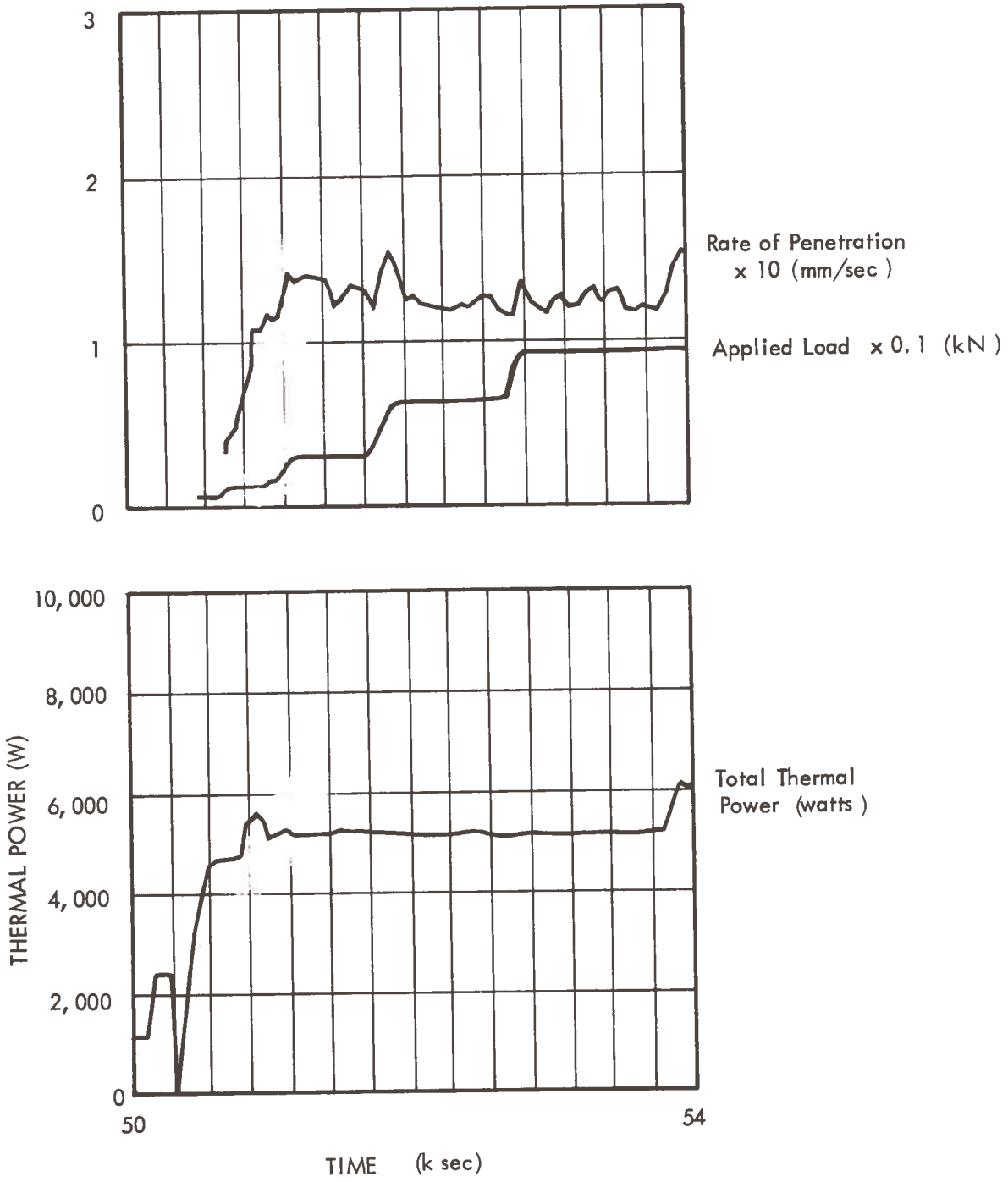

Figure 7-2. Typical Transient Rate, Applied Load, and Total Thermal Power Traces for 75 mm Consolidating Penetrator in Dried Tuff

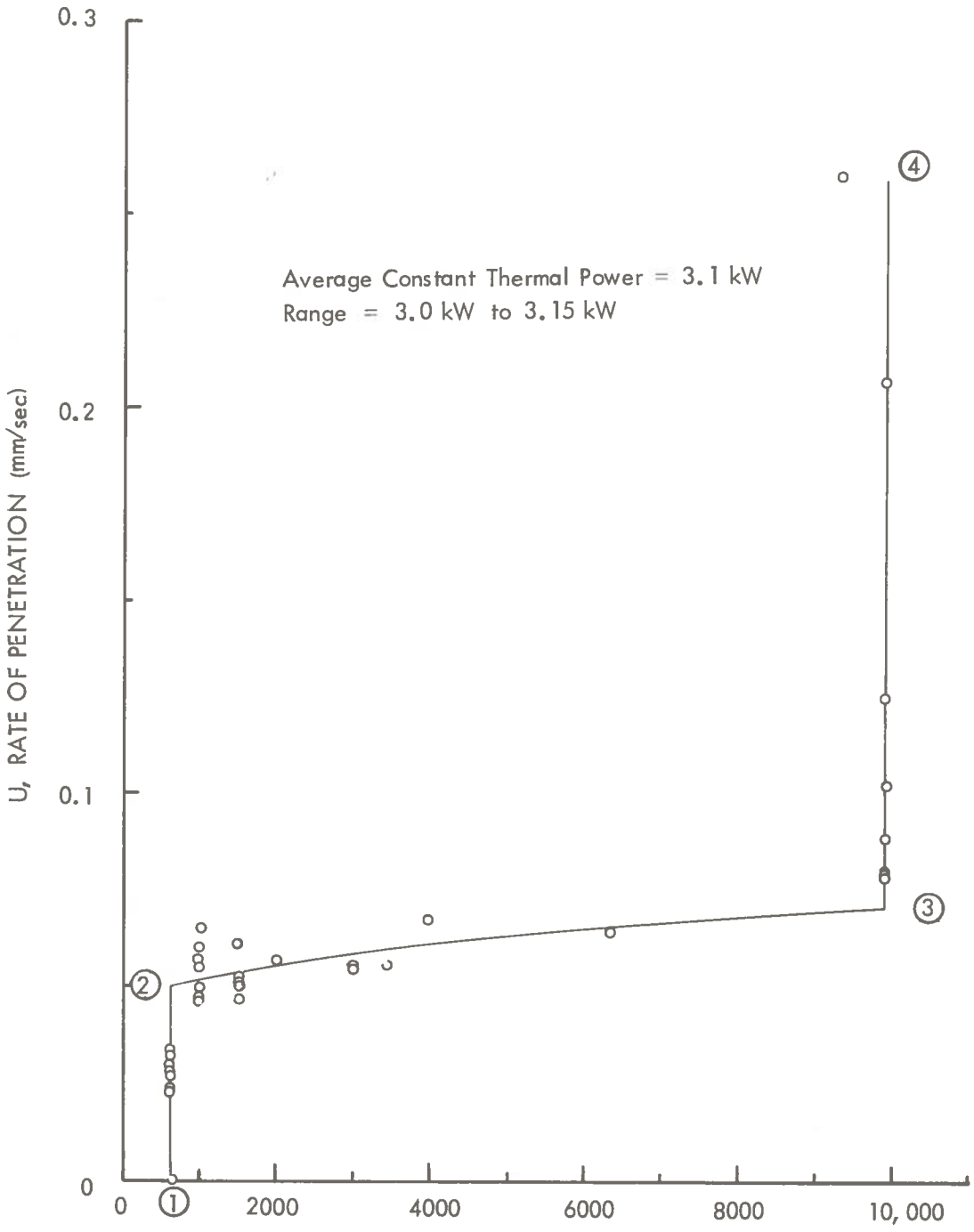

Figure 7-3. Experimental Effect of Applied Thrust Loads on the Rate of Penetration through Tuff

region of the melt so that more heat is available to increase the advance of the penetrator (see the figures below). In addition, the lower melt temperature increases the viscosity

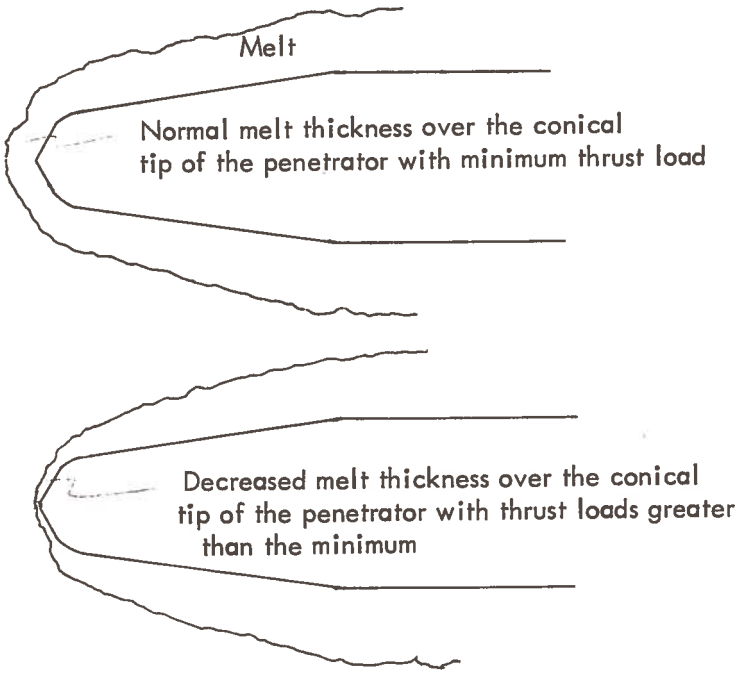

while decreasing the effective thermal conductivity. There is an upper limit on the applied thrust load. At this point, the unmolten earth/rock may yield, be compressed, or be cracked so that volume is created to accommodate the melt. Following this, a higher rate of penetration becomes possible. For a 75 mm diameter penetrator moving through tuff, the upper limit on the applied thrust load is approximately 10, 000 newtons. This results in a calculated compressive stress of 330 psi. Experimental measurements at LASL on the crushing strength of tuff gives a value of 400 psi. The yield strength is expected to be lower so that the calculated value can be considered to be in fairly good agreement with the data.

The scatter in the data observed in Figure 7-3 is due to transient effects. It was noted that whenever the applied thrust load was stepped up to a higher level, the rate of penetration increases rapidly initially and then drops down to a steady-state value. Similarly, when the thermal power is increased with the thrust load held constant, the rate of penetration increases rapidly at first and then drops to a steady-state level. This phenomenon can be noted in Figure 7-2. In order to eliminate the effect of transients, only the apparent steady-state values were used in the data correlations to be discussed in the next section. The resultant steady-state data are presented in Figure 7-4.

7.2.2 Correlation of Data

Since the data were obtained with a conical consolidator, Equation (7-38) was used in attempts to correlate the data. Numerical evaluation of the terms in the equation showed that the frictional drag terms are negligible when compared to the pressure drag terms. Using a 75 mm consolidator operating in tuff as an example, the total thrust load for a thermal power level of 4 kW(net) is calculated to be 600 newtons. Pressure drag accounts for 495 newtons while the frictional drag estimated is only 2 to 20 newtons (depending on the value of the viscosity assumed). Furthermore, the minimum pressure drag calculated, based on an assumed ambient pressure of 14.7 psia, is 100.7 lb_f or 448 newtons. This is in excellent agreement with the minimum experimental thrust loads observed. Therefore, stem drag must be negligible. The frictional drag over the melt cooldown section was negligible because of the relatively short length of cooldown section (pyrographite section) used. As a consequence, for all practical purpose, Equation (7-38) reduces to only two terms:

$$F_T = S_p P_\infty + \frac{3 \mu_m U_\infty S_p r_p^2}{2 g_c \delta^3 \sin\theta} \qquad (7\text{-}42)$$

The rate of penetration, U_∞, associated with a given thermal power level can be calculated from Equation 6-39 if the stem losses are known. The stem losses were calculated as follows:

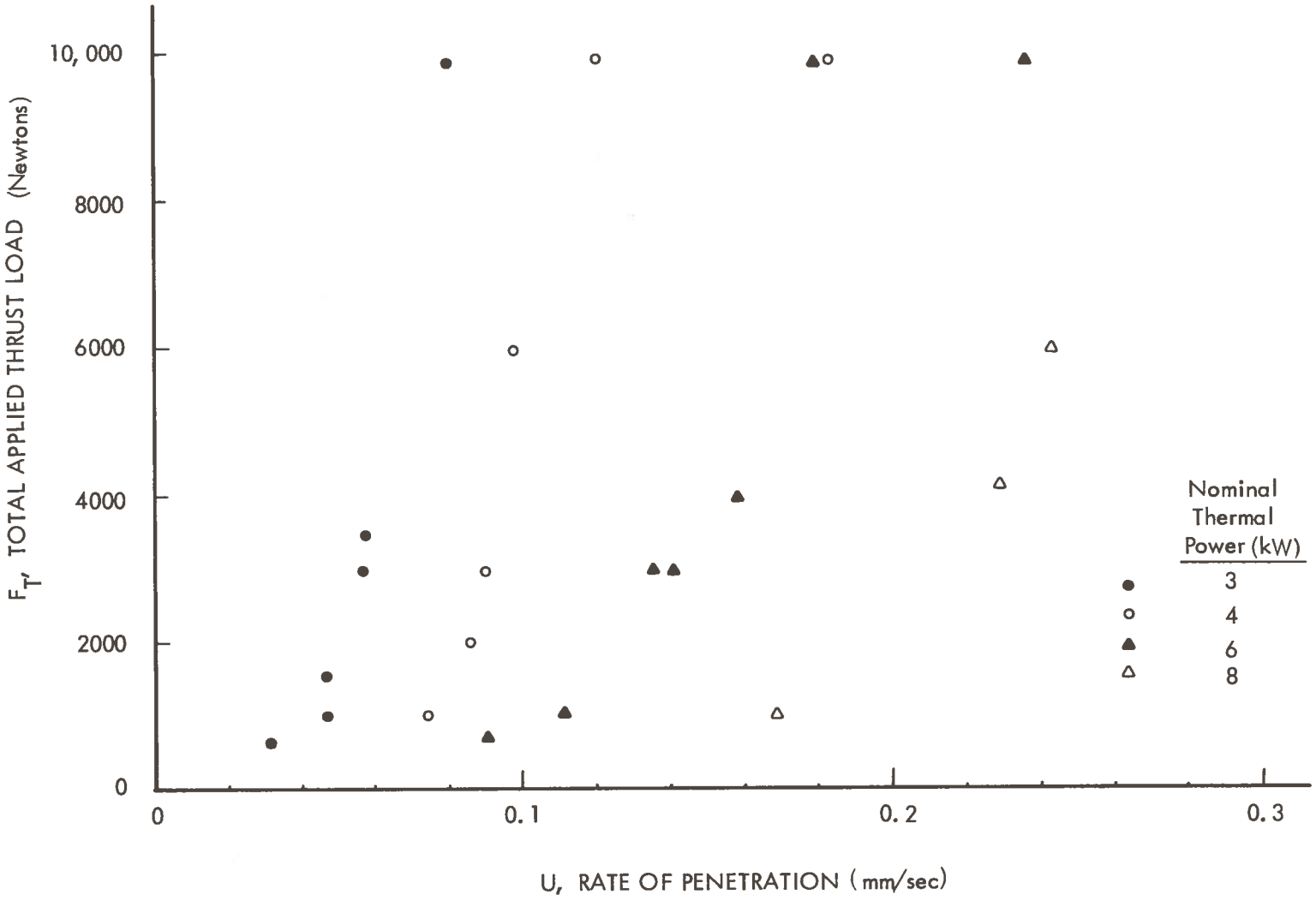

Figure 7-4. Steady State Experimental Data on the Effects of Thermal Power and Applied Thrust Loads on the Rate of Penetration 75 mm Consolidator in Dried Tuff

The total thermal power (excluding stem losses) was calculated for given rates of penetration, i.e.,

$$Q_T = f(U) + q_a \qquad (7\text{-}43)$$

where q_a is the stem loss. For each nominal thermal power level, the minimum observed rate of penetration was obtained from the experimental data. A set of 4 data points was therefore obtained. Equation 7-43 was fitted to the data by assuming various values of q_a. The best correlation was obtained with a stem loss of 875 watts. This correlation is illustrated in Figure 7-5. Based on the theory discussed in Section 7.2.1, it is assumed that Equation 7-42 gives the minimum thrust load when the rate of penetration is that derived from the thermal power equation. At thrust loads greater than the minimum, the rate of penetration can be increased. To evaluate this effect, a relation must be developed between the fluid flow phenomenon and the heat transfer phenomenon. This relation would be available if the equations of motion were solved simultaneously with the equations of energy. However, in order to permit closed form analytic solutions, the equations of motion were decoupled from the energy equations. Therefore, empirical methods are now used to link the two. In the development of a method for calculating melt superheat (see Section 6.1.6), a series of assumptions were made. These same assumptions are adopted here. Based on these assumptions, the following relations are available:

$$q_T = \frac{k_m}{\delta} A_p (T_s - T_m) \qquad (7\text{-}44)$$

and

$$q_T = S_m \rho_e U_\infty \left[C_p (T_m - T_\infty) + \lambda\right] \qquad (7\text{-}45)$$

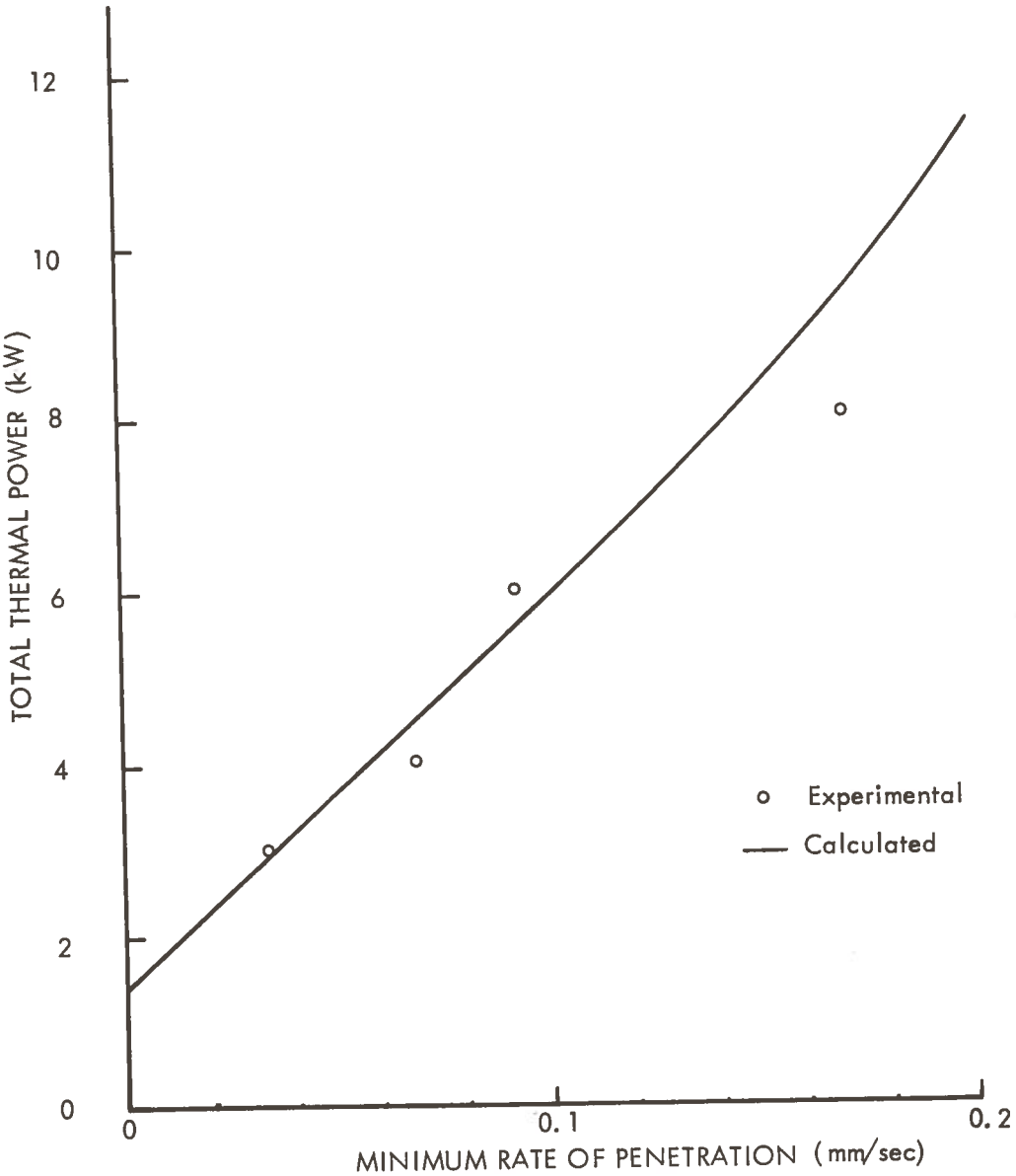

Figure 7-5. Correlation of Minimum Rate of Penetration Data 75 mm Consolidator in Dry Tuff

where the static heat loss has been neglected when relatively large tunnels or rates of penetrations are considered. Combining the two equations results in the relation

$$\delta = \frac{k_m A_p (T_s - T_m)}{U_\infty S_m \rho_e [C_p (T_m - T_\infty) + \lambda]} \qquad (7\text{-}46)$$

Equations 7-47 suggests that for a given penetrator design, the melt thickness is directly proportional to the effective thermal conductivity of the melt, and the melt superheat, while it is inversely proportional to the rate of penetration. When this relation is substituted into Equation 7-42, the result is

$$F_T - S_p P_\infty = a \frac{\mu_m U_\infty^4}{k_m^3 (T_s - T_m)^3} \qquad (7\text{-}47)$$

where a is a constant. It was theorized in Section 7.2.1 that when a thrust load over and above the minimum value is applied, the melt layer is compressed, resulting in the following:

1. Melt superheat is reduced
2. μ_m is increased
3. k_m is decreased

As a consequence of 1, a greater rate of penetration can be obtained for the same thermal power level. Since the effect of thrust loads on the melt thickness is not readily predicted, an empirical approach is used by assuming that

$$\frac{\mu_m}{k_m^3 (T_s - T_m)^3} = c U_\infty^b \qquad (7\text{-}48)$$

where c and b are empirical constants. Equation 7-47 then becomes

$$F_T - S_p P_\infty = a \ (U_\infty)^{4+b} \qquad (7\text{-}49)$$

Equation 7-49 predicts that a plot of $F_T - S_p P_\infty$ vs. U_∞ on log-log paper should yield a straight line with a slope equal to 4 + b. This is shown in Figure 7-6. Attempts were made to select an integral value of b. The best fit to the data yields a value of b equal to unity. Correlation of the data is further illustrated on Cartesian coordinates in Figure 7-7. It is obvious that there is excellent correlation of the data at all thermal power levels. The average deviation between experimental and calculated thrust loads is + 4.1% while the average absolute deviation is 18.1%.

The agreement between experimental and calculated thrust loads is excellent in view of the fact that the thermal power level could not be held at a steady value and that stem losses were not measured. For nominal power settings, the actual power fluctuated over a fairly narrow range as shown below:

Nominal Power Level (kW)	Range of Power (watts)
3	3097 - 3128
4	4105 - 4217
6	6172 - 6262
8	8263 - 8353

These power fluctuations are expected to affect directly the rate of penetration. The maximum fluctuation calculated, however, is only 3.2%; consequently, this cannot account for the deviations observed. One major unknown is the stem loss which can have an appreciable effect on the calculated rate of penetration. A constant stem loss was

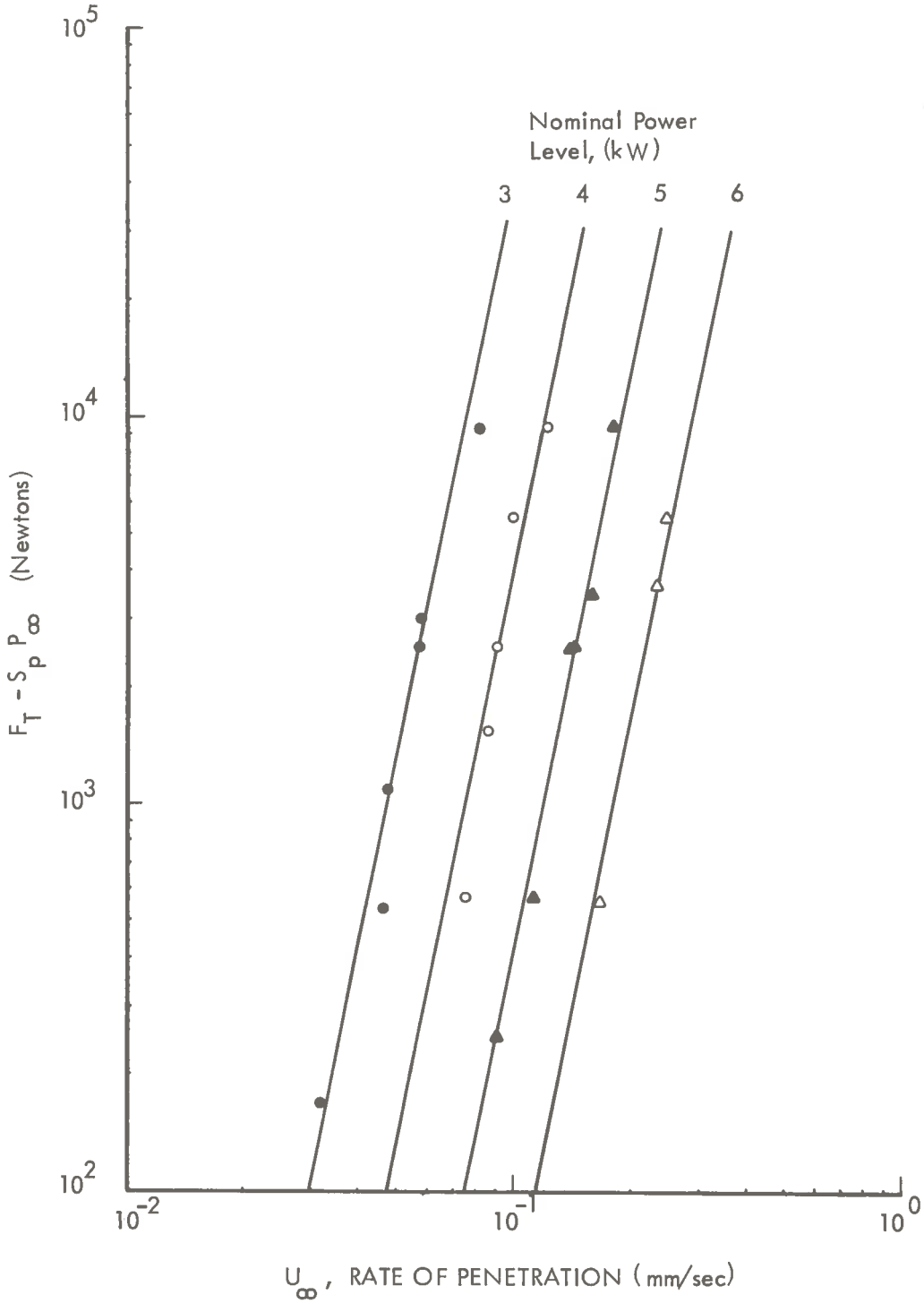

Figure 7-6. Correlation of Thrust Load Data
75 mm Consolidator Through Tuff

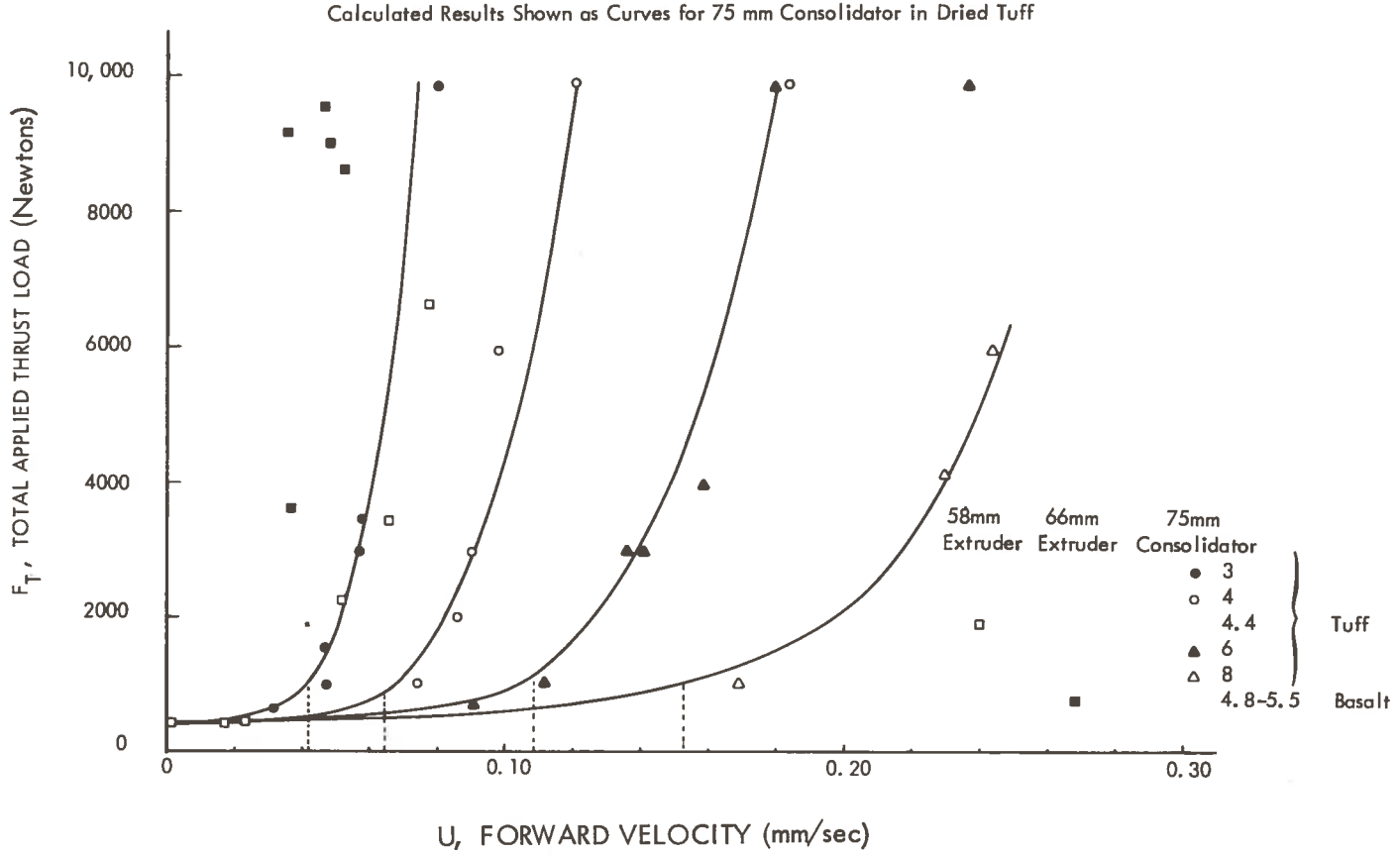

Figure 7-7. Comparison of Experimental and Calculated Applied Thrust Loads

assumed for all thermal power levels, whereas stem losses are expected to increase with increasing power because of increasing penetrator temperatures. Since stem losses were not measured, this factor cannot be taken into account.

The calculated rates of penetration for the 4 power levels are shown as dotted lines on Figure 7-7 from which the following conclusion is drawn. For conical full consolidation type penetrators, there is a minimum applied thrust load for a given thermal power level. This minimum thrust load is determined by the minimum rate of penetration which can be estimated from Equation (7-42), where μ_m is evaluated at the melting point of the earth/rock, and U_∞ is evaluated from the thermal power equation (Equation 6-39).

It is obvious that for practical tunneling, operations should be carried out under the minimum thrust load condition. For any other thrust load, the rate of penetration can be estimated from the relation

$$U = U_{min} \left(\frac{F_T}{F_{T,\,min}} \right)^{1/5} \qquad (7\text{-}50)$$

The validity of this approach is illustrated in Figure 7-8, which is merely another way of illustrating the correlation that has been established.

7.3 EXTENSION TO OTHER MODES/MATERIALS

7.3.1 Extruders

Very limited data had been obtained with a 58 mm extruder in tuff and a 66 mm extruder in basalt, for which descriptions are found in References 7-4 and 7-5, respectively.

Steady state data points are plotted on Figure 7-7. By comparing these data with those obtained with the conical penetraor, it appears that the general trends are identical. However, it is also apparent that for the same power level and total applied thrust load, the rates of penetration attainable with the smaller extruders are lower than those attainable

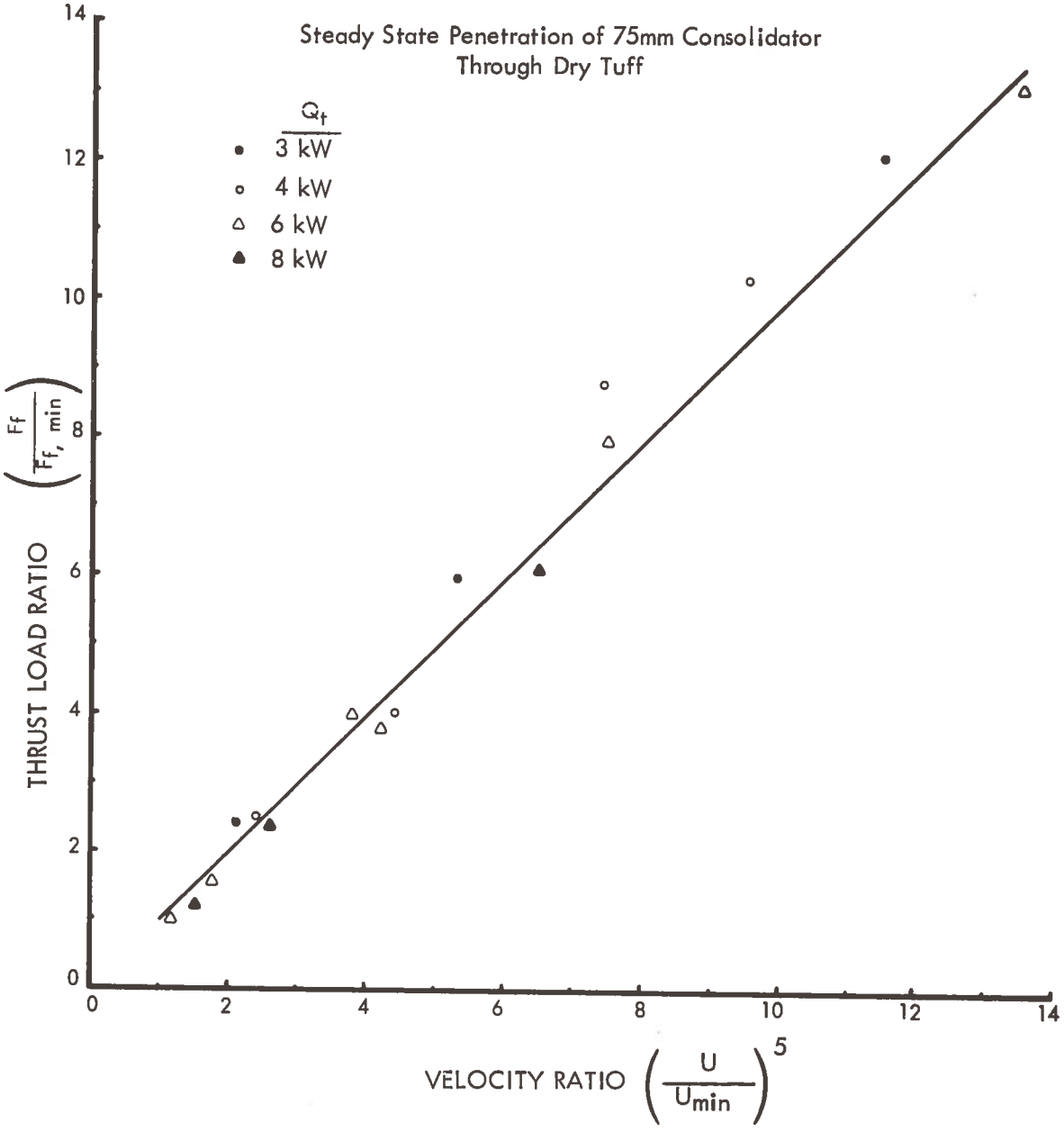

Figure 7-8. Semi-Empirical Correlation of Applied Thrust Load Data

with the larger conical penetrator. Based on thermal power considerations alone, it is expected that for the same thermal power level, a smaller penetrator should yield higher rates of penetration.

These observations suggest that in the extruders tested, a greater portion of the thermal power is consumed in melt superheat because of relatively thick layers of melt in the extruder throat, thus limiting the rates of penetration.

The experimental data on extruders are inadequate for the evaluation of the functional relations developed for the extruders. In particular, data that are needed, but missing, are the following:

- Melt thickness
- Stem losses
- Rate of extrusion, and
- Applied thrust load as a function of thermal power.

It became apparent that the functional relations developed for extruders, Modes 2 through 5, cannot be verified at this time. In any case, the penetrator designs associated with these modes of tunneling are viable only if thin layers of melt are created. It has been suggested that for large scale tunneling, penetrators must be designed with extended surfaces. For such designs, frictional drag due to melt flow over the heated portion may become important. Moreover, new functional relations may be required. The study of these, however, is not within the scope of this program.

7.3.2 Other Materials

Limited experimental data were also obtained for extruders and consolidators operating in alluvium. These data are presented in Figures 7-9 and 7-10. Figure 7-9 gives the data

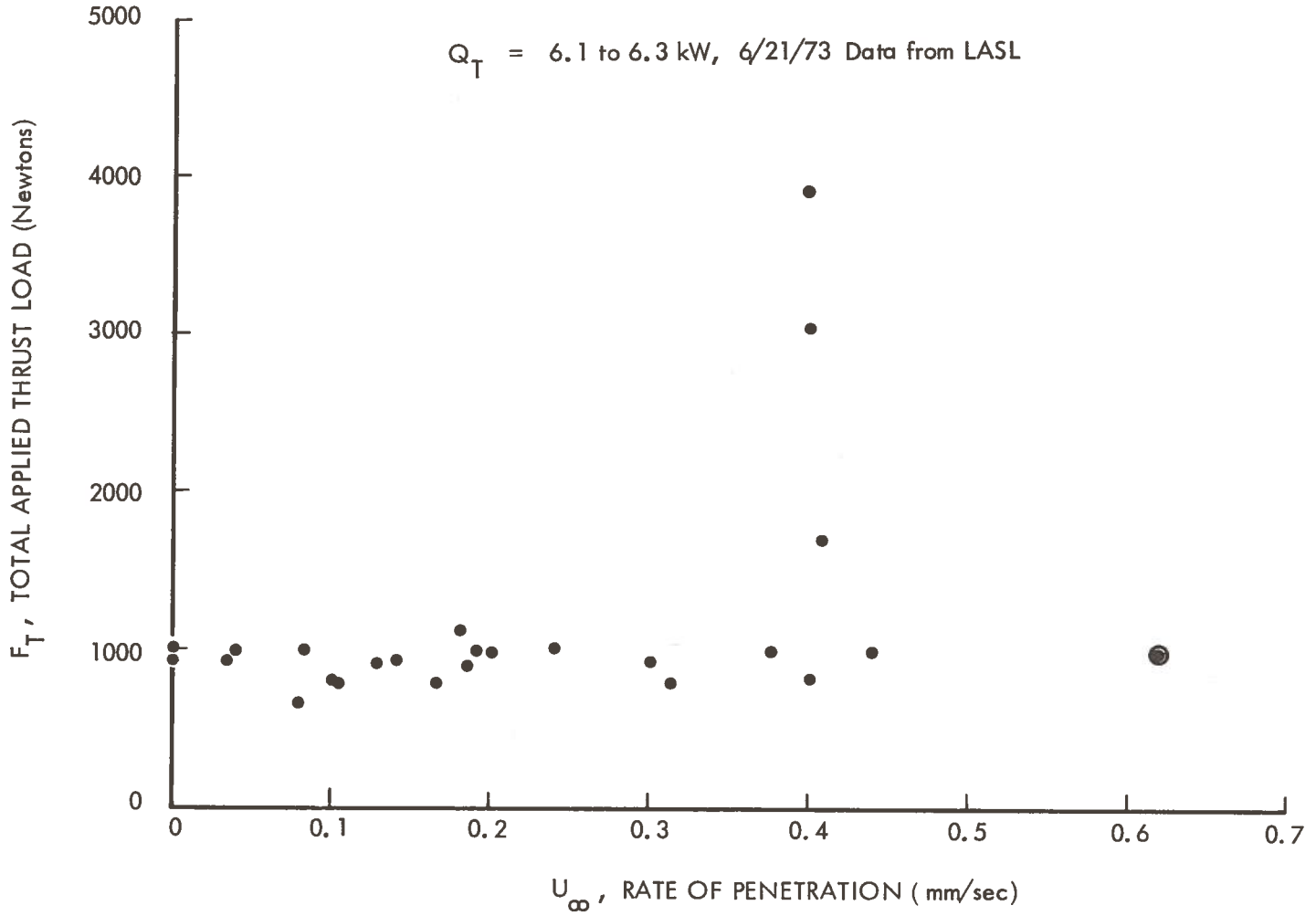

Figure 7-9. Effect of Applied Thrust Loads on the Rate of Penetration Through Alluvium
75 mm Conical Consolidator

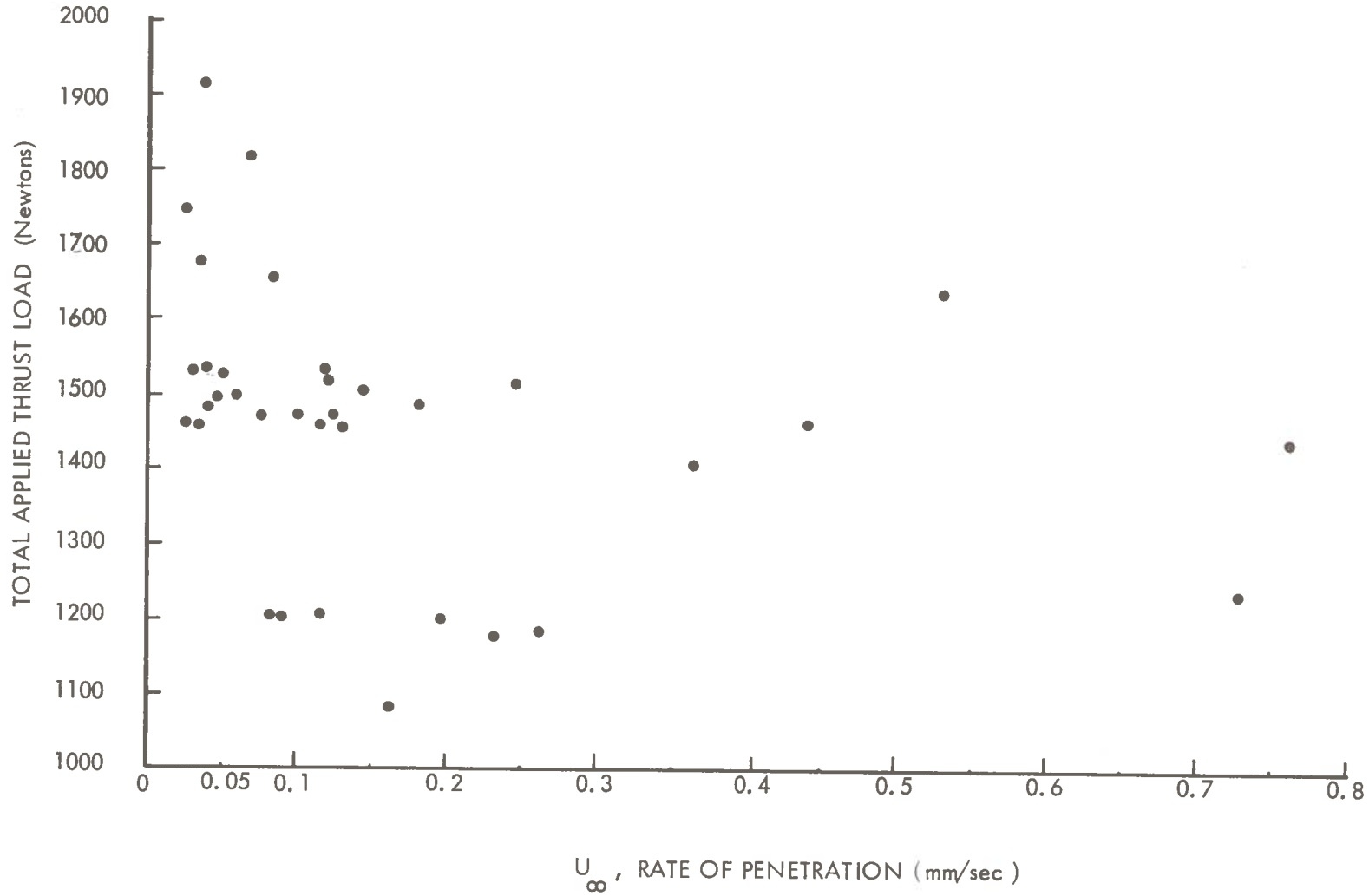

Figure 7-10. Effect of Rate of Penetration on Applied Thrust Load Requirements

obtained with the 75 mm conical consolidator. It can be seen that except for one data point (circled on the figure), the general trend is identical to that observed for tuff (see Figures 7-3 and 7-7). Comparison of these figures suggests that for the same power level, the minimum rate of penetration is greater when tunneling through alluvium than it is through tuff. (about 4 times greater). This is inconsistent with earlier observations with TOTAVI alluvium[7-6]. This inconsistency has not been resolved. It is also observed that the increase in thrust load requirements with increases in the rate of penetration above the minimum (at a constant power level) is much greater for alluvium. This can be explained with reference to Equation (7-47).

$$F_T - S_p P_\infty = a \frac{\mu_m U_\infty^4}{k_m^3 (T_s - T_m)^3} \qquad (7\text{-}47)$$

It has been estimated that the thermal conductivity of alluvium is approximately 1/2 of that for tuff. Even if the viscosities of the melt are about the same, the thermal conductivity effect suggests that above the minimum rate of penetration, the thrust loads required for alluvium is at least 8 times greater than that required for tuff. This effect is also apparent from the minimum applied thrust loads for the two materials. For tuff, the minimum observed total thrust load is on the order of 500 newtons, whereas for alluvium, it is on the order of 800 newtons. By subtracting out $S_p P_\infty$ or 450 newtons, the results give 50 newtons for tuff and 350 newtons for alluvium. The ratio from these values is 7, which provides a reasonable check of the theory. The calculated minimum rate of penetration, based on an assumed stem loss of 850 watts, is 0.38 mm/sec. This is in excellent agreement with the experimental observation of 0.39 mm/sec.

One set of experimental measurements was made with the 66 mm extruder in alluvium. The data given in Figure 7-10, show that in this mode of operation, significant increases in the rate of penetration can be obtained with very little increase in the thrust load above the minimum. This is contrary to the general trends observed. This suggests that for the alluvium material used in the extruder test, the strength of alluvium is relatively low, compared to

that used in the consolidator so that it is readily displaced and compressed to effect high rates of penetration.

7.3.3 Conclusions and Recommendations

The functional relations developed have been verified for Mode 1 where relatively extensive data are available for tuff. For the other modes of tunneling, there is only qualitative agreement with the functional relation because of inadequate data. Experimental data taken with alluvium show inconsistent and anomalous behavior. This may be due largely to the extreme variability in physical properties expected with this type of material. However, these apparent inconsistencies may be resolved when more experimental data become available.

7.4 NUMERICAL ILLUSTRATIONS

The applied thrust load required for tunneling is an important parameter in penetrator design, for it determines the stresses on the penetrator surface and the thrust on the glass wall. The first establishes another potential operating limit, while the second determines the required strength and thickness of the glass liner and the size of the grip pads for propulsion. The previous sections have established the following:

1. The functional relations for large scale corers has not been verified.
2. The penetrator designs associated with the modes of tunneling studied are not viable in large scale tunneling, and
3. Advanced penetrator designs are needed for large scale tunneling.

In view of the above facts and the fact that a design suitable for large scale tunneling has yet to be defined, a simple penetrator geometry is adopted to estimate the thrust load required. This model assumes a corer configuration with a planar frontal heated surface. The side is also heated in order to produce a glass liner. The glass liner thickness required is based on the earth model chosen and the overburden. The amount of overburden

is a function of the depth at which tunnel operations take place. The following were assumed:

1. The melt pressure at the shoulder is equal to the ambient lithostatic pressure, a function of the depth of tunneling (z) only.

2. The length of the melt cooldown section is equal to the penetrator diameter.

3. The applied thrust load is dominated by pressure drag and frictional drag. The latter is due to melt flow over the melt cooldown section.

4. Other thrust load components are relatively small.

Calculations were performed for 6 and 10 meter diameter penetrators. The core diameter was calculated based on the same assumptions used for thermal power estimates (see Section 6.0). Two earth models, UNCON and MASIG, were used. The other models are sufficiently similar to these that UNCON and MASIG should provide adequate illustrations. The melt viscosity over the melt cooldown section was based on the arithmetic average temperature of the melt in this section.

The first assumption gives the maximum melt pressure and the maximum thrust load requirements. In actual practice, the penetrator can be designed so that the melt is extruded continuously along the heated penetrator. In this manner, the melt pressure can be controlled and reduced.

The length of the cooldown section was assumed to be equal to the diameter of the penetrator. This is optimistic; however, it is based on the assumption that the melt cooldown section can be reduced by advanced concepts.

The calculated applied thrust load due to pressure drag and frictional drag is presented in Figures 7-11 and 7-12, respectively. It is noted from Figure 7-11 that the thrust load increases non-linearly with increasing depth of operation. This is due to the increasing overburden pressure. The frictional drag decreases with increasing depth because of the increasing liner thickness required. The total applied thrust load is summarized in Figure 7-13.

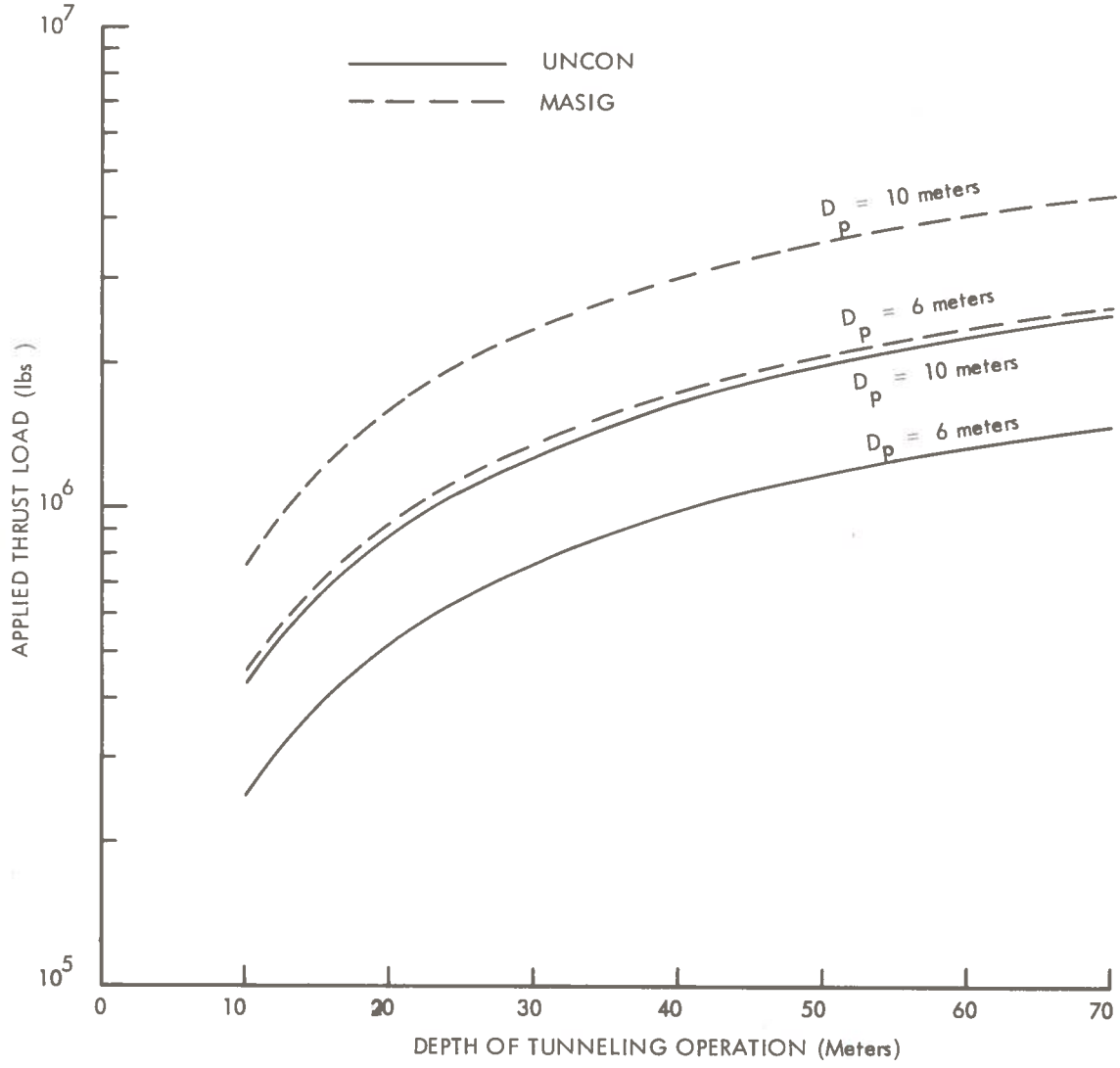

Figure 7-11. Effect of Depth of Tunneling Operation, Tunnel Diameter, and Earth/Rock Materials on Thrust Load Required to Overcome Pressure Drag

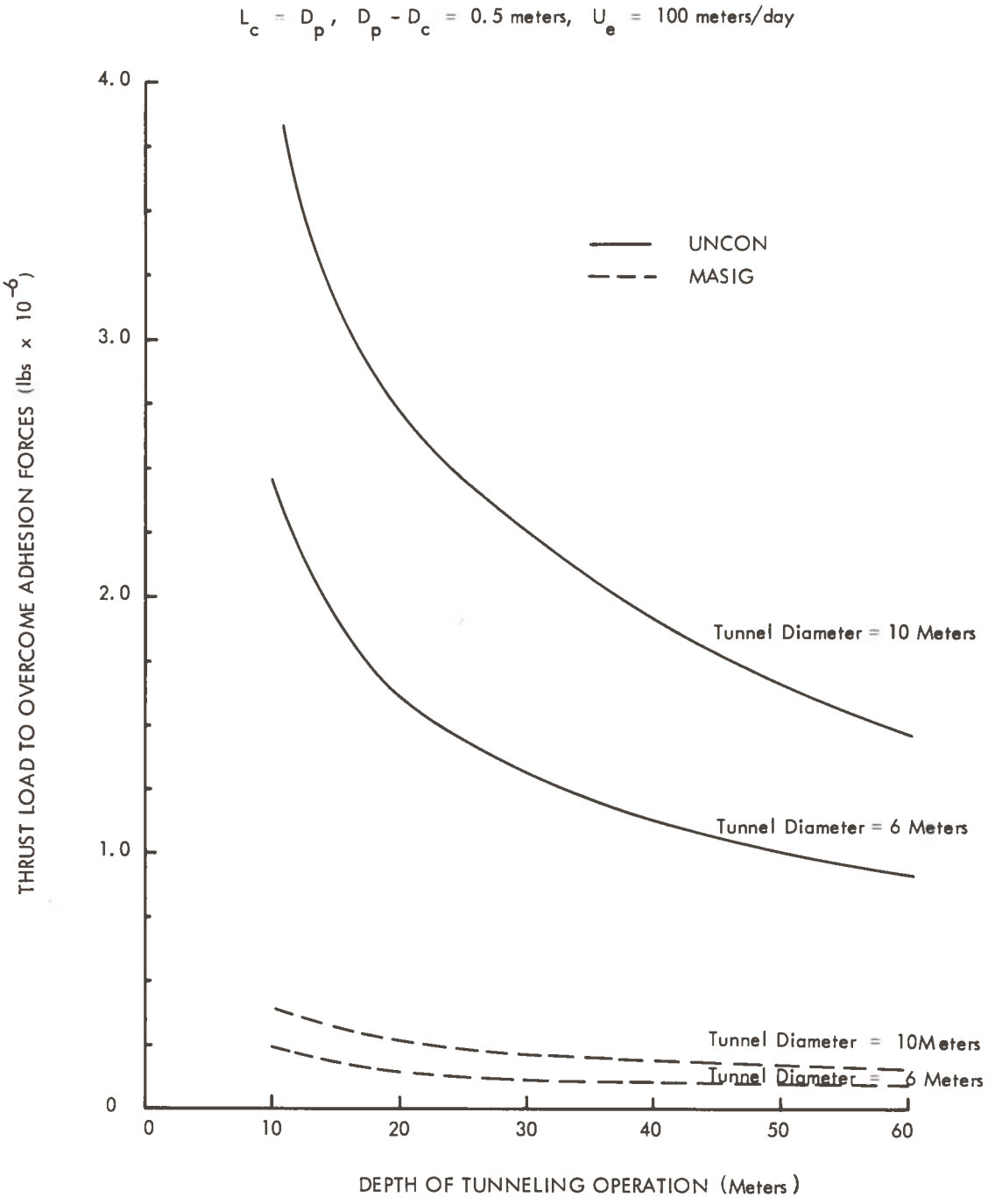

Figure 7-12. Effect of Depth of Tunneling on Required Thrust Loads to Overcome Adhesion Forces

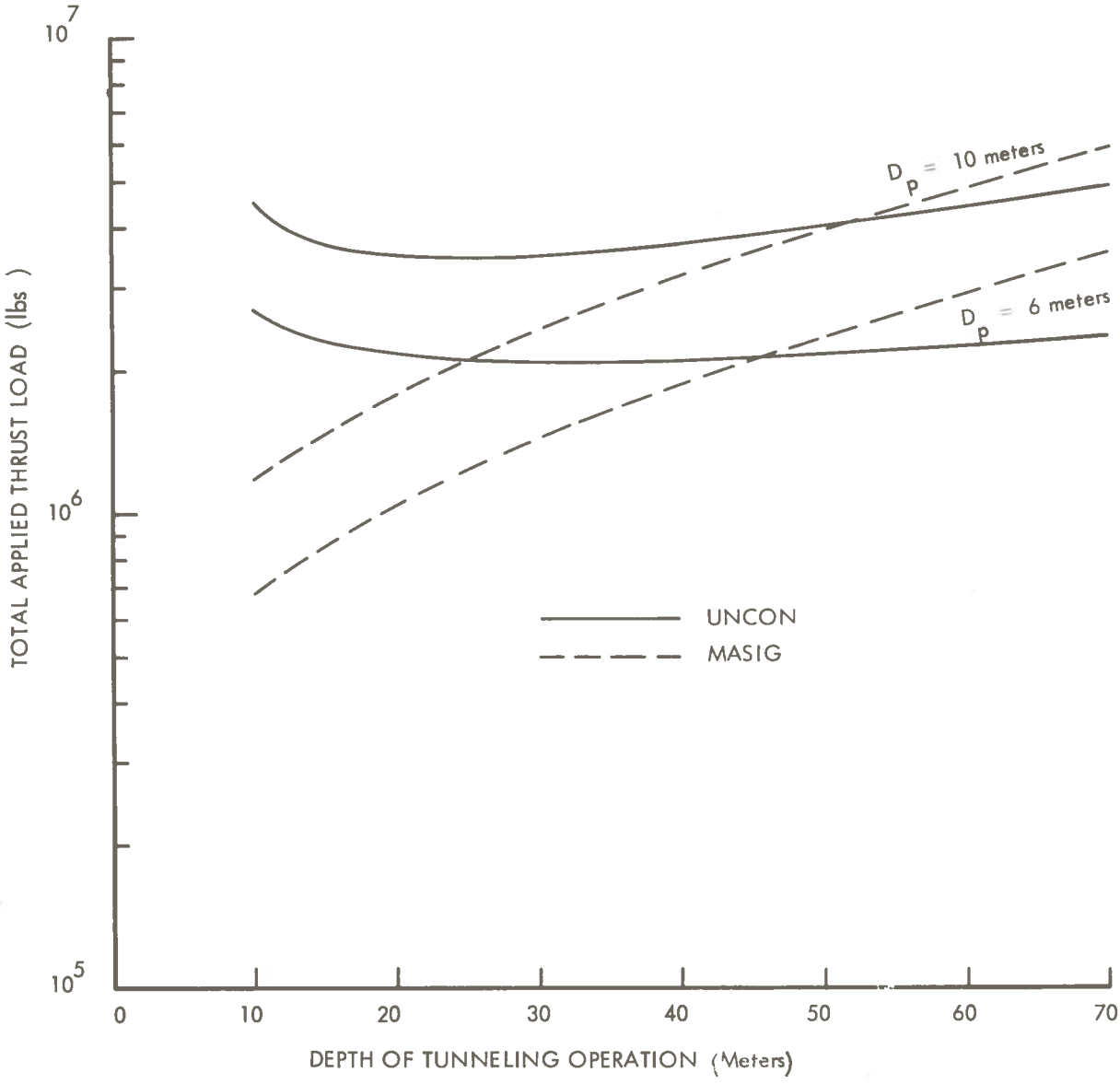

Figure 7-13. Effect of Applied Thrust Loads, Depth of Operation and Tunnel Diameter on Total Applied Thrust Load

The average pressure on the penetrator surface can now be calculated. This is merely the total applied thrust load divided by the penetrator surface area. This pressure is directly dependent on the shape of the penetrator. A tapered shape such as that shown on page 7-13 was assumed. The results of the calculation are shown in Figure 7-14.

It is noted that the mean melt pressure is less than one psi. This low pressure is the result of the relatively large heated surface area assumed, consistent with the assumptions used in the thermal power calculations, i.e., $D_p = L_H$. At the other extreme, the projected area only may be used as an estimate of the maximum melt pressure. The results are shown in Figure 7-15. The effect of tunnel diameter is negligible for tunnels in the 6 to 10 meter diameter range, because pressure drag is the dominant force and it is directly proportional to the projected area.

For large scale penetrators, the melt pressure can be controlled by extruding the melt through the heated sides of the penetrator. This may indeed be a necessary design feature when tunneling through highly consolidated materials. Melt pressure control is also necessary from the standpoint of earth upheaval. It is pointed out in Section 8.0 that the melt pressure must not exceed approximately twice the overburden pressure, otherwise upheaval of the earth's surface (above the penetrator) would take place. It is obvious that this is an undesirable phenomenon that must be avoided.

Finally, the pressure on the penetrator must not exceed the tensile or yield strength of the penetrator material of construction. Figure 6-10 is a plot of the tensile and yield strengths of molybdenum and tungsten as a function of temperature. Unfortunately, data at the higher temperatures of interest are not available. Therefore, the operating limits as a result of surface stress cannot be established at this time.

7.5 REFERENCES

7-1 Bird, R. B., et al., Transport Phenomena, John Wiley and Sons, Inc.,

7-2 McFarland, R. D., "Preliminary Analysis of Fluid Rock Around a Thermal Penetrator," LASL Office Memorandum S-2, April 6, 1971.

7-3 Armstrong, D. E., et al., "Rock Melting as a Drilling Technique," LA-3243, March 15, 1965.

7-4 Neudecker, J. W., et al., "Design and Development of Prototype Universal Extruding Subterrene Penetrators," LA-5205-MS, March, 1973.

7-5 Neudecker, J. W., "Melt Removal Methods in Universal Rock Melters," LASL Memo S-53, October 10, 1972

7-6 Meissner, J. A., "Rock Melting in Wet Alluvium," LASL Office Memorandum S-55, October 11, 1972.

8.0 EARTH STRUCTURAL

This evaluation is presented to describe earth rupture conditions either at the tunnel wall adjacent to melt or at the earth's surface. Rupture or fracture induction at either of the boundaries is assumed to occur when tensile stress exceeds the modified strength. Strength modifications are positive when stress is compressive, and strength is referred to here as a modification because it is assumed that earth samples in the size range of 3 to 10 m diameter possess zero parent material tensile strength. Furthermore, it is assumed that earth cohesion is small compared to crack tip stress intensities and therefore it is neglected. Both of these assumptions may appear conservative, but statistically they are quite realistic and likewise practical when compared to the extreme determination of earth flaw (non-continuous) probabilities over a given length and depth of tunneling through various media, both locally and regionally over the continental U.S.A. Consequently, the earth's strength is defined in this work as the compressive stress which will resist the fissure creating tensile stress induced by melt pressure.

There are three mechanisms that can produce a compressive stress in the tunneling zone.

1) The compressive overburden and the resultant horizontal condition of elastic or plastic equilibrium (S_o):
   A problem to be considered here is the disturbance of this original condition of stress when the mass of earth is pierced by a tunnel. There are conditions given in Reference (8-1), to be discussed later, in which mass removal can produce a disturbance of tensile stress, thereby providing some negative strength input to the superposition of strength inputs.

2) Tectonic compression and the influence of mountain topography upon overburden (S_T): The presence of either of these earth compressive mechanisms provides for additional earth strength. It would therefore be conservative to assume their absence when evaluating earth effects. But, these loads do provide additional increments which must be supported by the glass liner, and therefore they may not be ignored when considering liner effects. The effect of mountainous topography upon in situ stresses can be estimated by considering the mountains to be distributed loads on the boundary of a semi-infinite plane. Tectonic stress can, as demonstrated in Reference (8-2), only be inferred as the difference between an actual site measurement and the calculated in situ stresses. The tectonic stress values could be due to present-day straining of the earth's crust or to elastic strains locked into the earth's crust during past tectonic events.

3) Thermal compressive stress (S_E):
The free thermal expansion of the heated region of unmelted earth is prevented by the surrounding restraint of unheated earth. The heated earth zone is therefore in a state of compression.

The tensile stress field(s) is produced by fluid melt pressure and potentially assisted by superheated water vapor pressures; and if it exceeds the above combined mechanisms of compression at either the tunnel or earth surface, an earth fracture will be initiated. The equation for fracture induction is:

$$s > S_o + S_T + S_E$$

8.1 OVERBURDEN STRESS (S_o)

The problem here is to establish the state of stress in the earth which has been disturbed by mass removal to form a tunnel. Only the disturbance to the earth's initial condition of elastic equilibrium associated with mass removal is considered here. The thermal, tectonic and melt pressure disturbances to be examined later will then be superimposed upon this separate effect from mass removal. By separating the thermal, tectonic and melt pressure disturbances from the total stress field, it is assumed that these do not depend on a body force potential such as gravity. This must be considered a significant term in the stress field equations of equilibrium for the problem of mass removal when tunneling in close proximity to the earth's surface.

The basic assumptions applied to achieve a solution to overburden stress disturbances follow:

1) The methods of the theory of elasticity are applied to an isotropic, homogeneous media.

2) The length of the tunnel is assumed to be large in comparison to its diameter, and combined with assumed uniformity of body force, the problem treatment is one of plane strain.

3) The surface of the earth is "level" and free of dead-weight.

Although assumption 1) appears to be quite idealistic, there is significant field data on both wellbore fracturing operations and corresponding surface uplift provided in References (8-3), (8-4), and (8-5) to substantiate that predictions can be bracketed by elastic laws. But, the basic justification for assumption 1) should be the requirement that an understanding of the approachable ideal situation is a prerequisite for further study or qualitative inferences concerning anomalous conditions.

The plane strain assumption, 2), for tunneling is quite realistic, but there is inherent conservatism to be found here because the earth's region of interest is located in a plane occupied by melt which is not too far from the penetrator tip. In other words, the uncompleted tunnel always has a "dead end". Here, the end effects will be neglected, even though the plane of interest is only one heated penetrator length from the penetrator foreward tip. The net result of neglecting this semi-infinite end cap will be a prediction of less compression than the actual hoop-type compression, and this is conservative because hoop compression is considered here to be equivalent to strength.

Assumption 3) simply provides for superposition in that if tunneling is conducted in mountainous terrain the added load effects can be given separte treatment within the category of tectonic and topographic effects. Furthermore, tunneling is generally considered removed from the foundation loading effects of the large structures found within and around the cities.

The problem solution of mass removal effects upon overburden loads has been extensively treated in the literature by Yamaguti[8-6], Anzo[8-7], and more recently by Mindlin[8-1]. Without reproducing their works, a description of the general solution approach will be given here along with the pertinent results derived by Mindlin.

The problem involves expressing the components of stress in terms of the body force potential and derivatives of a stress function. Through the introduction of a bipolar co-ordinate system an exact solution of the classical elasticity equations is obtained by finding a solution to the stress function differential equation that satisfies the particular boundary conditions. The boundary conditions are that normal and shearing stresses are zero at the earth's surface and at the tunnel's surface. At a great distance below the tunnel, there is a zero shear stress and a uniform normal stress equal to the overburden. On vertical planes normal to the earth's surface and situated at a great distance from the tunnel, the distribution of stress will depend upon the state of stress assumed to have existed in the earth before the boring of the tunnel.

Three conditions for the initial undisturbed state of stress were considered by Mindlin in order to include a great range of possibilities for this initial state of stress. These conditions as shown on Figure 8-1 are:

Condition I

The solid is initially under a state of isotropic pressure. The stress in the earth at great depths is probably in this state, approximately. Under this condition, the lateral boundary condition is a linear distribution of normal pressure.

$$\sigma_x = -\rho_e y$$

Condition II

It is assumed that initially (long before the boring of the tunnel) the material was restrained from lateral displacement during a supposed application of the gravitational field. In this case the lateral pressure is

$$\sigma_x = -\frac{\nu}{1-\nu}\rho_e y$$

Condition III

An assumption which might be made is that there is no lateral stress at all in which case the initial stress system is

$$\sigma_x = 0$$

For all three cited conditions the body force potential is equal to

$$\Omega = -\rho_e y$$

In these expressions

$\rho_e \equiv$ weight per unit volume of material

$\nu \equiv$ Poisson's ratio

Condition I
(Hydrostatic Pressure)

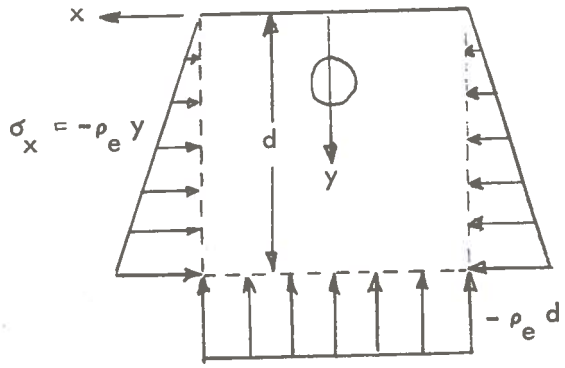

Condition II
(No Lateral Deformation)

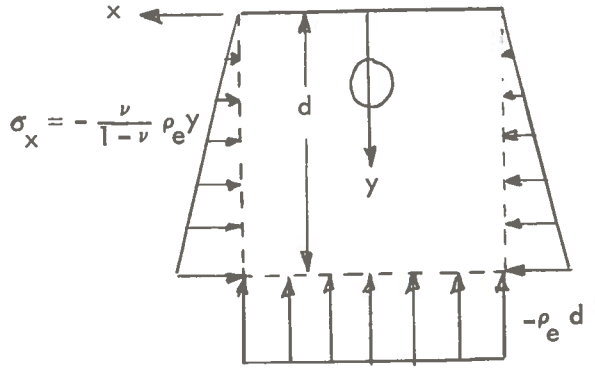

Condition III
(No Lateral Restraint)

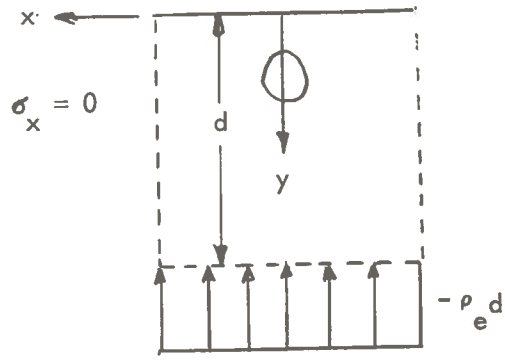

Figure 8-1. Overburden Model Boundary Conditions

The solutions are given in bipolar co-ordinates. Figure 8-2 is provided for definition of terms which relate the bipolar co-ordinate system (α, β) to the rectangular Cartesian system (x, y).

$$x + iy = i a \coth \frac{1}{2} (\alpha + i\beta)$$

$$x = \frac{a \sin \beta}{\cosh \alpha - \cos \beta}$$

$$y = \frac{a \sinh \alpha}{\cosh \alpha - \cos \beta}$$

or, conversely (see Figure 8-3)

$$\alpha + i\beta = \ln \frac{x + i\,(y + a)}{x + i\,(y - a)}$$

$$x + i\,(y + a) = r_1 e^{i\theta_1}$$

$$x + i\,(y - a) = r_2 e^{i\theta_2}$$

$$\alpha = \ln \frac{r_1}{r_2}$$

$$\beta = \theta_1 - \theta_2$$

The curves α = constant are coaxial circles of radius

$$R = a \operatorname{csch} \alpha$$

having poles $(0, -a)$ and $(0, +a)$ as limiting points. The centers of these circles lie on the y-axis at distances $a \coth \alpha$ from the origin. A parameter of interest in the stress solutions which identifies the relative tunnel depth is the ratio C/R, where C is the distance from the center of the hole to the free surface and R is the hole radius.

$$C/R = \frac{a \coth \alpha_1}{a \operatorname{csch} \alpha_1} = \cosh \alpha_1$$

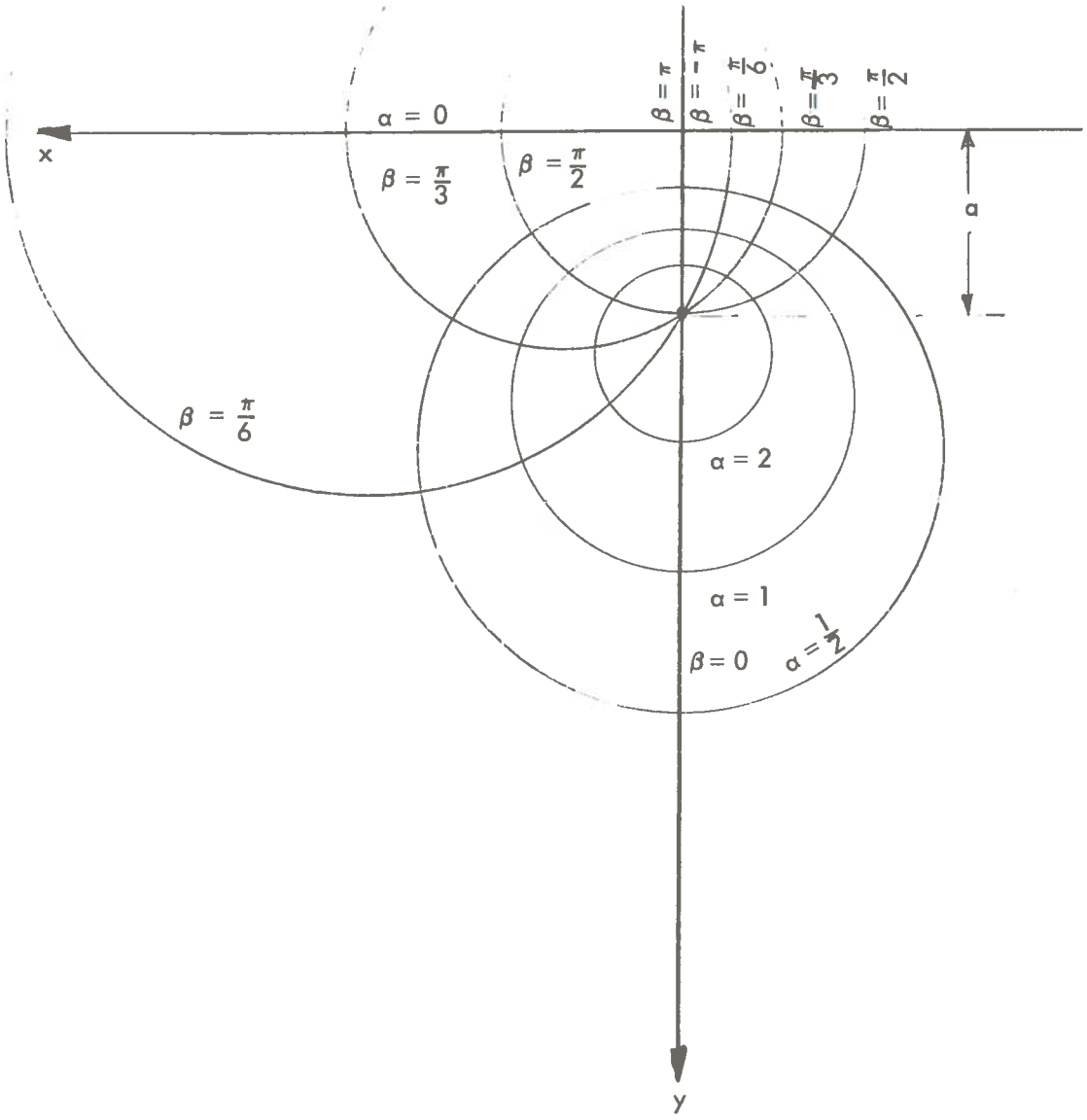

Figure 8-2. Bipolar Coordinates

(Values of a and $\beta \neq 0$ or π Are Provided To Only Illustrate the Trend of Increasing Values)

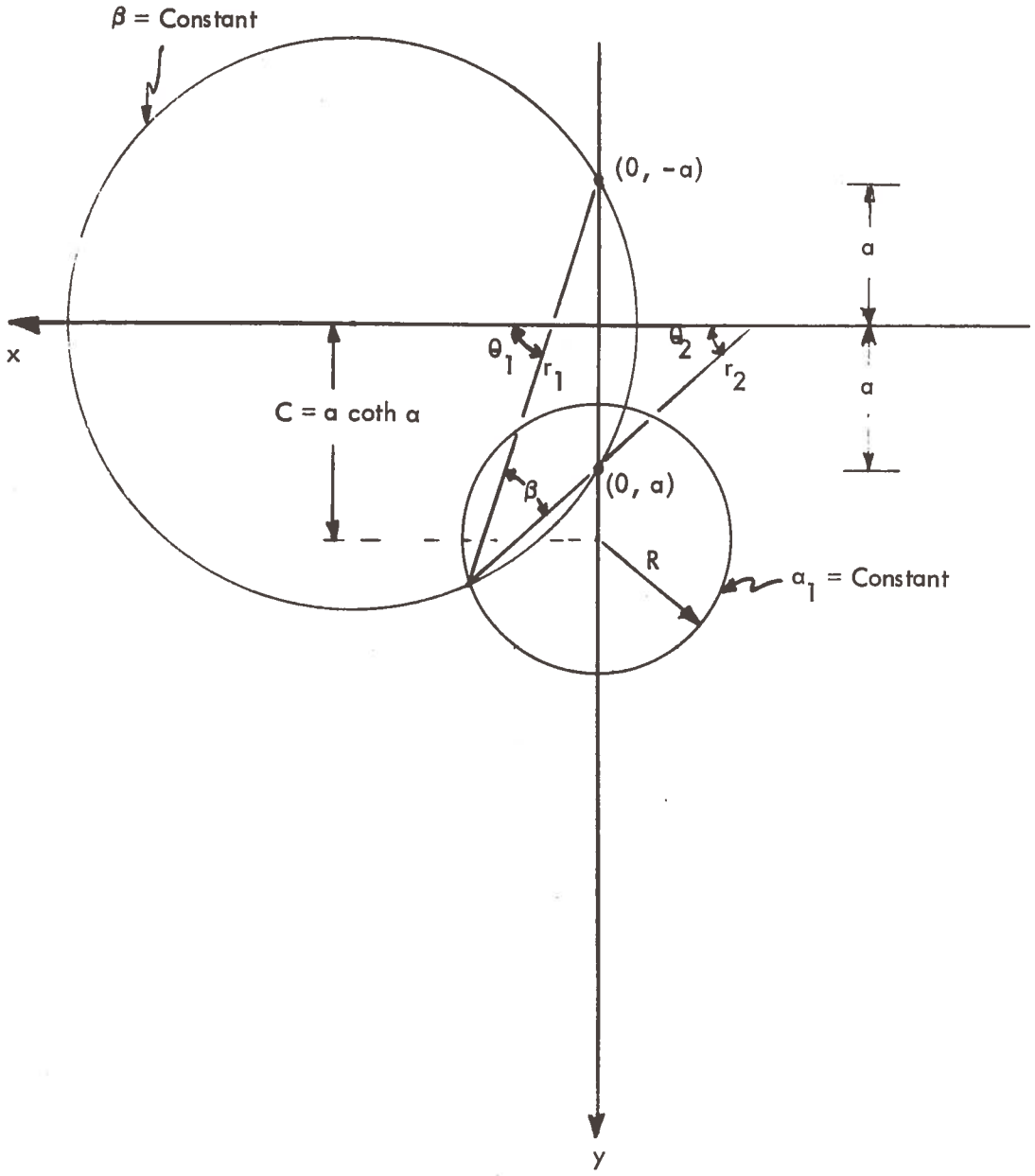

Figure 8-3. Additional Relationships for the Bipolar Co-Ordinates

The subscript (1) denotes the circle $\alpha = \alpha_1$ which is used to define the tunnel perimeter.

The principal stress component tangent to the α = constant curves in bipolar representation as related to the body force potential (Ω) and the stress function (ψ/J) is:

$$S_o = \frac{1}{a}\left\{(\cosh\alpha - \cos\beta)\frac{\partial^2}{\partial\alpha^2} - \sinh\alpha\frac{\partial}{\partial\alpha} - \sin\beta\frac{\partial}{\partial\beta} + \cos\beta\right\}(\psi/J) + \Omega$$

In essence this is the newly created hoop stress along α = constant which is different from the original undisturbed stress field.

The stress function as derived by Mindlin[8-1] is:

$$\begin{aligned}
\left(\psi/J\right) = {} & -\frac{1}{2}\rho_e a^2 \operatorname{csch}^2\alpha_1 \left\{\sin\beta \arctan\left(\frac{\cosh\alpha\cos\beta - 1}{\sinh\alpha\sin\beta}\right)\right. \\
& -\frac{1-2\nu}{2(1-\nu)}\alpha\sinh\alpha + \frac{5-6\nu}{2(1-\nu)}\coth\alpha_1(\cosh\alpha - \cos\beta)\alpha \\
& -\frac{3-4\nu}{4(1-\nu)}(\cosh 2\alpha - 1)\cos\beta + \frac{1}{2}\left(\frac{5-6\nu}{2(1-\nu)}\coth\alpha_1 - 1\right)\sinh 2\alpha\cos\beta \\
& + \sum_{n=2}^{\infty}\frac{2\sinh\alpha_1 e^{-n\alpha_1}}{\sinh^2 n\alpha_1 - n^2\sinh^2\alpha_1}\left[\sinh n\alpha_1 \sinh n\alpha \sinh(\alpha - \alpha_1)\right. \\
& \left.\left. - n\sinh\alpha_1\sinh\alpha\sinh n(\alpha - \alpha_1)\right]\cos n\beta\right\} \\
& + G\rho_e a^2\left\{\cosh\alpha + 2\sum_{n=1}^{\infty}(\cosh\alpha + n\sinh\alpha)e^{-n\alpha}\cos n\beta\right. \\
& + B_o\left[\alpha(\cosh\alpha - \cos\beta) + \sinh\alpha(\cosh\alpha\cos\beta - 1)\right] \\
& + A_1(\cosh 2\alpha - 1)\cos\beta + \sum_{n=2}^{\infty}\left(A_n\left[\cosh(n+1)\alpha - \cosh(n-1)\alpha\right]\right. \\
& \left.\left. + E_n\left[(n-1)\sinh(n+1)\alpha - (n+1)\sinh(n-1)\alpha\right]\right)\cos n\beta\right\},
\end{aligned}$$

where

$$B_o = 3 \coth \alpha_1 \operatorname{csch}^2 \alpha_1$$

$$A_1 = -3/2 \operatorname{csch}^2 \alpha_1$$

$$E_n = \frac{n \sinh \alpha_1 (n \sinh \alpha_1 + \cosh \alpha_1) + e^{-n\alpha_1} \sinh n\alpha_1}{\sinh^2 n\alpha_1 - n^2 \sinh^2 \alpha_1}$$

$$A_n = -\frac{n(n^2 - 1) \sinh^2 \alpha_1}{\sinh^2 n\alpha_1 - n^2 \sinh^2 \alpha_1}$$

$G = 0$ for Condition I (Isotropic Pressure)

$G = \frac{1 - 2\nu}{6(1 - \nu)}$ for Condition II (Elastic Equilibrium)

$G = \frac{1}{6}$ for Condition III (No Lateral Restraint)

In Reference (8-1) the solution of this equation is provided in detail for the stress $(S_o)\ \alpha = \alpha_1$ on the boundary of the hole. Figure 8-4 contains the results corresponding to $\beta = \pi$ which is at the very top of the hole. Reference (8-1) also provides tabular results of $(S_o)\ \alpha = \alpha_1$ as β sweeps from 0 to π in 20° increments, and this tabulation shows that for $\nu \neq 0$ and for $(C/R) > 1.5$ that indeed the location of $\beta = \pi$ is the location of maximum tension (or least compression) for Conditions I and II. Condition III which isn't considered to be an appropriate earth model has its maximum tension at the location of $\beta = 0$ which is at the hole bottom location.

Referring to Figure 8-4 some pertinent conclusions are:

1) The wide variation of the stresses for the three separate conditions shows the necessity of knowing the initial state of stress.

2) The apparent great change in the stresses of Condition II shows the necessity of knowing Poisson's ratio values.

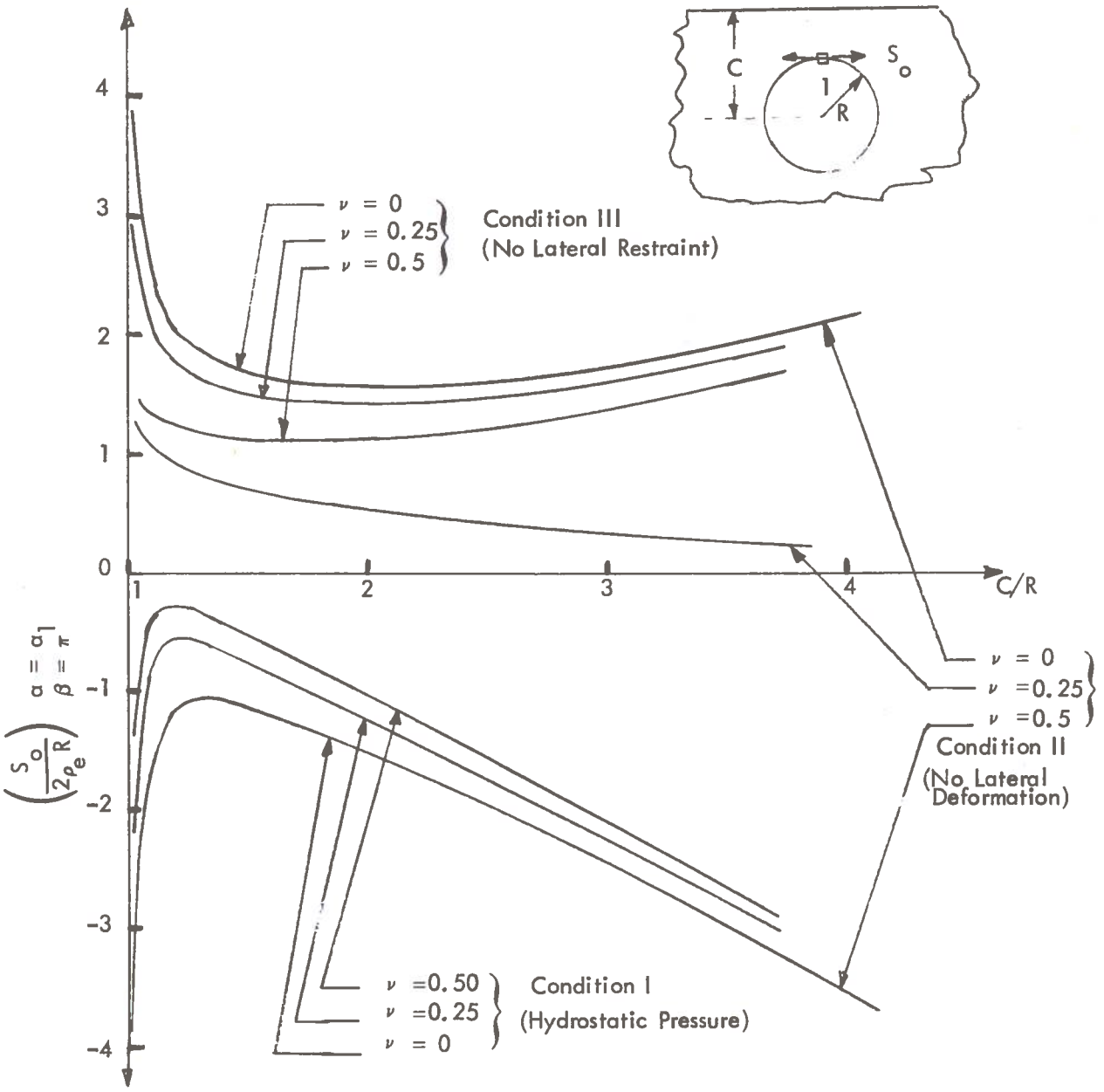

Figure 8-4. Hoop Stress at Tunnel Top Surface for Mass Removal Effect Upon Different Lateral Conditions

3) Conditions I and III provide very useful information as limiting conditions for Condition II which is the most probable earth model. With $\nu = 0$ in Condition II, there are no lateral strains created by an overburden, which by definition requires no lateral restraint, and therefore Condition II degenerates to Condition III. With $\nu = 1/2$ in Condition II, by definition the material is perfectly plastic, and therefore the resultant isotropic pressure degenerates Condition II to Condition I. In essence, this explains the wide range of possible stress conditions when the initially existent lateral pressure defined by Condition II is:

$$\sigma_x = - \frac{\nu}{1 - \nu} \rho_e y$$

4) When $C/R < 1.2$ the stresses rapidly increase in magnitude as the hole approaches the upper surface of the earth, and therefore the choice of a 10 foot tunnel depth would appear to be a safe choice from the aspect of magnified mass removal effects evident in the $C/R < 1.2$ range.

Attention is now focused upon a likely earth model from which additional conclusions may be drawn.

Under the influence of the vertical overburden load, rock tendency would be lateral expansion; but the surrounding material offers constraint. This tendency induces a horizontal stress which, in the ideal situation, is equal in all horizontal directions. In the elastic zones of the earth's crust the relationship between the vertical stress and the induced horizontal stresses should be governed by the elastic laws and be expressed by the equation given for Condition II:

$$\sigma_x = - \frac{\nu}{1 - \nu} \rho_e y$$

The relationship between the stresses in much of the earth's crust is governed by nonelastic properties, the shear strength, cohesiveness, and frictional resistance to deformation. It has been shown in Reference(8-8) that this Condition II relationship can be approximated by the below equation where f is the coefficient of internal friction of the earth material.

$$\sigma_x = - \frac{1}{\left(f + \sqrt{1 + f^2}\right)^2} \rho_e y$$

This condition by which principal stresses may be governed by other than the material's elastic properties is often called the plastic state of stress. This equation can describe Condition I, that of isotropic pressure restraint, only when the material's coefficient of internal friction is zero. The unrealism of this condition for earth materials would therefore eliminate Condition I as a probable earth model. This is consistent with the fact that normal faulting, generally recognized as a manifestation of shear, is occurring in many areas at the present time. Similarly, this equation can describe Condition III, that of no lateral restraint, only when the material's coefficient of internal friction is infinite. The unrealism of this condition for earth materials would eliminate Condition III as a probable earth model. Therefore, it is Condition II bounded by the limiting cases of $\nu = 0$ and $\nu = 1/2$ that will now receive detailed treatment as the most probable earth model; but before further considerations are made, cognizance should be taken of the not uncommon belief that the competent formations of the earth's crust support the overburden in such a way as to lessen the vertical stress in underlying formations. In Reference (8-3), citation is made upon the analyses of Hubbert[8-9] which indicated that the effective strength of formations of reservoir size is negligible. This tends to support the initial assumption made in this work that earth sample sizes in the range of 3 to 10 m diameter possess zero parent tensile strength. Others[8-10], investigating the strengths of natural arches, have found that in order to support even moderate loads over geologic time, arches must rise almost as high as they span. Therefore, it appears that in all cases the vertical stress of overburden is expressed as, $-\rho_e y$, as previously assumed.

In Reference (8-1), Midlin did not derive the limiting values of stress for Condition III as the C/R ratio becomes large. He did present the limit values for Conditions I and II at $\beta = \pi$ as follows:

$$S_I = -2\rho_e C + \rho_e R \frac{(3 - 4\nu)}{2(1 - \nu)}$$

$$S_{II} = \left[\rho_e C - \frac{\rho_e R}{2}\right]\left(\frac{1 - 4\nu}{1 - \nu}\right)$$

The first term in these equations represents the overburden and the twice-stress concentration factor to be expected for Condition I. The second term represents the mass removal effect. The Condition I equation is quite accurate for C/R greater than about 2, because at these depths the mass removal term becomes quite small compared to the overburden load. This same statement cannot be made concerning the Condition II equation because error percentages can be quite large as ν approaches 1/4, but the statement that error magnitudes would be small for C/R greater than 2 is in fact true.

It was observed from Mindlin's work that the similar limiting equation could be derived for Condition III with relative ease. In Reference (8-1), it was observed that

$$S_{II} = S_I + \frac{1}{6}\frac{(1 - 2\nu)}{(1 - \nu)} F$$

$$S_{III} = S_I + \frac{1}{6} F$$

where F was a function of many variables which for the limiting value of large C/R is solvable in terms of S_I and S_{II}. Substitution into the latter equation yields:

$$S_{III} = \rho_e C - \frac{\rho_e R}{2(1 - \nu)}$$

This derivation was made only to corroborate for large (C/R) that:

$$S_{II} = S_{I} \quad \text{when} \quad \nu = \frac{1}{2}$$

and

$$S_{II} = S_{III}, \quad \text{when} \quad \nu = 0.$$

Attention is now focused upon Figure 8-5 for Condition II which is considered to be the most representative earth overburden model. The solid curves show solutions from Mindlin's work[8-1] in the range of relatively small C/R. The dashed curves represent the solutions for relatively large C/R. Since Poisson's ratio, ν, for sedimentary rocks ranges between 0.18* and 0.27[8-11], the algebraically largest hoop stress at the tunnel surface is likely to be tensile. To generalize the condition in which principal stresses are governed by other than the material's elastic properties, the strong sedimentary rocks have coefficients of internal friction, f, in the vicinity of 0.7[8-8]; and further if it is assumed that f is relateable to an equivalent Poisson's ratio, ν, then this corresponds to a 0.21 Poisson ratio on Figure 8-5. The coefficient, f, for softer shales, clays, and loosely consolidated sands lies in the vicinity of 0.3[8-8]. For these materials, Figure 8-5 indicates the algebraic maximum hoop stress to be compressive at the 0.36 equivalent Poisson's ratio. A conclusion that should be made at this time about strength modifications to an earth which is assumed to possess zero parent tensile strength is that the contribution from earth removal perturbations, S_o, is in general negative for strong sedimentary rock models; and it is likely to be favorably positive in the softer or loosely consolidated materials. A conclusion that may be of value once all other earth stress field perturbations have been evaluated is that if $C/R > 2$, the stress at the earths surface should be insignificant due to mass removal perturbations. This is apparent from Figure 8-5 by observation for these larger values of C/R that the mass removal effect term in stress equations is small.

*Earth/rock properties may be altered by the passage of a heat wave from a Subterrene tunneler. Data on this transient effect are not available, so that the original unheated material properties are used herein.

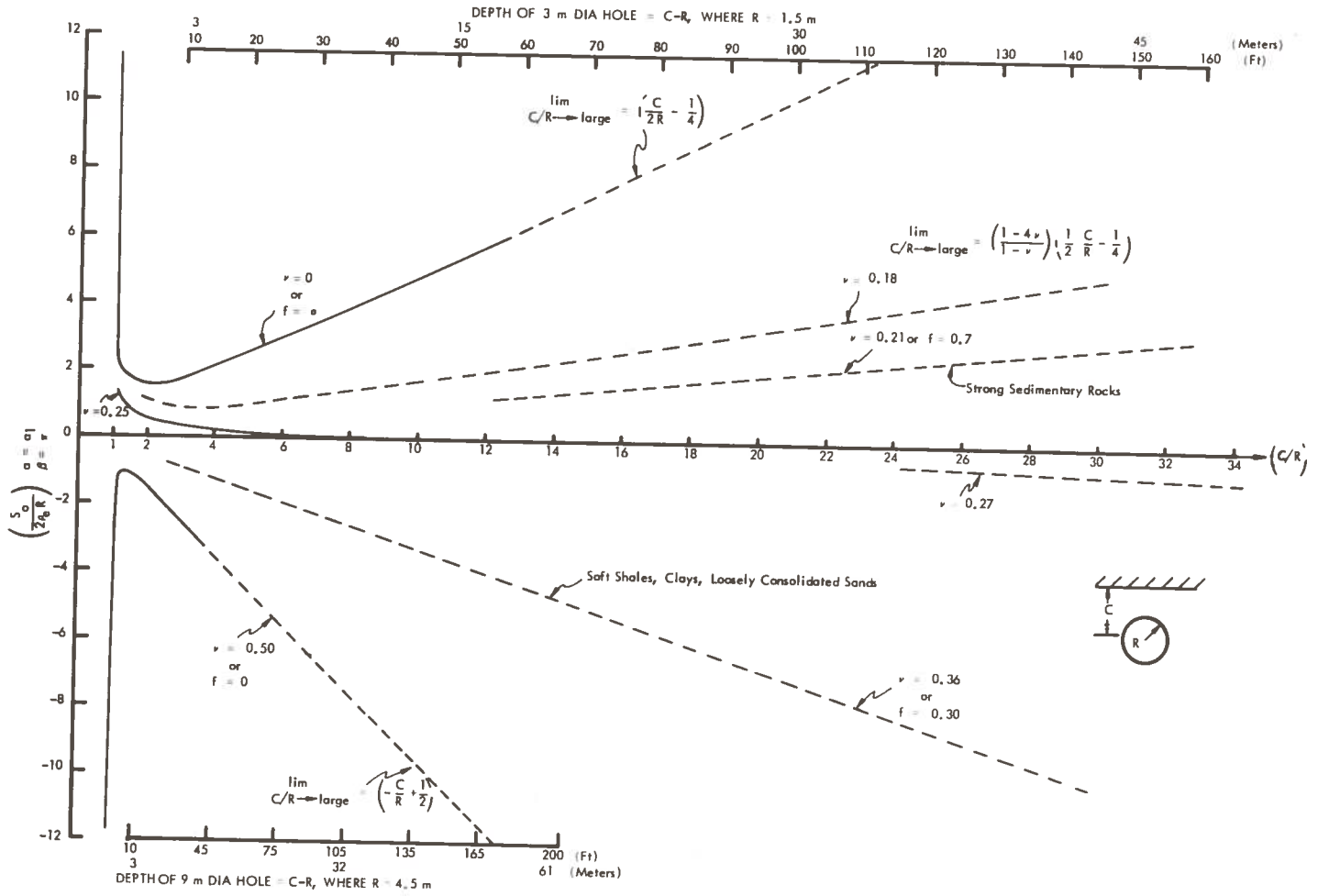

Figure 8-5. Hoop Stress at Tunnel Top Surface

Some additional information provided on Figure 8-5 is the variation of hole depth with the C/R ratio for both 10 and 30 foot diameter holes. It should be recognized from the previous development that penetrator diameter and liner thickness are related to tunnel radius by

$$2R = D_p + 2\delta$$

8.2 TECTONIC COMPRESSION AND THE INFLUENCE OF MOUNTAIN TOPOGRAPHY (S_T)

The residual tectonic and the additional topographic overburden loads could be superimposed upon the in situ conditions that would prevail in their absence. The superposition of tectonic residuals, if known, would be readily expressible if it is assumed that this stress exists uniformally at large distances from the tunnel. The presence of a mountain creates a locally nonuniform overburden which could influence the mass removal perturbations. Consequently, efforts here would require transforming the presence of a mountain into some equivalent extra depth. For tunneling under or through mountains approximate solutions can be obtained by the methods provided in the previous paragraph concerning mass removal effects. However, there are a number of reasons why efforts to model the tectonic and the topographic overburdens could lead to serious theoretical misrepresentations mainly due to the unknown variable of previous geologic history. Some pertinent observations given in Reference (8-12) concerning geologic history summarize the problem. Mountains infer valleys. The erosion of stream valleys through the sedimentary sequence may relieve horizontal stresses near the valley walls and lead to a stress concentration near the valley floor analogous to the stress rarefractions and concentrations around a notch in a tension or compression structural member. The erosion and removal of a significant depth of overlying material over a wide area will lead to a reduction of the vertical overburden stress proportional to the depth removed; but the horizontal stress would not be reduced proportionally due to any inelastic behavior of the earth. This same effect can be produced by the melting of great thicknesses of ice such as existed in areas of continental glaciation during the Pleistocene. The only conclusion which can be drawn concerning a tectonic residual is that they are very intimately related to unknown details of the geologic environment.

The influence of tectonic residuals would be one of favorable compression at certain tunnel depths and as such they could be conservatively neglected. If in the event these are experimentally measured in a geologic site as the difference between the estimated overburden and the actual site measurement, its effect upon the earth's surface and the tunnel wall surface could be evaluated from Equations (2.180) and (2.181) on page 124 of Reference (8-13).

The essential conclusion from these equations is that at large C/R the tectonic compressive stress would be concentrated by a factor of three at the tunnel top and bottom locations due to the presence of the hole. But, a tensile stress of value equal to the tectonic magnitude would exist at the wall location identified by the intersection of a horizontal plane passing through the tunnel centerline. Figure 8-6 is a plot of stress values at several locations near the tunnel, and the computed data are from Table 21, page 127 of Reference (8-13). On this figure the uniform tectonic stress is p_t, and S_T is the stress given at points A, O, and B. The examination of stress at point O indicates a tensile stress at the earth's surface for $C/R < 2$. Consequently, even though the tectonic stress, p_t, may be an unknown, its adverse effects such as a surface fissure can be precluded by tunneling at a depth (O-A) greater than the tunnel radius. At a tunnel depth of twice the tunnel radius, $C/R = 3$, all stresses are closely approaching their assymptotic values, and the net effect when combined with mass removal perturbations is to shift the location of the algebraically largest stress from point A in the direction of point B. Therefore, with large enough tectonic stresses the probable fracture direction would be horizontal rather than vertical indicating that fracture propagation would have to overcome the vertical overburden load. Without tectonic compression, the probable fracture direction is vertical, in which case propagation must only overcome a horizontal stress less than the vertical overburden.

If tectonic stresses are to be measured as the difference between computed overburden stresses and measured overburden stresses, Reference (8-2) provides the methods. If the computed determination of stresses must consider the influence of topography, page 89 of Reference (8-14) provides the applicable equations.

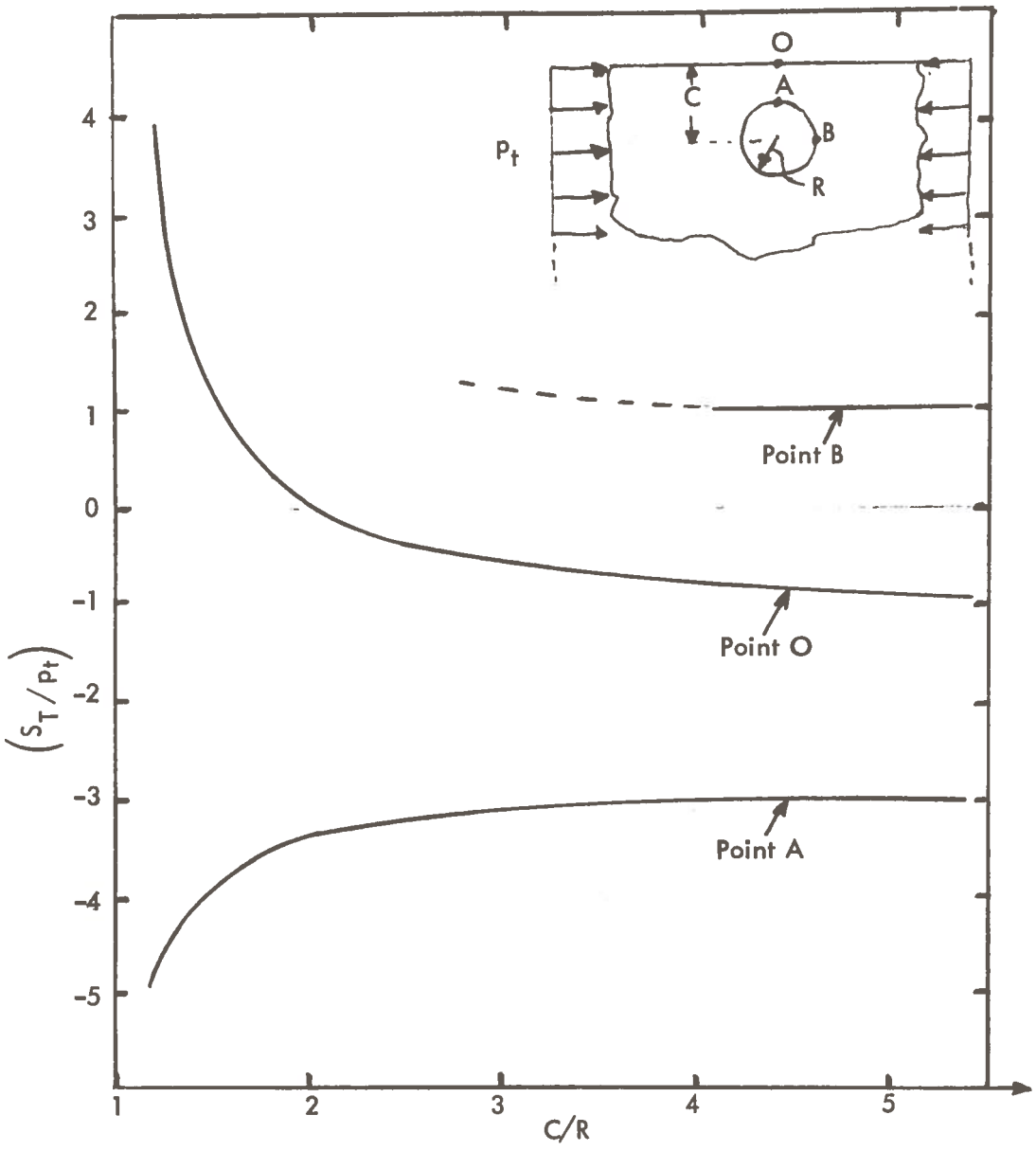

Figure 8-6. Circumferential Stresses from Uniform Compressive Tectonic Stress, p_t

The effects of overburden, tectonics and mass removal perturbations upon the glass liner have not been considered yet, but it is noted here that the interactions with solidifying melt will be treated later when the liner is given sole attention as an entity of importance.

8.3 THERMAL COMPRESSIVE STRESS (S_E)

Thermal stresses which are a result of equilibrium within a thermally induced strain field are secondary in nature. This differs from a primary stress condition in that thermal stresses are strain or deformation limited. Thus, if the deformation restraining mechanism is degraded or removed, the stress will likewise diminish or dissappear. With a primary stress, deformations and material degradations may have little or no effect upon a stress reduction. If the thermal stress field in the vicinity of a heated penetrator were treated with classical thermo-elastic theory, the peak compressive stress at the earth melt interface would take on the form of $\alpha E \Delta T/(1 - \nu)$ and in the absence of degradations such as spalling, cracking, compressibility and decomposition the stress computation could be meaningful for elastic materials. Likewise, for materials which would exhibit plastic behavior this computation becomes meaningless. Considering the nature of a thermal stress, it is difficult to justify it as an earth strength modification which will resist the fissure creating tensile stress induced by melt pressure. Realistically, the earth will not act elastically and these degradations will preclude the self equilibration required to sustain a thermal stress. Therefore, it is conservatively concluded in this work that thermal stresses do not resist an earth fracturing mechanism.

8.4 FLUID MELT PRESSURE STRESS (s)

The earth structural condition has been defined up to this point to include the overburden with mass removal effects, the tectonic and topographic influences and the thermal equilibration effects. The net effect of these perturbations is an alteration of the earth's parent tensile strength to a state of conditional residual strength. One load in particular which

would tend to "tear the earth apart" by overcoming the residual compressive stresses is the melt pressure (p). Another load to be treated later would be potential steam pressure. The tensile stress created by melt pressure is treated here with the same basic assumptions that were outlined for the overburden stress which included elasticity within an isotropic, homogeneous media in a state of plane strain with a level earth free of dead weight. The assumption of an elastic media would imply, by the same arguments used to discredit the realism of thermal stresses, that the stresses computed here at the earth's surface should be conservatively high. The real inelastic effects will prevent the expected elastic transmittal of tunnel surface pressures to the earth's surface. The plain strain assumption which neglects the tunnel "dead-end" effects would indicate that the melt pressure of interest in this analysis should be in the zone of near fully-developed tunnel diameter. It should not include the pressure rise toward the penetrator tip resulting from viscous drag.

The analysis of a semi-infinite plane containing a circular hole to the inside of which there is a uniformly distributed pressure is given by Savin in Reference (8-13). The results of this work are reconstructed below to non-dimensionalize the variables of interest and these are plotted on Figure 8-7 for the different locations as indicated.

$$(s/p)_O = \frac{4}{(C/R)^2 - 1}$$

$$(s/p)_{max} = \frac{\left(\frac{C}{R}\right)^2 + 1}{\left(\frac{C}{R}\right)^2 - 1}$$

$$(s/p)_B = 1 + \frac{2}{(C/R)^2}$$

$$(s/p)_A = 1$$

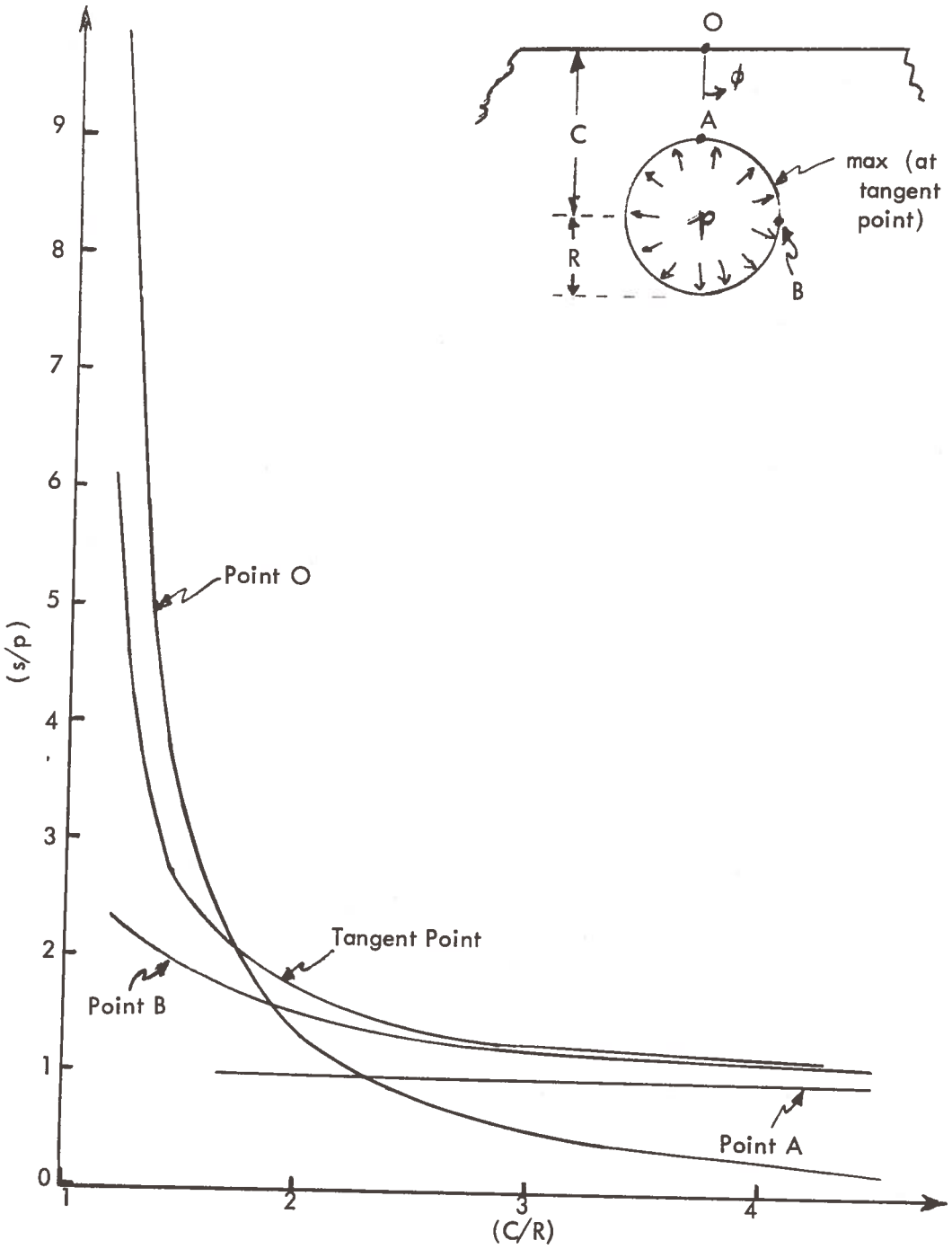

Figure 8-7. Circumferential Stress (s) from Uniform Internal Melt Pressure (p)

The peak tensile stress on the earth's surface is identified by point O. Referring to the above equation or Figure 8-7, it is apparent that this stress decreases quite rapidly as the relative tunnel depth increases. Realistically the stress at the earth's surface would be virtually non-existent for a $C/R > 3$ if the responses are inelastic in the absence of a fracture originating at the tunnel surface. The peak tensile stress at the tunnel surface is located at the tangent of a line drawn between the tunnel surface and the point O. For stress values at locations of magnitude greater than p and less than the peak stress the applicable equation is:

$$s/p = 1 + 2 \tan^2 \phi$$

where ϕ is the angle between the vertical and the line passing through any point (of interest) on the tunnel surface. For values of $C/R < 2$, the relative closeness of the tunnel to the earth's surface is shown to have a large effect upon tensile stress concentrations. But for $C/R > 3$, the tunnel surface circumferential tensile stress is rapidly approaching the asymptotic value of melt pressure (p).

8.5 EARTH STRESS/STRENGTH SUMMARY

The comparison of expected earth stresses from the effects of mass removal, in situ tectonic residuals and rupture tending pressures allows for some immediate observations concerning fissure initiation, fracture propagation and some likely limitations upon allowable operating pressures. For the purpose of this discussion a shallow tunnel will be referred to as one with a $C/R = 3$ ratio, and a deep tunnel as one with a $C/R = 15$ ratio. The latter corresponds approximately to a 10 meter (30 ft) tunnel at a depth of about 61 meters (200 ft). The former or shallow tunnel could possibly result as a recommendation of the least allowable shallowness in order to avoid the amplified stress effects of the tunnel being too close to the earth's surface. But coincidentally, it also corresponds to a 3 meter (10 ft) tunnel at a depth of 3 meters.

Irrespective of depth, fissure initiation at the tunnel surface will be resisted by the compressive circumferential tunnel wall stress. The preceeding analyses have shown that this compression can be provided by either tectonic residuals or possibly mass removal perturbations in the sense that a compressive stress concentration may be set up near the tunnel surface as a result of piercing a hole into the media's stress field. At locations away from the tunnel surface there remains the in situ overburden and possibly tectonic compression to resist the fissure propagation. Thus, the trend for discussion should be in terms first of initiation and then propagation.

Referring to Figures 8-6 or 8-7, points A and B are now discussed as possible origins for vertical and horizontal fractures, respectively. One immediate reaction is that if a fracture originates at point A, the likelihood of it progressing to the earth's surface would appear to be greater for a shallow tunnel.

8.5.1 Shallow Tunnels (C/R = 3)

The criteria established in this work for fracture initiation is

$$s \geq S_o + S_T$$

By using Figures 8-5 through 8-7 a range of possibilities at point A is:

$$p \geq (\pm 1)\ (2\ \rho_e R) + 3\ p_T$$

The statement here is that vertical fracture is initiated when the melt pressure (p) equals or exceeds the overburden compressive stress plus the tectonic compressive stress at point A. The (± 1) preceeding the overburden stress is given to cover the range of earth materials described by Figure 8-5. A (- 1) indicates that a tensile overburden stress can exist at point A when tunneling through strong sedimentary rocks. Consequently, fracture initiation is quite probable in the absence of a residual tectonic compressive stress. The (+ 1) indicates that tunneling through shales, clays and sands would require only a very small melt pressure, from 10 to about 30 psi ($\sim 0.7 \times 10^5$ to 2×10^5 N/m^2), in the absence of tectonic compression for fracture initiation.

Again with no tectonic stress, the pressure required for vertical propagation is of the order of:

$$p \geq \frac{\nu}{1-\nu} \rho_e (C - R) = \frac{\nu}{1-\nu} 2\rho_e R$$

This is less than the initiation stress shown for the shales, clays, and sands but greater than that for the strong sedimentary rocks. Therefore, it is concluded here that a vertical fracture is very probable in the absence of tectonic compression, but the extent of propagation will depend to a large extent upon how much of a volume availability of melt or steam can be supplied to the crack opening.

The condition for horizontal fracture initiation, originating at point B is that of the melt pressure stress exceeding the overburden compressive stress less the tectonic tensile stress.

$$1.2\,p \geq 4\,(2\rho_e R) - p_T$$

The factor of (4) on the overburden stress was interpolated from tables provided by Mindlin in Reference (8-1) at a 0.25 Poisson ratio. At location B the tectonic stress is tensile and therefore aids the fracture initiation. In the absence of a tectonic residual stress some representative stress conditions for fracture are:

$p \geq 6.6\,(\rho_e R)$ (33 to 100 psi for initiation) (2.3×10^5 to 6.9×10^5 N/m^2)

$p \geq \rho_e C = 3\rho_e R$ (15 to 45 psi for propagation) (1.0×10^5 to 3.1×10^5 N/m^2)

Again the propagating pressure which only needs to overcome the overburden is less than the initiation pressure in the absence of a tectonic residual. A tectonic compression should not effect propagation in the horizontal direction.

Prior to the discussions of deep tunnels it should be mentioned that the extent of propagation will depend primarily upon the volume availability of melt or steam as a pressure supply source to the newly created crack void volume, and this topic is to be treated in detail subsequent to the present discussion.

8.5.2 Deep Tunnels (C/R = 15)

The deep tunnel criterion for vertical fracture initiation is different from the shallow tunnel criterion:

$$p \geq \binom{+5}{-1} (2\rho_e R) + 3 p_T$$

The major difference, related to depth, shows up at the early stages of propagation where

$$p \geq \frac{\nu}{1-\nu} \rho_e (C - R) = \frac{\nu}{1-\nu} 14 \rho_e R$$

Thus, in the absence of a tectonic residual the propagating pressure must be about seven times greater for the deep tunnel when compared to the shallow tunnel. Clearly the vertical crack propagation pressure for a deep tunnel is likely to be greater than the crack initiation pressure without a tectonic effect in hard rock (-1), but not so in soils (+5).

The condition for horizontal fracture initiation is greater than that for horizontal propagation without a tectonic residual.

$$p \geq 2 \rho_e C = 30 \rho_e R \text{ (initiation)}$$

$$p \geq \rho_e C = 15 \rho_e R \text{ (propagation)}$$

The initiation criterion is simply a compressive stress concentration of two on the overburden at the tunnel location described by point B. These pressures are increased over the shallow tunnel fracture criteria by a factor of about 5.

The comparison of deep and shallow tunnel fracture propagating forces have indicated that:

1. In the absence of anisotropies the preferred fracture direction is vertical; that is, toward the earth's surface.

2. The influence of a large tectonic compressive stress would tend to incline the preferred fracture direction toward the horizontal.

3. Horizontal propagation must overcome the local overburden.

4. Vertical propagation, in the absence of a tectonic residual, must only overcome a load less than the local overburden.

5. The estimations of propagating pressure are quite low when compared to potential pressures of superheated steam at the required penetrator temperatures.

Some experimental data for deep well fracture initiation taken from Reference (8-3) are presented on Figures 8-8 and 8-9. These results substantiate the tendency for vertical fractures, at least for the well depths shown. On these curves the predicted elastic range is based upon:

vertical stress $= \rho_e C$

$\rho_e = 1$ psi/ft $(22,600 N/m^3)$

horizontal strength $= \frac{2\nu}{1-\nu} \rho_e C + S$

Where for a vertical hole, such as an oil well there is a compressive stress concentration of 2 at the hole surface and S represents a material strength. For Figure 8-8 the operation involved fracturing various limestones in the Permian Basin of West Texas and New Mexico. The breakdown pressures were recorded during acidizing operations. It is seen that most of the data falls within the predicted region. Figure 8-9 is a graph of rupturing pressure versus depth from wells in some lightly consolidated sands of the Texas and Louisiana Gulf Coast during squeeze cementing operations. The formations are expected to exist in a plastic state of stress more characteristic of the large equivalent Poisson ratios. Consequently, these rupturing pressures are expected to be , and were higher than, those which occurred at corresponding depths in the Permian Basin. For plastic behavior, stress concentration and strength are ignorable items.

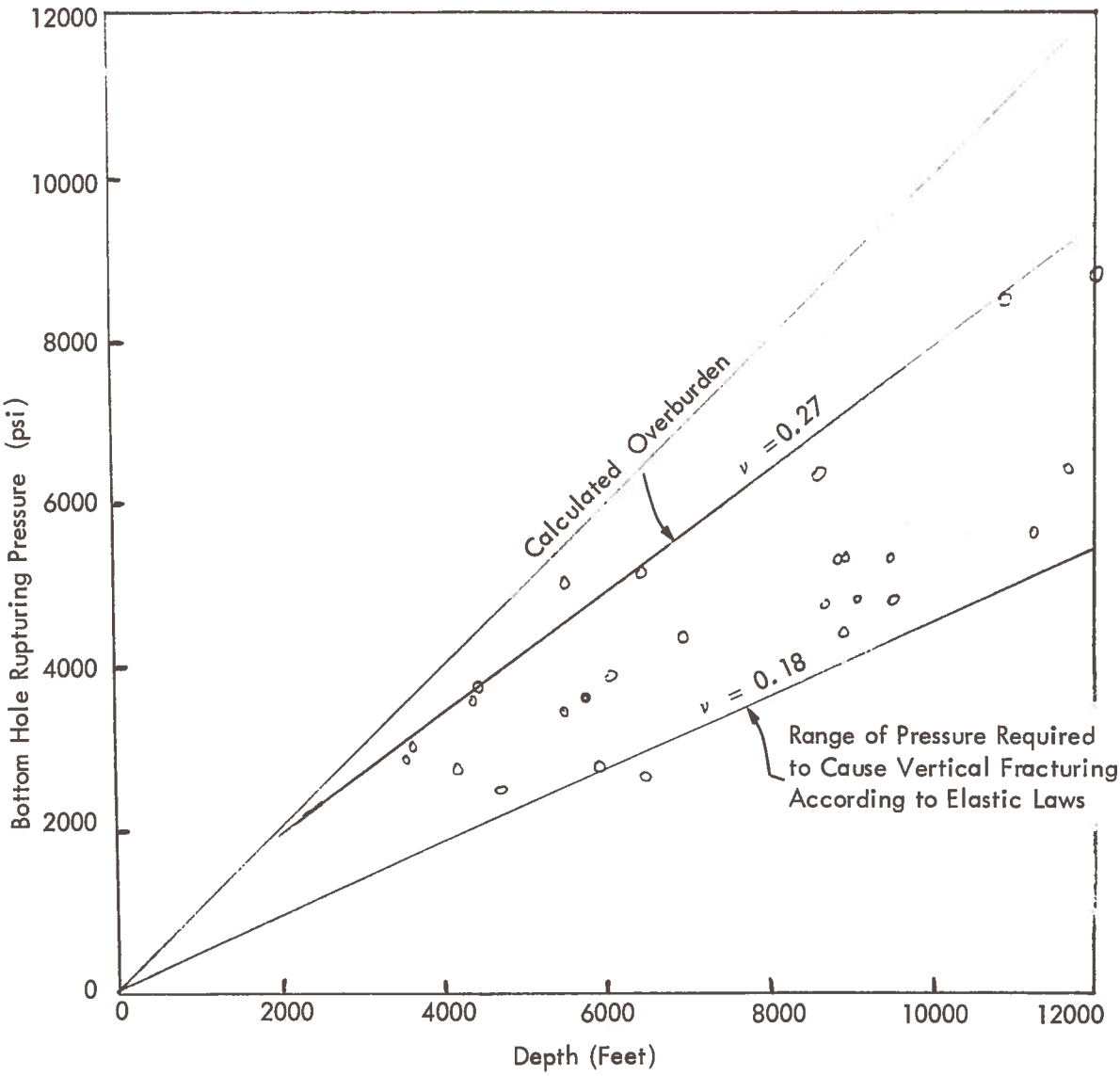

Figure 8-8. Breakdown Pressure VS. Depth from 27 Wellbore Fracturing Operations in the Permian Basin (Limestones)

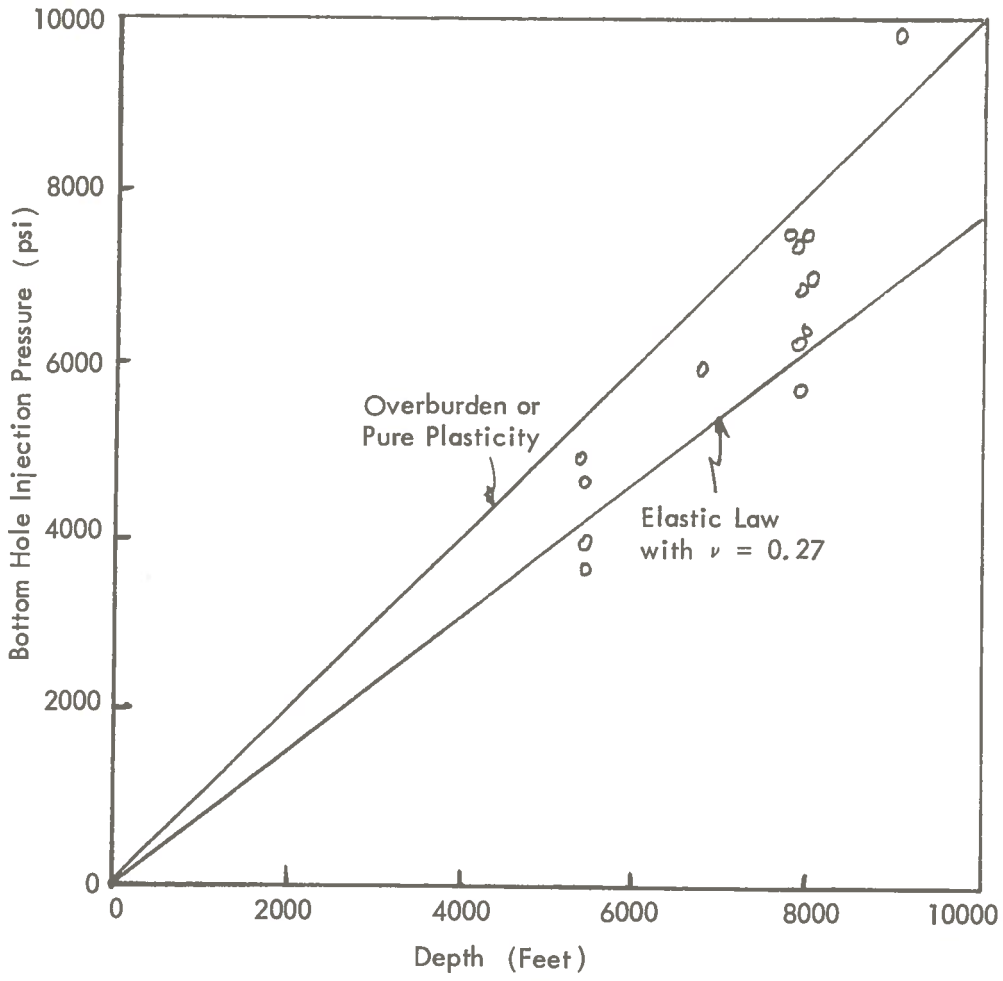

Figure 8-9. Injection Pressures on Gulf Coast Wells

8.6 FRACTURE PROPAGATION CONTROL

The limiting values of melt pressure which could cause a tunnel tensile failure initiation were established by superposition of the circumferential stress inducing mechanisms at the tunnel surface. The subsequent propagation of a fissure then depends upon the melt pressure and the volume availability of a substance which can fill and occupy the created crack void volume. From the previous section, some generalized conclusions follow:

1) In hard sedimentary rock, the melt pressure for crack initiation is less than that for crack propagation. This is merely a statement of the fact that tunnel surface circumferential compressive stress magnitude is less than the in-situ compressive stress condition which existed prior to the tunnel's presence. In a region of no tectonic compression, the fracture initiation and subsequent propagation would be vertical (toward the earth's surface) and in a region of reasonable tectonic compression ($p_T > 3.3\,\rho_e R$ for $C/R=3$, $p_T > 15\,\rho_e R$ for $C/R = 15$) the fracture initiation and subsequent propagation would tend toward a horizontal direction.

2) In the plastically behaving soils such as shales, clays and sands, the melt pressure for crack initiation is less than that for horizontal propagation in a region of reasonable ($p_T > \rho_e C$) tectonic compression.

3) In the plastically behaving soils such as shales, clays and sands, the melt pressure for crack initiation is greater than that for propagation in a region of no tectonic compression.

From these conclusions, some additional conclusions are made concerning crack propagation control:

1) When crack propagation is undesirable, it can be precluded with operational melt pressures of value less than the local vertical overburden in zones of moderate ($p_T \geq \rho_e C$) tectonic compression or with operational melt pressures of value less than the local horizontal overburden in zones of no tectonic compression. Without prior determinations of residual tectonic compressive stresses, a conservative melt pressure for the avoidance of crack propagation would be: $p \leq \frac{\nu}{1-\nu}\,\rho_e C$

2) When crack propagation is desirable, such as may be required for excess melt disposal or water disposal, melt pressures must exceed the local overburden stress component, and in the absence of a residual tectonic compressive stress, crack propagation toward the earth's surface is the preferred direction in an isotropic media.

If earth surface fissures are to be avoided, control must be imposed by melt pressure limitations once the required disposal volume has been established. As a precursor to what can be expected in terms of crack geometry for a fixed volume, larger pressures will give a short wide crack whereas smaller pressures will give a long narrow crack. Thus with increasing pressure, given a fixed volume, the extent of crack propagation will decrease as width increases.

The problem of inducing a fracture in an infinite medium has been studied among others by Sneddon[8-15], Green[8-16], Barenblatt[8-17] and Sun[8-5]. Their mathematical models are for an impervious, homogeneous, isotropic medium which enable the calculation of fracture width, extent and ground surface uplift.

Sneddon assumed an infinite elastic media with the hydraulic pressure, p, being the only pressure within the induced fracture applied uniformly over the entire surface of the fracture. The crack geometry relationships derived from his work are:

$$B = \frac{8\,(1-\nu^2)\,p\,a}{\pi\,E}$$

$$a = \left(\frac{3\,EV}{16\,(1-\nu^2)\,p}\right)^{1/3}$$

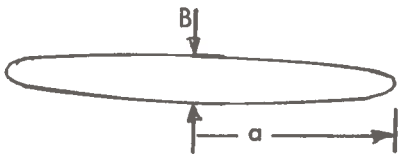

where "a" was derived from the relationship that volume is $V = 2/3\,\pi\,B\,a^2$ for a circular crack of elliptic cross section. The shape of elliptic cross section was shown mathematically from the crack separation versus radius equation provided by Sneddon. If the injection pressure and the injected volume are known, the above equations could provide the crack geometry. However, upon review of Sneddon's stress equations, analysis shows that there is an infinite tensile stress at the crack tip edge of the fracture. Consequently, it has been concluded that an equilibrium fracture cannot exist in the form provided by Sneddon. The theory is that Sneddon did not provide a model which could handle cohesive forces, should they exist. The inference

is that overburden, not included in Sneddon's model, is analogous to a cohesive force. Barenblatt[8-17] considered the cohesive forces in some detail by dividing the fracture into two regions: an inner region with opposite faces relatively far apart and subjected to a pressure $(p-\rho_e C)$ and an outer region with very small face separation to be regarded as a strain rather than a displacement subjected to the formation pressure of $\rho_e C$ and unoccupied by injection fluid.

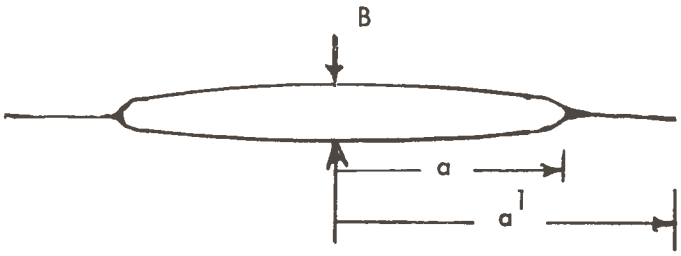

With these assumptions, Barrenblatt proved mathematically that a fracture has the following significant characteristics:

1) The tensile stress at the crack tip end is finite. If there are no cohesive forces, the tensile stress at the crack tip end is equal to zero.

2) The opposite faces of a fracture meet gradually at the crack tip end.

Barenblatt also stated that in comparison with the earth overburden pressure and the injection pressure, the forces of cohesion are so small that they can be neglected. With the above stated conditions and the condition of finiteness of stress at the contour of a horizontal fracture, the following relation was found by Barenblatt[8-17] and Zheltov and Khristianovich[8-18].

$$\left(\frac{a}{a'}\right)^2 = 1 - \left(\frac{p-\rho_e C}{p}\right)^2$$

In Reference(8-5), Sun has combined the efforts of Sneddon and Barenblatt to provide horizontal fracture geometry equations and has made comparisons with experimental field data. One of Sun's efforts was an evaluation of the effect of the free ground surface on the separation and radius of fracture formed in the subsurface by Sneddon's equations. Recall that Sneddon's work

was based upon an infinite media. Sun found that if the depth of fracture was twice the crack radius ($C \geq 2a$) that the influence upon geometry was only about 2 to 3%. Ustinov[8-19] found the same results by using a different method than Sun[8-5]. Sun concluded that the equations of Sneddon, after modified to contain the findings of Barenblatt, could be used to determine crack geometry with reasonable accuracy disregarding the effects of free ground surface. Sun did complete the displacement and stress field solution for a semi-infinite media in order to provide an expression for ground surface uplift. The modification which Sun[8-5] made to Sneddon's equations in order to incorporate the finding of Barenblatt includes replacing p by $(p-\rho_e C)$ and replacing $(p-\rho_e C)$ by $(a/a^1)^2(p-\rho_e C)$. His reasoning for this latter modification to include the condition of finiteness of stress at the crack tip follows:

> "If the pressure $(p-\rho_e C)$ is assumed to be uniformly distributed over the entire fracture area with a radius of "a", where p is the injection pressure, then the average pressure over the entire circular area with a radius of "a^1" can be assumed approximately as $a^2(p-\rho_e C)$."

Where

$$\alpha = \frac{a}{a^1}$$

therefore Sun's[8-5] description for crack geometry is:

$$B = \frac{8(1-\nu^2)(p-\rho_e C)a^2 a^1}{\pi E} = \frac{8(1-\nu^2)(p-\rho_e C)\alpha a}{\pi E}$$

$$a = \left[\frac{3EV}{16(1-\nu^2)\alpha^2(p-\rho_e C)}\right]^{1/3}$$

If these two equations are combined to solve for the fluid geometry volume, the result is:

$$V = 2/3\,\pi\,\alpha a^2 B$$

This is inconsistent with the original theory of Sneddon, which does not contain α. The alternative would be

$$B = \frac{8(1-\nu^2)(p-\rho_e C)\alpha^2 a}{\pi E}$$

where the modified pressure is by assumption still only acting on the crack radius of $r < a$. Now using the relationship that

$$V = 2/3\ \pi\ a^2 B$$

then

$$a = \left[\frac{3\ EV}{16\ (1 - \nu^2)\ a^2\ (p - \rho_e C)} \right]^{1/3}$$

which is the same as that given by Sun[8-5]. In his work, Sun does present evidence that some experimentally measured values of B were about 25% smaller than those which he calculated. These experimental values taken by Quaker State Oil Refinery Corp. were from records of oil well fracturing in the Reno oil field, Venango County, Pennsylvania. The B, as modified in in this work, is likewise a factor of (1 - a) smaller than that given by Sun. Typical values of a ranged from 0.73 to 0.85 in Sun's experimental work.

Generally speaking, Sun's calculated results are in fair agreement with the observed data. Figures 8-10 and 8-11 were extracted from Reference (8-5) along with the following table for the comparison purpose.

Calculated Maximum Separation and Radius of Fractures Produced by Injections of the Second Experiment, September 1960

Injection number	1	2
Injection date	Sept. 3	Sept. 10
Area of casing, cm²	85	85
Velocity of slurry, m/sec	1.04	1.86
Re	463	970
Total friction loss, kg/cm²	3.0	4.0
Static pressure of slurry in the well casing, kg/cm²	39	31
Injection pressure at bottom of the well (p_0), kg/cm²	166	179
Overburden pressure (γh), kg/cm²	77	57
α	0.844	0.732
$\alpha^2(p_0 - \gamma h)$, kg/cm²	64	65
Calculated maximum radius of the stress-altered region (a'), meters	68	88
Calculated radius of grout (a), meters	57	64
Calculated maximum separation of fracture (B), cm	5.94	7.92

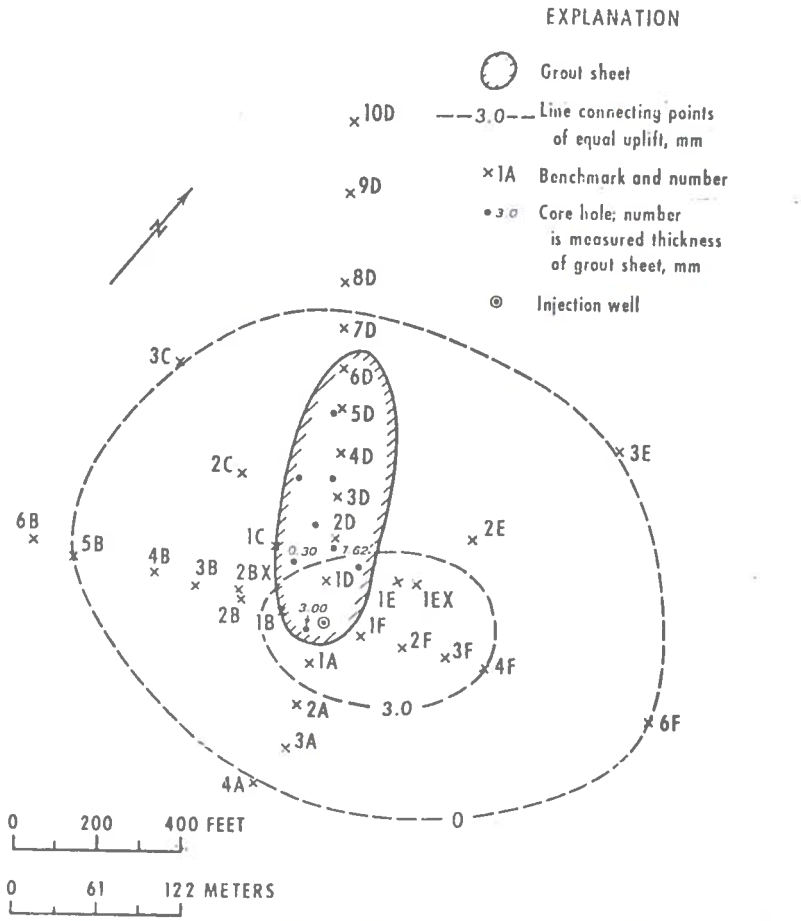

Surface uplift, extent, and thickness of the grout sheet of the injection of September 3, 1960 [after *DeLaguna et al.*, 1968, and W. DeLaguna (written communication, ORNL, June 10, 1968)].

Figure 8-10. Experimental Measurements from the Reference (8-5) Report, R. J. Sun

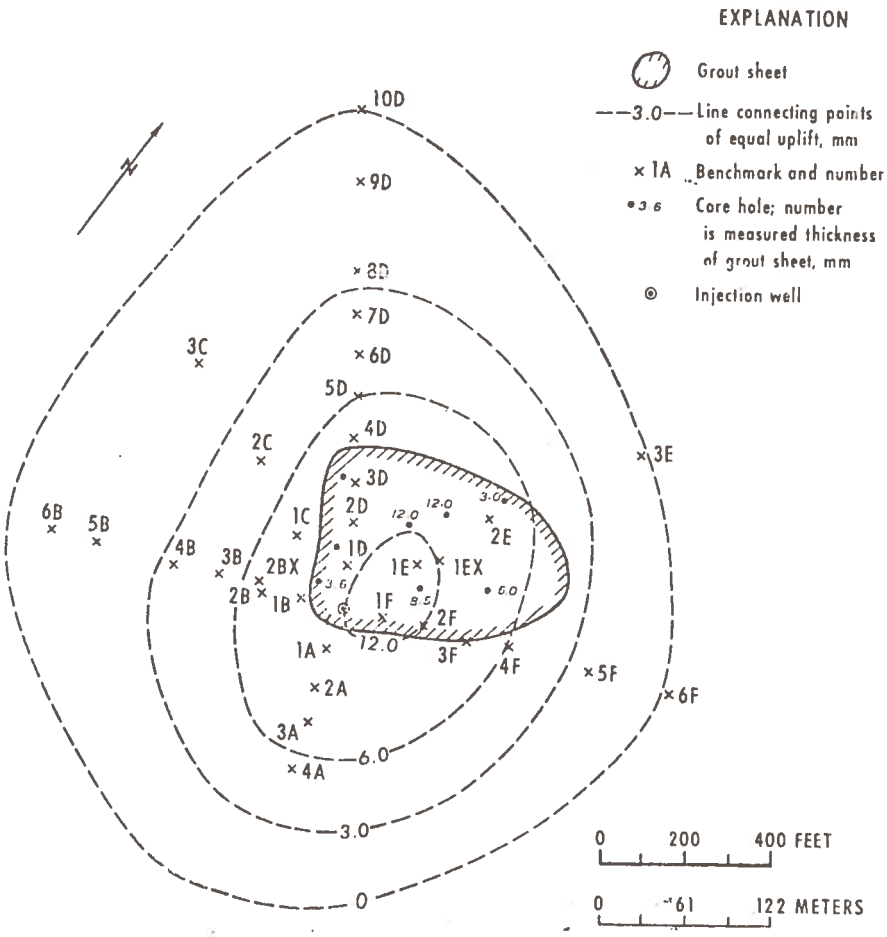

Surface uplift, extent, and thickness of the grout sheet of the injection of September 10, 1960 [after *DeLaguna et al.*, 1968, and W. DeLaguna (written communication, ORNL, June 10, 1968)].

Figure 8-11. Experimental Measurements from the Reference (8-5) Report, R. J. Sun

The calculated radii shown in this table are fair approximations to an average radius shown on Figures 8-10 and 8-11. The biggest shortcoming in the comparison is that the injected fluid did not spread at a constant radius from the well site. The comparison between calculated maximum separation, B, and those shown on the figures do not agree at all. Sun's explanation here was that the liquid phase of the injected slurry probably was squeezed out and the solid phase compacted by the overburden pressure. This is a plausible explanation when one examines the good agreement between surveyed and calculated surface uplift at the time of injection shown on Figure 8-12. A resurvey of the area (second experiment) 4 years later indicated that the ground surface had returned to its original elevation. Based on Sun's work, the following expression is provided for the calculation of maximum surface uplift:

$$W = B\left[1 - \frac{(C/a^1)^2}{(C/a^1)^2 + 1}\right]$$

This equation is in excellent agreement with the experimental survey results when W is calculated from calculated values of B and a^1.

For horizontal fractures, surface uplift is the limiting parameter of interest. The "design" curves for its calculation are now provided.

Let n be the ratio of fluid pressure to overburden pressure.

$$n = \frac{p}{\rho_e C}, \quad (n > 1.0 \text{ for fracture propagation})$$

or

$$p = n C \rho_e \tag{8-1}$$

then

$$a = \left[\frac{3\,EV}{16\,(1-\nu^2)\,a^2\,(p-\rho_e C)}\right]^{1/3} = \left\{\frac{3\,EV}{16\,(1-\nu^2)\,\rho_e C\,(n-1)\left[1-\left(\frac{n-1}{n}\right)^2\right]}\right\}^{1/3} \tag{8-2}$$

$$B = \frac{3V}{2\pi a^2} \tag{8-3}$$

$$a^1 = \frac{a}{a} = \frac{a}{\sqrt{1-\left(\frac{p-\rho_e C}{p}\right)^2}} = \frac{a}{\sqrt{1-\left(\frac{n-1}{n}\right)^2}} \tag{8-4}$$

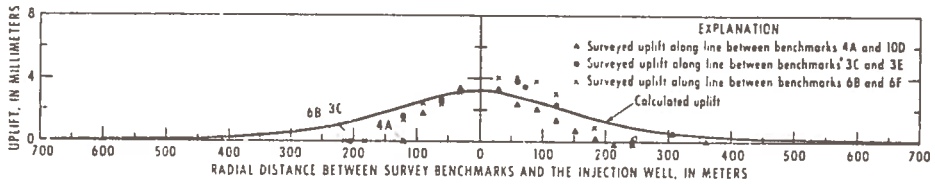

Calculated and surveyed uplift produced by injection 1, second experiment, September 3, 1960.

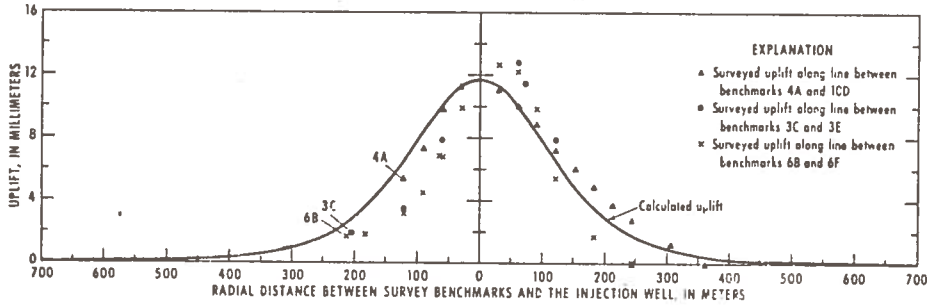

Calculated and surveyed uplift produced by injection 2, second experiment, September 10, 1960.

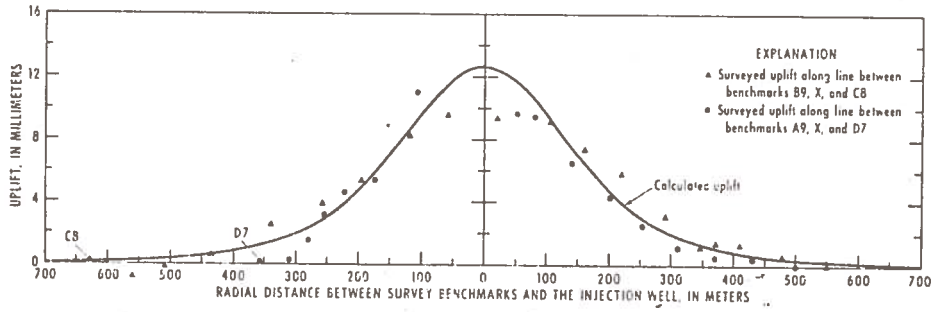

Calculated and surveyed uplift produced by injections 3, 4, and 5, third experiment, April 8 and 17 and May 28, 1964.

Figure 8-12. Experimental Measurements from the Reference (8-5) Report, with Calculated Comparisons, R. J. Sun

$$W = B\left[1 - \frac{(C/a^1)^2}{(C/a^1)^2 + 1}\right] \tag{8-5}$$

The graphical presentation of these equations are made by normalizing the variables with respect to the following values:

$E = 10^6$ kg/cm^2

$V = 10^6$ cm^3 (cubic meter)

$\rho_e = 0.0025$ kg/cm^3

$\nu = 0.3$

Now, Equations (8-1), (8-2), and (8-3) are rewritten as:

$$p\left(\frac{0.0025}{\rho_e}\right) = 0.0025\ n\ C \tag{8-1}$$

$$a\left\{3\sqrt{\left(\frac{10^6}{E}\right)\left(\frac{10^6}{V}\right)\left(\frac{1-\nu^2}{0.91}\right)\left(\frac{\rho_e}{0.0025}\right)}\right\} = \left[\frac{3\,(10^6)\,(10^6)}{16(0.91)(0.0025)C(n-1)\left[1-\left(\frac{n-1}{n}\right)^2\right]}\right]^{1/3} \tag{8-2}$$

$$B\left(\frac{10^6}{V}\right) = \frac{3\,(10^6)}{2\,\pi\,a^2} \tag{8-3}$$

Equations (8-1) through (8-5) are plotted on Figures 8-13 through 8-16. For the purpose of describing the manner in which these curves are applied, a sample problem is given here:

Example: A subterrene penetrator is to operate at a depth of 50 meters in a terrain of residual tectonic compression where horizontal fissures can be expected and are required for the disposal of excessive water contained in the earth to be melted. It has been determined that the required water disposal (a topic for which the determination is treated later in this work) is

$V = 4\ m^3 = 4 \times 10^6\ cm^3$

The earth properties are established as:

$E = 2 \times 10^6$ kg/cm^2

$\nu = 0.25$

$\rho_e = 0.00242$ kg/cm^3

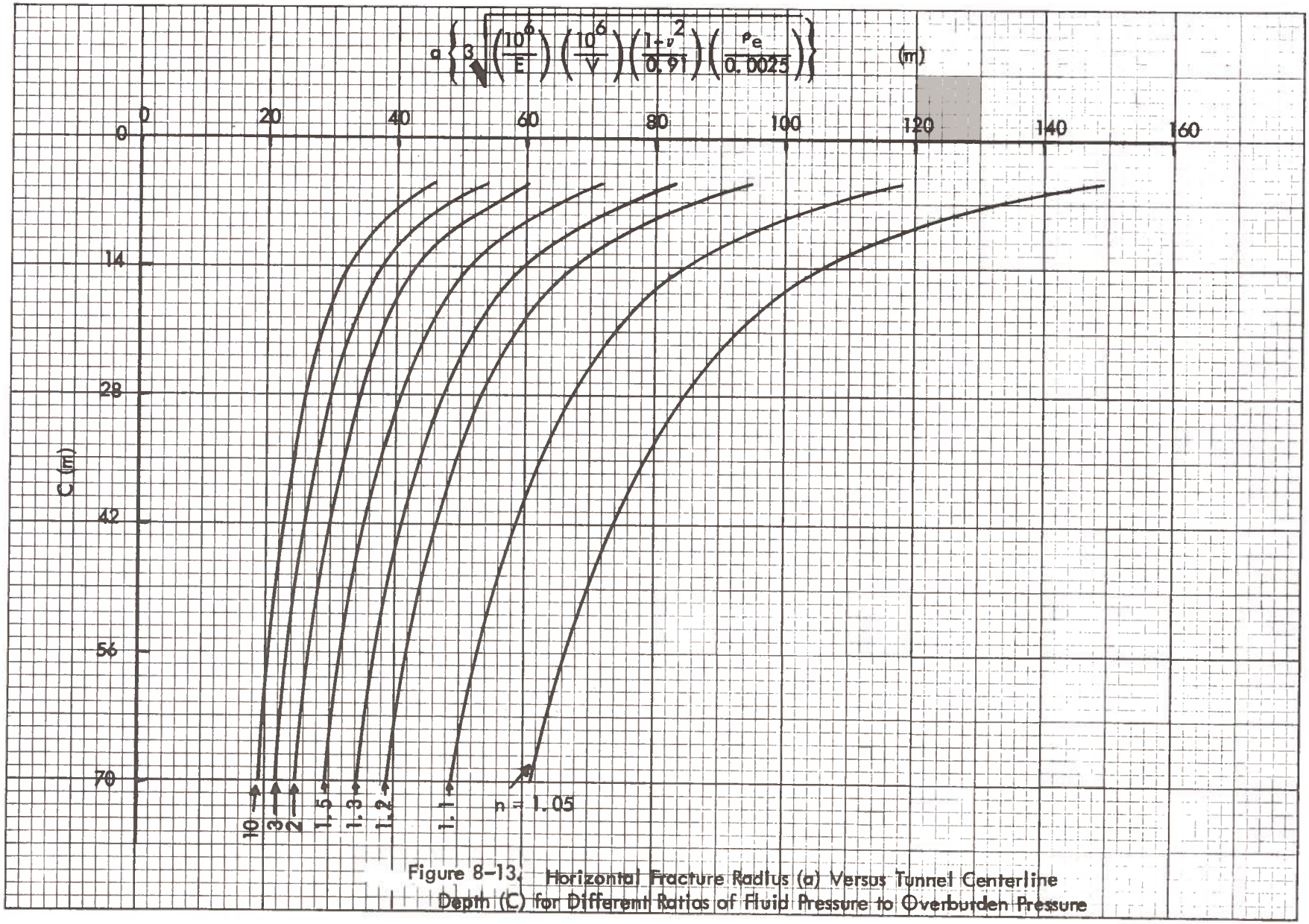

Figure 8-13. Horizontal Fracture Radius (a) Versus Tunnel Centerline Depth (C) for Different Ratios of Fluid Pressure to Overburden Pressure

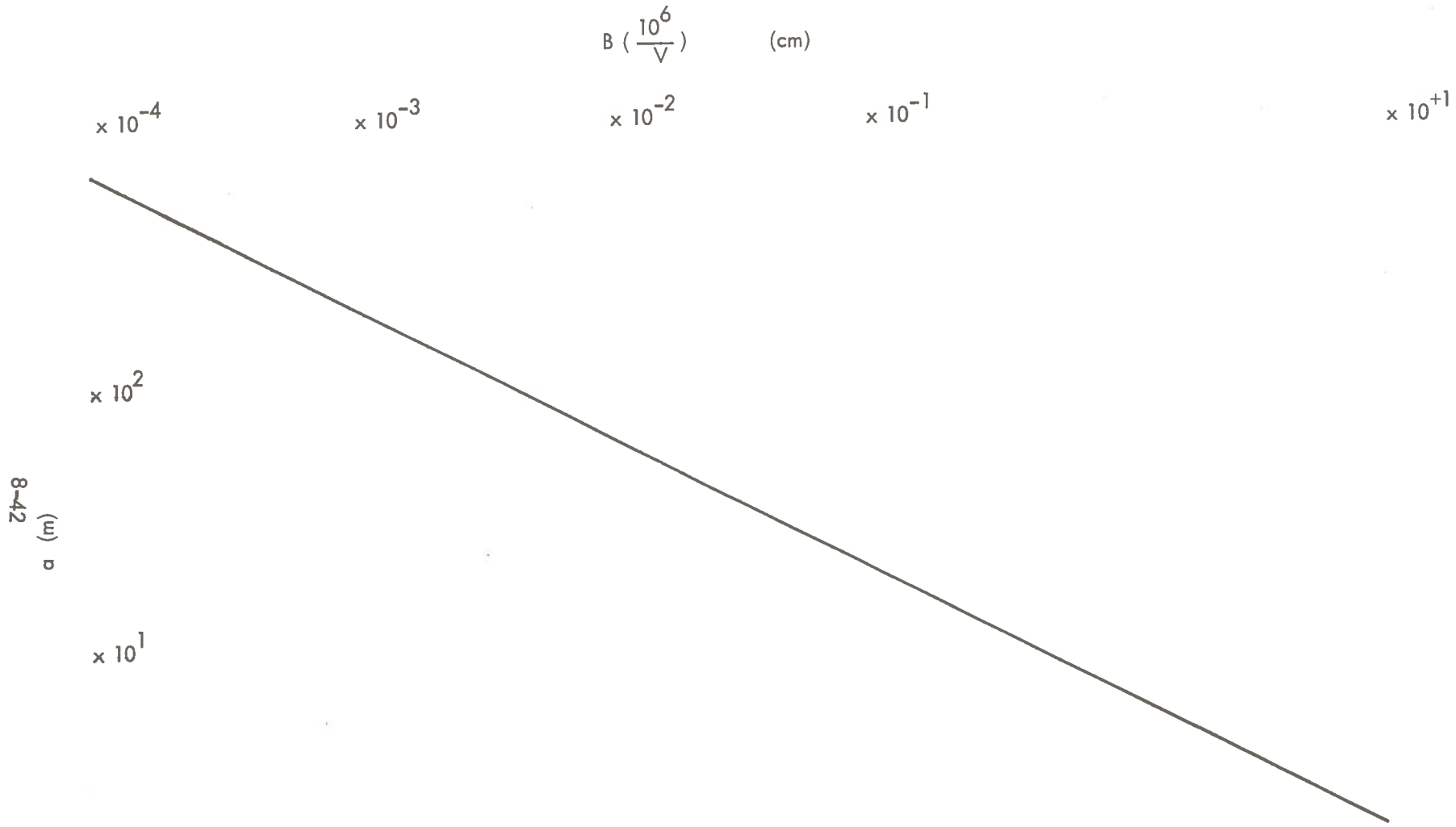

Figure 8-14. Maximum Crack Width (B) Versus Crack Radius (a)

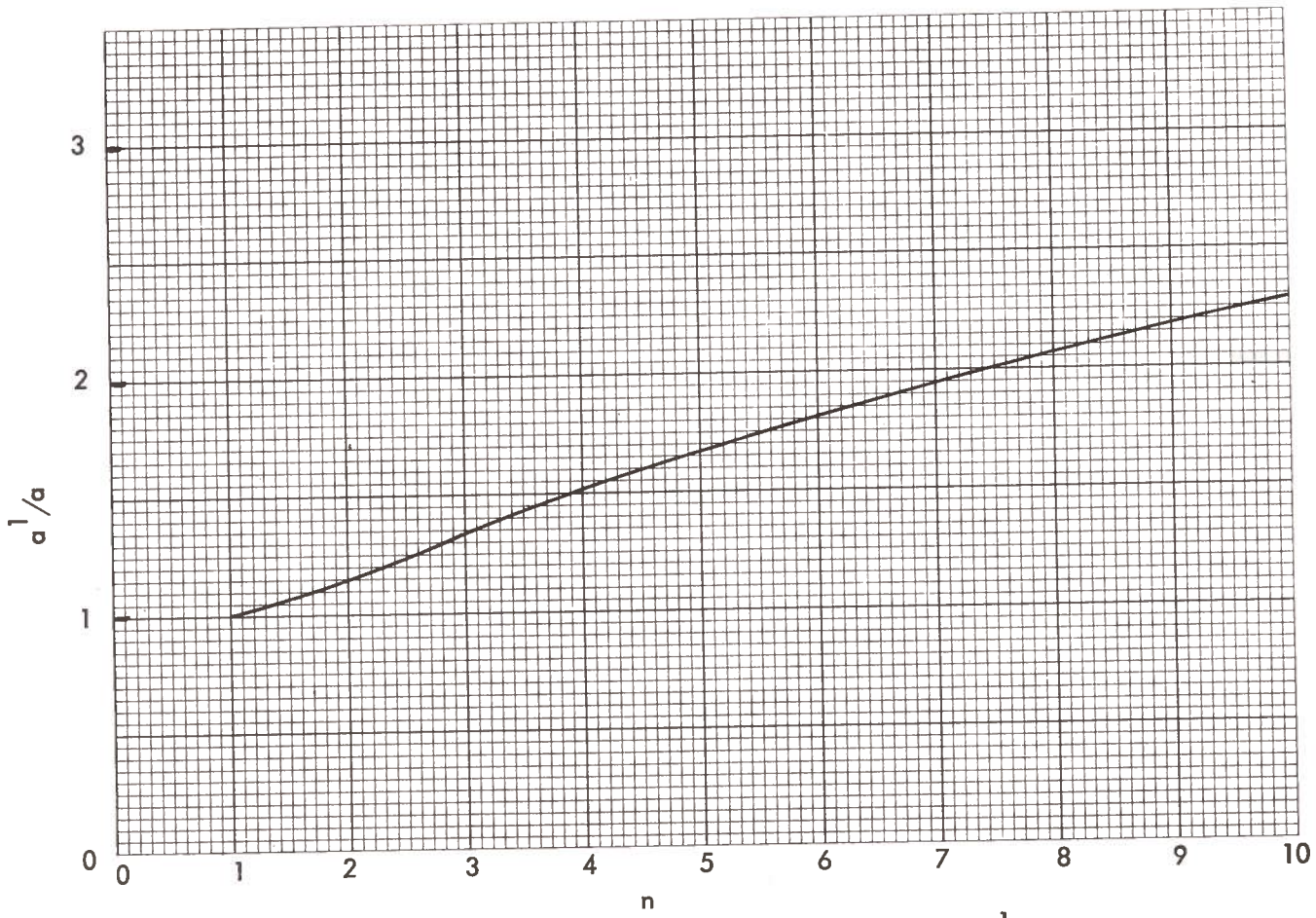

Figure 8-15. The Ratio of Strain Effected Radius (a^1) to Fracture Radius (a) Versus the Ratio of Fluid Pressure to Overburden Pressure (n)

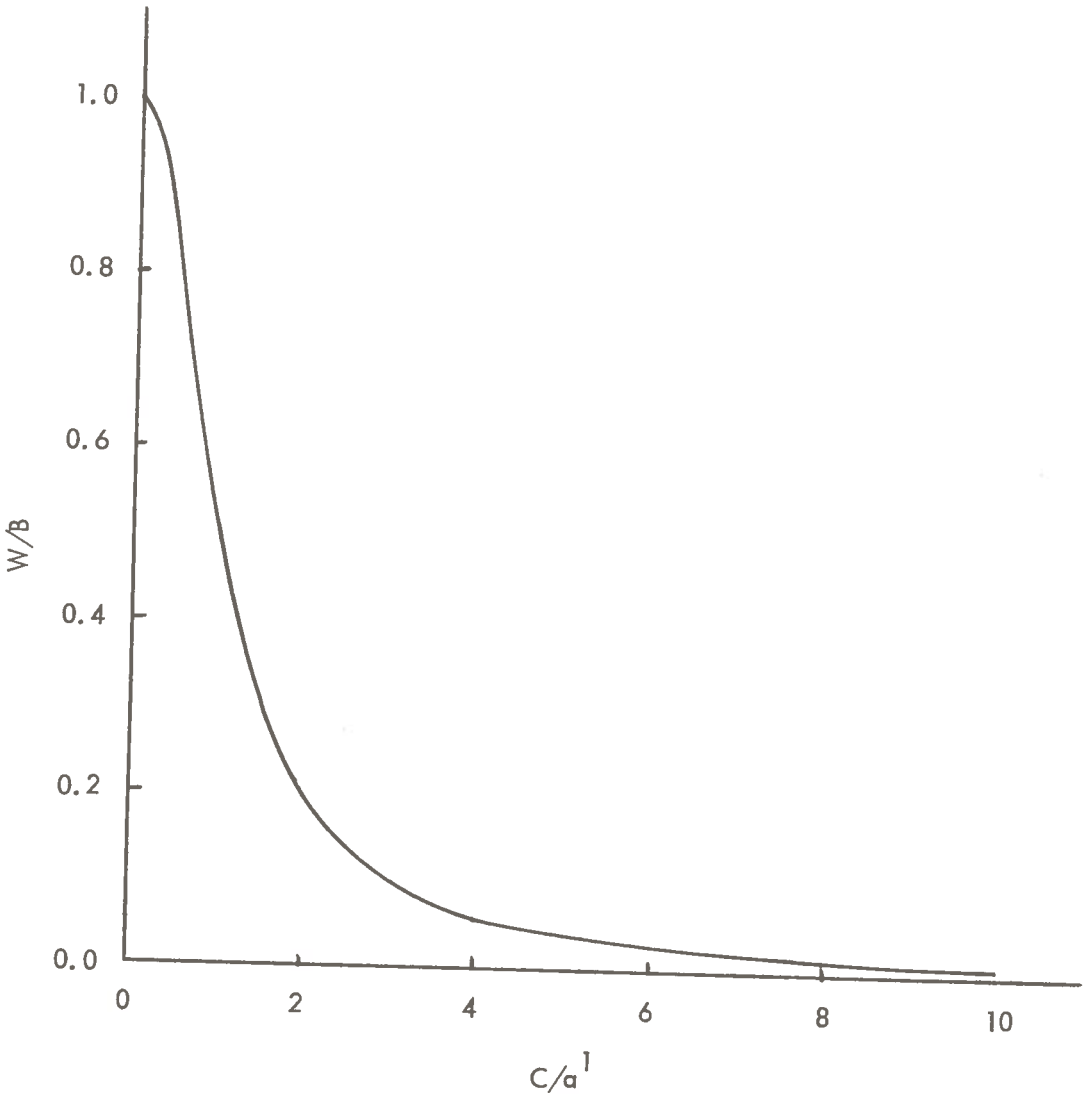

Figure 8-16. Maximum Surface Uplift (W) Versus Tunnel Centerline Depth (C)

If the penetrator is to operate with a melt pressure of twice the earth overburden, what is the maximum earth surface uplift to be expected?

Assumptions:

(1) Melt pressure is transmitted to the water liquid phase by the hydrostatic compression of the dry earth between the melt and the wet earth (a topic for later treatment in this work).

(2) Water mass diffusion through the wet unfractured earth is conservatively neglected.

Solution:

From Figure 8-13 at C = 50 m and n = 2,

$$a \sqrt[3]{\left(\frac{10^6}{2 \times 10^6}\right)\left(\frac{10^6}{4 \times 10^6}\right)\left(\frac{1 - .25^2}{0.91}\right)\left(\frac{0.00242}{0.0025}\right)} = 28 \text{ m}$$

$$a \sqrt[3]{\frac{1}{8}} = 28 \text{ m}$$

$$a = 56 \text{ m}$$

From Figure 8-14 at a = 56 m

$$B\left(\frac{10^6}{2 \times 10^6}\right) = 0.015 \text{ cm}$$

$$B = 0.030 \text{ cm}$$

From Figure 8-15 at n = 2

$$a^1/a = 1.15 \text{ m}$$

$$a^1 = (1.15)(56) = 65 \text{ m}$$

From Figure 8-16 at $c/a^1 = 50/65 = 0.77$

$$W/B = 0.63$$

$$W = 0.63\,(0.33) \approx 0.0189 \text{ cm}$$

This is the maximum surface uplift computed for the above illustrative sample problem.

A conclusion arrived at earlier in this discussion on fracture propagation control was that crack propagation toward the earth's surface is the preferred direction in an isotropic media free of compressive tectonic residual stress. The problem of vertical fracture propagation in a media of non-constant horizontal overburden such as that present in the earth is a unique problem for which a solution was not found in the literature. A limiting criterion that could be imposed upon the vertical fracture would be that of no earth surface fissure or no blowout of crack volume fluid to the earth's surface. With this criteria in mind, the following model is proposed for establishing fracture propagation control.

Consider a circular crack of elliptic cross section formed from a source of pressurized fluid at a depth C below the earth's surface.

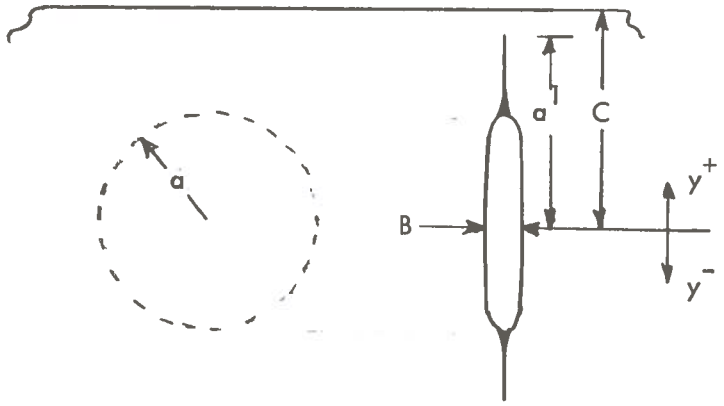

The source of pressure at depth C is considered to be the penetrator melt pressure, generalized as a multiple of the vertical overburden pressure by the factor n. For this condition, the fluid pressure within the crack volume is

$$p_f = nC\rho_e - \gamma y$$

where γ is the fluid density. Thus, the fluid pressure at the vertical upper ends of the fracture will be less than that at the deeper side. The earth's horizontal component of overburden pressure based upon the plane elastic restraint model is

$$p_e = \frac{\nu}{1-\nu} \rho_e (C - y)$$

This difference between the fluid pressure and the earth's overburden pressure is:

$$p_f - p_e = \rho_e C \left(n - \frac{\nu}{1-\nu}\right) + y \left(\frac{\nu}{1-\nu} \rho_e - \gamma\right)$$

The models derived by Sneddon, Barenblatt and Sun for the horizontal fracture were based on the fact that the pressure difference between the fluid and the earth overburden was a constant. This pressure difference shown above for the vertical crack is not a constant, since it will vary with the y position along the crack surfaces. But there is a condition for which the vertical pressure difference along the vertical crack surfaces will be a constant and this is now examined. By inspection of the above pressure difference equation, the fluid pressure in excess of the horizontal overburden is a constant

$$\Delta P = \rho_e C \left(n - \frac{\nu}{1-\nu}\right) = \rho_e C \left(n - \frac{\gamma}{\rho_e}\right)$$

if

$$\frac{\gamma}{\rho_e} = \nu/(1-\nu)$$

This condition is now examined in detail for earth material which would be: (1) likely candidates for high porosity in the water saturated condition, (2) likely candidates for isotropy, thereby facilitating the vertical fracture tendency, and (3) likely candidates for the absence of a residual tectonic compression, thereby facilitating the vertical fracture tendency. These are grouped into the category of sand, clay, gravel and soil.

A range of saturated bulk densities for this group of material, as reported in Reference (8-20) is 1.44 to 1.93 g/cc. Where the fluid contained in the crack is water of $\gamma = 1.0$ g/cc density, the equality of

$$\frac{\rho_e}{\gamma} = \frac{1-\nu}{\nu}$$

holds true if

$\rho_e = 2.7$ g/cc and $\nu = 0.27$	(hard rock)
$\rho_e = 1.93$ g/cc and $\nu = 0.34$	(sands, clay, soil and gravel)
$\rho_e = 1.44$ g/cc and $\nu = 0.41$	(sands, clay, soil and gravel)
$\rho_e = 1.0$ g/cc and $\nu = 0.5$	(water)

The latter point is included only to show that if the earth were composed of water, the behavior would be purely plastic as might be expected. The first point for hard rock is included to refine the trend of behavior on that end of the density spectrum. The Poisson ratios of 0.34 to 0.41 for decreasing bulk densities are consistent phenomena as evidenced by the extremes shown for hard rock and water. This equality does not appear to hold true in the strong sedimentary rocks more characteristic of a 0.20 Poisson ratio (rather than the required 0.27 as needed for equality). As the material densities decrease, the $\rho_e/\gamma = (1-\nu)/\nu$ equation does give the appearance of converging toward equality.

As an example to further the illustration, earlier in the earth overburden stress description on Figure 8-5, soft shales, clays, and sands were characterized with an internal friction coefficient of 0.3, corresponding to an equivalent Poisson's ratio of 0.36. This is quite consistent with the range of 0.34 to 0.41 as shown above to acquire the $\rho_e/\gamma = (1-\nu)/\nu$ equality so it is considered that the assumption of uniform crack pressure in excess of the overburden pressure may be applied with little error. Based on this assumption, the radius (a) of liquid filled fracture can be evaluated with the same equation used for the horizontal fracture with one additional assumption.

$$a = \left[\frac{3\,EV}{16\,(1-\nu^2)\,\alpha^2\,\Delta P}\right]^{1/3}$$

$$\Delta P = \rho_e C\left(n - \frac{\nu}{1-\nu}\right) = \rho_e C\,(n - \gamma/\rho_e)$$

$$\alpha^2 = 1 - (\Delta P/p)^2$$

The addition assumption is that

$$p = n\,\rho_e C - \gamma\, y$$

can be replaced by its average value over the entire fracture area. That is

$$p = n\,\rho_e C$$

Now the fracture radius is expressed as

$$a = \left[\frac{3\,EV}{16\,(1-\nu)^2\,\rho_e C\,\left(n - \frac{\nu}{1-\nu}\right)\left[1 - \left(\frac{n - \frac{\nu}{1-\nu}}{n}\right)^2\right]} \right]^{1/3}$$

where

$$\gamma/\rho_e = \nu/(1-\nu)$$

With this expression, the crack radius is further reduced to

$$a = \left[\frac{3\,EV}{16\,C\,\gamma\,(1-\nu^2)\left(\frac{1-\nu}{\nu}\right)\left(n - \frac{\nu}{1-\nu}\right)\left(1 - \left[\frac{n - \frac{\nu}{1-\nu}}{n}\right]^2\right)} \right]^{1/3}$$

Figure 8-17 is a plot of this equation and it is only valid when the corresponding ν and ρ_e are simultaneous, as indicated to satisfy that equality of past discussion. Once a value of "a" has been determined, the minimum required tunneling depth has been established to preclude an earth surface fissure. The maximum crack width B may be established with Figure 8-14, and then to be conservative the minimum required tunnel depth may be established as a^1.

Sample: Earth properties for a tunnel are given by

$E = 10^6\ kg/cm^2$

$V = 10^6\ cm^3$

$\gamma = 0.001\ kg/cm^3$

$C = 5000\ cm$

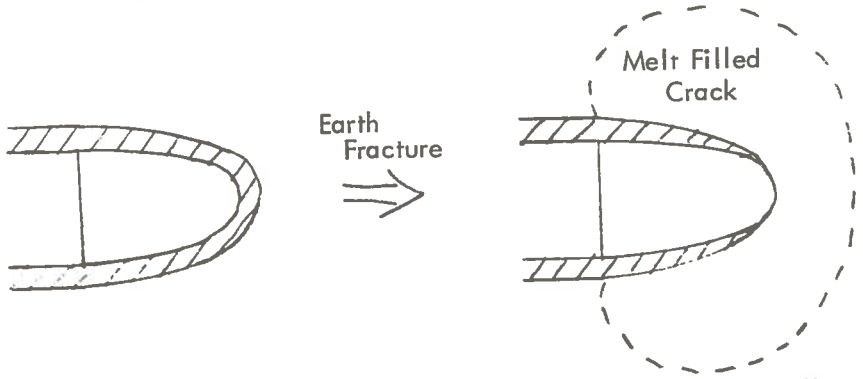

During this process a conservative maximum possible amount of melt expelled to a crack can be evaluated by making the conservative assumption that the melt thickness is everywhere constant and equal to the planned liner thickness δ. With this assumption, available melt volumes are:

$$V = \frac{\pi}{4} D_p^2 \delta \quad \text{(Mode 1)}$$

$$V = \frac{\pi}{4} (D_p^2 - D_o^2) \delta \quad \text{(Coring or Extrusion Modes)}$$

where D_p is the penetrator outer diameter and D_o is the penetrator diameter at which melt flow separates into the liner and into the core region.

Sample Calculation

Assume: $\delta = 0.05\ D_p$, $D_o = 0.8\ D_p$, $D_p = 20$ m, then

$$V = \frac{\pi}{4} (D_p^2 - 0.64\ D_p^2)\ (0.05\ D_p) = (\frac{\pi}{4})\ (0.05)\ (0.36)\ D_p^3$$

$$V = \frac{\pi}{4}\ (0.05)\ (0.36)\ (20)^3 = 113\ m^3$$

Whether or not all of this volume will create a single circular crack of elliptic cross section will depend largely upon the viscous flow impedance and the solidification rate as the melt traverses to fissure the earth.

Water Volume Availability

The earth media of low density and high porosity are the likely candidates for the tendency of vertical fissures due to the increased likelihood of property isotropy and the decreased likelihood of a tectonic residual compression. Similarly, these media are potential candidates for excessive water content due to the high porosity. The conservative assumptions made here are:

1) The porous volume is saturated with liquid water

2) Water mass diffusion in the unfractured regions of ambient temperature earth is negligible, and

3) There is a zone in the unmelted earth very close to the melt/earth interface at which the saturated liquid begins to acquire the latent heat of vaporization at the pressure provided by the melt. The entire value of the latent heat of vaporization need not be acquired to effect a volumetric change sufficient to degrade the earth to the extent that both: (a) porous mass diffusion is great, and (b) the earth can now transmit the melt pressure to this zone of degradation.

This zone is now the source for water origination and disposal through a fracture. Based upon the above assumptions, the water volume availability is:

$$V = f_e V_b$$

where

$$\frac{dV}{dt} = f_e \left(\frac{\pi}{4}\right) \left[(D_p + 2\delta)^2 - D_o^2 \right] U_\infty$$

where f_e is a water saturated earth porosity and V_b is the volume occupied by the penetrator and melt exterior to the stagnation diameter (D_o, for modes other than Mode 1) and forward of the fully developed melt diameter. That volume of water interior to the stagnation diameter is likely to "aid" the expulsion of extruded and cored material as it likewise is expelled through the core area.

Examples:

Mode 1 Coring or Extrusion Modes

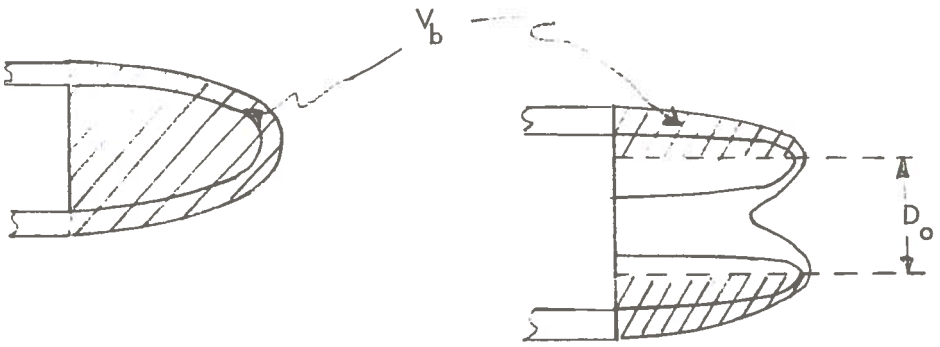

Assume by penetrator design that:

$$V_b \cong \frac{2}{3}(D_p + 2\delta)\frac{\pi}{4}\left[(D_p + 2\delta)^2 - D_o^2\right]$$

Further assume that

$$\delta = 0.05\, D_p \quad \text{and} \quad D_o = 0.8\, D_p$$

$$D_p = 20 \text{ m} \quad \text{and} \quad f_e = 0.10$$

then

$$V = f_e V_b = (0.1)(2/3)\, D_p (1+0.10)\left[D_p^2 (1+0.10)^2 - D_p^2 (0.8)^2\right]$$

$$V = (0.1)(2/3)(20)^3 (1.10)\left[1.21 - 0.64\right] = 334 \text{ m}^3$$

The conclusion that can be drawn from this example is that a very large stagnation diameter along with a thin liner is required to minimize the disposal of excess water into earth fractures.

8.8 EARTH STRUCTURAL-SUMMARY

The development of functional relations for the earth stress fields evolved with concern for the variables which could control or limit the earth tunneling process. The descriptions for earth structural behavior included the environmental boundary conditions imposed by the earth's own weight, tectonic residual stress, imposed temperature changes, melt pressure and earth moisture.

The criteria imposed upon the earth to arrive at tunneling limitations consistent with the earth stress analysis were those of no surface fissures, no significant surface upheaval, and no earth collapse into the melt zone which would be evidenced by an earth surface collapse. With these criteria a minimum allowable tunneling depth was established, and the limitations for melt pressure were established for any tunnel depth greater than the minimum allowable. The conclusions derived from the idealizations of elasticity, isotropy, homogeneity and plain-strain are:

1. If the earth's surface is free of dead weight, the crown of the tunnel bore should be at least a tunnel bore diameter below the earth's surface.

2. Under adverse operating conditions such as a water saturated highly porous medium, the direction of earth fissures and therefore the likelihood of surface upheaval or surface fissures can be estimated only after first conducting field experiments to determine the tectonic residuals, the percent water saturation and porosity, the extent of medium non-uniformity, and the direction of any earth medium anisotropies. For example, in an isotropic media without a tectonic residual stress, the preferred fracture direction is vertical. With a horizontal tectonic stress ($P_T > \rho_e C$) in excess of the tunnel centerline depth component of vertical overburden, the fracture tendency would be horizontal. In a non-uniform medium with an overlying hard sedimetary rock strata a vertical fracture is likely to be arrested and diverted to a horizontal plane.

3. When crack propagation is undesirable, it can be precluded with operational melt pressures of values less than the local vertical overburden in zones of moderate ($p_T \geq \rho_e C$) tectonic compression or with operational melt pressures of values less than the local horizontal overburden in zones of no tectonic compression. Without prior determinations of residual tectonic compressive stresses, a conservative melt pressure for the avoidance of crack propagation would be:

$$p \leq \frac{\nu}{1 - \nu} \rho_e C$$

4. The propagation of a fissure will depend upon the melt pressure and the volume availability of a substance which can fill and occupy the created crack void volume. To this end, methods were provided to evaluate melt and water volume availability.

5. When a fissure is desirable, such as may be required for the disposal of excess water, melt pressures must exceed the local overburden stress component. This eventuality has been considered here by providing relationships which define the allowable and required penetrator melt pressure consistent with both surface upheaval and surface fissure.

6. The alternative approach to minimizing any water disposal problems is by penetrator design. The design configuration must tend toward a very thin liner and a large percentage of mucking.

8.9 REFERENCES

8-1 R. D. Midlin, "Stress Distribution Around A Tunnel", Proc. Am. Soc. of Civil Engineers, Vol. 65, No. 4, 1939, pp. 619-642.

8-2 V. Hooker, D. Bickel and J. Oggson, "In Situ Determination of Stresses in Mountaneous Topography", Bureau of Mines Report of Investigations, RI 7654, 1972.

8-3 E. Harrison, W. Kieschnick, W. McGuire, "The Mechanics of Fracture Induction and Extension", Petroleum Transactions, AIME, Vol. 201, 1954, pp. 252-263.

8-4 M. Hubbert, D. Willis, "Mechanics of Hydraulic Fracturing", Petroleum Transactions, AIME, Vol. 210, 1957, pp. 153-168.

8-5 R. J. Sun, "Theoretical Size of Hydraulically Induced Horizontal Fractures and Corresponding Surface Uplift in an Idealized Medium", Journal of Geophysical Research, Vol. 74, No. 25, November 15, 1969, pp. 5995-6011.

8-6 Z. Anzo, "On the Stresses in a Gravitating Elastic Body Having a Circular Hole Near Its Horizontal Surface", Technology Reports of the Kyushu Imperical University, Vol. XII, No. 3, June 1937.

8-7 S. Yamaguti, "On the Stresses Around a Horizontal Circular Hole in a Gravitating Elastic Solid, " Journal of the Civil Engineering Society of Japan, Vol. 15 (1929), pp. 291-303.

8-8 R. Fenner, "Studies on the Determination of Stresses in the Earth", Gluckauf, August 13, 1938, Vol. 74, p. 681.

8-9 M. K. Hubbert, "Strength of the Earth", Bulletin AAPG (November 1945), 29, p. 1630.

8-10 R. P. Shoemaker, "A Review of Rock Pressure Problems", Quarterly of the Colorado School of Mines, 1951, Vol. 46, p. 133.

8-11 F. Birch, J. F. Schairer and H. C. Spicer, Handbook of Physical Constants, Geological Society American Special Papers 36 (January, 1942), p. 76.

8-12 R.E. Heuer, Geomechanical Model Study of the Behavior of Underground Openings in Rock Subjected to Static Loads, University of Illinois Ph.D. Dissertation, 1971, University Microfilms.

8-13 Savin, Stress Concentration Around Holes, Pergamon Press, New York, 1961, pp. 116-133.

8-14 L. Obert and W.I. Duvall, Rock Mechanics and the Design of Structures in Rock, John Wiley and Sons, New York, 1967, 650 pp.

8-15 Sneddon, I.N., "The Distribution of Stress in the Neighborhood of a Crack in an Elastic Solid", Proc. Roy. Soc. London, A, 187, 229-260, 1946.

8-16 Green, A.E., "On Boussinesg's Problem and Penny-Shaped Cracks", Proc. Cambridge Phil. Soc., 45, 2, 251-257, 1949.

8-17 Barenblatt, G.I., "The Mathematical Theory of Equilibrium Cracks in Brittle Fracture", Advances in Applied Mechanics, edited by H.L. Dryden and Th. Von Karman, pp. 55-129, Academic Press, New York, 1962.

8-18 Zheltov, Yu. P., and S.A. Khristianovich, The Hydraulic Fracturing of an Oil-Producing Formation (English Translation, Ass. Tech. Serv. RJ-742), Izv. Akad Nauk SSSR Mekhan. Mashinostr., 5, 3-41, 1955.

8-19 Ustinov, Yu. A., On the Influence of the Free Boundary of a Half Space on the Fracture Propagation (in Russian), Izv. Akad. Nuak SSSR Mekhan. Mashinostr., 4, 181-183, 1959.

8-20 D.B. Roberts, Subterrene Midterm Briefing Materials.

9.0 LINER STRUCTURAL

A structural integrity evaluation of the glass liner is provided to describe the state of stress for both the primary and secondary loading conditions. The primary loads include the externally applied earth loads and the internally applied thrust and penetrator weight loads. The purpose of primary load analysis is to define glass tube thickness requirements consistent with tunneling depth, material strength and geometric instability or buckling. In addition, the limitations of different thrusting schemes consistent with tube geometry, tube strength and penetrator weight are to be defined.

The secondary loads include the transient and residual thermal stresses. The purpose of secondary load analysis is to define cooling rate requirements consistent with both the thermoelastic stress limits and the desired heat treatment effects for a beneficial residual stress condition.

9.1 EXTERNALLY APPLIED PRIMARY LOADS

The source of primary loads exterior to the glass liner is the earth burden. As melt solidifies into the glass liner, the natural tendency is a volumetric contraction of the glass liner. The early solidification of the interior surface of the liner is a mechanism which tends to restrain the volumetric contraction which, in turn, creates a radial tensile stress at the melt/earth interface. This interface will either separate or remain in radial tension for some period of time. During this transient period, the radial compressive stress which the melt pressure used to exert upon the earth is lost due to the above described solidification process which is treated in detail in Section 9.3.

With no additional earth deformations after glass solidification, there would be no external earth compressive overburden loads. Here it is assumed that the earth will not arch itself about the tunnel wall in the steady state, but as time passes the earth will tend to either collapse

upon or plastically relocate itself about the tunnel wall. Based upon this assumption, three models are chosen for providing the steady state external compressive primary overburden loads These are a state of isotropic stress, a condition of no lateral restraint, and a condition of restrained lateral deformation in proximity of the glass liner. The condition of hydrostatic pressure describes the behavior of the porous, water saturated, plastically behaving earth materials like sands, clay, soil and gravel. The condition of no lateral restraint describes a condition of earth settling directly above the tunnel, and the condition of restrained lateral deformation describes earth elastic behavior after long term earth settling around the tunnel walls.

9.1.1 State of Hydrostatic Pressure

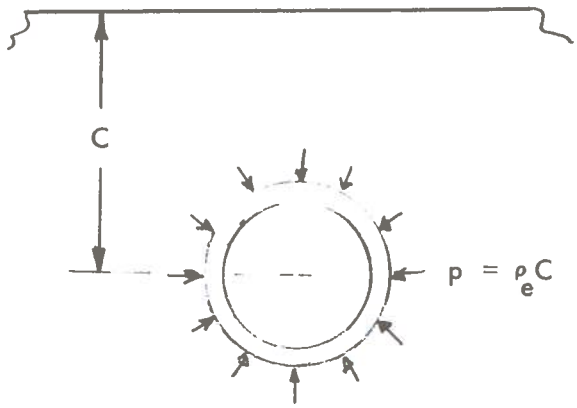

Under this condition, the glass liner plane-strain critical buckling load is:

(See Reference (9-1), pp. 612-613)

$$P_{cr} = \frac{3 E_g}{(1 - \nu_g^2)} \quad \frac{I}{b^3}$$

$$(\rho_e C)_{cr} = P_{cr}$$

$$I = \frac{1}{12} (b - a)^3$$

where

g ≡ subscript for glass properties

b ≡ glass liner outer radius

a ≡ glass liner inner radius

When the above equations are combined the critical tunneling depth is defined as:

$$C_{cr} = \frac{E_g}{4\rho_e (1 - \nu_g^2)} \quad (1 - \frac{a}{b})^3$$

Then

$$C < C_{cr}$$

is the criterion for a safe tunnel depth with respect to buckling. In non-dimensional from:

$$\frac{C (1 - \nu_g^2)\rho_e}{E_g \times 10^{-6}} < \frac{1}{4} (1 - \frac{a}{b})^3 \times 10^6 \qquad (9\text{-}1)$$

The maximum glass liner stress which occurs under the condition of hydrostatic pressure is circumferential compression at the inner radial surface. For thin walled tubes ($0.9 < a/b < 1.0$) this is also approximately a uniform compressive hoop stress across the entire thickness of the tube. From Reference (9-2), case 34, p. 308, the peak compressive hoop stress is:

$$\sigma = \frac{2\,p\,b^2}{b^2 - a^2} = \frac{2\,\rho_e\,C}{1 - \left(\frac{a}{b}\right)^2}$$

If stress (σ) is replaced by ($S - s$) where (S) is the crush strength and (s) is a compressive hoop stress from a primary load, such as a vacuum condition interior to the tunnel wall and/or a residual thermal hoop compression, then the criterion for a safe tunnel depth with respect to glass liner crushing is:

$$C < \frac{(S - s)}{2\,\rho_e}\left[1 - \left(\frac{a}{b}\right)^2\right]$$

In non-dimensional form

$$\frac{C\,(1 - \nu_g^2)\,\rho_e}{E_g \times 10^{-6}} < \left[\frac{(S - s)\,(1 - \nu_g^2)}{E_g \times 10^{-6}}\right] \left[\frac{1 - \left(\frac{a}{b}\right)^2}{2}\right] \qquad (9\text{-}2)$$

Equations (9-1) and (9-2) are plotted on Figure 9-1, and an example problem follows to illustrate the application of this curve.

Typical Parametric Glass Liner vs. Tunnel Depth Relation

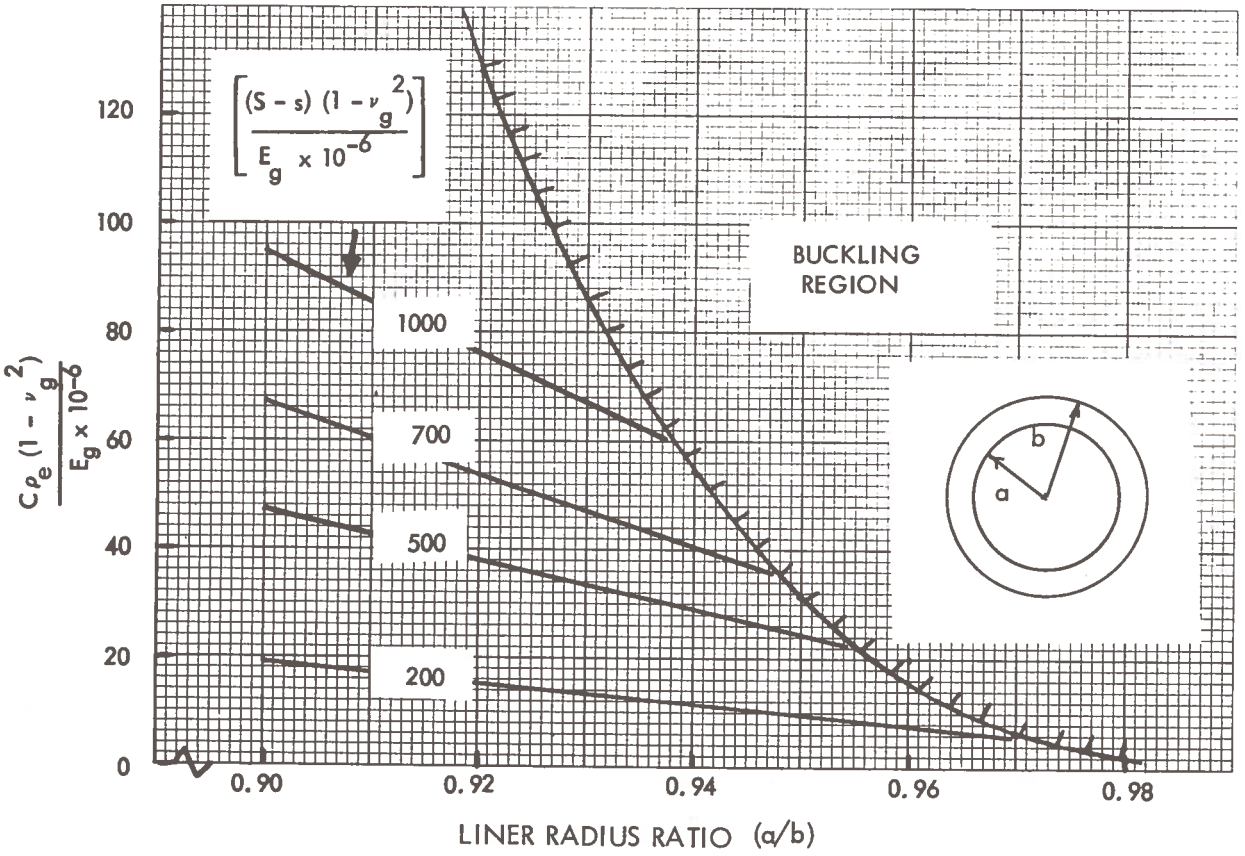

Figure 9-1. Maximum Allowable Tunnel Depth to Preclude Crushing and/or Buckling with Hydrostatic Compressive Primary Earth Load

Example:

What is the maximum allowable tunneling depth in a porous water saturated earth medium for the following conditions?

ρ_e = 0.0015 kg/cm^3

E_g = 0.7 x 10^6 kg/cm^2 (10 x 10^6 psi)

ν_g = 0.2

S = 175 kg/cm^2 (2500 psi)

a/b = 0.95

s = 0

Solution:

$$\frac{(S - s)(1 - \nu_g^2)}{E_g \times 10^{-6}} = \frac{(175)(0.96)}{0.7} = 240$$

From Figure 9-1 at a/b = 0.95

$$\frac{C\rho_e (1 - \nu_g^2)}{E_g \times 10^{-6}} < 31 \quad \text{(to preclude buckling)}$$

But more restrictive in the case,

from Figure 9-1 at a/b = 0.95 and at

$$\frac{(S - s)(1 - \nu_g^2)}{E_g \times 10^{-6}} = 240$$

$$\frac{C_e (1 - \nu_g^2)}{E_g \times 10^{-6}} < 10 + \frac{240 - 200}{500 - 200} (24 - 10) = 11.8 \text{ (linear interpolation of figure)}$$

$$C < \frac{(11.8)(0.7)}{(0.0015)(0.96)} = 5700 \text{ cm} = 57 \text{ m}$$

It should be noted here that an error in the properties of ν_g or E_g does not introduce an error into the latter C computation. The solution to this problem must logically be extended to define the permissible melt pressure consistent with an allowable fracture radius for excess water disposal. Reference to the example provided for water volume availability, and the example provided in conjunction with Figure 8-17 provide the method for extending this solution to obtain the permissible melt pressure at some tunneling depth less than 57 meters.

9.1.2 Condition of No Lateral Restraint

This earth model as an external compressive primary load on the glass liner is conceived by envisioning vertical but no lateral earth settlement in a zone of high porosity and residual radial tension immediately exterior to the glass liner. The zone of residual radial tension is assumed to be created by the melt volumetric dilitation during solidification.

An earth medium in which settlement would tend to be vertical is the anisotropic rock stratification shown below which had been fissured and uplifted by excess water disposal. Another possible medium is one with vertical stratification and settlement.

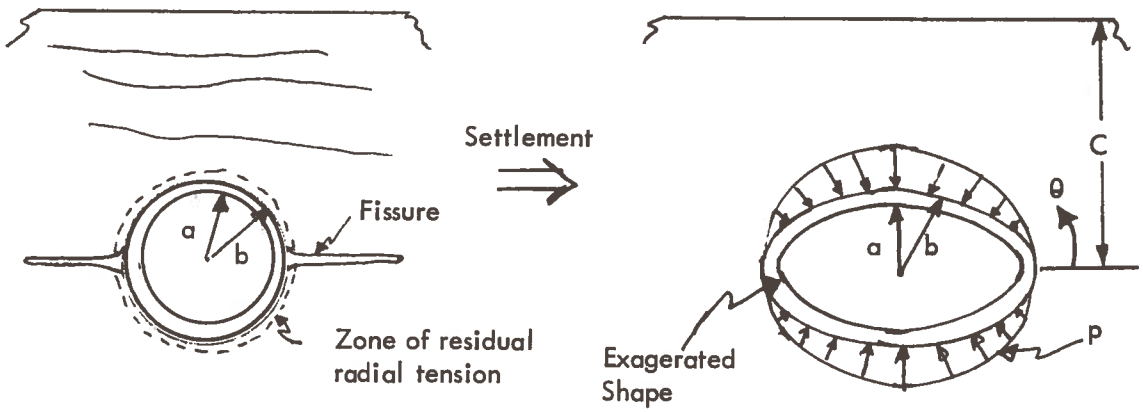

The average pressure acting on this liner is the vertical component of overburden,

$$\bar{p} = \rho_e C$$

The assumed non-uniform pressure distribution is

$$p = p_o \sin^2 \theta$$

where p_o is the maximum value of the non-uniform pressure distribution, and θ is defined in the above illustration.

The average pressure based on this distribution is:

$$\bar{p} = \frac{1}{2\pi} \int_o^{2\pi} p_o \sin^2 \theta \, d\theta = \frac{p_o}{2}$$

or

$$p_o = 2 \rho_e C$$

In Reference (9-3), Anderson and Boresi studied the stability behavior of a ring subjected to the above assumed centrally directed pressure distribution, and found in the equation

$$(p_o)_{cr} = K_{cr} \frac{EI}{b^3} \qquad \text{(plain stress)}$$

that K_{cr} is identically equal to twice the value which is obtained for the ring subjected to a uniform centrally directed pressure distribution, and substitution of the above shows that

$$(2\bar{p})_{cr} = \left[(2)(3)\right] \frac{EI}{b^3}$$

or

$$\bar{p}_{cr} = \rho_e C_{cr} = 3 \frac{EI}{b^3 (1 - \nu^2)} \qquad \text{(plane strain)}$$

which is identical to the tunneling depth criterion for the condition of uniform hydrostatic pressure. However, the maximum circumferential stresses which arise from this assumed non-uniform pressure distribution are drastically different from and quite limiting when compared to those resulting from a uniform pressure distribution. From the work in Reference (9-3) it was possible to determine that the maximum hoop stress occurs at the inner radial boundary, and the applicable equation provided in Reference (9-3) is:

$$(\sigma)_{r=a} = \left[- \frac{2 p_o (b^2 + a^2)}{(b^2 - a^2)^2} \right] \cos 2\theta - \frac{p_o b^2}{b^2 - a^2}$$

This circumferential stress is tensile at $\theta = \pi/2$ and compressive at $\theta = 0$. The tension at $\theta = \frac{\pi}{2}$ is slightly less than the compression at $\theta = 0$, but the form for tension will be developed here on the basis that the glass tensile strength is likely to be much less than its compressive strength. This maximum hoop tensile stress can be rewritten as:

$$\frac{\sigma}{p_o} = \frac{1 + 3\left(\frac{a}{b}\right)^2}{\left[1 - \left(\frac{a}{b}\right)^2\right]^2} < \frac{(S_t - s)}{2 \rho_e C}$$

This is the tensile failure criteria where $p_o = 2 \rho_e C$ and where the glass tensile stress is replaced by its tensile strength (S_t) minus any hoop residual thermal tensile stress (s) which may be present and/or any other hoop tensile stress (s) possibly provided by the primary loads of the penetrator thruster. In non-dimensional form this equation can be rewritten as:

$$\frac{C \rho_e (1 - \nu_g^2)}{E_g \times 10^{-6}} < \frac{1}{2} \left[\frac{(S_t - s)(1 - \nu_g^2)}{E_g \times 10^{-6}} \right] \left\{ \frac{\left[1 - \left(\frac{a}{b}\right)^2\right]^2}{1 + 3\left(\frac{a}{b}\right)^2} \right\} \qquad (9\text{-}3)$$

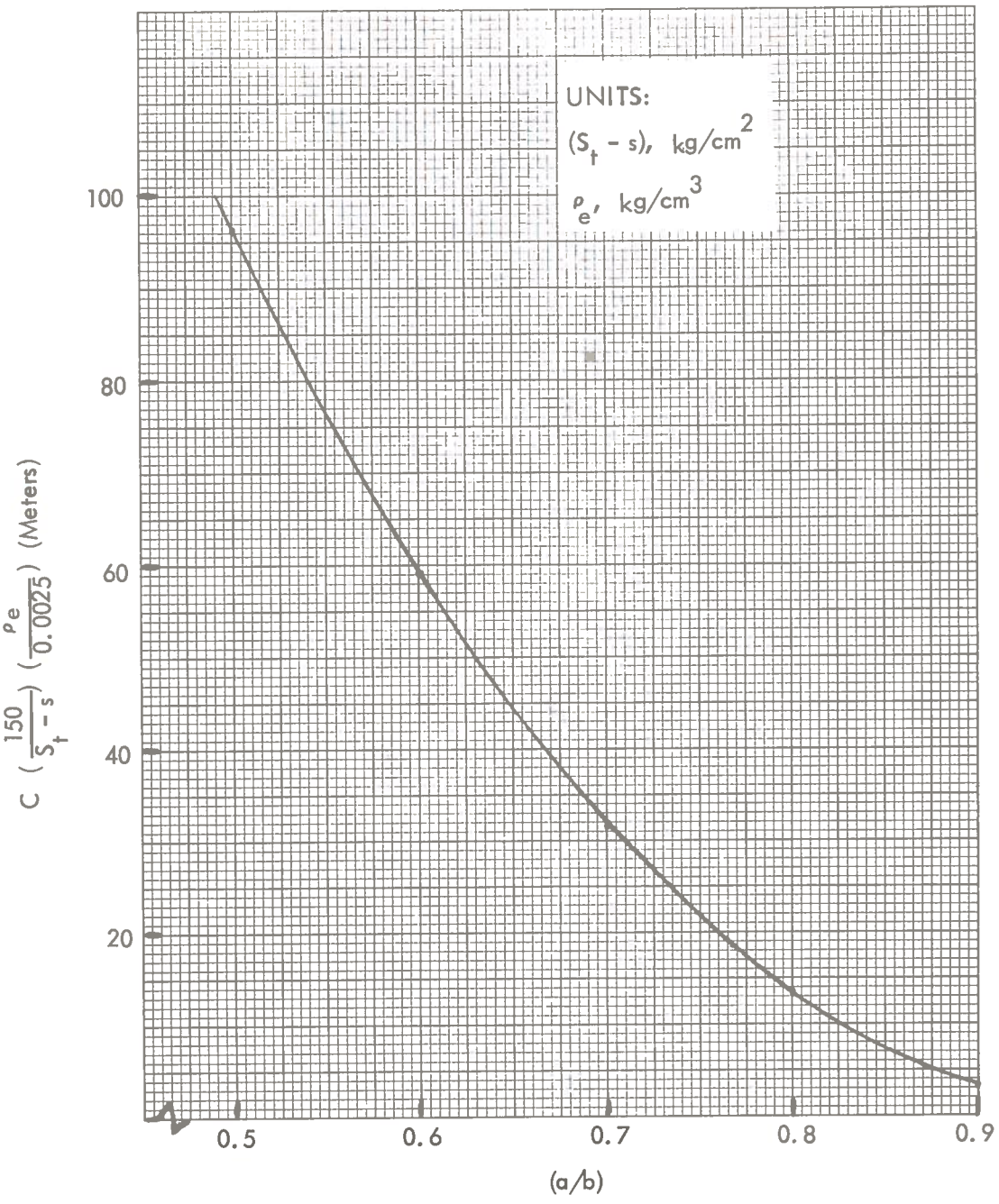

Figure 9-3. Maximum Allowable Tunnel Depth to Preclude Tunnel Wall Tensile Failure with the Condition of No Lateral Restraint in the Primary Earth Load (Use Figure 9-2 if a/b > 0.9)

$$\left(S_t - s\right) > \left(\frac{50}{13.5}\right)\left(\frac{0.002}{0.0025}\right) \quad (150) \quad = \quad 444\ k/cm^2 \quad = 4.4 \times 10^7\ N/m^2\ (6350\ psi)$$

$$S_t \quad > \quad (444 + s)\ kg/cm^2$$

Here (s) is residual thermal tensile hoop stress and/or a primary tensile hoop stress from the tunnel interior pressure or penetrator thrusting mechanism.

9.1.3 Condition of Restrained Lateral Deformation

This is a primary earth load model with structural consequences lying between those of the hydrostatic pressure model and the model of no lateral restraint. It assumes that earth settlement about the glass liner is such that it returns to the overburden condition which existed prior to the tunnel formation. Evidence of current practice within the framework of this model is provided by Monsees[9-4]. In his work, Monsees referred to the San Francisco Bay Area Rapid Transit (BART) tunnels, the Washington, D. C. subway design manual, the Lisbon Subway design specifications, and the Chicago subway design practice. Some excerpts follow:

> "The consultants for the BART system believed that the tunnel lining would offer little resistance to the unbalanced ground forces on the horizontal and vertical planes. They believed that the ground the lining would distort together until largely uniform forces acted on the circumference of the lining. Their design recommendations, therefore, included a combination of radial loads related to the overburden and stresses in the liner caused by its distortion. Arching was considered to begin being important in granular materials at a depth of burial to the crown of about 26 ft (1.5 times the diameter) but it does not appear explicitly in the equations until the depth of burial is 35 ft. Beyond 35 ft of cover, only one-half of the overburden was considered to load the tunnel. No arching was considered in soft clay."

"The design manual for the Washington, D. C., subway recommends a ratio of horizontal pressure to vertical overburden pressure of 0. 875 for the design of reinforced concrete rigid earth tunnel sections. Wherever possible, the following guide was used in establishing the minimum rock cover for the Washington subway:

Maximum Excavated Width	Minimum Sound Rock Cover
20 ft.	10 ft.
35 ft.	15 ft.
70 ft.	30 ft.

With rock cover of these amounts, the rock was believed capable of supporting itself and the overburden with no more than rock bolt reinforcement. For any condition in either soil or rock not covered by the above paragraphs the design manual instructs the designer to follow the recommendations of the Soils Consultant. "

"The vertical and horizontal loads on Lisbon Subway tunnels driven in sand and silt were estimated according to Terzaghi's recommendations. Loads for tunnels in rock were also estimated as recommended by Terzaghi. In clays the vertical pressure was taken as the overburden pressure minus an amount depending on the effective shear strength of the material. Horizontal pressures in clay were estimated as 0. 5 to 0. 7 times the vertical pressure. "

A final quote from Monsees[9-4] concerning the Chicago subway and tunnel liner design practice in general is now appropriate.

"The recent design specifications discussed in this section illustrate an important point: the process of developing design methods is repeated for every new project, but the results seldom represent innovations or generalizations. The original design of the Chicago subway tunnels in soft ground serves as an example. This design followed the existing practice for sewers in that city (Terzaghi, 1942). The vertical pressure on the top of the tunnel was taken equal to the overburden and the vertical pressure on the base was taken as the sum of the pressure on the top and the weight of the arch. Side pressures were assumed equal to the pressure of a fluid with a density of 1/3 to 2/3 of the actual weight of the soil. These concepts are very similar to those used four decades later in the Washington and the Lisbon subways, although the actual numbers have been adjusted to more realistic values. "

The current literature cited above on tunnel liner design practice gave no justification for the earth/liner model in Section 9.1.2 referred to as the condition of no lateral restraint. The application of the concept of tunneling with a heated penetrator would be a new project. The structural behaviors unique to tunneling with a heated penetrator are the potential need for planned earth fracture and upheaval, the potential for unplanned or accidental earth fractures and the volumetric contraction tendency of the solidifying liner. It is the combination of these unique phenomena that has led to the innovative design method described as the condition of no lateral restraint. As such, it is recommended here that this model, which would be considered quite overly conservative in conventional tunneling practice, should be regarded as a potentially real situation for liners formed with a heated penetrator.

Before proceeding with the structural considerations for the condition of restrained lateral deformation, which is consistent with current tunnel liner practice, it is now mentioned that in none of the models considered in this work is the earth given credit for self support. This conservative assumption is based on the realization that:

1) Rock bolt reinforcement is not to be a likely practice during the solidification of a liner formed by a heated penetrator, and

2) Investigations[8-10] on the subject of natural arches have found that in order to support even moderate loads over geologic time, arches must rise as high as they span.

Additionally, for the models in this work the weight of the tunnel liner has been neglected as a self-inducing stress mechanism. This is non-conservative, but its basis evolves from the fact that external earth loads will govern the liner deformation and will likewise tend to support the liner weight.

The structural model for the condition of restrained lateral deformation follows. It is based upon the superposition of two "sine-square" pressure distributions.

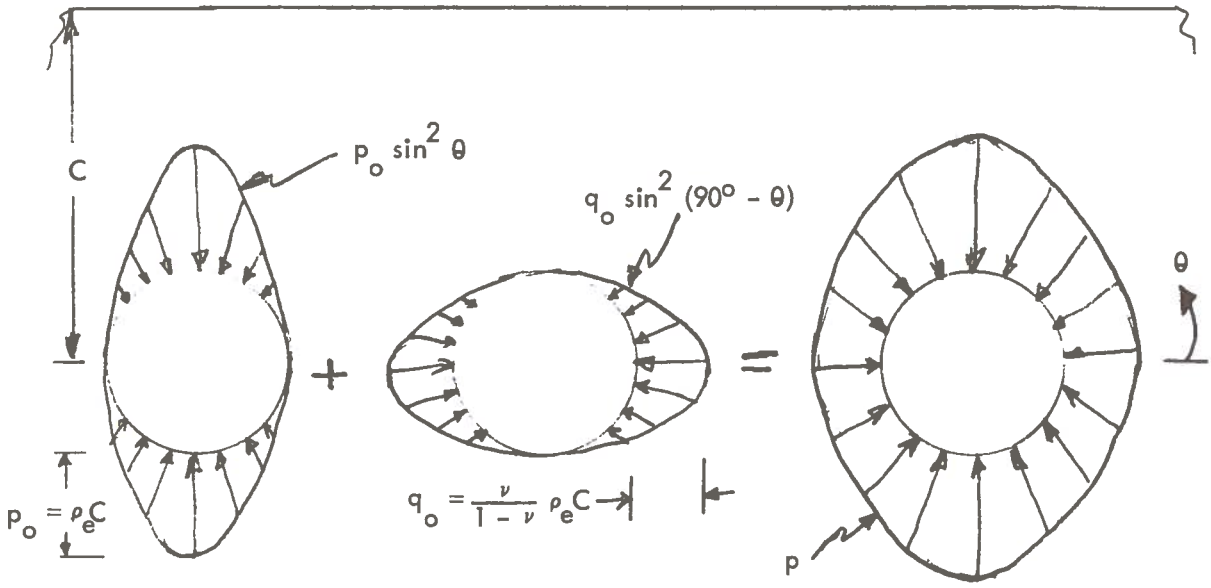

$$p = \rho_e C \sin^2 \theta + \frac{\nu}{1-\nu} \rho_e C \sin^2 (90^o - \theta)$$

Based upon the comparison which can be made for the critical buckling pressure given for the models provided in Sections 9.1.1 and 9.1.2, it can be concluded that Figure 9-2 would provide a conservative means for evaluating the critical tunneling depth with respect to liner buckling for the above primary earth load model.

The tunnel liner stress can be evaluated by superposition of the stress resulting from each of the "sine-square" pressure distributions. The circumferential stresses of interest, derivable from the works of Boresi[9-3] and based upon a pressure distribution of $p = p_o \sin^2 \theta$ are:

$$\sigma)_{r=a} = \left[- \frac{2 p_o b^2 (b^2 + a^2)}{(b^2 - a^2)^2} \right] \cos 2\theta - \frac{p_o b^2}{b^2 - a^2}$$

$$\sigma)_{r=b} = \frac{p_o}{2 (b^2 - a^2)^2} \left[(b^2 + a^2)^2 + 4 a^2 b^2 \right] \cos 2\theta - \frac{p_o (b^2 + a^2)}{2 (b^2 - a^2)}$$

The peak stresses occur at the inner radial surface, and the superposition provides:

$$\sigma)_{r=a} = -\left[2\,p_o \cos\theta + 2\,q_o \cos 2\,(90^\circ - \theta)\right]\left[\frac{b^2\,(b^2 + a^2)}{(b^2 - a^2)^2}\right] - (p_o + q_o)\,\frac{b^2}{b^2 - a^2}$$

The peak circumferential compression occurs at $\theta = 0^\circ$.

$$\sigma)_{\substack{\theta=0^\circ \\ r=a}} = -2\,p_o\,\frac{b^2}{b^2 - a^2}\left[\frac{b^2 + a^2}{b^2 - a^2} + \frac{1}{2}\right] + 2\,q_o\,\frac{b^2}{b^2 - a^2}\left[\frac{b^2 + a^2}{b^2 - a^2} - \frac{1}{2}\right]$$

The peak circumferential tension occurs at $\theta = 90^\circ$.

$$\sigma)_{\substack{\theta=90^\circ \\ r=a}} = -2\,q_o\,\frac{b^2}{b^2 - a^2}\left[\frac{b^2 + a^2}{b^2 - a^2} + \frac{1}{2}\right] + 2\,p_o\,\frac{b^2}{b^2 - a^2}\left[\frac{b^2 + a^2}{b^2 - a^2} - \frac{1}{2}\right]$$

The compressive and tensile stresses are now treated separately, recognizing that the tensile and compressive strengths and residual stresses will differ for the glass liner.

Compressive Stress

Where (S) is the compressive strength and (s) is residual thermal hoop compression or hoop compression from any other primary load, then the non-failure criterion for hoop compression is:

$$(S - s) > 2\rho_e C\,\frac{b^2}{b^2 - a^2}\left[\frac{b^2 + a^2}{b^2 - a^2} + \frac{1}{2}\right] - 2\rho_e C\,\frac{\nu}{1 - \nu}\,\frac{b^2}{b^2 - a^2}\left[\frac{b^2 + a^2}{b^2 - a^2} - \frac{1}{2}\right]$$

where ρ_e and ν are earth properties. Or

$$C < \frac{(S - s)\left[1 - \left(\frac{a}{b}\right)^2\right]}{2\,\rho_e\left\{\left[\frac{1 + \left(\frac{a}{b}\right)^2}{1 - \left(\frac{a}{b}\right)^2}\right]\left(1 - \frac{\nu}{1 - \nu}\right) + \frac{1}{2}\left(1 + \frac{\nu}{1 - \nu}\right)\right\}}$$

A normalization with respect to

ρ_e = 0.0025 kg/cm^3 and

(S - s) = 125 kg/cm^2 1.2 N/m^2 (1800 psi)

gives:

$$C\left(\frac{\rho_e}{.0025}\right)\left(\frac{125}{S-s}\right) < 25000\ \frac{\left[1-\left(\frac{a}{b}\right)^2\right]}{\left\{\left[\frac{1+\left(\frac{a}{b}\right)^2}{1-\left(\frac{a}{b}\right)^2}\right]\left(1-\frac{\nu}{1-\nu}\right)+\frac{1}{2}\left(1+\frac{\nu}{1-\nu}\right)\right\}} \qquad (9\text{-}5)$$

This equation is plotted on Figure 9-4 for various values of the earth's poisson ratio (ν).

Tensile Stress

The tunnel wall tensile strength requirement (S_t) with the residual thermal hoop tension (s) of hoop tension (s) from any other primary load is:

$$(S_t - s) > 2\rho_e C\ \frac{b^2}{b^2-a^2}\left[\frac{b^2+a^2}{b^2-a^2}-\frac{1}{2}\right] - 2\rho_e C\ \frac{\nu}{1-\nu}\ \frac{b^2}{b^2-a^2}\left[\frac{b^2+a^2}{b^2-a^2}+\frac{1}{2}\right]$$

where ρ_e and ν are earth properties. Or

$$C < \frac{(S_t - s)\left[1-\left(\frac{a}{b}\right)^2\right]}{2\rho_e\left\{\left[\frac{1+\left(\frac{a}{b}\right)^2}{1-\left(\frac{a}{b}\right)^2}\right]\left(1-\frac{\nu}{1-\nu}\right)-\frac{1}{2}\left(1+\frac{\nu}{1-\nu}\right)\right\}}$$

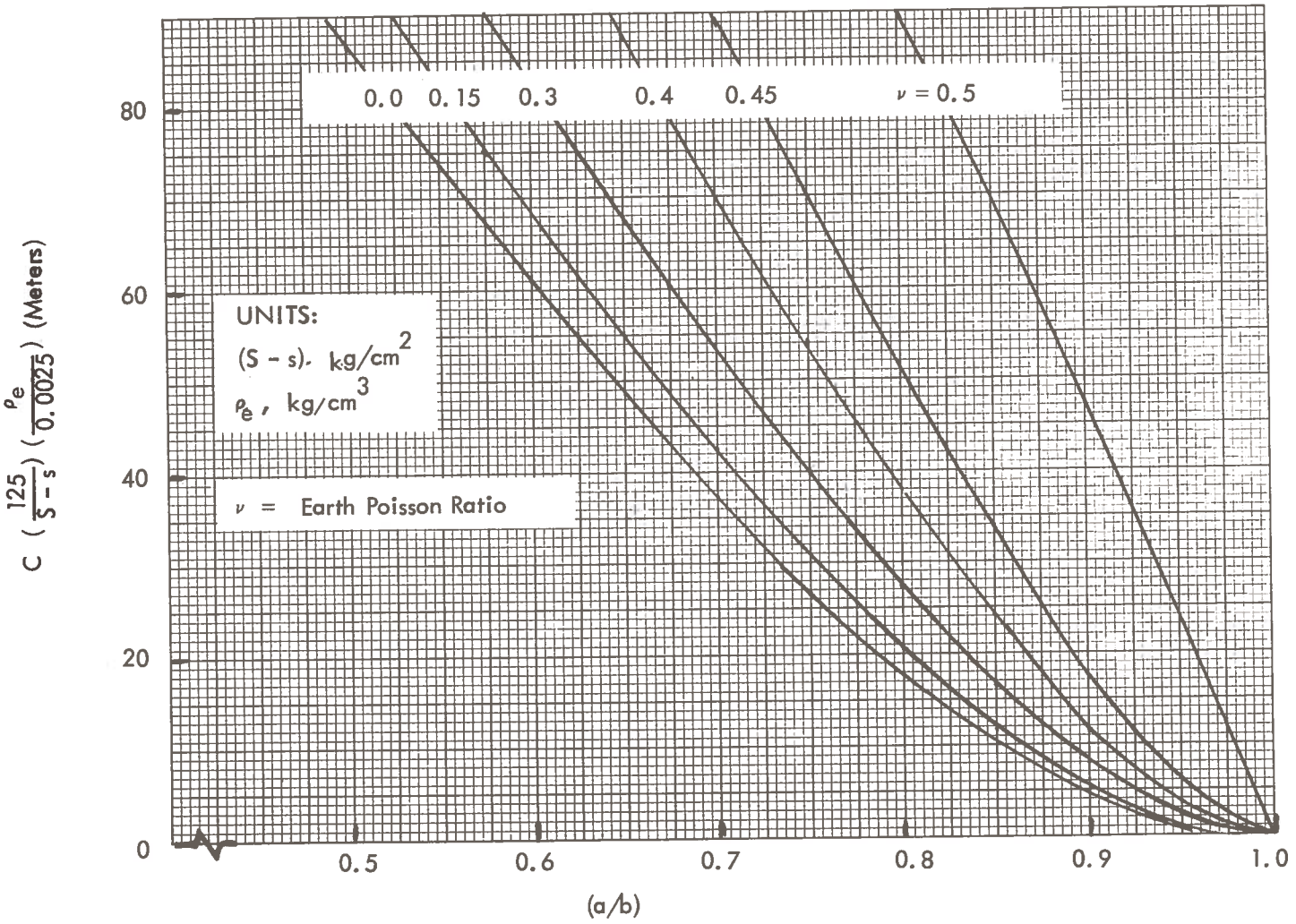

Figure 9-4. Maximum Allowable Tunnel Depth to Preclude Tunnel Liner Compressive Failure with the Condition of Restrained Lateral Deformation (Use Figure 9-1 for the Critical Buckling Criterion)

The normalization with respect to

ρ_e = 0.0025 kg/cm^3 and

$(S_t - s)$ = 125 kg/cm^2, 1.2 N/m^2 (1800 psi)

gives:

$$C \left(\frac{\rho_e}{0.0025}\right)\left(\frac{125}{S_t - s}\right) < 25000 \frac{\left[1 - \left(\frac{a}{b}\right)^2\right]}{\left\{\left[\frac{1 + \left(\frac{a}{b}\right)^2}{1 - \left(\frac{a}{b}\right)^2}\right]\left(1 - \frac{\nu}{1 - \nu}\right) - \frac{1}{2}\left(1 + \frac{\nu}{1 - \nu}\right)\right\}} \quad (9-$$

This equation is plotted on Figure 9-5 for various values of the earth's Poisson ratio (ν). It is here noted that if

$$\frac{1 + \left(\frac{a}{b}\right)^2}{1 - \left(\frac{a}{b}\right)^2} < \frac{1}{2(1 - 2\nu)}$$

then there is no tensile hoop stress, which is to say that stress is compressive at the $r = a$, $\theta = 90^\circ$ location. For this condition the peak compression is at the $r = a$, $\theta = 0^\circ$ location given by Figure 9-4.

A sample problem follows for the condition of restrained lateral deformation.

Example:

A tunnel is melted with the liner proportion of $a/b = 0.9$ at a depth of 50 meters in a medium of bulk density of 0.002 kg/cm^3 and of 0.3 Poisson ratio. What is the glass strength requirement?

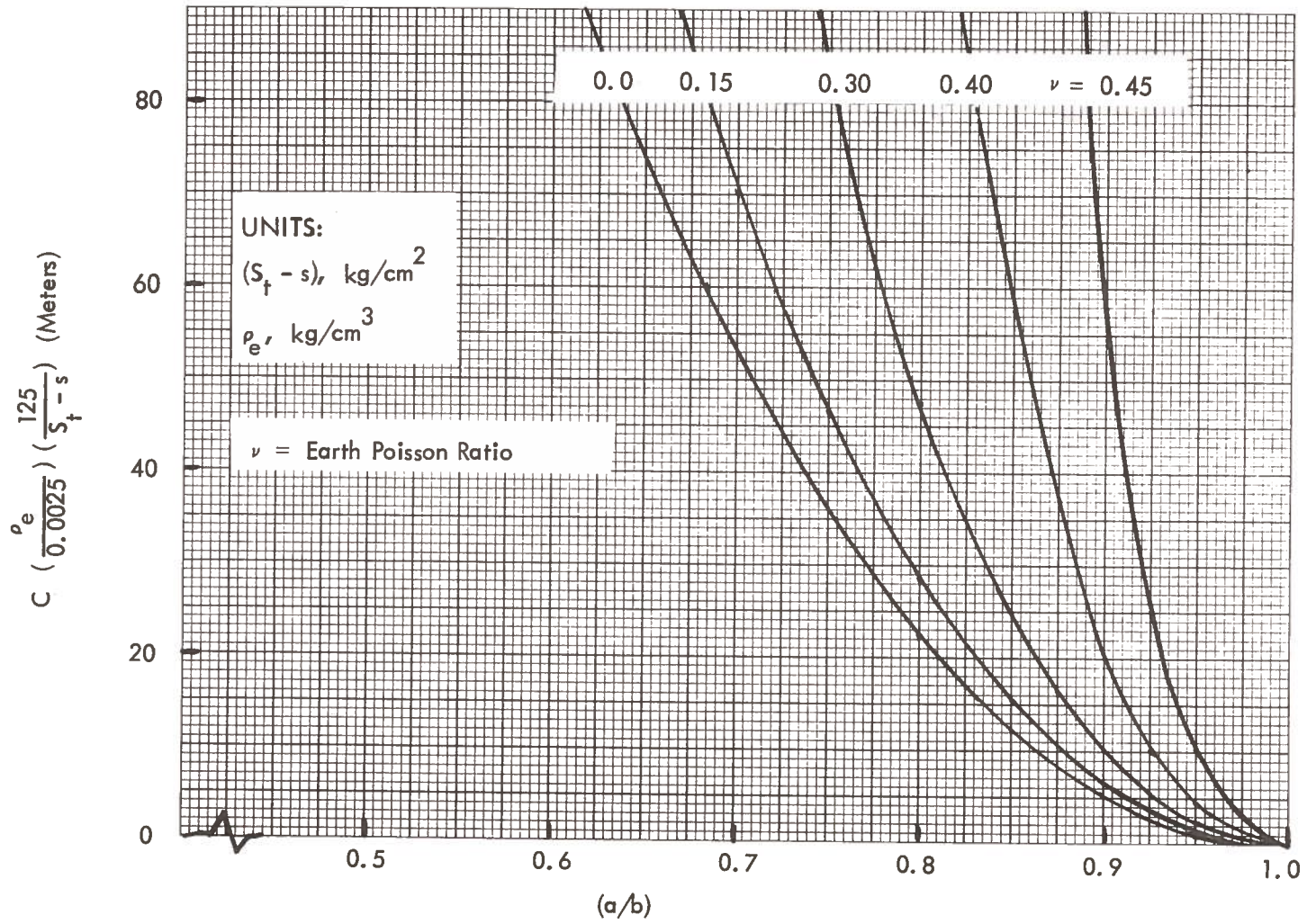

Figure 9-5. Maximum Allowable Tunnel Depth to Preclude Tunnel Liner Tensile Failure with the Condition of Restrained Lateral Deformation

Assumption:

The earth settlement about the glass liner is such that it returns to the overburden condition which existed prior to the tunnel formation.

Solution:

From Figure 9-4 at $a/b = 0.9$, $\nu = 0.3$

$$C\left(\frac{125}{S - s}\right)\left(\frac{\rho_e}{0.0025}\right) < 8.0$$

$$S - s > \left(\frac{50}{8}\right)\left(\frac{0.002}{0.0025}\right)(125) = 625 \text{ kg/cm}^2 = 6 \times 10^7 \text{ N/m}^2 \text{ (9,000 psi)}$$

$$S > (625 + s) \text{ kg/cm}^2$$

This is the strength requirement to preclude a compressive failure where (s) is a thermal residual or another primary compressive stress.

From Figure 9-5 at $a/b = 0.9$, $\nu = 0.3$

$$C\left(\frac{125}{S_t - s}\right)\left(\frac{\rho_e}{0.0025}\right) < 10$$

$$(S_t - s) > \left(\frac{50}{10}\right)\left(\frac{0.002}{0.0025}\right)(125) = 500 \text{ kg/cm}^2 = 5 \times 10^7 \text{ N/m}^2 \text{ (7,200 psi)}$$

$$S_t > (500 + s) \text{ kg/cm}^2$$

This is the tensile strength requirement.

9.1.4 Earth Primary Load On Liner-Summary

Three separate earth load models on the liner were considered. (1) A condition of hydrostatic pressure characterized the liner loads from an idealized earth model composed of a plastically behaving medium, possibly best characterized by quicksand. This is an unlikely earth medium in which design considerations would have to resolve the initial liner support problem during cooldown in parallel with a penetrator "sinking" problem. Nevertheless, this idealized earth model was included as a limiting case of a more general earth model, because it provided a valid liner stability criterion against buckling which was extrapolateable to other earth model liner loading conditions. (2) The condition of no lateral restraint characterized the liner loads from an earth settling directly above the tunnel liner. This model was conceived by envisioning vertical but no lateral earth settlement about the liner, and it was inspired by recognizing two unique features associated with tunneling by heated penetrators. These are the volumetric contraction tendency of the solidifying liner and the potential for both planned and unplanned earth fracture and upheaval. The sequence of events in arriving at this earth model liner loading condition is a horizontal fissure with unheaval followed by liner radial contractions and then a vertical earth settlement. (3) The condition of restrained lateral deformation characterized the liner integrity by an earth load model with structural consequences lying between those of the hydrostatic pressure model and the model of no lateral restraint. It assumed that earth settlement about the glass liner is such that it returns to the overburden condition which existed prior to the tunnel formation. This model is best envisioned as appropriate in unfractured earth media characterized by the Poission ratio values above 0.3, and these are the sands, clays, and shales.

The allowable tunneling depth for each of these models was established as a function of glass strength, earth density, liner thickness and other related material properties. The conclusions from this work are concerned with the models and the liner integrity.

a) The prediction of a glass liner tensile or compressive failure with these models can be considered appropriate only if the liner is initially free of cracks. This is to say, if a transverse thermal crack exists prior to the earth settlement, then the primary earth load models have no meaning.

b) The model for the condition of hydrostatic pressure is only a special case for the more general model referred to as the condition of restrained lateral deformation.

c) The model for the condition of restrained lateral deformation indicates the required liner thickness to be about 23% of the penetrator radius for a tunnel centerline depth of 70 meters. This corresponds to a zero margin of safety against a longitudinal tensile crack under the following conditions: earth density = 0.0025 kg/cm^3, earth Poisson ratio = 0.35, glass tensile strength = 1.48×10^7 N/m^2 ($\approx$2150 psi). Under these same conditions, the required thickness is about 8% of the penetrator radius for a tunnel centerline depth of 10 meters.

d) The model for the condition of no lateral restraint indicates the required liner thickness to be about 75% of the penetrator radius for a tunnel at 70 meters of centerline depth and about 21% for the 10 meter deep tunnel. This is based upon the same conditions given in c), above.

e) The liner thicknesses required to prevent liner cracking under external earth loading indicate that liner buckling is not a problem.

The recommendation for any future efforts in this area of analysis should logically be deferred until sufficient liners have been produced experimentally to generate good estimates for the liner material properties, especially its strength. If a cracked liner is the only alternative, it is recommended that tests be conducted on experimental liners under simulated earth loading conditions to evaluate the arching stability of scale models which may or may not be free of thermal stress cracks. The major uncertainity in scale model testing with a brittle material is that associated with Weibull's theory which would indicate the larger the sample size, the weaker the material.

9.2 INTERNALLY APPLIED PRIMARY LOADS

A source of primary loads interior to the glass liner is the penetrator. The penetrator will apply forces to the glass liner through the action of a thrust mechanism as well as its own weight. This portion of the analysis is presented to define permissible thrust loads and penetrator weights as a function of the glass liner, penetrator, and earth characteristics.

The assumptions applied to make the analysis tractable are summarized as follows:

1. Thrust is obtained through friction between the liner and penetrator.
2. The radial force exerted by the penetrator on the liner, in order to produce a thrust, is distributed uniformly around the internal circumference of the liner and away from its ends.
3. The liner stresses resulting from thrust are conservatively evaluated with thin wall cylinder theory by neglecting interactions with the earth surrounding the liner.
4. The weight of the penetrator is uniformly distributed along its length in contact with the liner.
5. The liner is treated as a "long" (see Section 9.2.2) beam on an elastic foundation in its support of the penetrator weight.

There is some uncertainty concerning a "short" beam versus a "long" beam, but nevertheless the above assumptions are considered realistic and not too restrictive as to nullify the results. A suggestion to be made in the event of further analysis, when the earth stiffness, the liner Young's modulus, and the liner area moment of inertia are more clearly defined, is that the length of the liner should be checked to verify the assumption that it can be treated as a "long" beam on an elastic foundation. If a short beam analysis is required, however, which could represent slightly worse cases than a long beam analysis, it is suggested that the methods indicated in References (9-1) and (9-13) be investigated.

9.2.1 Thrust Mechanism Effects

The maximum principal stresses in the liner due to a uniform radial loading condition are (see Reference (9-2), pp. 301):

$$S(\text{axial})_{max} = -\frac{3p}{2\lambda t^2} \quad \text{at inner surface}$$

$$S(\text{hoop})_{max} = \frac{p R \lambda}{2t}$$

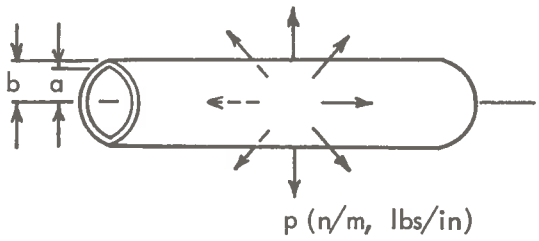

$t = b - a$ = liner thickness

$R = \frac{a+b}{2}$ = mean radius

ν = Poisson's ratio

$$\lambda = \sqrt[4]{\frac{3(1-\nu^2)}{R^2 t^2}}$$

The maximum principal stresses in the liner due to a uniform friction force (thrust) distribution are: (see Reference (9-2), pp. 302):

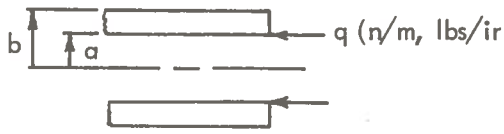

$$S(\text{axial})_{max} = -\frac{6M_1}{t^2} - \frac{q\,a\,(2\pi)}{R\,t\,(2\pi)}$$

$$S(\text{axial})_{max} = -\frac{q}{t}\left(\frac{3}{2} + \frac{q}{R}\right) \quad \text{at inner surface}$$

$$S(\text{hoop})_{max} = \nu\frac{6M_1}{t} + \frac{2M_1}{t}\lambda^2 R$$

$$S(\text{hoop})_{max} = \frac{q}{t}\left(\frac{3\nu}{2} + \frac{\sqrt{3(1-\nu^2)}}{2}\right)$$

at inner surface

$$M_1 = \frac{M_o}{2} = qt/4$$

Combining the effects of the thrust force and its coexistent radial force distribution, the maximum axial stress in the liner is:

$$S\,(\text{axial})_{max} = -\frac{3p}{2\lambda t^2} - \frac{q}{t}\left(\frac{3}{2} + \frac{a}{R}\right) \qquad (9\text{-}7)$$

The radial and friction force distributions are related as follows:

$$q = \eta p$$

where η is the coefficient of friction. Making the appropriate substitutions, Equation (9-7) can be transformed into the desired result.

$$S\,(\text{axial})_{max} = -\frac{q}{t}\left(\frac{3}{2\eta\lambda t} + \frac{3}{2} + \frac{2a}{a+b}\right)$$

$$= \frac{Q\,a}{2\pi a^2 t}\left[\frac{3}{2\eta\sqrt[4]{3(1-\nu^2)}\sqrt{\frac{t}{R}}} + \frac{3}{2} + \frac{2\left(\frac{a}{b}\right)}{\frac{a}{b}+1}\right]$$

$$S\,(\text{axial})_{max} = \frac{Q\left(\frac{a}{b}\right)}{2A\left(1-\frac{a}{b}\right)}\left[\frac{3}{2\eta\sqrt[4]{3(1-\nu^2)}\sqrt{\frac{2\left(1-\frac{a}{b}\right)}{1+\frac{a}{b}}}} + \frac{3}{2} + \frac{2\left(\frac{a}{b}\right)}{\frac{a}{b}+1}\right] \qquad (9\text{-}8)$$

(at liner inner surface)

where

$Q = q\,(2\pi a)$ = total thrust force

$A = \pi a^2$

Nondimensionalizing Equation (9-8) yields the following result:

$$\frac{Q}{S\,(\text{axial})\,A} = \frac{2\left(1-\frac{a}{b}\right)}{\left(\frac{a}{b}\right)\left[\frac{3}{2\eta\ \sqrt[4]{3\,(1-\nu^2)}\ \sqrt{\frac{2\left(1-\frac{a}{b}\right)}{1+\frac{a}{b}}}}+\frac{3}{2}+\frac{2\left(\frac{a}{b}\right)}{\frac{a}{b}+1}\right]} \qquad (9\text{-}9$$

The variation of the allowable penetrator thrust based on the allowable axial stress in the liner for various coefficients of friction and Poisson's ratios is shown in Figure 9-6. The figure indicates several trends which are detected by varying one or more variables. For a given liner allowable stress level and desired tunnel cross sectional area, the allowable thrust increases as the coefficient of friction increases. Also, for a given liner allowable stress level and tunnel cross sectional area, the allowable thrust decreases as the liner thickness decreases.

Combining the effects of the thrust force and its coexistent radial force distribution, the maximum hoop stress in the liner is:

$$S\,(\text{hoop})_{max} = \frac{p\,R\,\lambda}{2t}+\frac{q}{t}\left(\frac{3\,\nu}{2}+\frac{\sqrt{3\,(1-\nu^2)}}{2}\right) \qquad (9\text{-}1$$

Making the appropriate substitutions, Equation (9-10) can be transformed into the desired result.

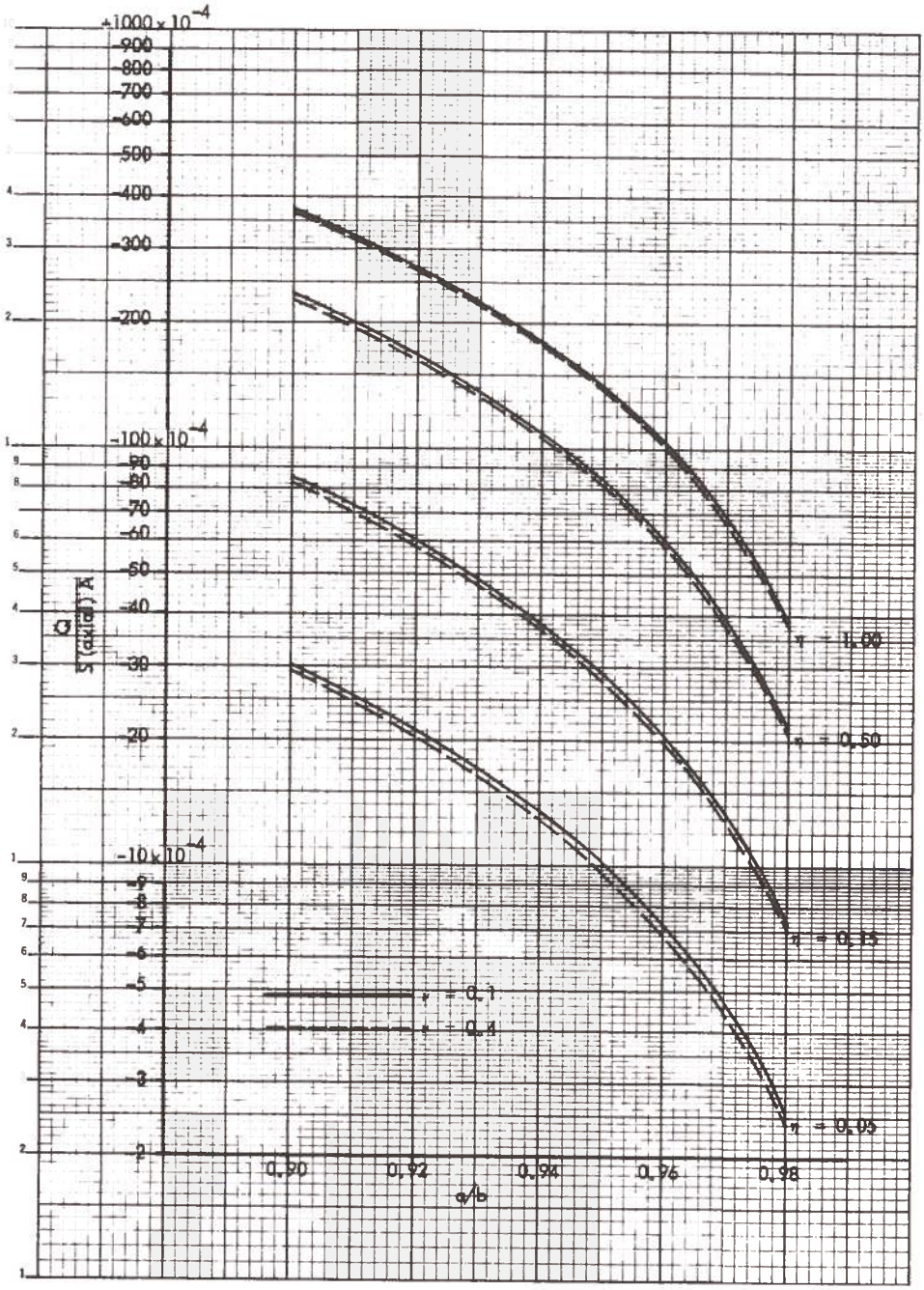

Figure 9-6. Maximum Allowable Penetrator Thrust Based on the Allowable Axial Stress in Liner

$$S(\text{hoop})_{max} = \frac{q}{t}\left(\frac{\sqrt[4]{3(1-\nu^2)}\sqrt{\frac{R^2}{t^2}}}{2\eta} + \frac{3\nu}{2} + \frac{\sqrt{3(1-\nu^2)}}{2}\right)$$

$$= \frac{Q}{2\pi a t}\left(\frac{\sqrt[4]{3(1-\nu^2)}\sqrt{\frac{R}{t}}}{2\eta} + \frac{3\nu}{2} + \frac{\sqrt{3(1-\nu^2)}}{2}\right)$$

$$= \frac{Q\,a}{2\pi a^2 (b-a)}\left[\frac{\sqrt[4]{3(1-\nu^2)}\sqrt{\frac{a+b}{2(b-a)}}}{2\eta} + \frac{3\nu}{2} + \frac{\sqrt{3(1-\nu^2)}}{2}\right]$$

$$S(\text{hoop})_{max} = \frac{Q\left(\frac{a}{b}\right)}{2A\left(1-\frac{a}{b}\right)}\left[\frac{\sqrt[4]{3(1-\nu^2)}\sqrt{\frac{1+a/b}{2(1-a/b)}}}{2\eta} + \frac{3\nu}{2} + \frac{\sqrt{3(1-\nu^2)}}{2}\right]$$

(at liner inner surface) (9-11)

Nondimensionalizing Equation (9-11) yields the following result:

$$\frac{Q}{S(\text{hoop})\,A} = \frac{2\left(1-\frac{a}{b}\right)}{\left(\frac{a}{b}\right)\left[\frac{\sqrt[4]{3(1-\nu^2)}\sqrt{\frac{1+a/b}{2(1-a/b)}}}{2\eta} + \frac{3\nu}{2} + \frac{\sqrt{3(1-\nu^2)}}{2}\right]} \quad (9\text{-}12$$

The variation of the allowable penetrator thrust based on the allowable hoop stress in the liner for various coefficients of friction and Poisson's ratios is shown in Figure 9-7. The observations in trends made earlier for Figure 9-6 also apply to Figure 9-7. By comparing Figures 9-6 and 9-7, it can be seen that Figure 9-7 (hoop stress) will permit higher thrust loads for a given liner stress level, coefficient of friction, Poisson's ratio, and a/b ratio than Figure 9-6 (axial stress).

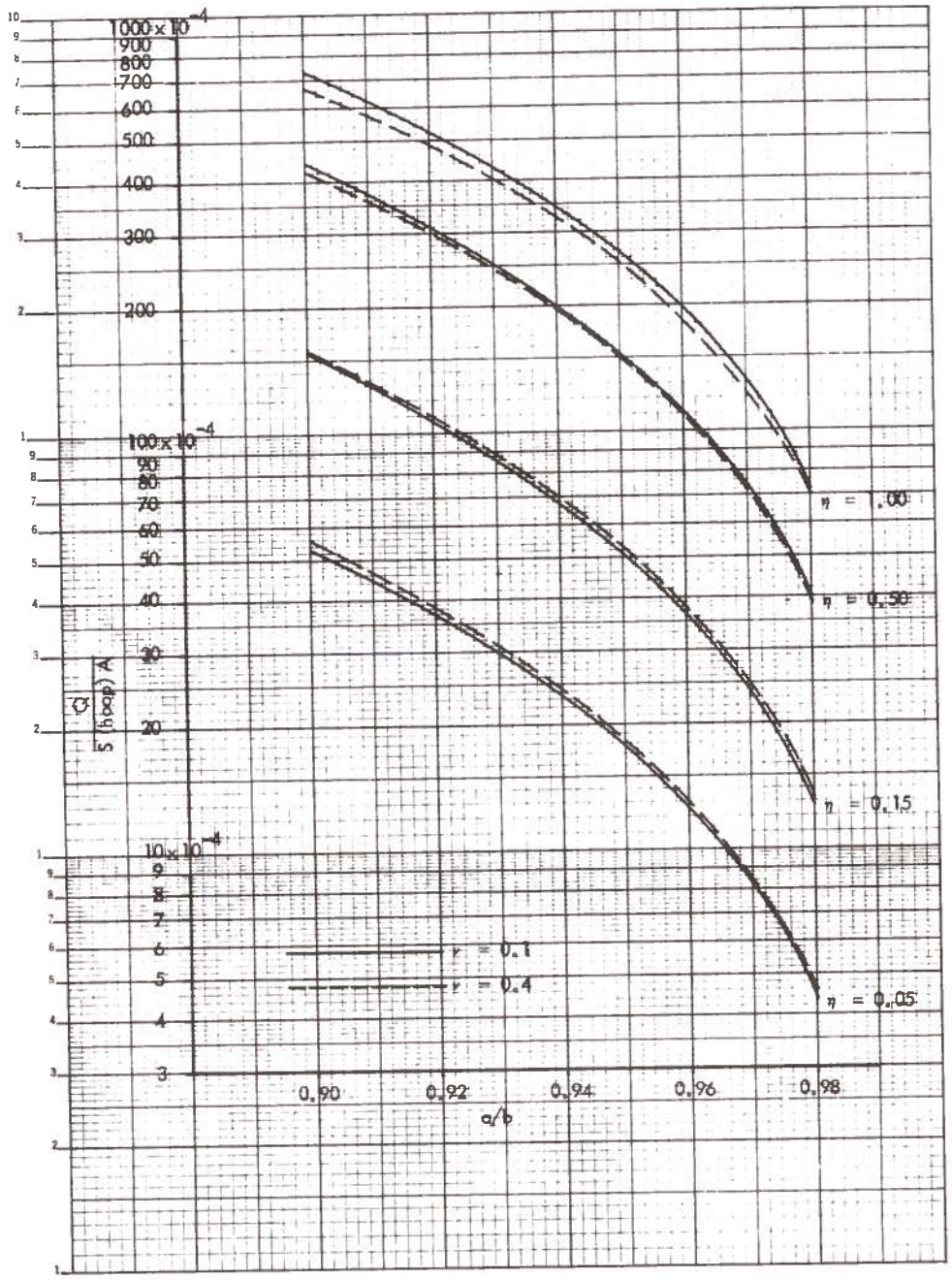

Figure 9-7. Maximum Allowable Penetrator Thrust Based on the Allowable Hoop Stress in Liner

Example:

What is the maximum allowable penetrator thrust based on the liner allowable stress level for the following assumed conditions?

S (allowable) = $2.07 \times 10^7 \frac{N}{m^2}$ [3,000 psi] (tension)

S (allowable) = $2.07 \times 10^8 \frac{N}{m^2}$ [30,000 psi] (compression)

A = $29.2\ m^2$ for a 6.10 m [20.0 ft] diameter tunnel

ν = 0.1

η = 0.15

a/b = 0.94

Solution:

From Figure 9-6,

$$\frac{Q}{S\,(\text{axial})\,A} = -38 \times 10^{-4}$$

$$Q = (-38 \times 10^{-4})(-2.07 \times 10^8)(29.2)$$

$$Q = 2.30 \times 10^7\ N \left[5.16 \times 10^6\ \text{lbs}\right]$$

From Figure 9-7,

$$\frac{Q}{S\,(\text{hoop})\,A} = 67.2 \times 10^{-4}$$

$$Q = (67.2 \times 10^{-4})\ (2.07 \times 10^7)\ (29.2)$$

$$Q = 4.06 \times 10^6\ N\ \left[9.13 \times 10^5\ \text{lbs}\right]$$

Allowable thrust = $4.06 \times 10^6\ N\ \left[9.13 \times 10^5\ \text{lbs}\right]$

The example problem demonstrates how the maximum allowable thrust will strongly depend upon the differences between the liner tensile and compressive strength properties.

A maximum possible melt pressure can be related to the maximum allowable thrust as follows:

$$p_m = \frac{Q}{A_o}$$

where A_o is the projected area of pressurized melt on the penetrator.

For a fully consolidated penetrator "A_o" is equal to "A" so therefore:

$$p_m = \frac{Q}{A}$$

$$= \frac{4.06 \times 10^6}{29.2}$$

$$p_m = 13.9 \times 10^4 \text{ N/m}^2 \left[20.2 \text{ psi}\right]$$

For an 80% coring penetrator "A_o" is approximately 20% of "A". Therefore, for this case

$$p_m = \frac{4.06 \times 10^6}{(0.20)(29.2)}$$

$$p_m = 69.5 \times 10^4 \text{N/m}^2 \left[101.0 \text{ psi}\right]$$

In Section 7.0 of this report, the thrust required to overcome adhesion forces and pressure drag was characterized. The above sample problem is completed by making the comparison. The results of Section 7.0 indicate that thrust loads in excess of one million pounds will be required to advance the penetrator, and melt pressures in excess of 100 psi are likewise required for penetrator advancement. These minimums are very close to the maximum allowable computed in this sample problem, and this indicates that if all the assumed conditions here are valid then the liners must always be thicker than a/b = 0.94, and/or the thrusting friction coefficient must be increased.

9.2.2 Penetrator Weight Effects

In evaluating the effects of penetrator weight both the shear and bending stresses in the glass liner are investigated. The glass liner is treated as a long beam on an elastic foundation. The length of the liner, in order to realistically use "long" beam analysis, should be $\geq 3\pi/2\beta$.

where

$\beta = \sqrt[4]{\frac{k}{4EI}}$ $\left[m^{-1}, in^{-1}\right]$

$k = k_o D$ $\left[N/m^2, psi\right]$

k_o = spring constant of earth supporting liner $\left[\frac{N}{m^2}/m, psi/in\right]$

D = outside diameter of liner $\left[m, in\right]$

E = Young's modulus of liner $\left[N/m^2, psi\right]$

I = inertia of liner $\left[m^4, in^4\right]$

The physical situation is shown as follows:

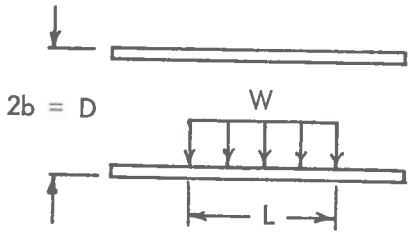

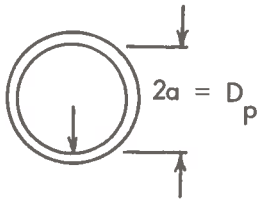

where

W = total weight of penetrator uniformly distributed [N, lbs]

L = length of liner over which penetrator weight is distributed [m, in]

The maximum shear in the glass liner due to the weight of the penetrator is given as follows (see Reference (9-1), pp. 207):

$$V_{max} = \frac{W}{4\beta L}\left[1 - e^{-\beta L}(\cos \beta L - \sin \beta L)\right] \quad \text{at ends of penetrator length } L$$

The maximum shear stress in the liner is computed according to:

$$S(\text{shear})_{max} = \frac{V\,T}{I\,d}$$

where

$$T = \left[\frac{\pi(b^2 - a^2)}{2}\right]\left[\frac{4(b^3 - a^3)}{3\pi(b^2 - a^2)}\right] = \frac{2(b^3 - a^3)}{3}$$

$$I = \frac{\pi}{4}(b^4 - a^4)$$

$$d = 2(b - a)$$

By substitution, the maximum shear stress in the liner is

$$S(\text{shear})_{max} = \frac{W\left[1 - e^{-\beta L}(\cos \beta L - \sin \beta L)\right](b^3 - a^3)}{3\pi(b^4 - a^4)(b - a)(\beta L)} \qquad (9\text{-}13)$$

(at ends of penetrator length L)

The nondimensionalized form of Equation (9-13) is

$$\frac{W}{S\,(\text{shear})\,A} = \frac{3\,(\beta L)\left(1-\frac{a}{b}\right)\left[1-\left(\frac{a}{b}\right)^4\right]}{\left[1-e^{-\beta L}\,(\cos\beta L-\sin\beta L)\right]\left[1-\left(\frac{a}{b}\right)^3\right]\left(\frac{a}{b}\right)^2} \qquad (9-$$

where

$$A = \pi a^2$$

$$\beta L = L\sqrt[4]{\frac{k}{E\pi\,(b^4-a^4)}}$$

$$= L\sqrt[4]{\frac{k_o\,(2\,b)\left(\frac{a}{b}\right)^4}{E\,\pi\left[1-\left(\frac{a}{b}\right)^4\right]a^4}}$$

$$= 2\left(\frac{L}{2\,a}\right)\sqrt[4]{\left(\frac{2\,a\,k_o}{E}\right)\frac{\left(\frac{a}{b}\right)^3}{\pi\left[1-\left(\frac{a}{b}\right)^4\right]}}$$

$$\beta L = 2\left(\frac{L}{D_p}\right)\sqrt[4]{\left(\frac{D_p\,k_o}{E}\right)\frac{\left(\frac{a}{b}\right)^3}{\pi\left[1-\left(\frac{a}{b}\right)^4\right]}}$$

The variation of the allowable penetrator weight based on the allowable shear stress in the liner for various $D_p k_o/E$ and L/D_p ratios is shown in Figures 9-8, 9-9, and 9-10. It is evident from all three figures that for a given liner configuration and allowable shear stress and a given penetrator configuration (L/D_p), the maximum allowable penetrator weight increases as the stiffness of the earth supporting the liner increases. A comparison between the three figures reveals that the maximum allowable penetrator weight increases as the penetrator weight distribution becomes less concentrated; i.e., as L/D_p increases for a given case of liner and earth characteristics.

The location of the maximum bending stress along the liner length depends on the value of $\beta L/2$. Figure 9-11 shows the variation of $\beta L/2$ with the parameters of the problem. For values of $\beta L/2 < \frac{\pi}{4}$, the maximum bending stress occurs at the midpoint of the distributed load. For values of $\beta L/2 \geq \pi/4$, the maximum bending stress occurs at two locations. The two locations are approximately at distances $\pi/4\beta$ from each end of the distributed load. The maximum bending moment for both of the above cases is as follows (see Reference (9-1), pp. 207):

$$M_{max} = \frac{W}{2\beta^2 L} e^{-\beta L/2} \sin(\beta L/2) \quad \text{for} \quad \frac{\beta L}{2} < \frac{\pi}{4}$$

$$M_{max} = \frac{W}{4\beta^2 L} \left[e^{-\pi/4} \sin\left(\frac{\pi}{4}\right) + e^{-\left(\beta L - \frac{\pi}{4}\right)} \sin\left(\beta L - \frac{\pi}{4}\right) \right] \quad \text{for} \quad \frac{\beta L}{2} \geq \pi/4$$

Utilizing the following,

$$c = b$$

$$I = \frac{\pi}{4} (b^4 - a^4)$$

$$S\ (\text{bending}) = \frac{Mc}{I}$$

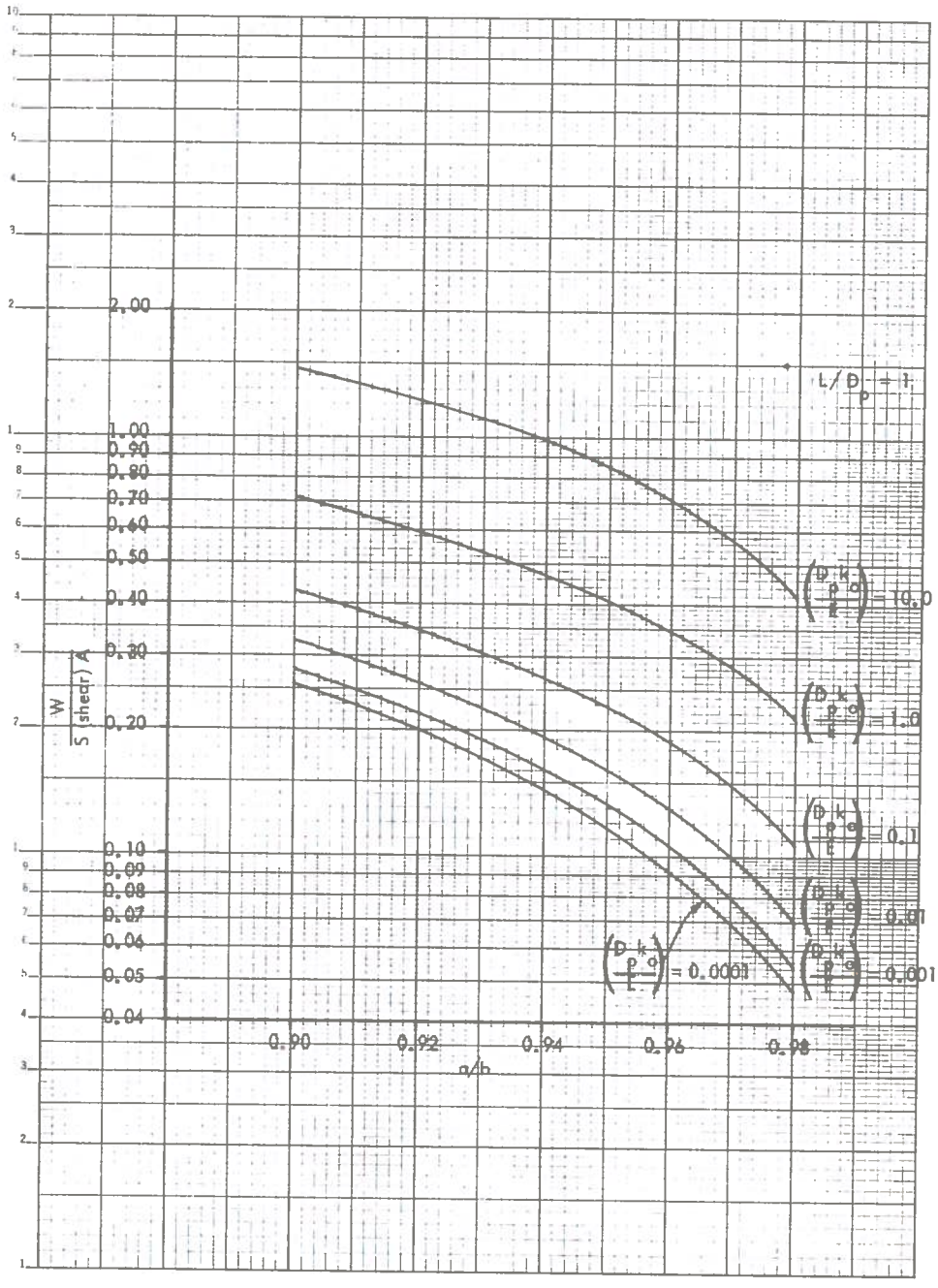

Figure 9-8. Maximum Allowable Penetrator Weight Based on the Allowable Shear Stress in the Liner for $L/D_p = 1$

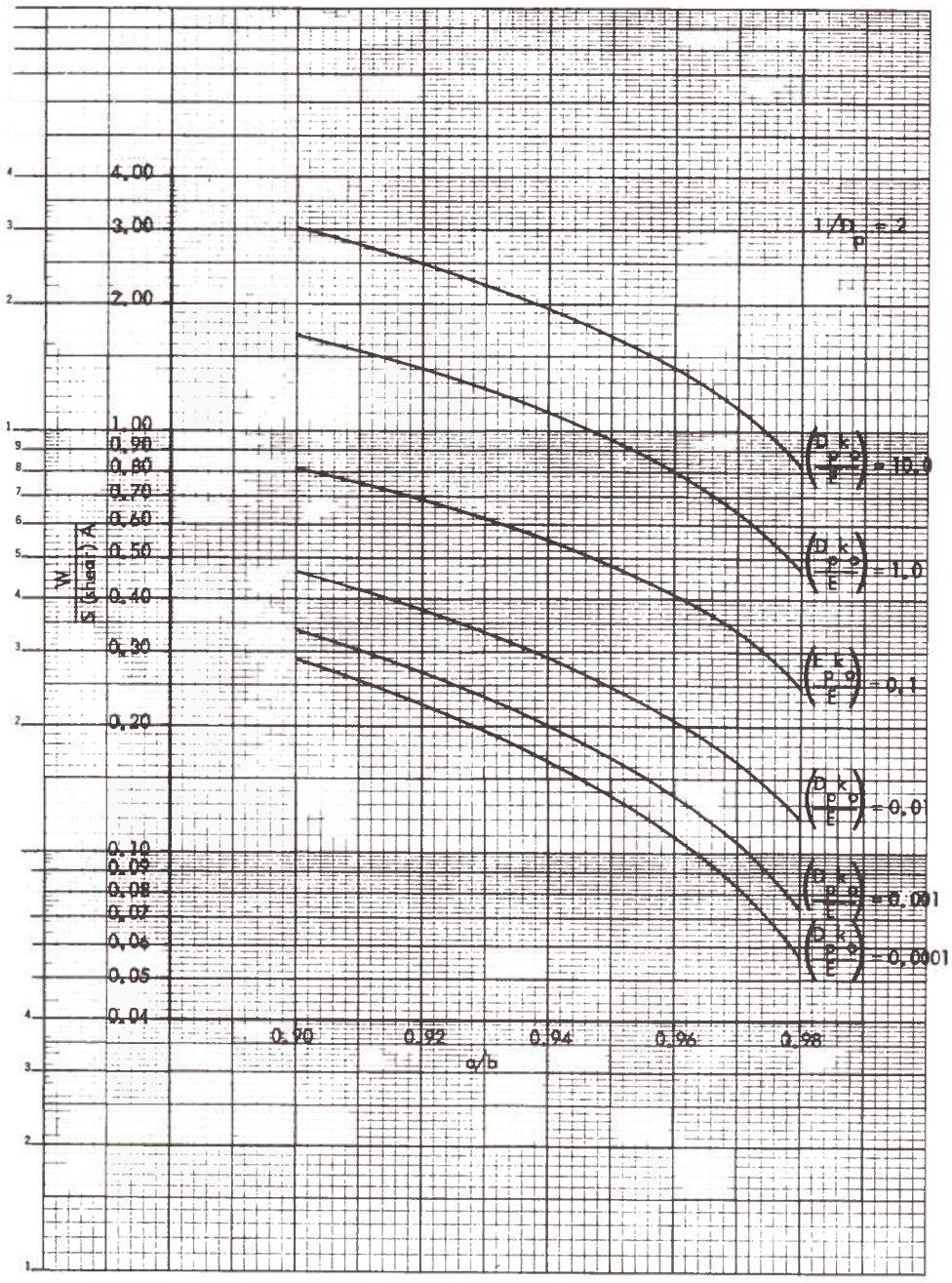

Figure 9-9. Maximum Allowable Penetrator Weight Based on the Allowable Shear Stress in the Liner for $L/D_p = 2$

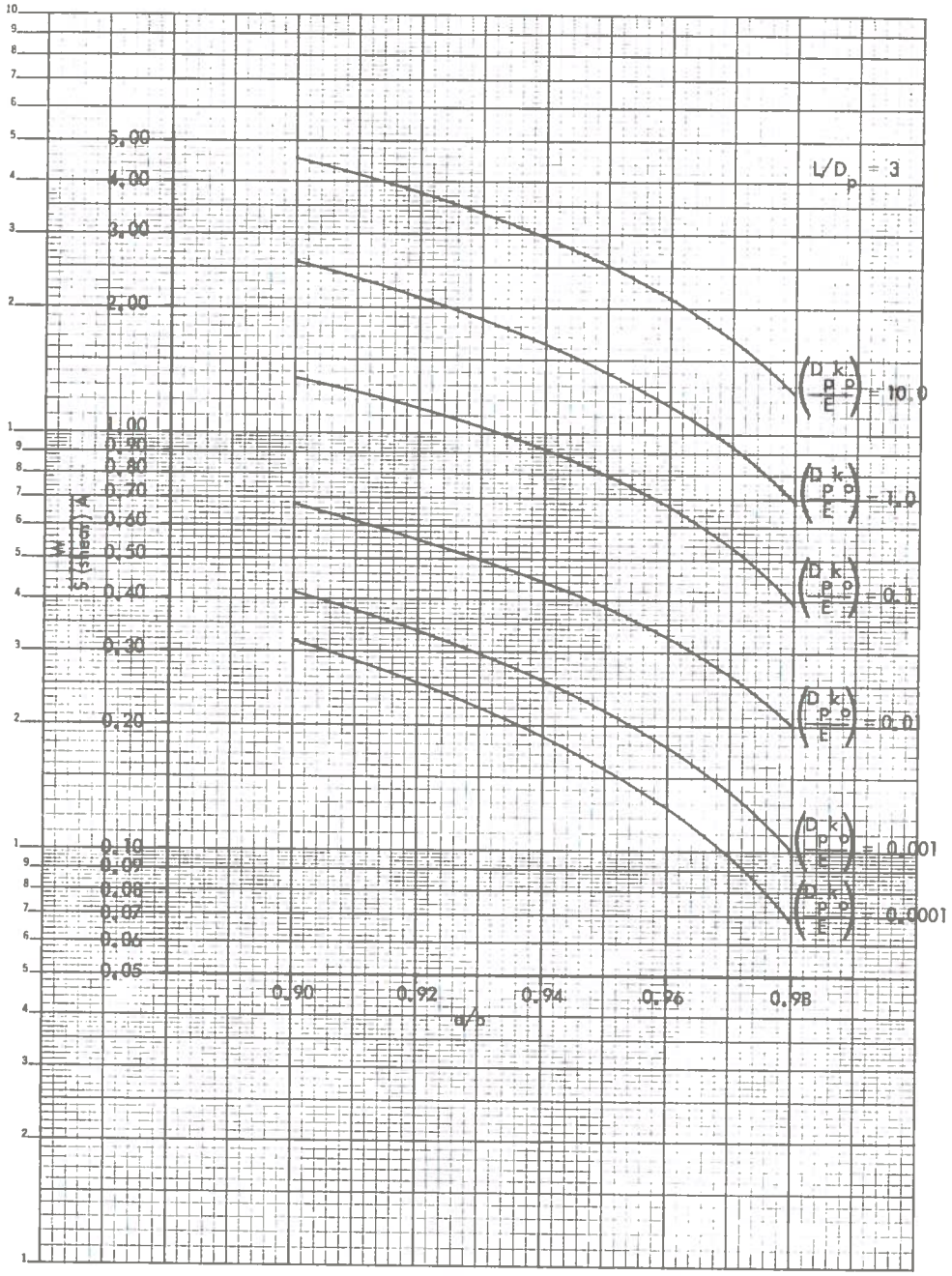

Figure 9-10. Maximum Allowable Penetrator Weight Based on the Allowable Shear Stress in the Liner for $L/D_p = 3$

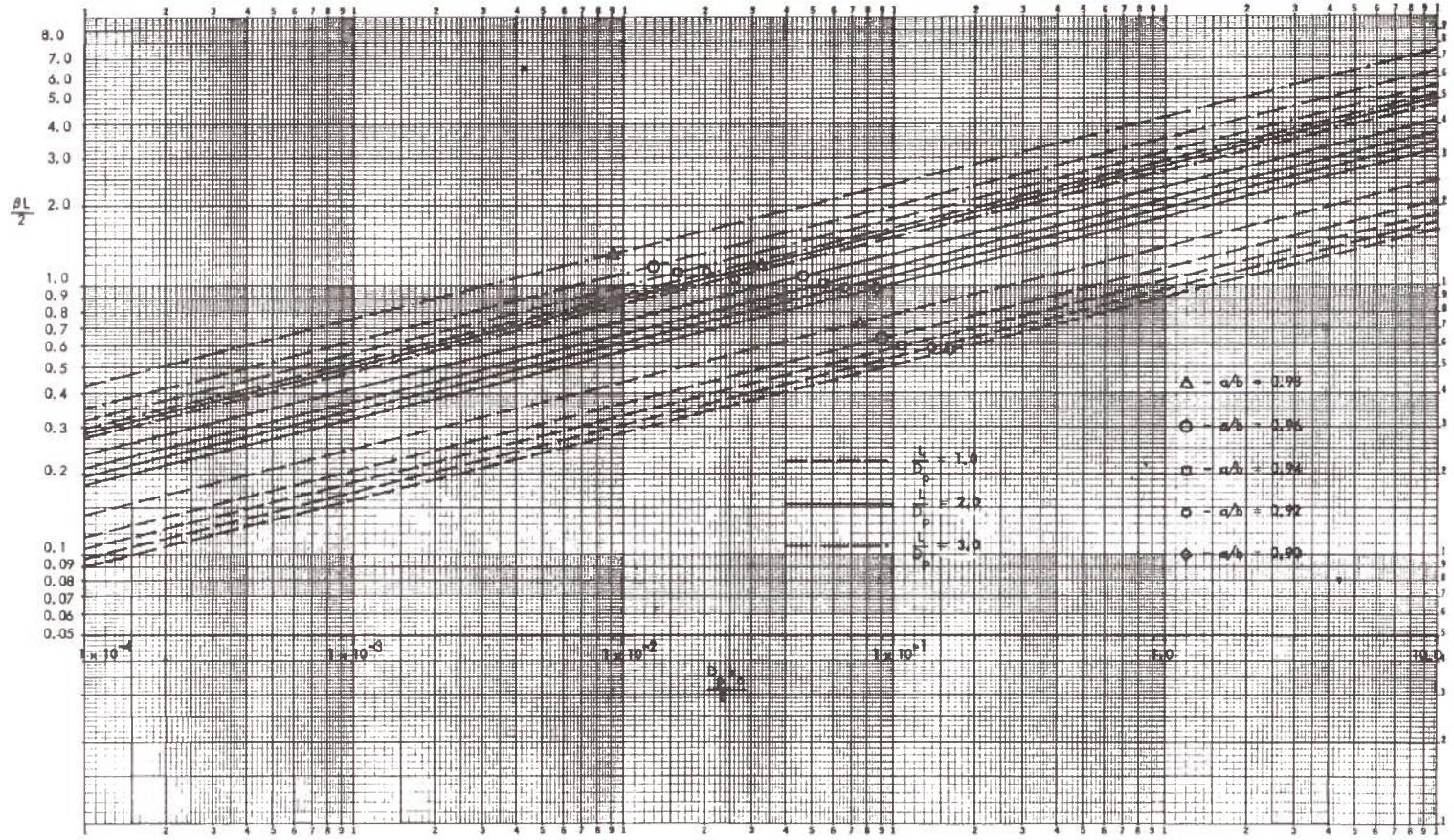

Figure 9-11. Relationship of Parameters Used in Determining the Location of the Liner Maximum Bending Stress Due to Penetrator Weight

The maximum bending stress in the liner due to penetrator weight can be written as

$$S(\text{bending})_{max} = \frac{2\,b\,W\,e^{-\beta L/2}\,\sin(\beta L/2)}{\beta^2\,L\,\pi(b^4 - a^4)} \quad \text{for} \quad \frac{\beta L}{2} < \frac{\pi}{4}$$

$$S(\text{bending})_{max} = \frac{b\,W\left[e^{-\pi/4}\sin(\pi/4) + e^{-(\beta L - \pi/4)}\sin(\beta L - \pi/4)\right]}{\beta^2\,L\,\pi(b^4 - a^4)} \quad \text{for} \quad \frac{\beta L}{2} \geq \frac{\pi}{4}$$

Nondimensionalizing these stress equations results in the following:

$$S(\text{bending})_{max} = \frac{2\left(\frac{a}{b}\right)^3 L\,W\,e^{-\beta L/2}\,\sin(\beta L/2)}{(\beta L)^2\,\pi\left[1 - \left(\frac{a}{b}\right)^4\right]a^3}$$

$$S(\text{bending})_{max} = \frac{\left(\frac{L}{2a}\right)\left(\frac{a}{b}\right)^3 W\,e^{-\beta L/2}\,\sin(\beta L/2)}{A\,(\beta L/2)^2\left[1 - \left(\frac{a}{b}\right)^4\right]} \quad \text{(at midpoint of penetrator length L}$$

$$\frac{W}{S(\text{bending})\,A} = \frac{(\beta L/2)^2\left[1 - \left(\frac{a}{b}\right)^4\right]}{\left(\frac{L}{D_p}\right)\left(\frac{a}{b}\right)^3 e^{-\beta L/2}\,\sin(\beta L/2)} \quad \text{for} \quad \frac{\beta L}{2} < \pi/4 \qquad \text{(9-1}$$

$$S\,(\text{bending})_{max} = \frac{\left(\frac{a}{b}\right)^3 W L \left[e^{-\pi/4} \sin\left(\frac{\pi}{4}\right) + e^{-(\beta L - \pi/4)} \sin(\beta L - \pi/4)\right]}{(\beta L)^2 \pi \left[1 - \left(\frac{a}{b}\right)^4\right] a^3}$$

$$S\,(\text{bending})_{max} = \frac{2\left(\frac{L}{2a}\right)\left(\frac{a}{b}\right)^3 W \left[e^{-\pi/4} \sin(\pi/4) + e^{-(\beta L - \pi/4)} \sin\left(\beta L - \frac{\pi}{4}\right)\right]}{A\,(\beta L)^2 \left[1 - \left(\frac{a}{b}\right)^4\right]}$$

(at $\pi/4\beta$ from each end of penetrator length L)

$$\frac{W}{S\,(\text{bending})\,A} = \frac{(\beta L)^2 \left[1 - \left(\frac{a}{b}\right)^4\right]}{2\left(\frac{L}{D_p}\right)\left(\frac{a}{b}\right)^3 \left[e^{-\pi/4} \sin(\pi/4) + e^{-(\beta L - \pi/4)} \sin(\beta L - \pi/4)\right]}$$

for $\frac{\beta L}{2} \geq \pi/4$ (9-16)

where

$$\frac{\beta L}{2} = \left(\frac{L}{D_p}\right) \sqrt[4]{\left(\frac{D_p k_o}{E}\right) \frac{\left(\frac{a}{b}\right)^3}{\pi\left[1 - \left(\frac{a}{b}\right)^4\right]}}$$

$$A = \pi a^2$$

The variation of the allowable penetrator weight based on the allowable bending stress in the liner for various $D_p k_o/E$ and L/D_p ratios is shown in Figures 9-12, 9-13, and 9-14. These curves were plotted utilizing both Equations (9-15) and (9-16), where applicable,

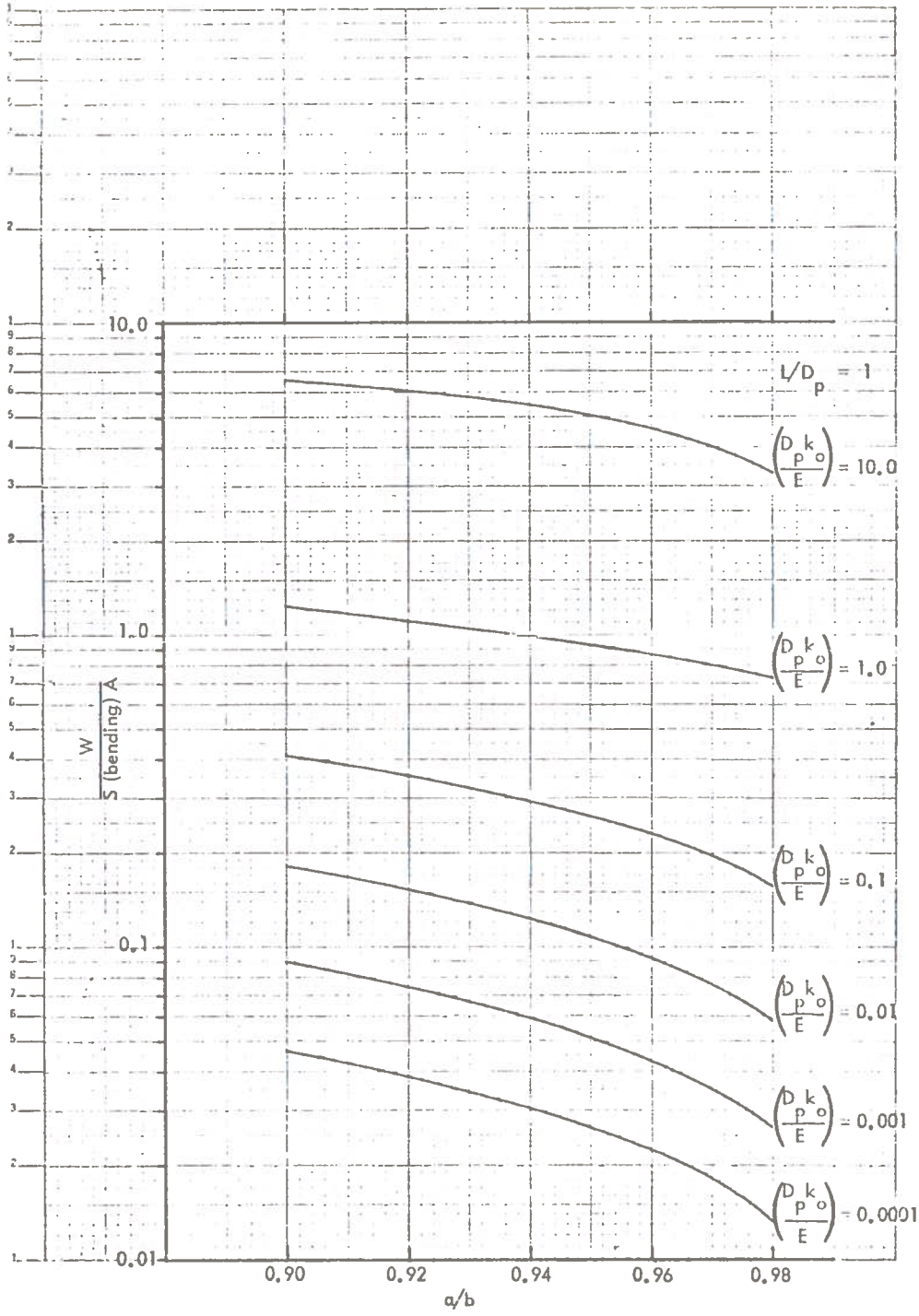

Figure 9-12. Maximum Allowable Penetrator Weight Based on the Allowable Bending Stress in the Liner for $L/D_p = 1$

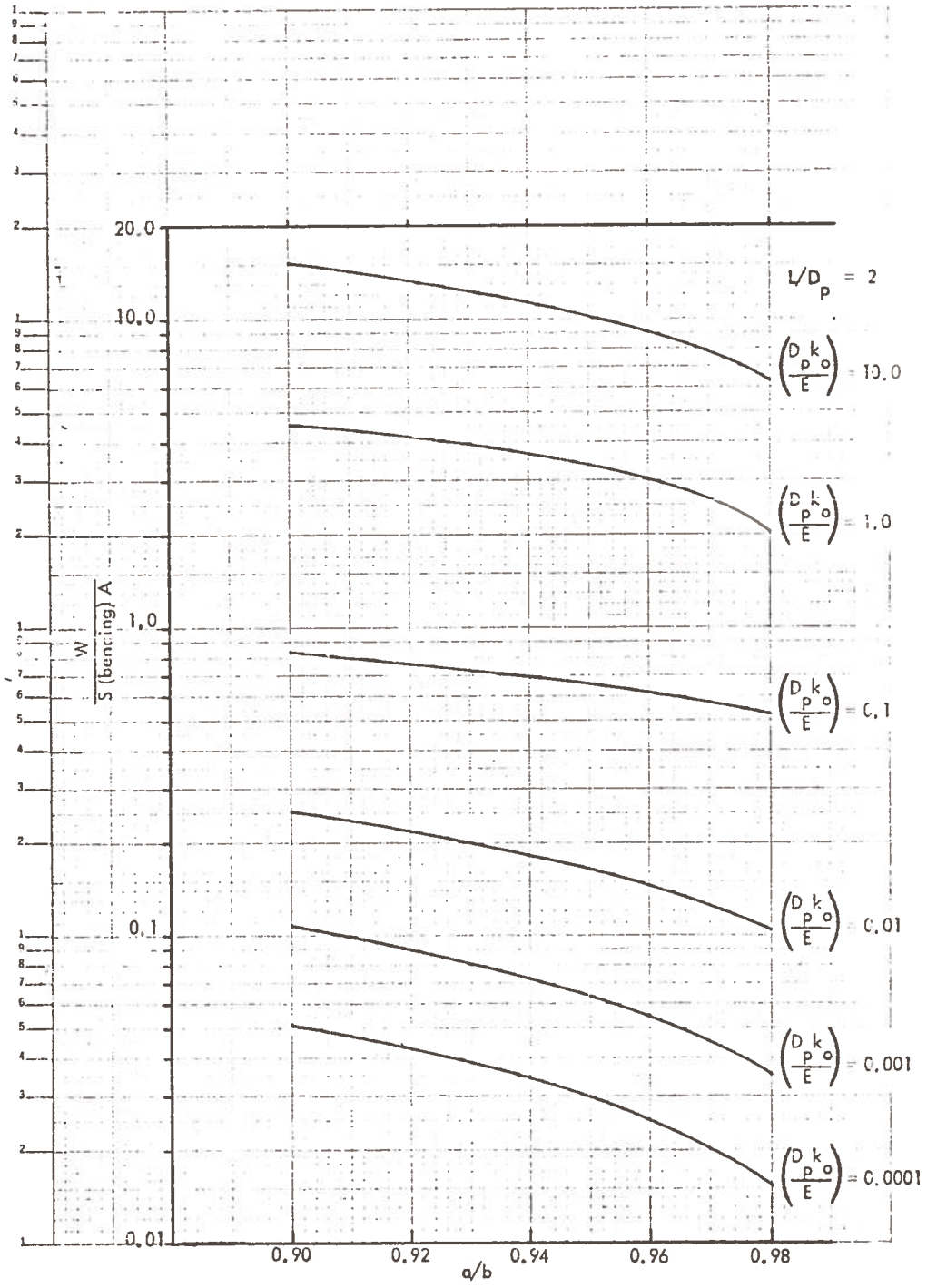

Figure 9-13. Maximum Allowable Penetrator Weight Based on the Allowable Bending Stress in the Liner for $L/D_p = 2$

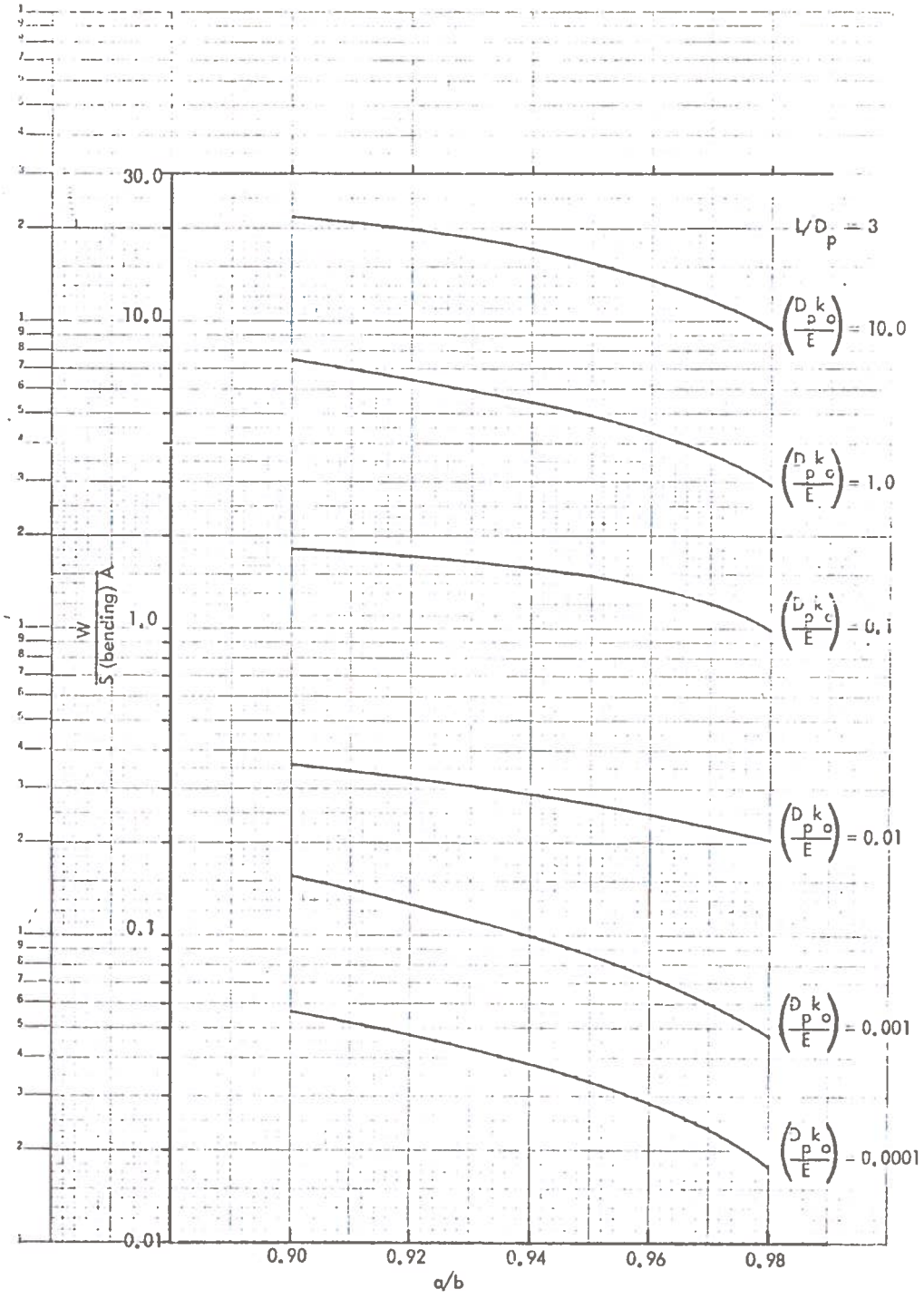

Figure 9-14. Maximum Allowable Penetrator Weight Based on the Allowable Bending Stress in the Liner for $L/D_p = 3$

depending on the value of $\beta L/2$. A similar trend exists for these three figures as existed for the shearing stress figures (Figures 9-8, 9-9, and 9-10) in that for a given liner configuration and allowable bending stress and a given penetrator configuration (L/D_p), the maximum allowable penetrator weight increases as the stiffness of the earth supporting the liner increases. Also, a comparison between the bending stress figures indicates that the maximum allowable penetrator weight increases as the penetrator weight distribution becomes less concentrated; i.e., as L/D_p increases for a given case of liner and earth characteristics.

Example:

What is the maximum allowable penetrator weight based on the level of the liner allowable stresses for the following assumed conditions?

$S\,(\text{allowable})_{\text{bending}} = 2.07 \times 10^7\ N/m^2$ [3,000 psi]

$S\,(\text{allowable})_{\text{shear}} = 1.03 \times 10^7\ N/m^2$ [1,500 psi]

$A = 29.2\ m^2$ $D_p = 6.10$ m [20.0 ft]

$L/D_p = 2$

$\frac{a}{b} = 0.94$

In selecting realistic values for $D_p k_o/E$ Reference (9-1) can be consulted. On pp. 218 the authors discuss experimental methods for determining "k_o". They cite Reference (9-14) as having experimentally determined values for "k_o" in the range of $2.26 \times 10^4 \frac{N}{m^2}/m$ (100 psi/in) for organic silt or inorganic clay to $1.81 \times 10^5 \frac{N}{m^2}/m$ (800 psi/in) for well-graded gravel or clay gravel. A representative room temperature modulus for glass from Reference (9-5) is $E = 6.89 \times 10^{10} N/m^2$ (10×10^6 psi).

If the following are assumed,

$E = 1.38 \times 10^{10}\ N/m^2 \quad \left[2 \times 10^6\ psi\right]$

$k_o = 2.26 \times 10^8\ \frac{N}{m^2}/m \quad \left[833\ psi/in\right]$

and if

$D_p = 6.10\ m,$ then

$\frac{D_p k_o}{E} = 0.1$

Solution:

From Figure 9-9,

$\frac{W}{S\ (shear)\ A} = 0.55$

$W = (0.55)(1.03 \times 10^7)(29.2)$

$W = 1.65 \times 10^8\ N \quad \left[3.73 \times 10^7\ lbs\right]$

From Figure 9-13,

$\frac{W}{S\ (bending)\ A} = 0.7$

$W = (0.7)(2.07 \times 10^7)(29.2)$

$W = 4.23 \times 10^8\ N \quad \left[9.49 \times 10^7\ lbs\right]$

$\therefore$ Allowable penetrator weight $= 1.65 \times 10^8\ N \quad \left[3.73 \times 10^7\ lbs\right]$

This maximum allowable penetrator weight implies a maximum penetrator average density of

$$\rho_p = \frac{1.65 \times 10^8}{(29.2)(2)(6.10)} \qquad \text{since} \quad L = 2 D_p$$

$$\rho_p = 4.63 \times 10^5 \text{ kg/m}^3$$

If the density of the earth displaced by the penetrator is assumed to be,

$$\rho_e = 2.50 \times 10^3 \text{ kg/m}^3$$

then the average density of the penetrator in terms of the earth density is

$$\rho_p = \frac{4.63 \times 10^5}{2.50 \times 10^3} \rho_e$$

$$\rho_p = 185 \rho_e$$

Therefore, the maximum allowable average density of the penetrator is 185 times the average displaced earth density.

Example:

Determine the location of the maximum shear and bending stresses in the liner for the previous problem.

- Maximum shear stress located at ends of uniformly distributed load

From Figure 9-11,

$$\frac{\beta L}{2} = 1.18, \text{ which is greater than } \pi/4$$

$$D_p = 6.10 \text{ m} \quad (20 \text{ ft})$$

$$L = 2D_p = 12.2\ m\ (40\ ft)$$

$$\beta = (1.18)\frac{2}{L} = 0.193\ m^{-1}$$

$$\frac{\pi}{4\beta} = 4.07\ m\ (13.4\ ft)$$

- Maximum Bending Stress located at approximately 4.07 m (13.4 ft) from the ends of the uniformly distributed load.

9.2.3 Liner Primary Loads from Penetrator - Summary

Two penetrator primary load models on the liner were considered. They were a thrust producing model and a penetrator weight model. The choice for a thrust model was a conservative radial ring pressure load with a coefficient of friction for the transmittal of this radial load to axial thrust.

1. With minimal design effort, the primary stresses induced by a thrusting mechanism are not limiting when compared to the stresses from the earth primary loads.

2. The design effort here would deal with providing an adequate friction coefficient at the thruster/liner interface. Based on a glass liner tensile strength of 150 kg/cm^2 (2150 psi) and tunnel diameters not to exceed 10 meters, it was determined that if the thrusting coefficient of friction is less than about 0.2, the thrust required to advance the penetrator may always exceed the allowable thrust. If the thrusting coefficient of friction is about 0.5, the required liner thickness is about 6 to 9% of the penetrator radius for tunnel diameters in the range of 10 to 6 meters. If the thrusting coefficient of friction is about 1.0, the required liner thickness is about 4 to 7% of the penetrator radius in the range of 10 to 6 meter tunnel diameters.

The penetrator weight primary load model considered the glass liner as a beam on an elastic foundation with the penetrator weight evenly distributed over a length which was studied as a variable defined by multiples of the penetrator diameter. The primary conclusions from the penetrator weight model were:

1. Penetrator allowable densities increase as the earth elastic foundation stiffness increases.

2. A sample problem with conservative assumptions indicated the penetrator weight should not limit the tunneling feasibility provided its average density over its liner-supported length does not exceed 460 gm/cm^3. This compares to an earth density of about 2.4 gm/cm^3 and a structural steel density of about 7.8 gm/cm^3.

9.3 THERMAL SECONDARY LOADS

The glass liner thermal stress considerations provide the equations which can be used to evaluate inner tunnel wall deformations, transient cooldown stress levels and residual stresses with the primary goal of defining the most desirable cooling rates consistent with a high strength liner.

The strength of glass can be improved by removing or controlling the residual strains which can arise during a cooldown process. This is achieved commercially either by annealing or tempering. With annealing the cooldown temperature is retained uniform in the body down to a level referred to as the lower annealing temperature. In Reference (9-5) the annealing point is defined by the temperature at which the viscosity is 10^{13} poises. At this viscosity internal residual stress can relax in a matter of a few minutes. For slower annealing, the lower annealing temperature could be taken as the strain point. Reference (9-5) defines this by the temperature at which the viscosity is $10^{14.5}$ poises. Here it takes a few hours for residual stress relaxation. The upper annealing temperature is the softening point with a viscosity of $10^{7.65}$ poises. Here glass can deform under its own weight. This is merely the condition for which temperatures should not be exceeded in a commercial reheat annealing process. Within the limitations of elastic thermal stress resistance, cooling may be achieved as rapidly as desired without inducing residual strains between the lower annealing temperature and the final cooldown point. It is important to note at this time that glass has a transformation temperature range dependent upon cooling rate which is used to define the transformation point, T_g, sometimes referred to as the "configurational" or "fictive" temperature. This is illustrated by the volume-temperature relationship shown below.

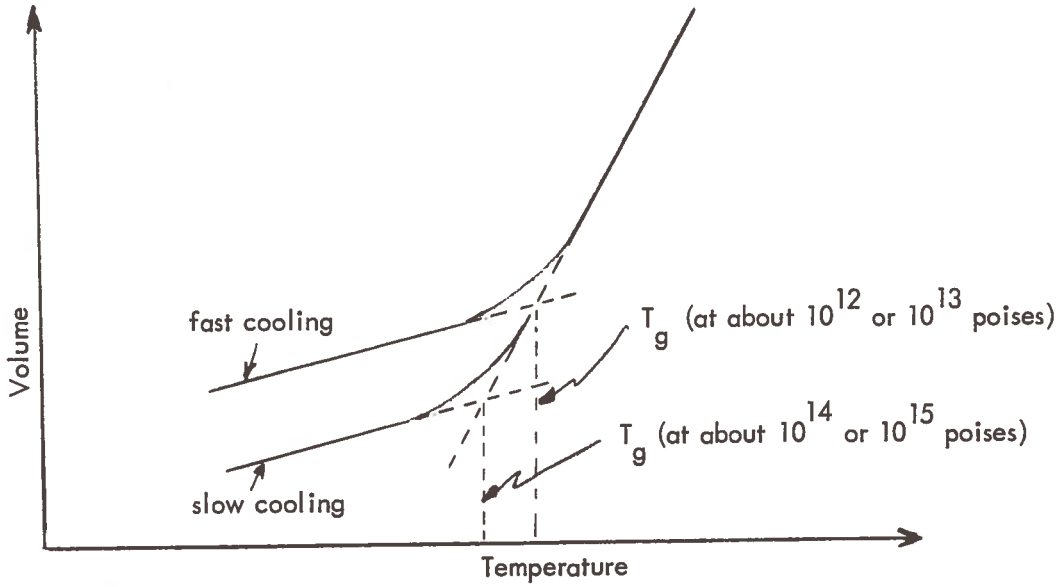

This behavior provides some definition for subsequent thermal stress analysis. At temperatures above T_g the glass will be considered purely plastic and below T_g the glass will be treated elastically. Likewise, in equation derivations, there will be a difference in the glass coefficient of thermal expansion above and below T_g.

Tempering differs from annealing in that residual strains are purposely induced to strengthen the glass. In a recent article[9-6] by Ernsberger, the generalization in the field of glass strengthening was made that there is only one practical way to strengthen glass, and that is to put the surface into compression. He didn't consider etching as a practical way, because the strength produced doesn't last very long. He referred to two general ways of surface compression strengthening: thermal and chemical. The thermal strengthening is accomplished with tempering by rapidly cooling the surfaces to induce residual strains effecting a compressive stress at the surface and tensile stresses toward the interior. Chemical strengthening includes any method of producing surface compression that requires alterations in the physicochemical properties of the surface material. Two kinds of chemical strengthening are cited by Ernsberger. (1) Increase the specific volume of the glass surface by either

forcing some extra atoms or molecules into it by ion exchange or somehow causing a surface transformation to a new phase of higher specific volume. He was not aware of any examples of the latter. (2) The other chemical method is based on the production of a decrease in the thermal expansion coefficient of the surface. He cites dealkalization by evaporation and surface crystallization as two mechanisms from a bewildering variety as means to accomplish this.

The objective in this work is to gain an understanding of effects from the thermal environments which can be imposed on the glass liner. The behavior of glass plates and rods for which description is provided in References (9-7) through (9-11) for the commercial tempering and annealing processes differs from the unique circumstances surrounding a subterrene glass liner. The difference in annealing is that commercially a surface restraining boundary condition is not imposed such as that provided by the glass liner/earth interface. With tempering, in addition to the restrained boundary, the difference is that commercially all surfaces are force-cooled. With the subterrene glass liner the outer boundary at the glass/earth interface is approximately insulated rather than force cooled. It is a combination of these circumstances which has led to the thermoviscoelastic equation development found in this work as opposed to reliance upon existing research in the area of commercial glass heat treatment descriptions.

9.3.1 Definition of Terminology

It was mentioned above that glass has a transformation temperature, and this concept is relied upon in this work to provide the distinction between elastic and inelastic behavior. Glass at a temperature greater than the transformation temperature will exhibit stress relaxation within the time period consistent with the cooling rate. Glass at temperatures below the transformation temperature behaves elastically. Consistent with a given cooling rate there will exist a narrow temperature range (or viscosity range) over which partial stress relaxation occurs. In this work, this range is neglected by considering part of that range as purely plastic and the remainder as purely elastic. The effect of this assumption diminishes as the cooling rate increases as evidenced[9-5] by the fact that at a viscosity of 10^{13} poises, internal residual stress relaxation can occur in a few minutes; but at a viscosity of $10^{14.5}$ poises stress relaxation takes a few hours.

The following schematic provides the definition of temperature terminology to be used in subsequent derivations.

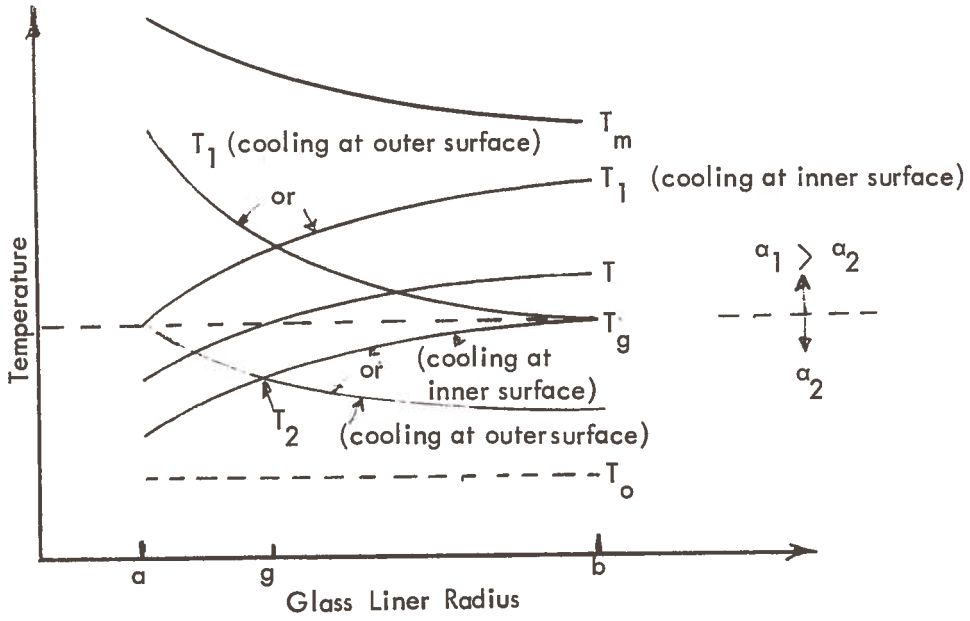

T_m, the glass liner temperature profile at the time of fully developed glass liner thickness, $\delta = b - a$

T_1, the glass liner temperature profile at the time when the glass liner inner or outer radius ceases to relax stress and begins to behave elastically.

T_g, the glass transformation temperature

α_1, the glass coefficient of thermal expansion at temperatures above T_g

α_2, the glass coefficient of thermal expansion at temperatures below T_g

T_2, the glass liner temperature profile at the time when the entire liner begins to behave elastically

T, a general glass liner temperature profile used in the description of transient stresses, where $g \leq b$, and where g is the radial location defined by T_g

T_o, the final ambient cooldown temperature for the glass liner.

Other terms to be found in Section 9.3 are without the glass property subscript, g, since it was unnecessary to distinguish them from earth properties.

E, glass Young's modulus

ν, glass Poisson's ratio

9.3.2 Ineleastic Deformations of the Glass Liner

This section deals with the glass liner plastic deformations related to the volumetric changes that occur from temperature decreases at temperature levels greater than T_g. It includes the stress free deformations which occur prior to the transition to elastically behaving glass and it provides an expression for the deformations which are prevented from occuring by the initial formation of an elastic glass ring at the tunnel liner inner or outer surface. These latter prevented deformations provide important boundary conditions for elastic analysis as the T_g isotherm transverses from the "a" to "b" or the "b" to "a" radial locations.

Consider a hollow cylinder of initial volume, V_i, which is free to expand or contract thermally.

$$V_i = \pi (b^2 - a^2) h$$

With the condition of no surface tractions, the final volume V_f associated with a uniform temperature change ΔT is

$$V_f = \pi (b^2 - a^2) h \ (1 + 3 \alpha \Delta T)$$

The volume change is

$$\Delta V = V_f - V_i = \pi h \ (b^2 - a^2) \ (3 \alpha \Delta T)$$

The inelastic description for glass deformation at its unrestrained boundary where all other surfaces are restrained from deformation is obtained by the constant volume assumption associated with plastic behavior. For the plane strain condition of no axial deformation and for a fixed outer boundary, b, at the earth glass interface, the volume change would be $\Delta V = 2\pi a \Delta a h$

Equating this to the total capacity for a thermal volumetric change gives

$$2\pi a \Delta a h = \pi h (b^2 - a^2) (3 \alpha \Delta T)$$

or

$$\Delta a = \left(\frac{b^2 - a^2}{2a}\right)(3 \alpha \Delta T)$$

For radially non-uniform temperature distributions the average temperature is

$$\bar{T} = \frac{2}{b^2 - a^2} \int_a^b T r \, dr$$

Therefore, the inelastic deformation at the inner liner radius resulting from the temperature change $T_m - T_1$ is:

$$\Delta a = \frac{3 \alpha_1}{a} \int_a^b (T_m - T_1) \, r \, dr \quad \text{for cooling at "a", and}$$

$$\Delta a = \frac{3 \alpha_1}{a} \int_a^b (T_m - T_g) \, r \, dr \quad \text{for cooling at "b"} \qquad (9\text{-}17)$$

This is deformation in the positive radial direction. At the time when the liner temperature profile reaches the T_1 distribution. With cooling at "a", the inner radial location of the liner has cooled to the extent that the glass is tending to behave elastically at the T_g temperature level. The transition to elastically behaving material provides a barrier to further plastic deformation at that location. With cooling at "a", the remaining glass at the T_1 temperature distribution and at temperature levels above T_g still has a capacity for plastic deformation which can only be achieved by either imposing a tensile stress on the elastically behaving region or by tearing itself away from the earth/glass interface. If it tears away from the interface, the radial

contraction at "b" for the remaining inelastic deformation capacity in going from T_1 to T_2, would be

$$\Delta b = -\frac{3\alpha_1}{b}\int_a^b (T_1 - T_g)\, r\, dr \quad \text{for cooling at "a", or} \tag{9-18}$$

$$\Delta b = 0 \quad \text{for cooling at "b" (because "a" just plastically grows)}$$

If the earth glass interface is not severed, the above deformation with a reversed sign provides the boundary condition for the additional stress which is imposed in the subsequent cooling. This additional stress is created in the elastic formation because the natural tendency for the full extent of inelastic contraction is prevented by the restraint of elastic formations at the liner interior and grasping or no break away at the liner/earth interface when surface "a" is cooled.

The resulting glass liner stresses are evaluated in subsequent sections for both conditions: that of break away and that of fixity at the earth/liner interface.

9.3.3 Glass Liner Transient with Residual Thermal Stress and Deformations

The general solution to the displacement formulation of the equation of thermoelastic equilibrium for a hollow cylinder in a state of plane strain is (see Reference (9-12):

$$u = \frac{(1+\nu)\alpha}{(1-\nu)r}\int_a^r \Delta T\, r\, dr + C_1 r + \frac{C_2}{r} \tag{9-19}$$

By the use of strain-displacement and stress-strain laws, the stresses are:(9-12)

$$\sigma_R = -\frac{\alpha E}{(1-\nu)r^2}\int_a^r \Delta T\, r\, dr + \frac{E C_1}{(1+\nu)(1-2\nu)} - \frac{E C_2}{(1+\nu) r^2} \tag{9-20}$$

$$\sigma_\theta = \frac{\alpha E}{(1-\nu) r^2}\int_a^r \Delta T\, r\, dr - \frac{\alpha E \Delta T}{(1-\nu)} + \frac{E C_1}{(1+\nu)(1-2\nu)} + \frac{E C_2}{(1+\nu) r^2} \tag{9-21}$$

$$\sigma_Z = \nu(\sigma_R + \sigma_\theta) - \alpha E \Delta T \tag{9-22}$$

The solutions associated with a fixed outer boundary and a traction-free outer boundary are now developed.

The Fixed Outer Boundary Problem

This solution applies for the case where the glass liner does not break away from the glass/earth interface. The results can provide insight as to whether or not this is a realistic assumption. A superposition of thermoelastic solutions is made in order to provide the separate boundary conditions which apply during elastic plastic behavior and during purely elastic behavior. These are only for cooling at "a" because of the impractacality of insulating the inner surface relative to cooling times and thrusting. (See Section 10.0)

$$\Delta T = T_2 - T_g$$

1) $\sigma_R = 0$ at $r = a$

2) $u = \Delta b = -\frac{3 a_1}{b} \int_a^b (T_g - T_1)\, r\, dr$ at $r = b$

$$\Delta T = T_o - T_2$$

1) $\sigma_R = 0$ at $r = a$

2) $u = 0$ at $r = b$

Substition of boundary condition 1) into Equation (9-20) gives

$$C_1 = \frac{(1 - 2\nu)}{a^2} C_2 \qquad (9\text{-}23)$$

Substitution of boundary condition 2) and Equation (9-23) into Equation (9-19) gives:

$$C_2 = \frac{-3\alpha_1 \int_a^b (T_g - T_1)\, r\,dr - \alpha_2 \left(\frac{1+\nu}{1-\nu}\right) \int_a^b (T_2 - T_g)\, r\,dr}{1 + (1-2\nu)\left(\frac{b}{a}\right)^2} \qquad (9\text{-}24.a)$$

for

$\Delta T = T_2 - T_g$, and

$$C_2 = \frac{-\alpha_2 \left(\frac{1+\nu}{1-\nu}\right) \int_a^b (T_o - T_2)\, r\,dr}{1 + (1-2\nu)\left(\frac{b}{a}\right)^2} \qquad (9\text{-}24.b)$$

for

$\Delta T = T_o - T_2$

Substition of these constants into the displacement equation gives the partial solutions as:

$$u = \frac{\alpha_2}{r} \left(\frac{1+\nu}{1-\nu}\right) \int_a^r (T_2 - T_g)\, r\,dr$$

$$-\left[\frac{1 + (1-2\nu)\left(\frac{r}{a}\right)^2}{1 + (1-2\nu)\left(\frac{b}{a}\right)^2}\right] \left\{ \frac{3\alpha_1}{r} \int_a^b (T_g - T_1) r\,dr + \frac{\alpha_2}{r} \left(\frac{1+\nu}{1-\nu}\right) \int_a^b (T_2 - T_g)\, r\,dr \right.$$

for

$\Delta T = (T_2 - T_g)$, and

$$u = \frac{\alpha_2}{r}\left(\frac{1+\nu}{1-\nu}\right)\int_a^r (T_o - T_2)\, r\, dr - \left[\frac{1 + (1-2\nu)\left(\frac{r}{a}\right)^2}{1 + (1-2\nu)\left(\frac{b}{a}\right)^2}\right]\left\{\frac{\alpha_2}{r}\left(\frac{1+\nu}{1-\nu}\right)\int_a^b (T_o - T_2)\, r\, dr\right\}$$

for

$$\Delta T = (T_o - T_2)$$

It must be recognized that these partial solutions to displacement are only true at the boundary $r = a$, because the ficticious condition of $u = \Delta b$ at $r = b$ was imposed to arrive at realistic stress solutions resulting from the restrained plastic behavior. By superposition of the above solutions at $r = a$, the elastic residual deformation is:

$$u\,(r=a) = -\frac{2\,(1-\nu)}{\left[1 + (1-2\nu)\left(\frac{b}{a}\right)^2\right]}\left\{\frac{3\,\alpha_1}{a}\int_a^b (T_g - T_1)\, r\, dr + \frac{\alpha_2}{a}\left(\frac{1+\nu}{1-\nu}\right)\left(\frac{T_o - T_g}{2}\right)(b^2 - a^2)\right\}$$

The plastic deformation was given by Equation (9-17), and when it is added to the above elastic residual deformation, the total deformation at the liner inner radius is:

$$u\,(r=a) = -\frac{3\,\alpha_1}{a}\int_a^b (T_1 - T_m)\, r\, dr - \frac{2\,(1-\nu)}{\left[1 + (1-2\nu)\left(\frac{b}{a}\right)^2\right]}\left\{\frac{3\,\alpha_1}{a}\int_a^b (T_g - T_1)\, r\, dr + \frac{\alpha_2}{a}\left(\frac{1+\nu}{1-\nu}\right)\left(\frac{T_o - T_g}{2}\right)(b^2 - a^2)\right\} \qquad (9\text{-}25.a)$$

A re-arrangement into non-dimensional form gives:

$$\frac{u\ (r = a)}{a\,\alpha_2\,(\bar{T}_o - \bar{T}_g)} = -\frac{3}{2}\,\frac{\alpha_1}{\alpha_2}\left(\frac{\bar{T}_1 - \bar{T}_m}{\bar{T}_o - \bar{T}_g}\right)\left[\left(\frac{b}{a}\right)^2 - 1\right]$$

$$-\frac{(1-\nu)}{\left[1 + (1-2\nu)\left(\frac{b}{a}\right)^2\right]}\left\{\frac{3\,\alpha_1}{\alpha_2}\left(\frac{\bar{T}_g - \bar{T}_1}{\bar{T}_o - \bar{T}_g}\right)\left[\left(\frac{b}{a}\right)^2 - 1\right] + \left(\frac{1+\nu}{1-\nu}\right)\left[\left(\frac{b}{a}\right)^2 - 1\right.\right. \qquad (9\text{-}25.b)$$

where the definition of average temperature is:

$$\bar{T} = \frac{2}{b^2 - a^2}\int_a^b T\,r\,dr$$

The same procedure applies in arriving at the stress equations. For the radial stress component, the substitutions of C_1 and C_2 into Equation (9-20) gives:

$$\sigma_R = -\frac{\alpha_2\,E}{(1-\nu)\,r^2}\int_a^r (T_2 - T_g)\,r\,dr - \frac{3\,\alpha_1\,E}{(1+\nu)\,r^2}\,\frac{\left[\left(\frac{r}{a}\right)^2 - 1\right]}{\left[1 + (1-2\nu)\left(\frac{b}{a}\right)^2\right]}\int_a^b (T_g - T_1)\,r\,dr$$

$$-\frac{E\,\alpha_2}{(1-\nu)\,r^2}\,\frac{\left[\left(\frac{r}{a}\right)^2 - 1\right]}{\left[1 + (1-2\nu)\left(\frac{b}{a}\right)^2\right]}\int_a^b (T_2 - T_g)\,r\,dr$$

for

$\Delta T = (T_2 - T_g)$, and

$$\sigma_R = -\frac{\alpha_2 E}{(1-\nu) r^2}\int_a^r (T_o - T_2)\, r\, dr - \frac{\alpha_2 E}{(1-\nu) r^2}\frac{\left[\left(\frac{r}{a}\right)^2 - 1\right]}{\left[1 + (1-2\nu)\left(\frac{b}{a}\right)^2\right]}\int_a^b (T_o - T_2)\, r\, dr$$

for

$$\Delta T = (T_o - T_2)$$

The superposition of solutions in non-dimensional form gives

$$\frac{\sigma_R (1-\nu)}{\alpha_2 E (T_o - T_g)} = -\frac{1}{2}\left[1 - \left(\frac{a}{r}\right)^2\right]\left[1 + \frac{\left[1 - \left(\frac{a}{b}\right)^2\right]}{\left[\left(\frac{a}{b}\right)^2 + (1-2\nu)\right]}\left\{1 + \frac{3(1-\nu)\alpha_1 (T_g - \bar{T}_1)}{(1+\nu)\alpha_2 (T_o - T_g)}\right\}\right] \tag{9-26}$$

By the same method and with Equations (9-21) and (-22), the circumferential and axial stress equations are:

$$\frac{\sigma_\theta (1-\nu)}{\alpha_2 E (T_o - T_g)} = -\frac{1}{2}\left[1 + \frac{a}{r}^2\right]\left[1 + \frac{\left[1 - \left(\frac{a}{b}\right)^2\right]}{\left[\left(\frac{a}{b}\right)^2 + (1-2\nu)\right]}\left\{1 + \frac{3(1-\nu)\alpha_1 (T_g - \bar{T}_1)}{(1+\nu)\alpha_2 (T_o - T_g)}\right\}\right] \tag{9-27}$$

$$\frac{\sigma_Z (1-\nu)}{\alpha_2 E (T_o - T_g)} = -1 - \nu\frac{\left[1 - \left(\frac{a}{b}\right)^2\right]}{\left[\left(\frac{a}{b}\right)^2 + (1-2\nu)\right]}\left\{1 + \frac{3(1-\nu)\alpha_1 (T_g - \bar{T}_1)}{(1+\nu)\alpha_2 (T_o - T_g)}\right\} \tag{9-28}$$

It is important to mention here that the last term in the above equations containing $(T_g - \overline{T}_1)$ is the residual stress contribution due to the inelastic behavior as the T_g isotherm traverses from the a to b radial locations. These equations clearly show the residual stresses increase as $(T_g - \overline{T}_1)$ increases in magnitude. At the other extreme if cooling is near uniform, such as for the case of annealing, this last term would disappear as $\overline{T}_1$ approaches the value of T_g. Therefore, with annealing the residual stresses as described by the above equations would be less by the contribution loss of the term containing $(T_g - \overline{T}_1)$, as $(T_g - \overline{T}_1)$ approaches zero.

The transient stress derivations for the arbitrary temperature profiles where $T(r)$ can be $T_2(r) < T(r) < T_1(r)$ or $T_o < T(r) < T_2(r)$ as separate case studies is not provided here because the final steady state residual stress solutions given above are the worst case by reason that the lower the final average liner temperature becomes, the greater the stresses will become because of the boundary condition that $u = 0.$ at $r = b$.

For the purpose of making further evaluations concerning the realism of this problem with the fixed outer boundary condition, the stress solutions for the best possible case of uniform cooling, $(\overline{T}_1 - T_g) \cong 0$, have been plotted on Figures 9-15, 9-16, and 9-17. To aid the discussion, the following representative property values which are considered realistic based on the glass properties provided in Reference (9-5), are assumed.

$\alpha_2 = 7 \times 10^{-6}/^{o}C$

$E = 0.7 \times 10^{6}$ kg/cm^2 7×10^{9} N/m^2 $(10 \times 10^{6}$ psi)

$\nu = 0.17$

$(T_g - T_o) = 500^{o}C$

Tensile Strength = 140 kg/cm^2 1.4×10^{7} N/m^2 (2000 psi)

$\dfrac{\alpha E (T_g - T_o)}{(1 - \nu)}$ = 2950 kg/cm^2 2.8×10^{8} N/m^2 (41, 000 psi)

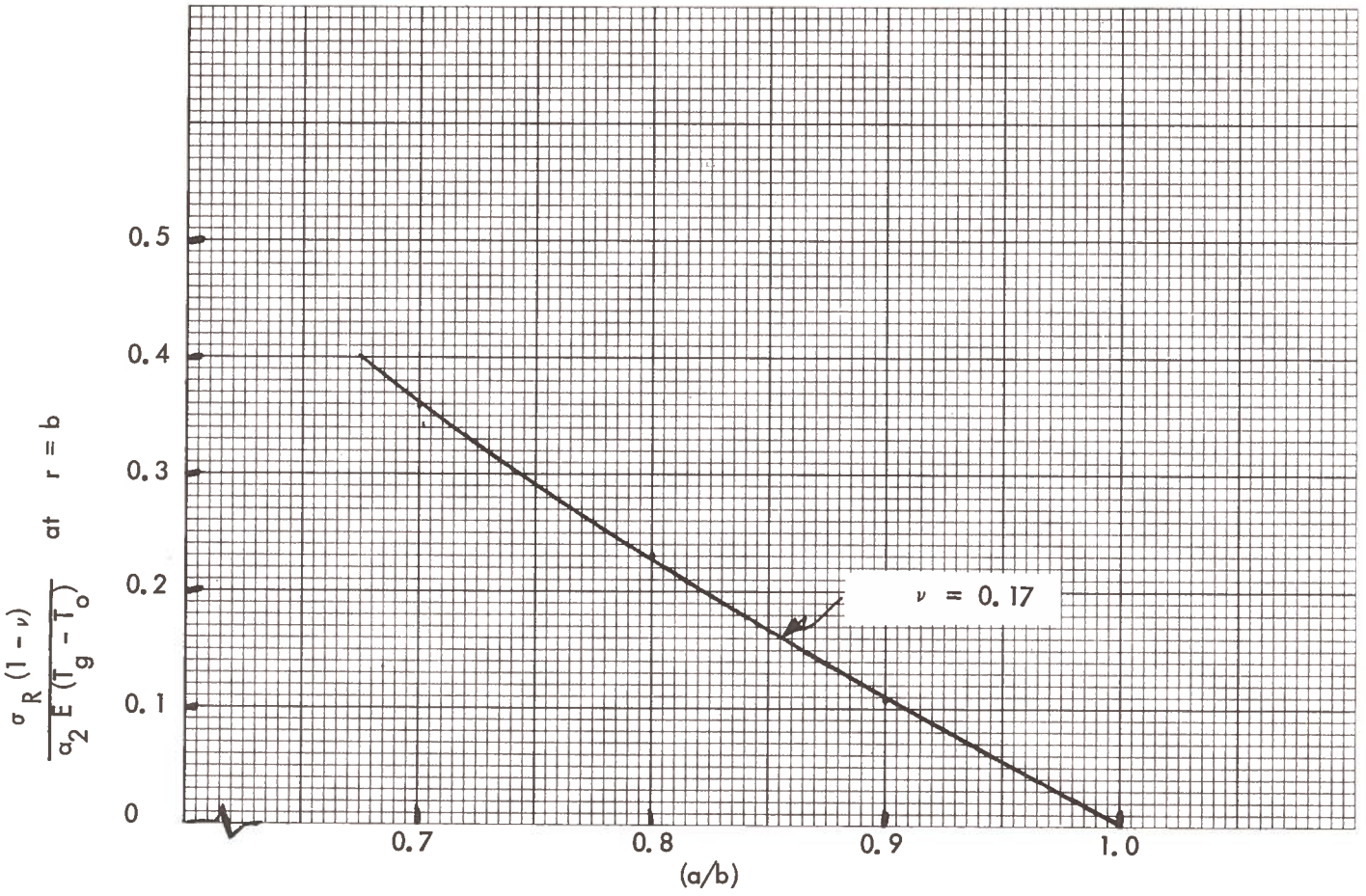

Figure 9-15. Tensile Surface Traction Required to Retain the Outer Boundary Condition of Zero Displacement with Uniform Thermal Cooling

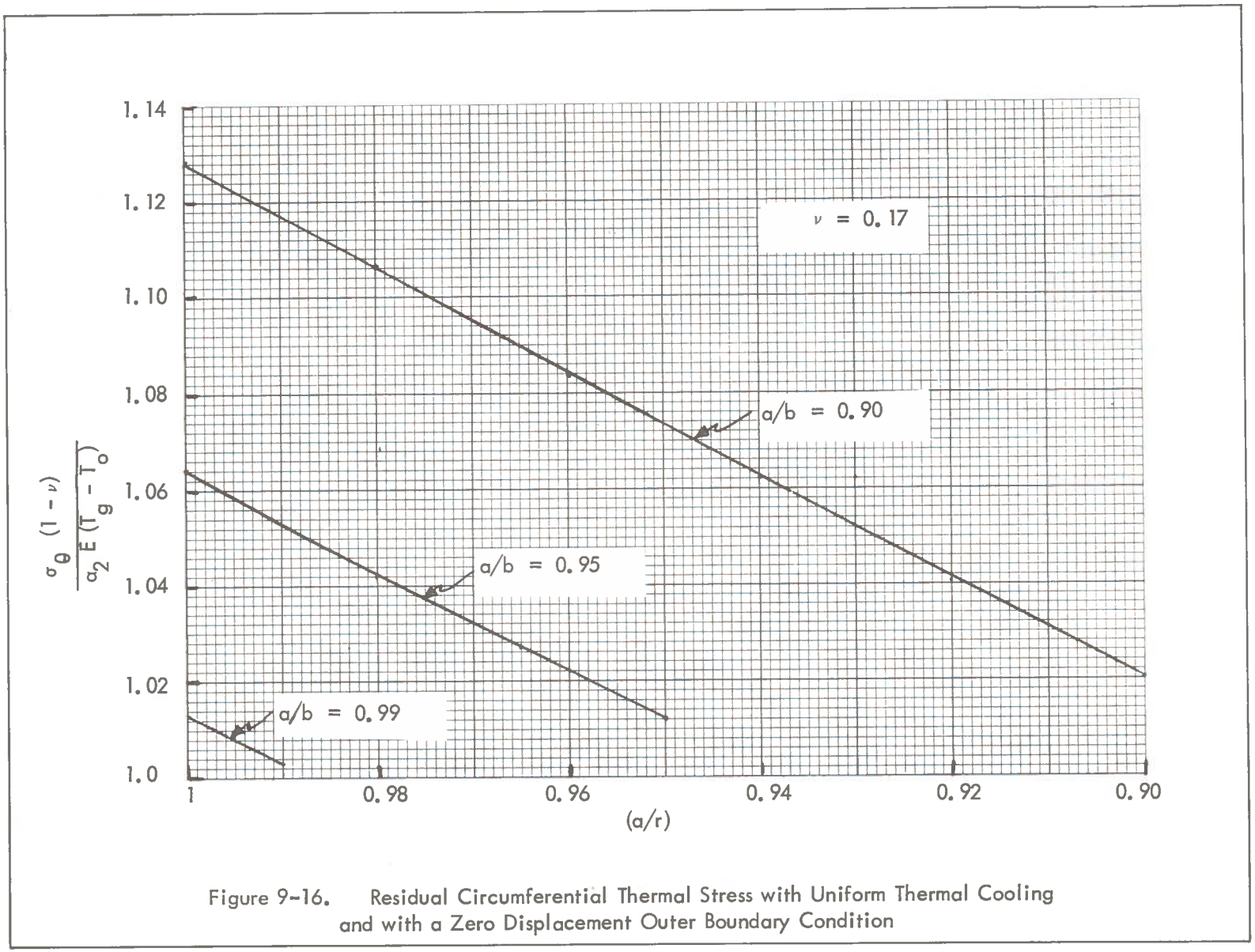

Figure 9-16. Residual Circumferential Thermal Stress with Uniform Thermal Cooling and with a Zero Displacement Outer Boundary Condition

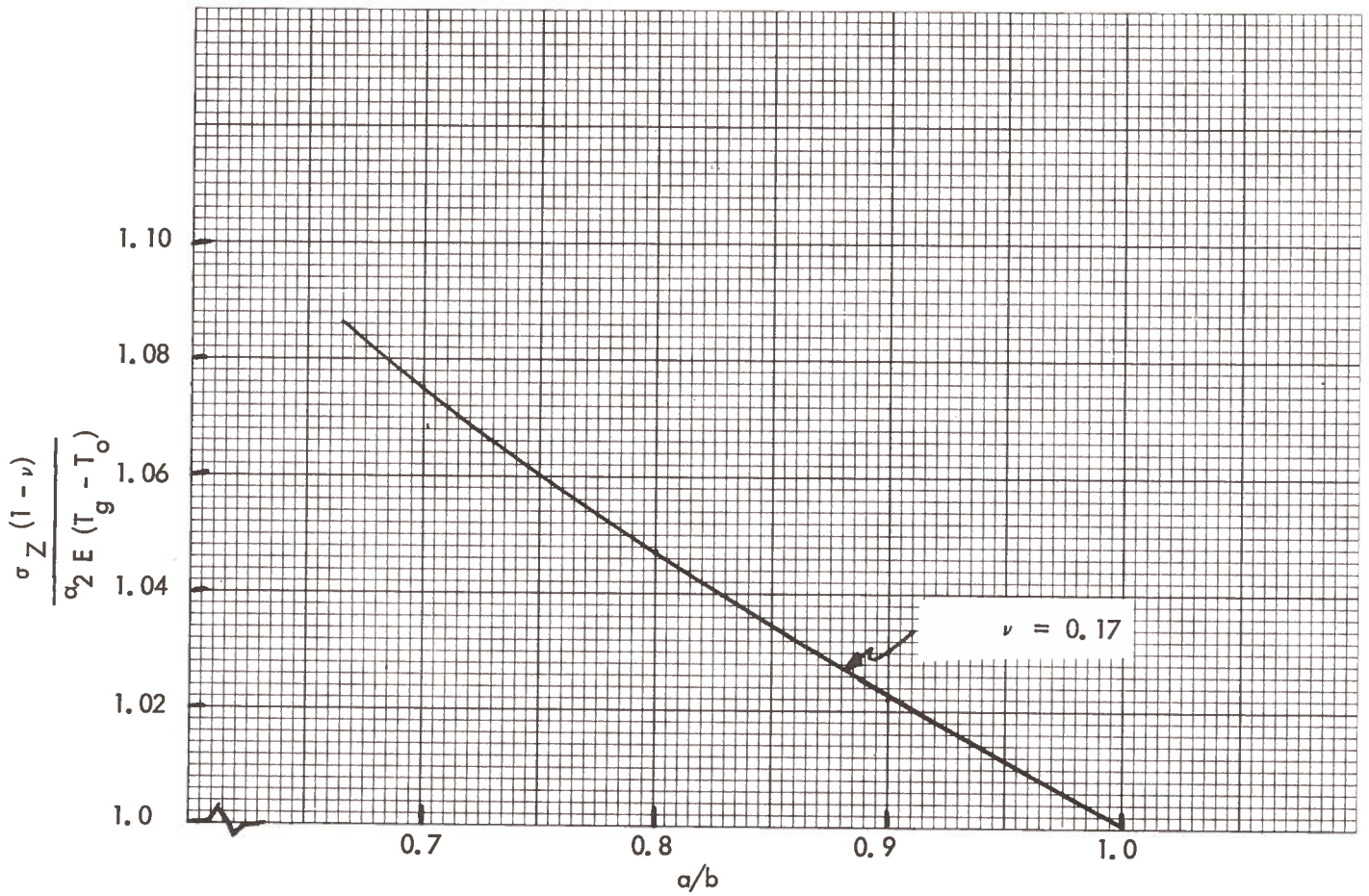

Figure 9-17. Residual Axial Thermal Stress with Uniform Thermal Cooling and with a Zero Displacement Outer Boundary Condition

Figure 9-15 shows the required outer boundary tensile surface traction to retain the glass in its state of stress consistent with zero displacement at that boundary. For relatively thin liners, $a/b \cong 1$, this surface traction could be small and the assumption of zero displacement at the earth boundary interface could be justifiable. But further examination of the axial and circumferential stresses provided on Figures 9-16 and 9-17 would indicate that these stress components would be of value greater than $\alpha E (T_g - T_o)/(1 - \nu)$ for any value of a/b, and this is a factor of about 20 in excess of glass tensile strength. As the relative liner thickness increases, the stresses likewise increase. The conclusion is that if the earth/glass interface remains stationary during the cooling process, the glass will experience both radial and longitudinal cracking. Even if the interface does not remain stationary during the cooldown process, these crack formations are still probable prior to the interface separation which in itself may relieve stress to the extent that the interface traction is lost without separation. This cracking pattern has been observed in polished glass specimens formed by a 50 mm penetrator in Los Alamos tuff.

In this condition the glass liner could not be considered as the primary retaining structure in mass transit transportation tunnels. Similarly in this condition the glass liner primary earth load models considered in Section 9.1 and 9.2 have very little meaning. By virtue of arching capability, this glass liner could serve as an intermediate structure prior to the construction of a more substantial liner interior to the glass formation. Without this secondary liner, the forces of vibration or water leakage could initiate the failure chain leading to a tunnel wall collapse.

Some additional discussion relative to the earth model effects upon the realism of this glass liner model is provided after the developments are completed for the glass liner with the condition of a non-stationery glass/earth interface. This problem provides the residual stress behavior for the glass liner which is free of surface tractions at its outer boundary. This model likewise will find itself to be more realistic in certain earth material environments.

The Outer Boundary of Zero Surface Traction (Cooling at Inner Surface)

The formulation of this problem is based upon the assumption that the earth at the earth/liner interface is incapable of providing tensile surface traction which would inhibit the natural tendency of glass liner thermal contractions during the formation of elastically behaving glass. Prior to the transition to elastic behavior, the interior surface of the plastically behaving liner will displace in the amount of Δa as given by Equation (9-17). The transition to elastically behaving material provides a barrier to further inelastic deformations at the inner surface location. The remaining glass at the T_1 temperature distribution and at temperature levels above T_g still has a capacity for plastic deformation, and it is this additional capacity for plastic contraction which causes the glass either to separate from the earth interface or which causes an earth de-densification at the location near the earth/glass interface. When all temperatures are below T_g, there will be additional elastic contraction of the glass liner in going to the final ambient temperature. This will cause even more interface separation or earth de-densification.

The distinguishing feature between the glass behavior here and that which occurs in commercial tempering is the free interface boundary. In commercial tempering, wherein a residual stress reversal is achieved, the exterior surfaces are cooled so as to encapsulate the plastically behaving material with cooler elastically behaving barriers. The additional capacity for interior glass contraction then results in a surface compression with equilibrating interior tension. Without traction or forced cooling at the liner/earth interface, this boundary is free to plastically deform as the hotter regions of the liner are cooling and undergoing a thermal contraction. Consequently, there is no beneficial residual stress formation in the rapidly cooled glass liner. On the contrary, the cooled inner surface of the glass liner can experience very large transient tensile hoop and axial thermal stresses for conditions of non-uniform cooling. At the steady state temperature, T_o, there may or may not be residual thermal tension depending upon the axial restraint boundary condition. Two possibilities are considered: plane strain where

the end faces of a long cylinder are free of traction, and pure plane strain in which axial displacements are prevented. The latter model must assume that shear forces at the earth/liner interface are great enough to prevent the glass liner elastic axial contraction over the $(T_g - T_o)$ temperature change. The former must assume the glass liner is free to contract axially within its earth encasement during the $(T_g - T_o)$ temperature change, and to be possible, this contraction must be absorbed by additional plastic deformation at the glass liner O. D. by drawing of the glass at temperatures above T_g. For this case, Equation (9-18) must be modified as shown below. The additional term for radial contraction under inelastic behavior shown here accounts for volumetric change that occurs from drawing, due to the axial contraction of the elastic glass liner in cooling from T_g to T_o.

$$\Delta b = -\frac{3\alpha_1}{b}\int_a^b (T_1 - T_g)\, r\, dr - \frac{\alpha_2 (b^2 - a^2)(T_g - T_o)}{2b} \qquad (9\text{-}29)$$

Its derivation comes from the constant volume assumption for plastic deformations.

$V_i = V_f$, where

$V_i = \pi(b^2 - a^2)\, h$

$V_f = \pi\left[(b - \Delta b)^2 - a^2\right]\left[h + \Delta h\right]$, where

$\Delta h = h\, \alpha_2\, (T_g - T_o)$

The steady state thermal stresses in cooling from T_g to T_o under the condition of no axial restraint are:

$$\sigma_R = 0 \qquad (9\text{-}30)$$

$$\sigma_\theta = 0 \qquad (9\text{-}31)$$

$$\sigma_Z = 0 \qquad (9\text{-}32)$$

and the elastic plus plastic deformation at the inner and outer radii are:

$$u(r=a) = -\alpha_2 a (T_g - T_o) + \frac{3\alpha_1}{a}\int_a^b (T_m - T_1) r\,dr \qquad (9\text{-}33)$$

$$u(r=b) = -\alpha_2 b (T_g - T_o) - \frac{3\alpha_1}{b}\int_a^b (T_1 - T_g) r\,dr - \frac{\alpha_2 (b^2 - a^2)(T_g - T_o)}{2b} \qquad (9\text{-}34)$$

It should be mentioned here that depending upon temperature profiles and expansion coefficients there does exist the possibility for a net radial contraction at the liner inner surface.

The steady state thermal stresses for cooldown to the uniform temperature, T_o, for the condition of complete axial restraint are:

$$\sigma_R = 0 \qquad (9\text{-}35)$$

$$\sigma_\theta = 0 \qquad (9\text{-}36)$$

$$\sigma_Z = \alpha_2 E (T_g - T_o) \qquad (9\text{-}37)$$

It was discussed in the earlier development of the fixed outer boundary problem that the following are representative glass properties:

$\alpha_2 E (T_g - T_o) = 2500 \text{ kg/cm}^2$

Tensile Strength $= 140 \text{ kg/cm}^2$

This would indicate a high probability of axial cracking for this model.

Without axial cracking, the elastic plus plastic deformation at the inner and outer radii would be:

$$u(r=a) = -\alpha_2 (1+\nu) a (T_g - T_o) + \frac{3\alpha_1}{a}\int_a^b (T_m - T_1) r\,dr \qquad (9\text{-}38)$$

$$u(r=b) = -\alpha_2 (1+\nu) b (T_g - T_o) - \frac{3\alpha_1}{b}\int_a^b (T_1 - T_g) r\,dr \qquad (9\text{-}39)$$

With axial cracking the $(1 + \nu)$ term in the above equations should correctly be removed from those equations.

It is again possible for a radial contraction at the liner inner surface depending upon the temperature profiles and the difference in expansion coefficients.

The transient thermal stresses are derived from Equations (9-20) and (9-21) with the boundary conditions that:

$\sigma_R = 0$ at $r = a$

$\sigma_R = 0$ at $r = g$, where $g \leq b$

The temperature profile is arbitrary as $T = T(r)$, and some added terminology is $T_a = T(r = a)$ and $T_g = T(r = g)$ where $g \leq b$.

The radial and circumferential transient thermal stresses are identical for both conditions of axial restraint and no axial restraint. These are:

$$\sigma_R = \frac{\alpha_2 E}{(1-\nu) r^2} \left[\frac{r^2 - a^2}{g^2 - a^2} \int_a^g (T - T_g)\, r\, dr - \int_a^r (T - T_g)\, r\, dr \right] \qquad (9\text{-}40)$$

$$\sigma_\theta = \frac{\alpha_2 E}{(1-\nu) r^2} \left[\frac{r^2 + a^2}{g^2 - a^2} \int_a^g (T - T_g)\, r\, dr + \int_a^r (T - T_g)\, r\, dr - (T - T_g) r^2 \right] \qquad (9\text{-}41)$$

The axial stress for the condition of no axial restraint is (see Reference (9-12):

$$\sigma_Z = \sigma_R + \sigma_\theta \qquad (9\text{-}42)$$

The axial stress for the condition of no axial displacement from Equation (9-22) is:

$$\sigma_Z = \frac{2 \alpha_2 E \nu}{(1-\nu)(g^2 - a^2)} \int_a^g (T - T_g)\, r\, dr - \frac{\alpha E}{(1-\nu)} (T - T_g) \qquad (9\text{-}43)$$

The liner location of maximum tensile stress is at the inner surface. Therefore, some comparisons are made between the above equations at $r = a$.

The transient condition with no restraint is:

$$\left(\sigma_Z = \sigma_\theta\right)_{r=a} = \frac{\alpha_2 E}{(1-\nu)} \left[\frac{2}{g^2 - a^2}\int_a^g T\,r\,dr - T_a\right]$$

$$\left(\sigma_Z = \sigma_\theta\right)_{r=a} = \frac{\alpha_2 E}{(1-\nu)} \left[\overline{T} - T_a\right] \qquad (9\text{-}42.a)$$

The transient condition with no axial displacement is:

$$\left(\sigma_Z\right)_{r=a} = \frac{\alpha_2 E}{(1-\nu)} \left[\nu\,\overline{T} + T_g\,(1-\nu) - T_a\right] \qquad (9\text{-}43.a)$$

This latter equation is demonstrated to be the worst possible transient stress if

$$\nu\,\overline{T} + T_g\,(1-\nu) > \overline{T}$$

$$T_g\,(1-\nu) > \overline{T} - \nu\,\overline{T} = \overline{T}\,(1-\nu)$$

$$\text{or} \quad T_g > \overline{T}$$

Since this inequality is true for any non-uniform temperature profile, the stress given by Equation (9-43.a) is greater than that of Equation (9-42.a) and it is the worst possible transient stress condition.

It also can be shown that this transient stress can be greater than the steady state stress by the comparison between Equations (9-37) and (9-43.a). The above is true if

$$T_g - \left[\frac{T_a - \nu\,\overline{T}}{1-\nu}\right] > T_g - T_o$$

or

$$T_a - \nu\,\overline{T} < T_o - \nu\,T_o$$

This inequality is quite likely when $T_a \tilde{=} T_o$, because $\bar{T}$ can be much greater than T_o.

Based upon the findings provided in the above problem solution, some conclusions are:

1) With rapid cooling at the interior surface of the liner on a liner which is not restrained from elastic contractions in the axial direction, surface cracking can be expected if

$$(\bar{T} - T_a) > \text{Tensile Strength} \left(\frac{1-\nu}{\alpha_1 E}\right)$$

A representative number would be:

$$(\bar{T} - T_a) > 140 \frac{kg}{cm^2} \left(\frac{1 - 0.2}{7/^{\circ}C\ (0.7)}\right) = 23^{\circ}C$$

This is an allowable temperature gradient between the inner or the outer liner surface and the average liner temperature in terms of preventing a tensile crack.

2) With a liner that is restrained by a "grasping earth" from axial contraction during cooldown, glass cracking is very likely, even for a uniform cooldown.

9.3.4 Earth Media Versus the Glass Liner Thermal Stress Models

Three separate models describing the thermoviscoelastic behavioral characteristics of the solidifying glass liner have been analyzed.

1) Plane strain with no axial deformation and with no radial deformation at the outer surface: The earth media in which this model could most likely represent the solidification process is dense rock formations which would be capable of arching in hoop compression as the liner unsuccessfully tends to contract at its outer surface.

2) Plane strain with unconstrained axial contraction and with unconstrained radial contraction at the outer surface: In this model the liner must be capable of separating itself from the earth at the glass/earth interface and the liner must be free to "slide" (contract) in the axial direction. For horizontal tunneling in any media, this is a very unlikely mode because even with separation at the interface, the weight of the liner and the weight of the penetrator/equipment will result in a large normal contact force along the bottom exterior side of the tunnel in contact with the earth. Possibly, the water saturated clays and sand would permit liner axial contraction by slipping conditions. Another possible earth media which may allow a liner axial contraction is dry, low density earth which would crush and densify in the process.

3) Plane strain with no axial deformation and with unconstrained radial contraction at the outer surface: With this model the earth offers virtually no tensile normal traction at the glass/earth interface, but rather than separating at that interface, the earth maintains sufficient contact to provide the friction that would prevent a glass liner axial contraction. This model is best visualized as being representative in the not so crushable materials, especially in zones where tunnel collapse is to be expected without a liner.

There does exist the possibility of encountering earth media in a long tunnel wherein any or all three of these models would best represent the glass solidification stresses at different regions of penetration. Realistically, combinations of these models will prevail in unknown proportions. For example, the "radially-fixed" outer boundary is an idealization which neglects the deformation of an earth media which may be elastically flexible. The "radially-free" outer boundary is an idealization of either a plastic or incontigious earth which may partially influence the liner by some elastic behavior. Similarly, the fixed and free axial deformation conditions were likewise idealizations. At both extremes of fixity and freedom, the transient thermal gradients have been characterized by limiting values to prevent glass cracking, and

the feasibility of satisfying these gradients are examined in Section 10.0. Even with uniform cooling, which would appear to be impractical from penetrator velocity and thrusting considerations, cracking should be expected as a worst case design condition strictly from the viewpoint that "fixity" cannot be overlooked as a near-approachable situation.

9.4 REFERENCES

9-1 F. B. Seeley and J. O. Smith, Advanced Mechanics of Materials, Second Ed., John Wiley and Sons, 1963.

9-2 R. J. Roark, Formulas for Stress and Strain, Fourth Ed., McGraw-Hill Book Company, 1965.

9-3 R. H. Anderson and A. P. Boresi, "Equilibrium and Stability of Rings under Non-uniformily Distributed Loads", Proceedings of the Fourth U. S. National Congress of Applied Mechanics, Vol. 1, 1962, pp. 459-467.

9-4 J. E. Monsees, Design of Support Systems for Tunnels in Rocks, University of Illinois Ph. D. Dissertation, 1970, University Microfilms.

9-5 J. R. Hutchinson, III and R. V. Harrington, Glass, Corning Glass Works, reprinted from Encyclopedia of Chemical Technology, 2nd Ed, Vol. 10, pp. 533-604, John Wiley and Sons, 1966.

9-6 F. M. Ernsberger, "Strength of Brittle Ceramic Materials", American Ceramic Society Bulletin, March 1973, Vol. 52, No. 3, p. 240.

9-7 H. D. Weymann, "A Thermoviscoelastic Description of the Tempering of Glass", ACS Journal, Vol. 45, November 1962, pp. 517-522.

9-8 O. S. Narayanaswamy and R. Gordon, "Calculation of Residual Stresses in Glass", ACS Journal, Vol. 52, October 1969, pp. 554-558.

9-9 O. S. Narayanaswamy and R. Gordon, "Stress and Volume Relaxation in Annealing Flat Glass", ACS Journal, Vol. 53, July 1970, pp. 380-385.

9-10 E. H. Lee, T. G. Rogers and T. C. Woo, "Residual Stresses in a Glass Plate Cooled Symmetrically from Bath Surfaces", ACS Journal, Vol. 48, 1965, p. 385.

9-11 W. R. Buessem and R. M. Gruver, "Computation of Residual Stresses in Quenched Al_2O_3 Rods", ACS Journal, Vol. 55, No. 2, 1972, p. 101.

9-12 B. A. Boley and J. H. Weiner, Theory of Thermal Stresses, John Wiley and Sons, New York, 1967.

9-13 M. Heteny, Beams on Elastic Foundation, University of Michigan Press, 1961.

9-14 T. A. Middlebrook and G. E. Bertram, "Soil Tests for Design of Runway Pavements", Proceedings of the Highway Research Board, Vol. 122, 1942, pp. 152 and 170.

10.0 MELT COOLDOWN

The molten glass formed over heated portions of the penetrator must be cooled down in order to provide structural strength so that thrusting on the glass wall by grip pads can be permitted to effect propulsion. The rate of melt cooldown is important because it determines the length of the controlled cooldown section needed, which in turn may establish the operating limits on the design.

The functional relations of variables controlling melt cooldown are derived in this chapter and scoping calculations were made to illustrate the application of the equations. The results are presented in terms of liner cooldown times and lengths of cooldown sections needed for reference design conditions.

The rate at which the molten glass liner must be cooled depends on a number of factors, some of which are the glass liner thickness required (δ), the allowed thermal stress (σ_a), and the temperature to which the melt must be cooled. These factors are related to the liner temperature distribution, the heat flux (ϕ_o), and the cooldown time (t_c). The cooldown time is in turn related to the length of the liner cooldown section (L_c) and the rate of penetration desired (U_∞). Functional relations of these controlling variables can be derived by an analysis of the melt cooldown process.

10.1 MELT COOLDOWN PROCESS AND PHYSICAL MODELS

The melt cooldown process and the resultant melt/glass temperature distribution during cooldown is dependant on the physical properties of the glass and the surrounding earth/rock material(s) and on the cooling rate. Because a variety of earth/rock materials may be encountered during a tunneling operation, different physical models must be considered. Potential liner cooldown conditions are illustrated in Figure 10-1. The figure shows schematically the temperature distributions in the glass liner during cooldown for various possible conditions, tabulated below:

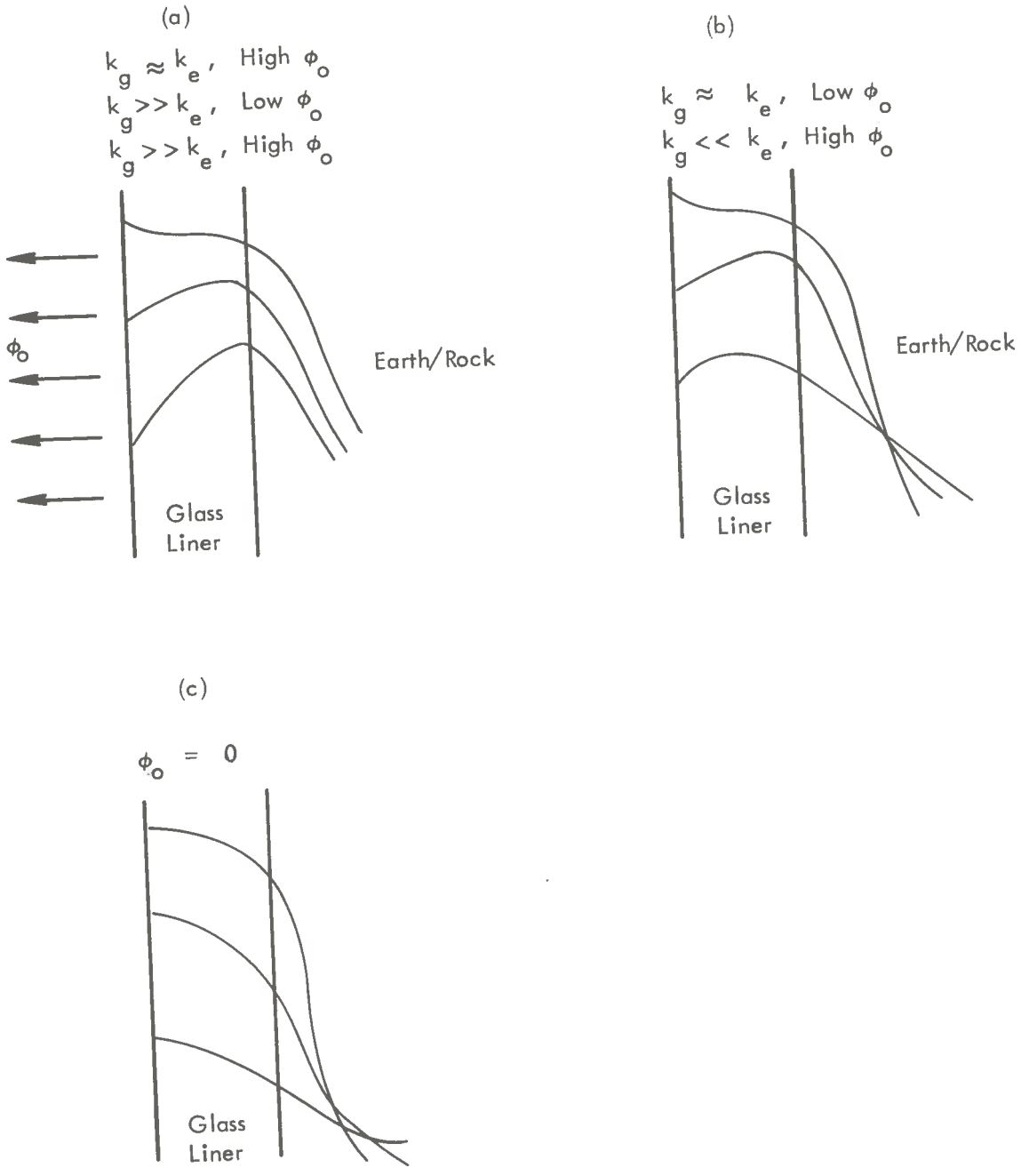

Figure 10-1. Potential Liner Cooldown Conditions

Condition	Figure	k, Thermal Conductivity	Cooldown Heat Flux
1	(a)	k glass $\approx$ k earth/rock	high
2	(a)	k glass > k earth/rock	high
3	(a)	k glass > k earth/rock	low
4	(b)	k glass $\approx$ k earth/rock	low
5	(b)	k glass < k earth/rock	high
6	(c)	All Conditions	zero

The cooldown time is related to the length of the cooldown section and the rate of advance through the definition of the residence time: $t_r = t_c = L_c/U_\infty$. In general, it is desirable to maximize the cooldown heat flux, because this will minimize the cooldown time and hence minimize the length of the cooldown section required and/or maximize the rate of advance. For this reason, the condition of low heat flux is generally of no interest. Zero heat flux occurs approximately when the cooldown section has passed any given point of the glass liner. For unconsolidated earth and soils, the glass (formed from melting such materials) tends to have appreciably higher thermal conductivities. For consolidated materials, their thermal conductivities are on the same order of magnitude as those of glasses formed from melting these materials. At the high temperatures encountered during cooldown, rarely does one encounter earth/rock materials whose thermal conductivities are greater than those of glass formed from melting such materials. It follows that of the 6 possible cases listed above, only models 1 and 2 are of primary interest here.

10.2 MATHEMATICAL ANALYSIS AND FUNCTIONAL RELATIONS

The general physical problem of glass liner cooldown is one of conduction. It is known that at relatively high temperatures, thermal radiation can be an important mode of heat transfer. Examination of published data on the thermal physical properties of glasses at high temperatures has shown that only effective thermal conductivities are reported. Consequently, by necessity, the problem must be treated as one of pure conduction, which greatly simplifies the problem. The general three dimensional equation of conduction is

$$\rho C_p \frac{\partial T}{\partial t} = k \left(\frac{\partial^2 T}{\partial x^2} + \frac{\partial^2 T}{\partial y^2} + \frac{\partial^2 T}{\partial z^2} \right) \qquad (10\text{-}1)$$

where T is the temperature, t is the time, k is the effective thermal conductivity, ρ is the glass density, and C_p is its specific heat.

Examination of typical earth/rock and glass thermal conductivities has shown that at temperatures below the melting point, the effective thermal conductivity decreases gradually with increasing temperature up to near the melting point. At temperatures greater than the melting point, the effective thermal conductivities increase sharply with increasing temperature. This is illustrated in Figure 10-2 (reproduced from Reference 10-1), where the effective thermal conductivities of various types of rocks are plotted as a function of temperature. The melting points of the materials are noted on the figure. It becomes apparent that with the exception of obsidian, the effective thermal conductivities of the materials below their melting points are relatively constant. Since glass liner cooldown occurs primarily below the melting point of the glass, it can be assumed that the effective thermal conducitivity of the glass is a constant. The density and specific heat of glass are relatively independent of the temperature. Equation (10-1) can then be written in the form:

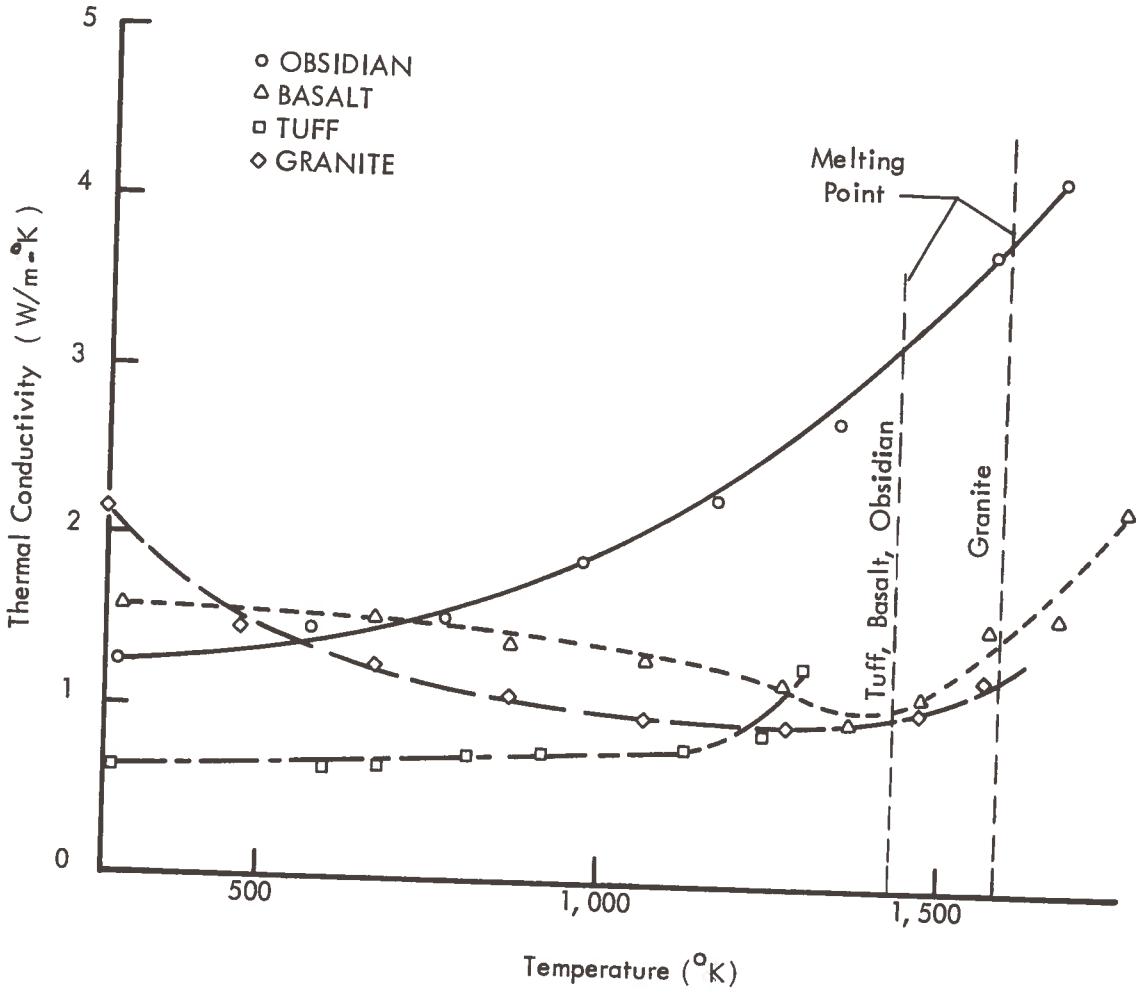

Figure 10-2. Thermal Conductivities of Various Types of Rocks at High Temperature

$$\frac{\partial T}{\partial t} = \alpha \left(\frac{\partial^2 T}{\partial x^2} + \frac{\partial^2 T}{\partial y^2} + \frac{\partial^2 T}{\partial z^2} \right) \qquad (10\text{-}2)$$

where α is the thermal diffusivity, $k/\rho C_p$, a constant.

Equation (10-2) can now be considered for cases 1 and 2.

10.2.1 Model 1, Uniform Initial Temperature and Physical Properties

It is known that for some earth/rock materials such as tuff and alluvium, the glass formed from melting the parent material has a higher density than that of the parent material. In such cases, the thermal conductivity of the glass is expected to be greater than that of the parent material. On the other hand, if the densities of the glass and its parent material are approximately equal, then their effective thermal conductivities may be expected to be more nearly equal, i.e.,

$$\frac{k_g}{\rho_g} = \frac{k_e}{\rho_e} = \text{constant} \qquad (10\text{-}3)$$

Based on the limited experimental data available, it appears that the specific heat of glass and its parent earth/rock material are about the same at the same temperature. Consequently

$$\alpha_e = \alpha_g = \text{a constant} \qquad (10\text{-}4)$$

With the above assumptions, cases 1 and 2 reduce to a single model where the glass liner and the surrounding earth/rock parent material can be treated as a homogeneous mass having the same thermal diffusivity.

In practical tunneling applications, the glass liner thickness is expected to be small compared to the tunnel diameter. For analytical purposes, the problem can be treated in one dimension, reducing Equation (10-2) to the following:

$$\frac{\partial T}{\partial t} = \alpha \frac{\partial^2 T}{\partial x^2} \qquad (10\text{-}5)$$

Letting the inner surface of the glass liner be the origin, the physical model shown below depicts the transient temperature distribution in the glass liner during cooldown with the surrounding earth/rock acting as an infinite heat sink.

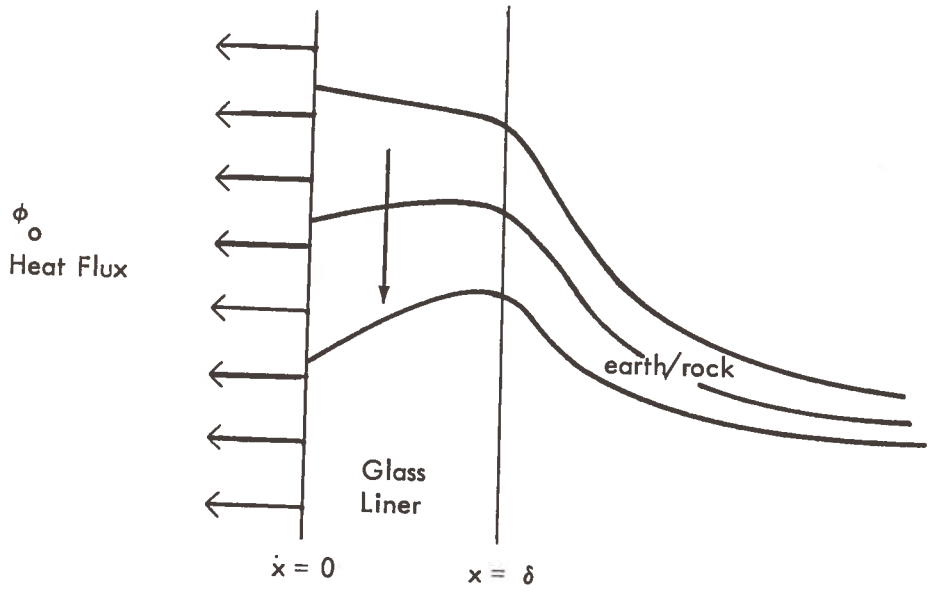

By defining a new variable U such that

$$U = T_i - T \tag{10-6}$$

where T_i is the initial temperature, Equation (10-5) can then be written in terms of U:

$$\frac{\partial U}{\partial t} = \alpha \frac{\partial^2 U}{\partial x^2} \tag{10-7}$$

A solution is sought with the following initial and boundary conditions

$$U(x, 0) = 0 \qquad (x > 0) \tag{10-8}$$

$$-k \frac{\partial U}{\partial x}(0, t) = \phi_o \qquad (t > 0) \tag{10-9}$$

where ϕ_o is the cooldown heat flux, a constant.

$$U(x, t) = 0 \qquad (t > 0,\ x \rightarrow \infty) \tag{10-10}$$

The solution to Equation (10-7) with the initial and boundary conditions (10-8) to (10-10) gives the temperature at any point in the liner during cooldown:

$$T = T_i - \frac{\phi_o}{k} \left[\sqrt{\frac{4 \alpha t}{\pi}}\, e^{-x^2/4\alpha t} - x \operatorname{erfc}\left(\frac{x}{\sqrt{4 \alpha t}} \right) \right] \tag{10-11}$$

The difficulty of this problem lies in the unknown initial temperature distributions through the glass melt and through the surrounding earth/rock. Even if these distributions are known, they are expected to be relatively complex and render the problem difficult to solve and/or use. In the interest of deriving closed form analytic solutions so that the resultant functional relations can be readily used in subsequent analyses, the assumption was made that the initial temperature distribution is a constant equal to a mean temperature of the molten glass. Although this assumption may appear to be grossly in error (see figure below), the temperature distributions in the glass liner during cooldown may be fairly well approximated by this assumption. This is due to the fact that the glass liner thermal conductivity is high compared to the thermal conductivity of the unmolten earth/glass far away from it (see the figure below)

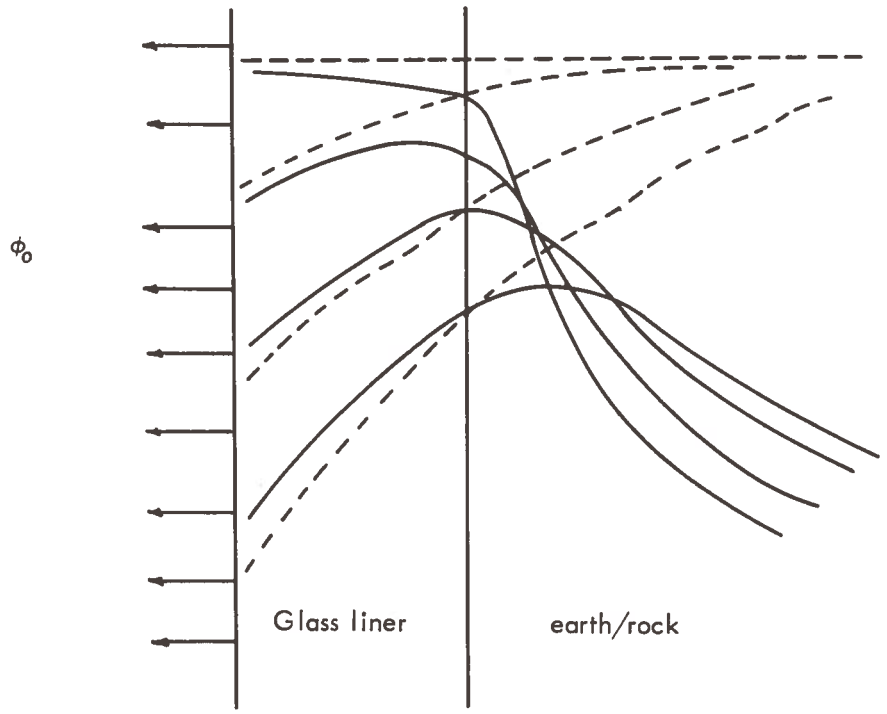

——— actual

– – – model

The glass liner inner surface temperature, T, is evaluated at $x = 0$. From Equation (10-11)

$$T = T - \frac{\phi_o}{k}\sqrt{\frac{4\,\alpha\,t}{\pi}} \qquad (10\text{-}12)$$

The glass liner outer surface temperature, T_δ, is evaluated at $x = \delta$, or

$$T_\delta = T - \frac{\phi_o}{k}\left[\sqrt{\frac{4\,\alpha\,t}{\pi}}\; e^{-\delta^2/4\,\alpha\,t} - \delta\,\mathrm{erfc}\left(\frac{\delta}{\sqrt{4\,\alpha\,t}}\right)\right] \qquad (10\text{-}13$$

The temperatures calculated by Equations (10-12) and (10-13) are expected to be conservative because of the assumption of a uniform initial temperature in the liner and the earth/rock. This assumption implies that there is no heat loss to ambient earth/rock during cooldown. However, in cases where the glass liners are thick and the effective thermal conductivity is appreciably greater than the earth/rock thermal conductivity, heat losses to ambient earth/rock are expected to be insignificant if cooldown is rapid. Under these circumstances, the glass liner inner surface temperature predicted by Equation (10-12) is expected to be reasonably good, while the liner outside surface temperature predicted by Equation (10-13) is still expected to be appreciably higher than actual values. For a more realistic determination of the liner outer surface temperature, the following model is proposed.

10.2.2 Model 2, Adiabatic Interface

In this case, the effective thermal conductivity of the glass liner is appreciably greater than that of the earth/rock. The following is assumed:

1. The liner - earth/rock interface is adiabatic.
2. The initial liner temperature is uniform.

3. The liner cools down with heat removed from the surface at a constant heat flux, ϕ_o .

4. Liner thickness is small compared to the diameter.

5. There are no axial effects.

Because of assumptions (4) and (5), the problem can be treated in one dimension. A schematic diagram of the physical model is shown below:

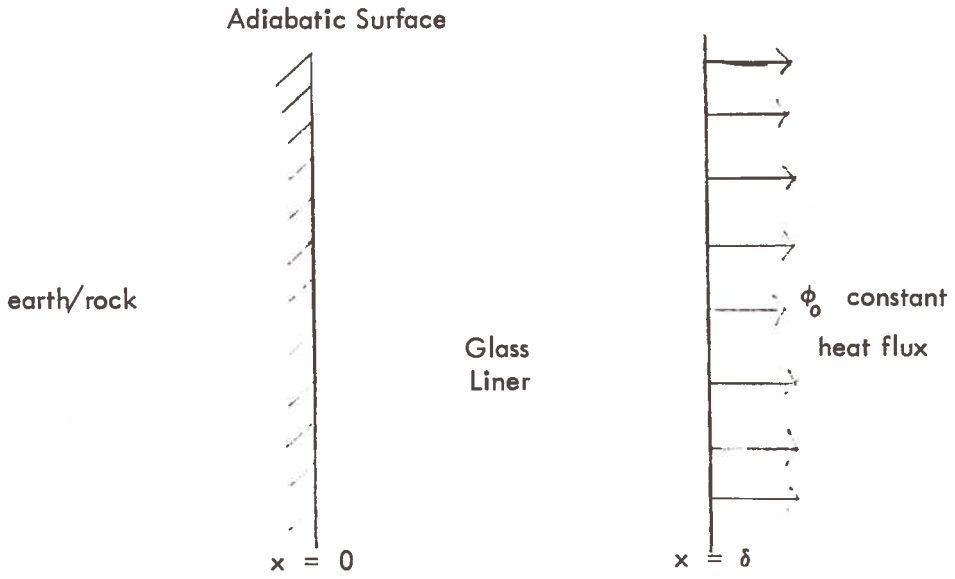

For this model, one can again use Equation (10-7) as the starting partial differential equation. The initial and boundary conditions are the following:

$$U\ (x, 0) = 0 \qquad (\ 0 \leq x \leq \delta\ ) \tag{10-14}$$

$$-k_g \frac{\partial U}{\partial x}\ (\delta,\ t\ ) = \phi_o\ (\ t > 0) \tag{10-15}$$

$$\frac{\partial U}{\partial x}\ (0,\ t\ ) = 0 \qquad (t > 0\ ) \tag{10-16}$$

Carslaw and Jaeger (10-3) had developed a solution to Equation (10-7) with boundary conditions similar to those treated here. Their solution can be adapted to the problem here to yield

$$T = T_i - \frac{\phi_o \sqrt{4 \alpha t}}{k} \sum_{n=0}^{\infty} \left\{ 2\,\text{ierfc}\left[\frac{(2n+1)\delta - x}{\sqrt{4 \alpha t}}\right] + 2\,\text{ierfc}\left[\frac{(2n+1)\delta + x}{\sqrt{4 \alpha t}}\right]\right\} \quad (10\text{-}17)$$

where

$$\text{ierf}\, x = \int_x^{\infty} \text{erfc}\, \xi \; d\xi \quad (10\text{-}18)$$

and erfc x is the complementary error function,

$$\text{erfc}\, x = 1 - \text{erf}\, x \quad (10\text{-}19)$$

The function 2 ierf x is tabulated in Reference (10-3). For the glass liner inner surface temperature during cooldown, Equation (10-17) reduces to

$$T = T_i - \frac{\phi_o \sqrt{4 \alpha t}}{k} \sum_{n=0}^{\infty} \left\{ 2\,\text{ierfc}\left[\frac{2n\delta}{\sqrt{4 \alpha t}}\right] + 2\,\text{ierfc}\left[\frac{(2n+2)\delta}{\sqrt{4 \alpha t}}\right]\right\} \quad (10\text{-}20)$$

For the glass liner outer surface temperature,

$$T_\delta = T_i - \frac{\phi_o \sqrt{4 \alpha t}}{k} \sum_{n=0}^{\infty} 2\,\text{ierfc}\left[\frac{(2n+1)\delta}{\sqrt{4 \alpha t}}\right] \quad (10\text{-}21)$$

Because of assumptions (10-1) and (10-2), the temperatures predicted by the above model are still conservative although much less so than those predicted by the equations developed for model 1. However, the liner surface temperature is much less affected by the conservative assumptions than the liner outer surface temperature. Equation (10-20) and (10-21) are therefore recommended for the estimation of liner cooldown temperatures.

10.2.3 Model 3, Zero Heat Flux

This case is potentially important if it is necessary to study the time-temperature relation when the partially cooled glass liner loses heat only to the ambient earth/rock. The physical model for this case considers the liner inner surface to be adiabatic, and the earth/rock temperature to be at a constant value T_∞ . The following are therefore assumed:

(1) No heat loss on the liner inner surface.

(2) The earth/rock temperature is a constant at all times, equal to the initial or ambient earth/rock temperature.

These assumptions are needed to arrive at a closed form analytic solution. The first assumption is reasonable, because following the passage of the penetrator, internal heat sinks are then non existent. The second assumption is non-conservative and a more rapid cooldown would be predicted by this assumption.

The physical model is illustrated below:

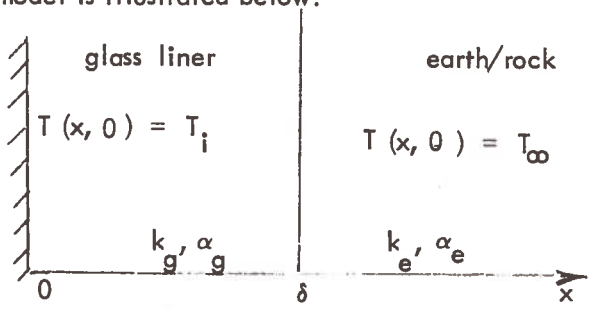

By defining a new variable U such that:

$$U = T - T_\infty \qquad (10\text{-}22)$$

Equation (10-7) is then applicable here. For the two regions, Equation (10-7) becomes

$$\frac{\partial U}{\partial t} = \alpha_g \frac{\partial^2 U}{\partial x^2} \qquad (0 < x < \delta,\ t \geq 0) \qquad (10\text{-}23)$$

$$\frac{\partial U}{\partial t} = \alpha_e \frac{\partial^2 U}{\partial x^2} \qquad (x > \delta,\ t > 0) \qquad (10\text{-}24)$$

The following are the initial and boundary conditions

$$U(x, 0) = U_o \qquad (0 < x < \delta) \qquad (10\text{-}25)$$

$$U(x, 0) = 0 \qquad (x > \delta) \qquad (10\text{-}26)$$

$$\frac{\partial U}{\partial x}(0, t) = 0 \qquad (t > 0) \qquad (10\text{-}27)$$

$$\lim_{x \to \infty} U(x, t) = 0 \qquad (t \geq 0) \qquad (10\text{-}28)$$

$$U(\delta - 0, t) = U(\delta + 0, t) \quad (t > 0) \qquad (10\text{-}29)$$

$$k_g \frac{\partial U(\delta - 0, t)}{\partial x} = k_e \frac{\partial U(\delta + 0, t)}{\partial x} \quad (t > 0) \qquad (10\text{-}30)$$

A solution to Equations (10-23) and (10-24) with the initial and boundary conditions (10-25)- (10-30) is the following.*

$$\frac{T - T_\infty}{T_o - T_\infty} = 1 - \frac{1 + \lambda}{2} \sum_{n=o}^{\infty} \lambda^n \left\{ \text{erfc} \left[\frac{(2n+1)\delta - x}{2\, kgt \sqrt{\alpha t}} \right] + \text{erfc} \left[\frac{(2n+1)\delta + x}{2\sqrt{\alpha t}} \right] \right\} \qquad (10\text{-}31)$$

for $o < x < \delta$

where $$\lambda = \frac{k_g \sqrt{\alpha e} - k_e \sqrt{\alpha g}}{k_g \sqrt{\alpha e} + k_e \sqrt{\alpha g}} \qquad (10\text{-}32)$$

10.3 VERIFICATION OF FUNCTIONAL RELATIONS

Prior to using these functional relations developed for glass liner cooldown, their validity must be verified. One set of limited experimental melt and glass liner temperatures has been measured by the Los Alamos Scientific Laboratory. The temperature measurements were made with a 75 mm conical consolidating penetrator melting vertically through dried tuff. The rate of penetration was established at 0.085 mm/second.

In this experiment, two thermocouples were buried in the dried tuff sample, well below the surface of the sample. One of the thermocouples was placed along the centerline of the path of the penetrator while the other was placed at a position that corresponds to the liner outside surface temperature but at a vertical position 25 mm below the first thermocouple. As the penetrator melts through the tuff sample and approaches the thermocouples, both record temperature rises with time. After the tip of the penetrator reaches the centerline thermocouple, that thermocouple would be displaced by the penetrator and flow with the

* Derivation of this solution can be found in Reference (10-2) , pp. 141-143

melt along the surface of the penetrator. As the heated portion of the penetrator flows past the thermocouple, the melt cools down and the thermocouple becomes frozen into the glass liner at a position close to the inner surface of the glass liner. This thermocouple would then record the glass liner inner surface temperature during cooldown. Prior to complete liner cooldown, the penetrator was withdrawn. This perturbed the normal cooldown process. The transient temperature recordings are reproduced in Figure 10-3. As the penetrator approaches the centerline thermocouple, it registers a steady increase in temperature (curve 1-2) and then decreases erratically as the melt becomes displaced and flows with the melt around the conical penetrator (curve 2-3). When the shoulder and melt cooldown section is reached, the melt/glass liner cools down steadily (curve 3-4). However, at point 4, the penetrator is retracted, perturbing the normal cooldown process by partially reheating the glass liner. It follows that only the portion of the data given by curve 3-4 may be considered to be representative of actual liner cooldown conditions. Unfortunately, the initial portion of the recording for the outer thermocouple is missing as a result of a temporary failure of the data acquisition system. This thermocouple records a lower temperature than the liner inner surface temperature caused by the former being located 25 mm below the latter so that it was not heated up to as high a temperature as the latter. Under normal conditions, the glass liner outer surface temperature can be the same, higher, or lower than the inner surface temperature, depending on the glass liner thickness, relative thermal conductivity of the glass liner and the earth/rock materials, and the magnitude of the cooldown heat flux.

The glass liner inner surface temperature during cooldown is given by Equation (10-12), which can be rewritten in the form

$$T_i - T_s = \frac{2\,\phi_o}{\sqrt{\pi\, k\, \rho\, C_p}} \qquad \sqrt{t} \qquad (10\text{-}33)$$

Based on the assumptions of constant heat flux and constant physical properties, Equation (10-33) predicts that a plot of $T_i - T_s$ vs. the square root of the cooldown time should yield a straight line that passes through the origin. The length of the heated penetrator is 158 mm. Dividing this by the rate of penetration, 0.085 mm/sec, yields the time (1860 seconds) that took the centerline thermocouple to move from the penetrator tip to the penetrator shoulder, after which cooldown is initiated. This time span permits the initial melt temperature (1560°K) and time at the initiation of cooldown (2100 seconds) to be established. The cooldown time scale was therefore adjusted by subtracting 2100 seconds. The results are plotted as $T_i - T_s$ vs. $\sqrt{t}$ as shown in Figure 10-4. It is evident that there is excellent correlation of the data by the derived functional relation.

The significant correlation observed above may be the result of two compensating errors in the assumptions used to derive the functional relationship. These assumptions are constant heat flux and constant effective thermal conductivity of the glass liner. The glass liner was cooled by a stream of gas that originates near the shoulder of the penetrator and flows upward between the glass liner and the penetrator stem (cooldown section). As a result, the glass liner surface comes into contact with an increasingly hotter gas with increasing cooldown time. Since the gas flow rate is kept relatively constant, the forced convective heat flux is expected to decrease with increasing cooldown length. This fact suggests that the parameter $2\phi_o/(\pi k \rho C_p)^{1/2}$ may be a constant because the effective thermal conductivity of the glass liner also decreases with cooldown time, i.e., it decreases with decreasing temperature. This is true even if heat transfer is dominated by thermal radiation, i.e., radiation from the glass liner surface to the stem, because radiation heat flux decreases with decreasing temperature. Whether this model can be applied to earth/rock materials remains to be determined by further experimental testing.

As discussed in a previous paragraph, the glass liner inner surface temperature is

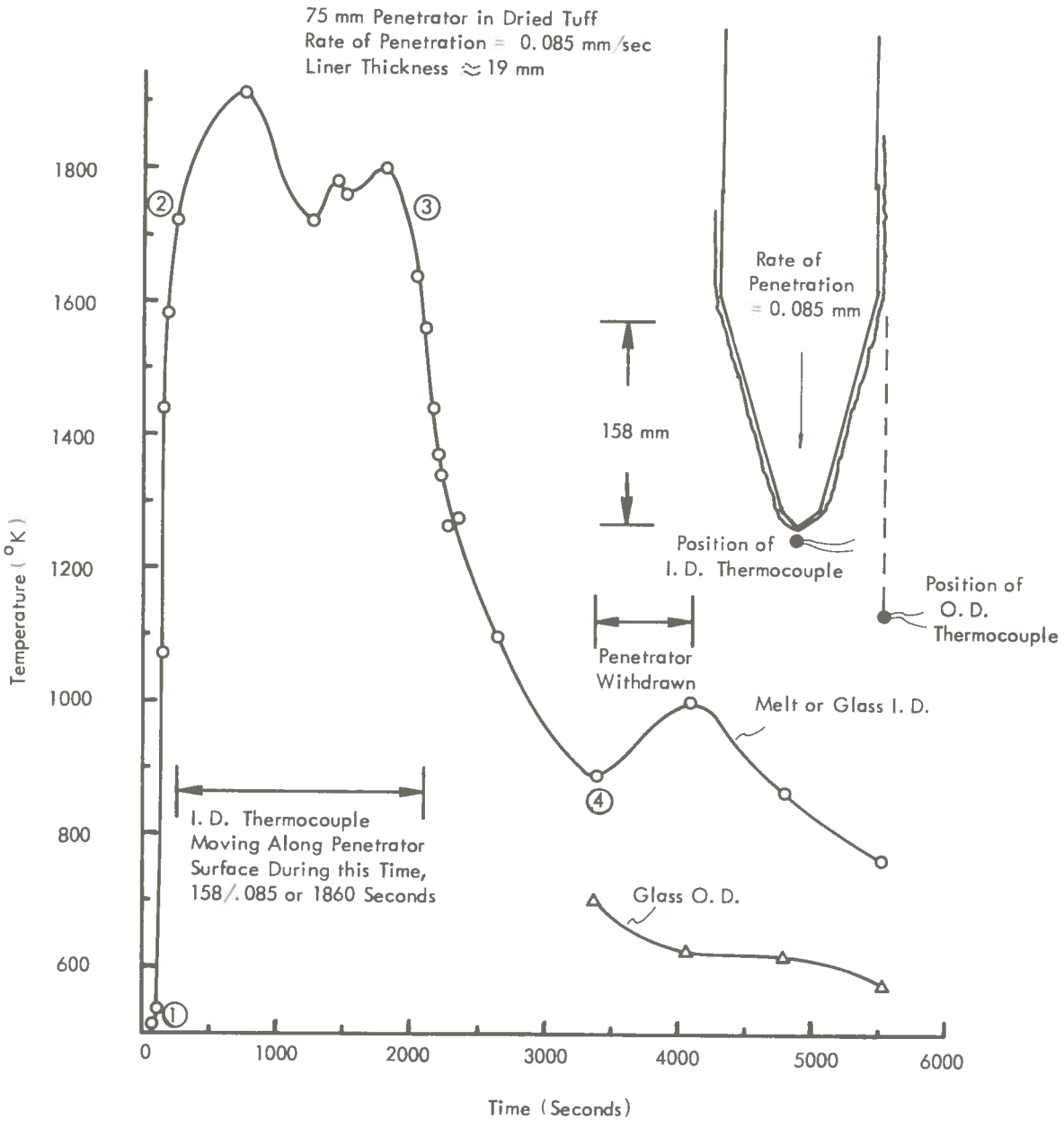

Figure 10-3. Effect of Time on Melt and Glass Liner Temperature

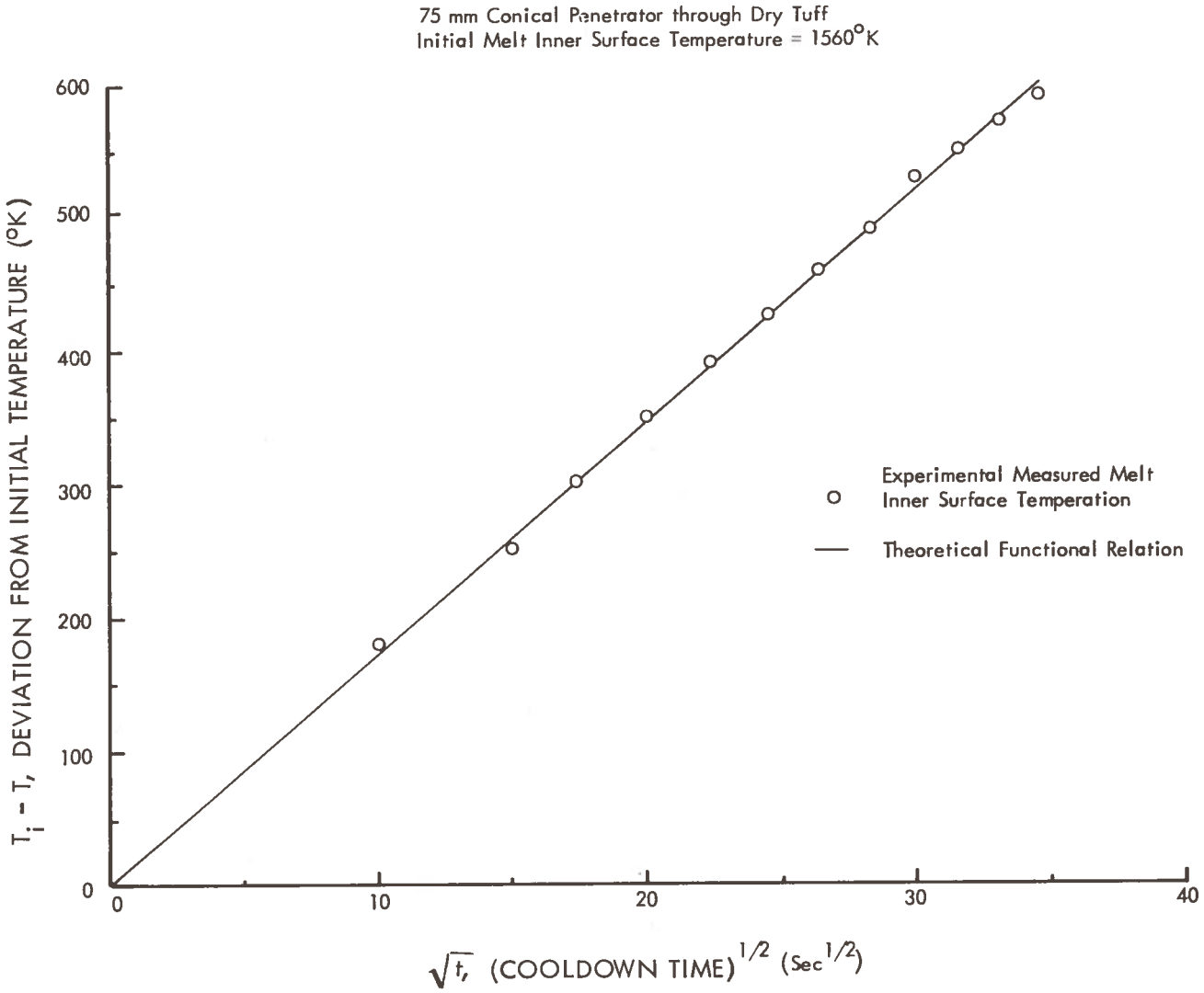

Figure 10-4. Correlation of Melt Cooldown Data

expected to be fairly well represented by Equation (10-12) derived for model 1. However, the liner outside surface temperature given by Equation (10-13) is expected to show significant errors. For this reason, Equations (10-20) and (10-21) developed for model 2 are recommended for the prediction of glass liner temperatures. The verification of Equation (10-12) by the limited experimental data suggests that the ratio of $\phi_o \sqrt{k}$ is a constant. Since this ratio also appears in Equations (10-20) and (10-21), the validity of those equations within the limits of the model is therefore assumed.

10.4 COOLDOWN HEAT FLUX AND COOLDOWN LENGTH REQUIREMENTS

One of the most attractive features of the rock melting concept for tunneling is the potential capability of forming a self-supporting glass liner for tunnel support and for tunneler propulsion through thrusting on the wall. For this purpose, the glass must possess adequate strength. The strength of the glass liner is directly related to the glass liner cooldown process, the depth of the tunnel operation, the diameter of the tunnel and the thickness of the glass liner. The criteria for penetrator designs to meet certain strength requirements are discussed in the following section.

10.4.1 Glass Liner Design Constraints

The extreme upper use temperature for glass is that temperature at which glass becomes rigid and self-supporting. This point is defined by a viscosity of 10^{15} poise. During cooldown, thermal stresses are set up by temperature differences across the glass liner. The tensile stress on the cold side is given by the relation

$$\sigma_a = \frac{E \alpha \Delta T}{2(1-\nu)} \qquad (10\text{-}34)$$

Where E is the Young's modulus, α is the coefficient of linear thermal expansion, ΔT is the temperature difference, and ν is the Poisson's ratio. According to Reference (10-4) the normal maximum long-term design stress in glass is about 1000 psi. This includes a safety factor of 2.

Glass strength can be improved by removing moisture. During cooldown, moisture is absent from the glass liner and the resultant glass is expected to have higher strength than that at room temperature. This is consistent with the fact that glass strength improves with increasing temperature. On the otherhand, if the glass is non-homogeneous, its tensile strength becomes reduced appreciably. Since the composition of the glass formed during tunneling cannot be controlled, the use of a lower design stress limit would appear to be reasonable.

Based on the foregoing discussion, the following values are selected as reasonable for the scoping calculations on cooldown time and afterbody length requirements.

1. Above a maximum "end use" temperature, T_{eu}, determined by a glass viscosity of 10^{15} poise, the melt/glass liner can be cooled down rapidly (i.e., with any ΔT across the liner).

2. Below a temperature, T_{eu}, (extreme or maximum end use temperature) determined by a viscosity of 10^{15} poise, the temperature drop across the glass liner must not exceed $2\ \sigma\ (1-\nu)/\alpha E$.

3. The maximum design tensile strength is 2000 psi.

4. The glass liner shall be cooled by controlled cooldown to no less than the "end use" temperature, T_{eu}.

It is a design goal to minimize the controlled liner cooldown time within the constraints listed above. The cooldown time, t_c, is related to the length of the cooldown section L_c (of the subterrene penetrator) and the rate of advance, U_∞, through the definition of the residence time, t_r:

$$t_c = t_r = \frac{L_c}{U_\infty} \qquad (10\text{-}35)$$

It is evident that when the cooldown time is minimized, the length of the cooldown section is minimized for a given rate of penetration and/or the rate of advance can be maximized for a given length L_c.

In order to meet the design goals and the design constraints listed above, glass liner cooldown time can be minimized in a number of ways, depending on the liner thickness and the glass-earth/rock physical properties involved. Ideally, it would be desirable to cool the liner in one step without going below the maximum use temlerature at the surface and without exceeding the thermal stress criterion. This is always possible if a sufficiently low heat flux is imposed. However, a more optimum (minimum total cooldown time) method may be a two-step cooldown process. In the first step, the inner liner surface is rapidly cooled down to the maximum use temperature, while the liner ΔT is well in excess of the thermal stress criterion. Following this period, the cooldown heat flux is terminated to maintain a relatively constant liner inner surface temperature while the liner outer surface cools down gradually by heat loss to earth/rock. During step 2, the liner temperature drop is not expected to exceed the thermal stress limit because the liner inner surface temperature can actually rise slightly as a result of conduction while the outer surface temperature drops gradually. Scoping calculations are made in the next section to determine the magnitude of cooldown heat flux, cooldown times and lengths of cooldown section (afterbody) needed under practical tunneling conditions.

For scoping calculations, Equations (10-20) and (10-21) were used. The heat flux and cooldown time required to cooldown the liner inner surface to the maximum use temperature, (T_{eu}) is of interest, while the liner ΔT is maintained at or above the thermal stress value, i.e.

$$T_s = T_{eu} \; ; \; T_\delta = T_{eu} + \Delta T \qquad (10\text{-}36)$$

It is noted from Equations (10-20) and (10-21) that the temperatures are implicit functions of the cooldown time. A graphical technique was used to obtain the solution for time.

Equations (10-20) and (10-21) can be rewritten in terms of two dimensionless variables ψ and ξ, where

$$\psi_s = \frac{2\,k\,(T_i - T_s)}{\phi_o\sqrt{4\,\alpha\,t}} = \sum_{n=0}^{\infty} 2\ \text{ierfc}[(2\,n\,\xi)] + 2\ \text{ierfc}\ [(2n+2)\xi] \qquad (10\text{-}37)$$

and $$\xi = \frac{\delta}{\sqrt{4\ \alpha\ t}} \qquad (10\text{-}38)$$

$$\psi_\delta = \frac{k\ (T_i - T_s)}{\phi_o\sqrt{4\alpha\,t}} = \sum_{n=0}^{\infty} 2\ \text{ierfc}\ [\ (2\,n+1)\ \xi\ ] \qquad (10\text{-}39)$$

The functions ψ_s and ψ_δ are presented in Figure 10-5.

For a given earth/rock material, the glass liner physical properties are fixed. Then, for a specified glass liner thickness δ, there may be a unique solution with the constraints specified in Equation (10-36), or a number of solutions may be possible since t and ϕ_o can be varied. If the latter is true, then the conditions for a minium cooldown time may be determined.

10.5. NUMERICAL EXAMPLES AND SCOPING CALCULATIONS

In order to evaluate the time required for cooldown (t_c), the cooldown heat flux (ϕ_o), the initial melt temperature (T_i), and the maximum (or extreme) end use temperature (T_{eu}) must be specified. In addition, the glass liner effective thermal conductivity (k) and thermal diffusivity (α) must be known.

10.5.1 Initial Melt Temperature

The initial melt temperature in the previously verified relation was taken to be the melt temperature at the shoulder of the penetrator. In general, these values are design dependent and not readily calculated. Most types of earth/rock materials melt over a range of temperatures. The upper value of this range is used as the initial melt temperature.

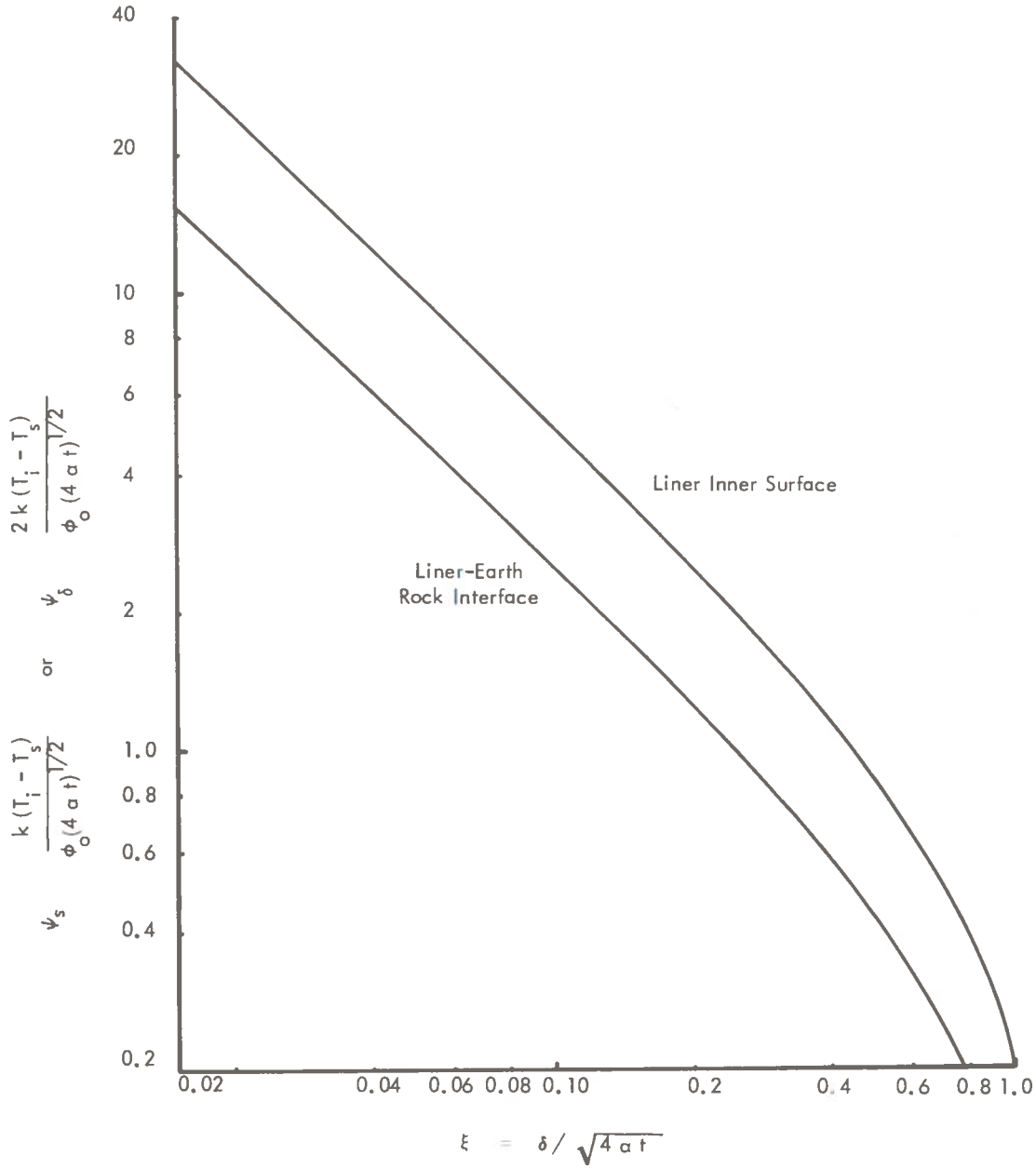

Figure 10-5. Dimensionless Temperature-Time Relations During Liner Cooldown

This is a reasonable approximation because for practical penetrator/tunneler designs, it is a design goal to minimize the melt superheat and hence the penetrator surface temperature. For the 5 earth models described in Section 5.0, the melting temperature ranges are given in the following table. It is seen from the table that except for CALCI, the melting point of typical earth/rock materials occurs within a fairly narrow range.

TABLE 10-1

MELTING RANGES OF TYPICAL EARTH MODELS

Earth Model	Melting Range: Initial Temperature, °K	Melting Range: 90% Fusion
TUFF		1420
BASALT		1420
UNCON	1300	1500
SOSED	1300	1400
MASIG	1400	1500
FOLIA	1300	1450
CALCI	1673	1773

10.5.2 Maximum or Extreme End Use Temperature, T_{eu}

The maximum end use temperature of glasses is defined as the temperature that corresponds to a viscosity of 10^{15}. Complete data on the viscosity of glasses at or near this temperature are not available for the materials of interest in this study, i.e., tuff, basalt, and the five earth models. However, it is known that the viscosity of glasses tends to follow the Arrhenius relation, i.e.,

$$\mu = \mu_o \exp\left(\frac{\Delta E}{T}\right) \qquad (10\text{-}40)$$

Taking the logarithm of this equation yields the following:

$$\ln \mu = \ln \mu_o + \frac{\Delta E}{T} \qquad (10\text{-}41)$$

where ΔE is the activation energy.

If the logarithm of the viscosity is plotted versus 1/T, the data should yield a straight line. Data on the viscosities of various earth/rock materials plotted this way are shown in Figure 10-6. The data for Tuff and Basalt were obtained from Reference (10-5). The data for the five earth models were from Figures 5-7c to 5-7g. Except at the higher temperatures, greater than 1600°K, the data are well correlated by the Arrhenius relationship indicating that it can be used with confidence to extrapolate high temperature viscosity data to lower temperatures. The "maximum use" temperature calculated in this manner are tabulated below.

TABLE 10-2
CALCULATED MAXIMUM USE TEMPERATURE
OF VARIOUS EARTH/ROCK MATERIALS

Earth/Rock Material	μ_o Poise	ΔE	T at 10^{15} Poise, Maximum Use Temperature, °K
TUFF	5.89×10^{-7}	4.606×10^{4}	944
BASALT	8.974×10^{-6}	2.709×10^{4}	587
UNCON	3.251×10^{-5}	3.09×10^{4}	689
SOSED	8.81×10^{-6}	2.83×10^{4}	609
MASIG	6.92×10^{-5}	2.88×10^{4}	652
FOLIA	4.73×10^{-5}	2.76×10^{4}	620
CALCI	1.9×10^{-5}	2.65×10^{4}	583

There are no discrepancies between the melt temperatures and maximum use temperatures for the five earth models chosen for study from Tables 10-1 and 10-2.

10.5.3 Maximum Allowable Temperature Drop

The maximum allowable temperature drop across the liner for liner inner surface temperature below the maximum use temperature can be calculated from Equation (10-34), i.e.,

$$\Delta T_a = \frac{2 \sigma_a (1 - \nu)}{\alpha E} \qquad (10\text{-}42)$$

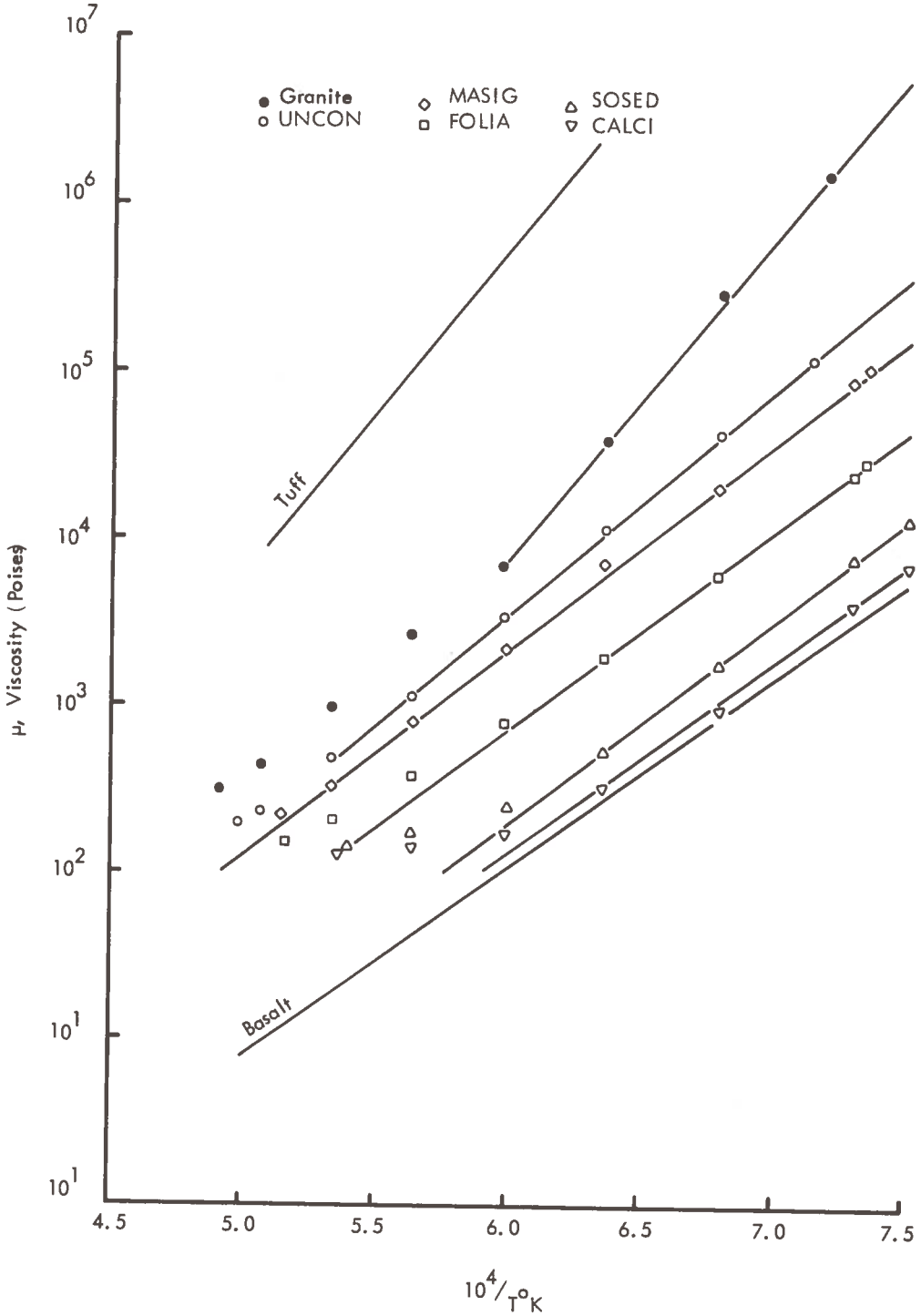

Figure 10-6. Viscosities of Various Earth/Rock Materials

However, the experimental physical properties needed to calculate this ΔT_{st} for the materials of interest are not available. Based on the given composition of the earth models, the physical properties α, σ_a, ν, and E can be estimated. Alternatively, ΔT values may be calculated from glasses that have known physical properties and are similar in composition to the glasses made from the earth models in question. Hutchins and Harrington[10-4] have presented calculated ΔTs for a large number of glasses, based on a design stress of 2000 psi. Moreover, a large number of physical and mechanical property data were given, but the properties available for the glasses of interest are the glass density and glass viscosity only. An attempt was made to match these properties to the published list of glasses. The results show that there are only a limited number of glasses that can match the two properties. These glasses and their corresponding earth models are presented in Table 10-3 along with some of the more pertinent properties. Again, there does not appear to be any significant difference among the thermal stress resistances of the first four models and an average value of 48°C may be used for scoping calculations.

10.5.4 Physical Properties

The cooldown time required to lower the glass liner inner surface to the maximum use temperature (T_{eu}) can be calculated from Equation (10-37) provided that heat flux and the liner thickness are specified and that the thermal conductivity and the thermal diffusivity of the glass material(s) are known.

For the earth models, these properties are specified only at the melting point. However, since it is assumed that

$$\frac{\phi_o \sqrt{\alpha}}{k}$$

is a constant, one can use the properties evaluated at the melting point in conjunction with the heat flux value selected. This is at least consistent with the manner in which the heat flux was calculated.

TABLE 10-3

COMPARISON OF EARTH MODELS AND GLASS PROPERTIES

Earth Model Specifications			Closest Glass & Properties						
Model	Glass Density g/cc	Temperature at 10^4 poise, °C	Glass Code	Density g/cc	Temperature at 10^4 poise, °C	Young's Modulus 5×10^6	Poisson's Ratio	Coefficient of Thermal Expansion $\times 10^6$ from 0-300° C	Thermal Stress Resistance °C
UNCON	2.3	1306	7740	2.23	1245	9.1	0.2	3.3	53
SOSED	2.3	1082	7040	2.24	1080	8.6	0.23	4.8	37
MASIG	2.5	1260	7760	2.23	1210	9.1	----	3.4	52
FOLIA	2.4	1166	7720	2.35	1140	9.1	0.2	3.6	49 (Avg= 48)
CALCI		1043	2475	2.59	1040	10.0	----	9 9.3	17
CALCI		1043	7056	2.29	1045	9.2	0.21	5.1	34

10.5.5 Liner Thickness Requirements

The liner thickness requirement is dependent on the glass parent earth material properties, specifically the earth Poisson ratio (υ), on the depth of the tunneling operation (Z) and on the diameter of the tunnel (D_t). The relation of these parameters can be determined from the maximum allowable depth of tunneling to preclude liner tensile failure with the condition of restrained lateral deformation (see Section 9.0). Therefore, given the earth Poisson ratio and the depth of tunneling desired, the minimum ratio of tunnel diameter to glass liner outside diameter can be determined from Figure 9-5. The Poisson ratios of the various earth models are given in Table 5-1.

The required glass liner thickness for various depths of tunneling and tunnel diameters are shown parametrically in Figures 10-7 to 10-10 for the four earth models.

10.5.6 Liner Cooldown Procedure

Based on the glass liner design constraints established in Section 10.4.1, a liner cooldown procedure can be devised to minimize the cooldown time and to minimize the length of controlled cooldown section required:

1. A rapid controlled initial cooldown from the liner molten state to a temperature range in which the glass liner can be self-supporting and have sufficient strength to allow thrusting on its wall. This range is defined as follows:

   Inner liner surface temperature must be decreased to a value equal to the maximum end use temperature (corresponding to a viscosity of 10^{15} poises).

2. Following the initial rapid cooldown, controlled cooldown is terminated. Slow, gradual liner cooldown then takes place by conduction losses to the ambient earth/rock characterized by:

   Inner liner surface becomes adiabatic by insulating potential heat sinks from the liner wall.

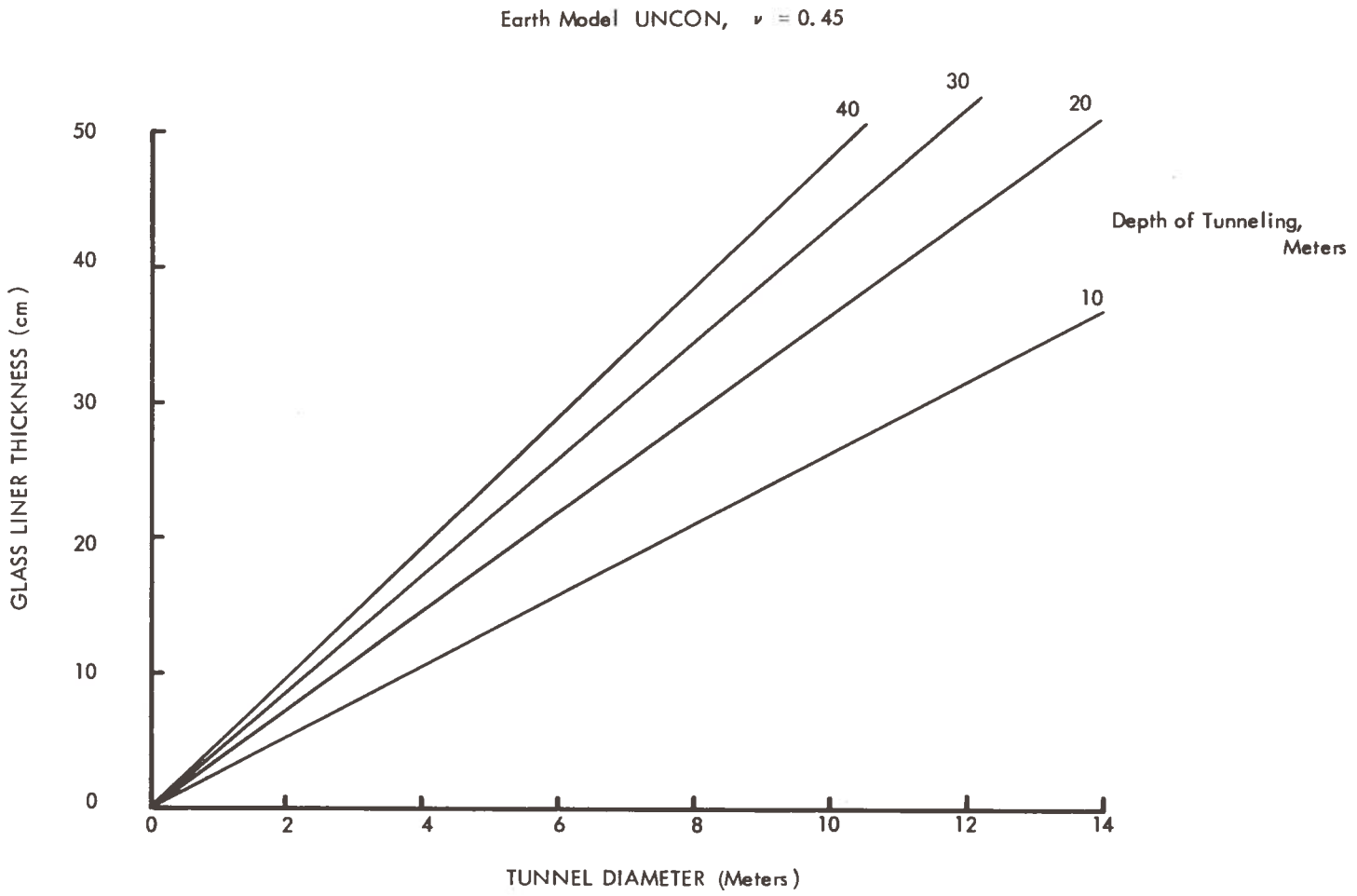

Figure 10-7. Glass Liner Thickness Requirements to Preclude Liner Tensile Failure with the Condition of Restrained Lateral Deformation

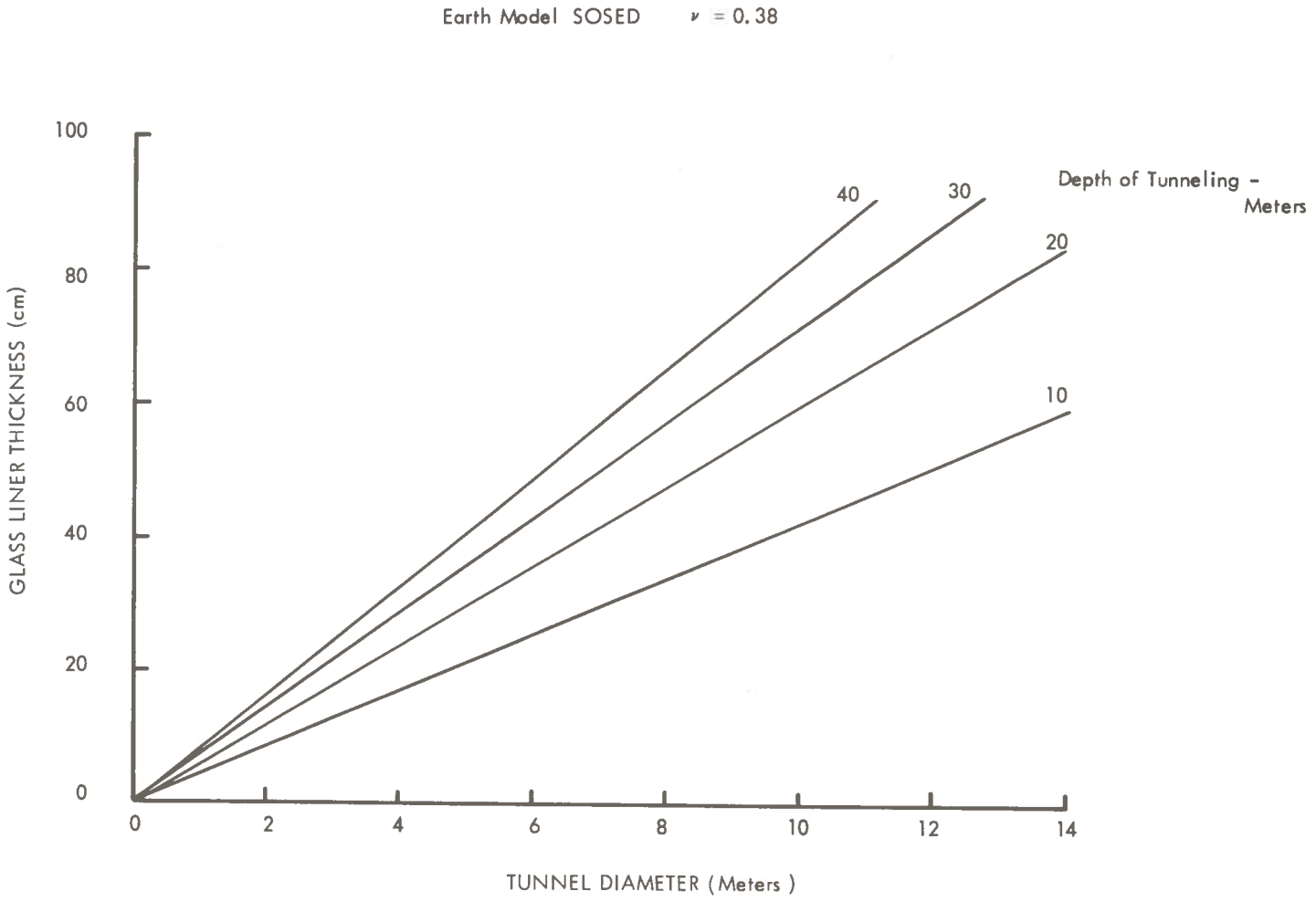

Figure 10-8. Glass Liner Thickness Requirements to Preclude Liner Tensile Failure with the Condition of Restrained Lateral Deformation

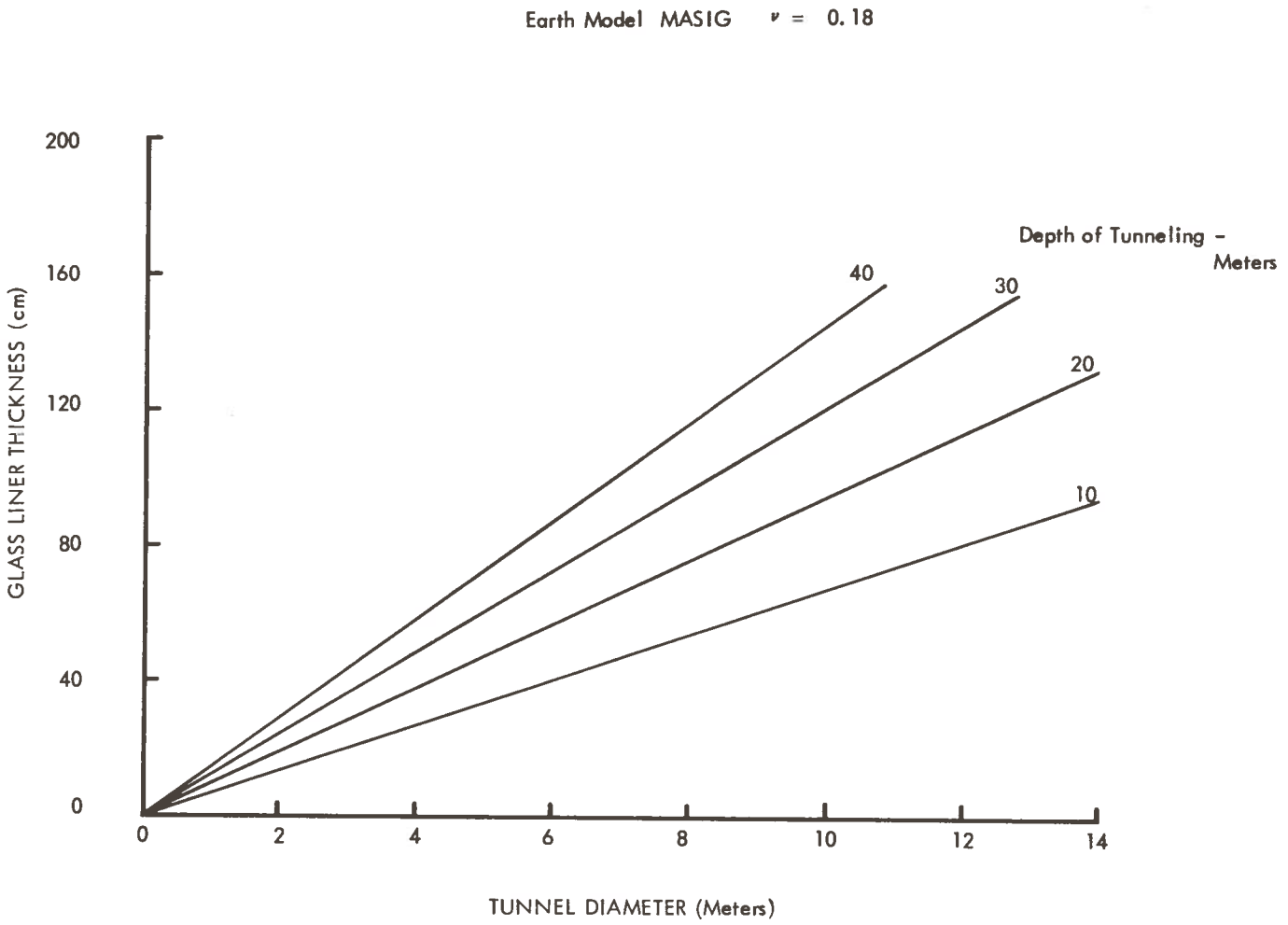

Figure 10-9. Glass Liner Thickness Requirements to Preclude Liner Tensile Failure with the Condition of Restrained Lateral Deformation

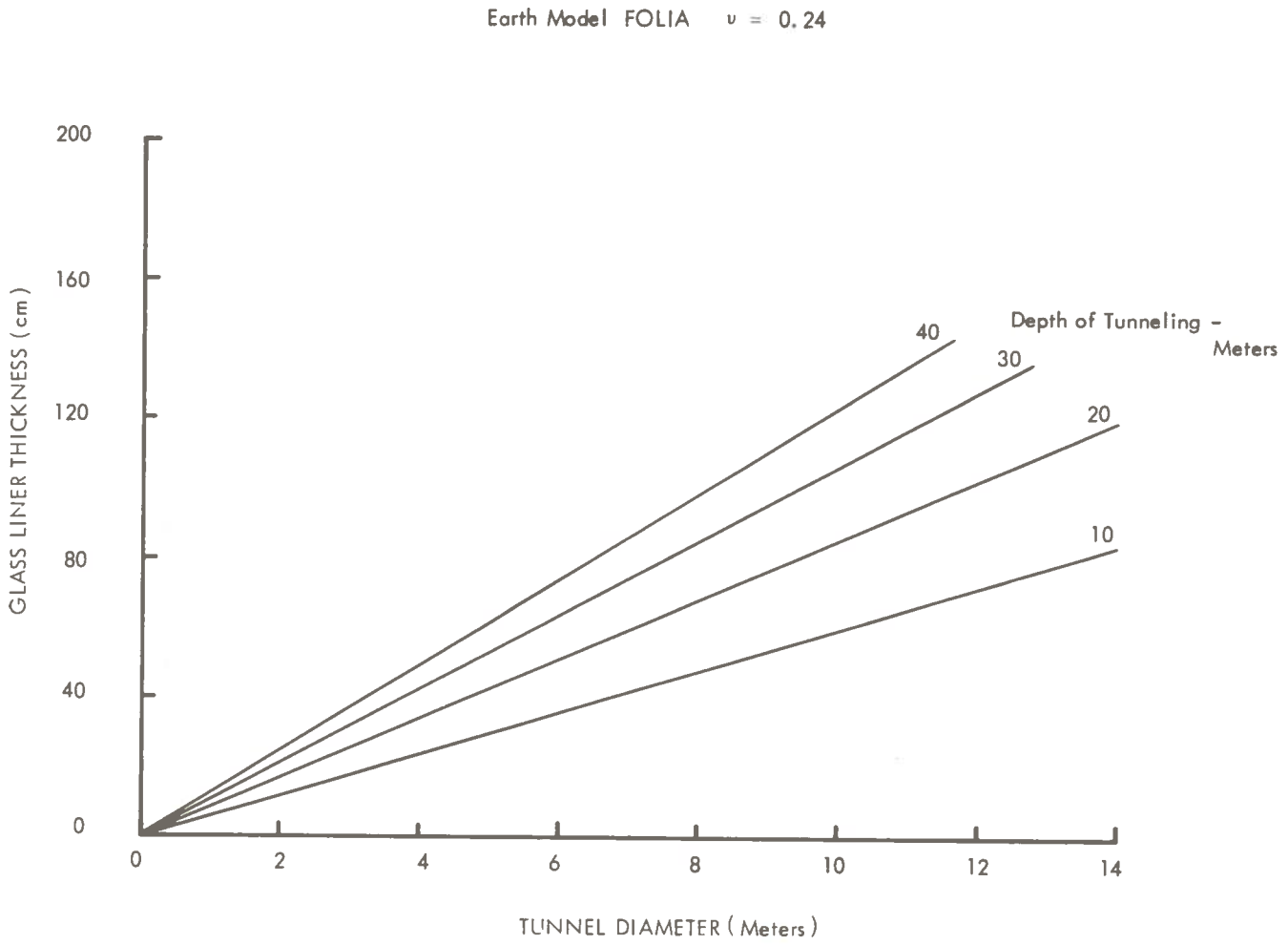

Figure 10-10. Glass Liner Thickness Requirements to Preclude Liner Tensile Failure with the Condition of Restrained Lateral Deformation

Inner liner surface temperature may or may not rise above the maximum end use temperature.

Temperature drop across the glass liner will not exceed the thermal stress limits when the liner temperature drops below the maximum end use temperature.

The transient liner temperatures under the above conditions are illustrated schematically in Figure 10-11. The liner cooldown time of interest is that required in the first step, because this determines the length of the controlled cooldown section required. Methods for evaluating the required cooldown time are discussed in the following section.

10.5.7 Controlled Liner Cooldown Time

The cooldown time required to lower the glass liner inner surface to the maximum use temperature can be calculated from Equation (10-12) if the heat flux is specified and if the thermal conductivity and the thermal diffusivity of the glass material are known. For the earth models, these properties are specified only at the melting point. However, since it is assumed in the derivation of the equation that

$$\frac{2\,\phi_o}{k} \qquad \sqrt{\frac{\alpha}{\pi}}$$

is a constant, the properties evaluated at the melting point can be used in conjunction with the heat flux value selected.

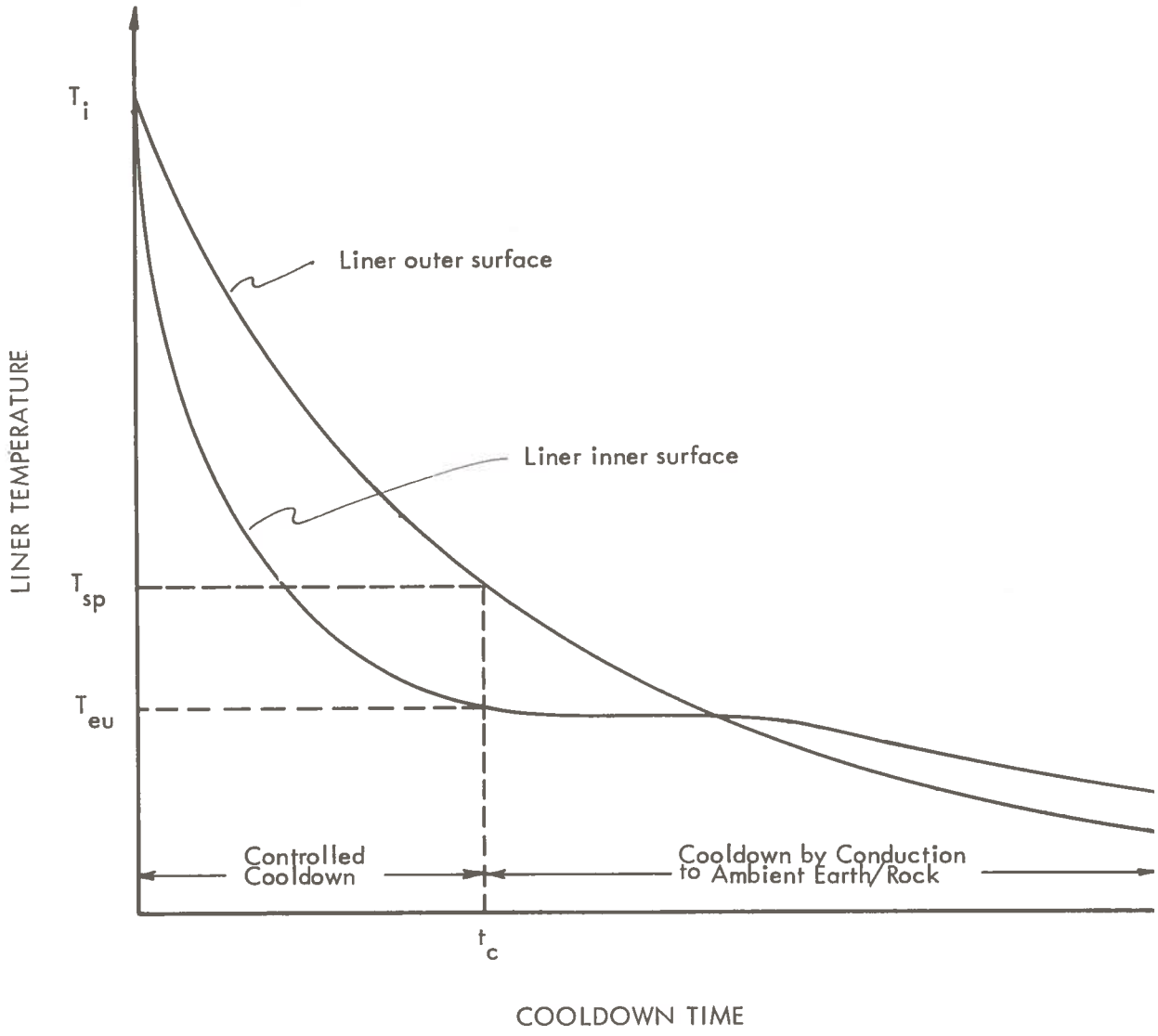

Figure 10-11. Schematic Liner Cooldown Temperatures Under Given Constraints

The cooldown time based on the inner liner end use temperature is therefore given by the equation

$$t = \frac{\pi}{4\alpha} \left[\frac{k}{\phi_o} \left(T_i - T_{eu} \right) \right]^2 \qquad (10\text{-}43)$$

Simultaneously, the liner outer surface temperature should not exceed that determined by the strain point defined as the temperature corresponding to $10^{13.5}$ poise. The equation developed from model 2 is expected to give a more realistic value. From Equation (10-21),

$$T_i - T_{sp} = \frac{\phi_o \sqrt{4\alpha t}}{k} \sum_{n=0}^{\infty} 2 \, \text{ierfc} \frac{(2n+1)\delta}{\sqrt{4\alpha t}} \qquad (10\text{-}44)$$

where T_{sp} denotes the strain point, evaluated at $10^{13.5}$ poise.

Equation (10-43) can be rewritten in the form

$$\sqrt{4\alpha t} = \sqrt{\pi} \frac{k}{\phi_o} \left(T_i - T_{eu} \right)$$

Rewriting Equation (10-43) in terms of the variable ψ, we have

$$\frac{\phi_o}{k} = \frac{T_i - T_{sp}}{\psi \sqrt{4\alpha t}} \qquad (10\text{-}46)$$

Eliminating $\frac{\phi_o}{k}$ from these two equations,

$$\psi = \frac{1}{\sqrt{\pi}} \frac{(T_i - T_{sp})}{(T_i - T_{eu})} \qquad (10\text{-}47)$$

This equation states that when T_{sp} and T_{eu} are specified, ψ becomes fixed, since

$$\psi = \sum_{n=0}^{\infty} 2 \text{ ierfc} [(2n + 1) \xi] \qquad (10\text{-}48)$$

and

$$\xi = \frac{\delta}{\sqrt{4 \alpha t}} \qquad (10\text{-}49)$$

is fixed.

The procedure to evaluate the cooldown time is as follows:

1. Given an earth model with its viscosity over a range of temperature, T_{eu} and T_{sp} can be determined.
2. Calculate ψ.
3. Determine graphically the corresponding value of ξ from Figure 10-5.
4. For the given earth model, evaluate α at the melting point.
5. The cooldown time can now be determined from Equation (10-49) for any given liner thickness δ.

Values of ψ and ξ determined for various earth/rock materials are presented in Table 10-4. For all of the materials selected for calculations, there are negligible differences among the values of ψ and ξ. Consequently, for further illustrations, a value of ψ of 0.515 and ξ of 0.44 are used for all of the earth/rock materials. The cooldown time is then a function of the liner thickness and the thermal diffusivity of the glass.

$$t_c = \frac{1.29 \delta^2}{\alpha} \qquad (10\text{-}50)$$

TABLE 10-4

VALUES OF ψ AND ξ FOR VARIOUS EARTH/ROCK MATERIALS

Earth Model	T_i, °K or at 90% Fusion	T_{eu}, °K	T_{sp}, °K	ψ	ξ	$T_i - T_{sp}$
Tuff	1420	944	1014	0.481	0.46	406
Basalt	1420	587	734	0.520	0.43	786
UNCON	1500	689	746	0.512	0.44	754
SOSED	1400	609	661	0.515	0.44	739
MASIG	1500	652	708	0.515	0.44	792
FOLIA	1450	620	672	0.517	0.43	778
CALCI	1773	583	631	0.530	0.42	1142

The cooldown times calculated by this equation for the various earth models are presented in Figure 10-12. It is obvious that for reasonable thickness of glass liners, the cooldown times required are excessive. It is pointed out that these cooldown times should be termed the maximum theoretical cooldown times because

1. Heat losses to earth/rock have been neglected in the rapid cooldown phase.
2. Constraint on the liner outer surface temperature ($10^{13.5}$ poise) is relatively stringent.

This constraint gives a liner temperature drop of ($T_{sp} - T_{eu}$) that is only slightly greater than that permitted by the thermal stress criterion. (See Table 10-4). Hence, a more realistic theoretical cooldown time may be evaluated by relaxing this constraint.

The first factor is expected to be particularly conservative when relatively long cooldown times are predicted, because under these conditions, the heat fluxes from the liner inner surface must be low and heat losses to earth/rock may become dominant. In order to estimate the effect of heat losses to ambient earth/rock, the equations developed in Model 6 Equation (10-31) may be used. At the liner inner surface, Equation (10-31) reduces to:

$$\frac{T_s - T_\infty}{T_i - T_\infty} = 1 - \frac{1+\lambda}{2} \sum_{n=0}^{\infty} 2\lambda^n \operatorname{erfc}\left[(2n+1)\xi\right] \qquad (10\text{-}51)$$

For the liner outer surface temperature (T_δ), Equation (10-31) reduces to

$$\frac{T_\delta - T_\infty}{T_i - T_\infty} = 1 - \frac{1+\lambda}{2} \sum_{n=0}^{\infty} \lambda^n \left\{\operatorname{erfc}(2n\xi) + \operatorname{erfc}\left[(2n+2)\xi\right]\right\} \qquad (10\text{-}52)$$

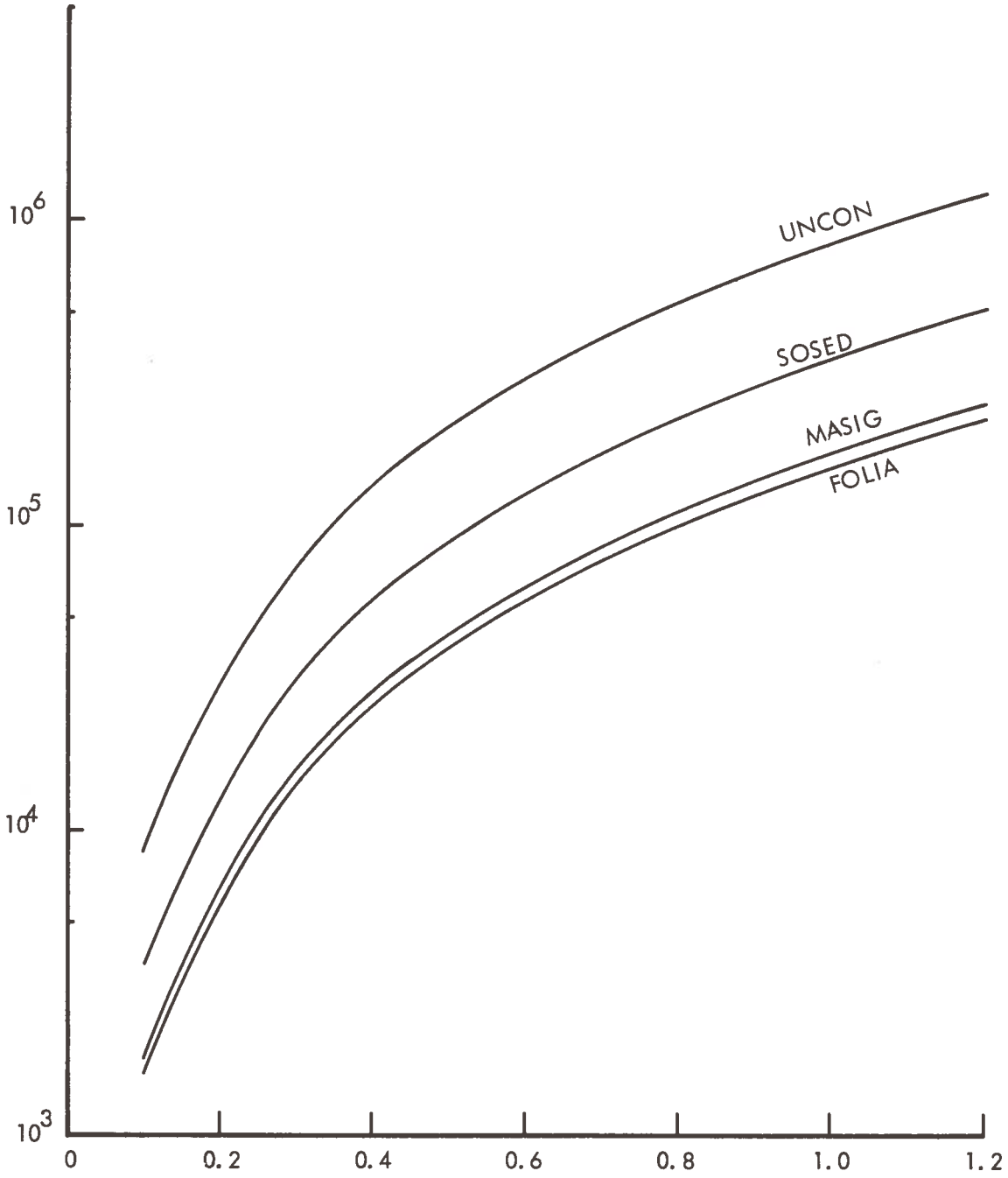

Figure 10-12. Maximum Liner Cooldown Times

The region of primary interest is around unity, as this minimizes the cooldown time for the relatively thick glass liners required for large tunnels. In the region of $0.4 < \xi < 1.0$, Equations (10-51) and (10-52), for all practical purposes, can be reduced to the following (because the complementary error function decreases rapidly with values of the argument when the argument is on the order of unity):

$$\frac{T_s - T_\infty}{T_i - T_\infty} = 1 - (1 + \lambda)\,\mathrm{erfc}(\xi) \qquad (10\text{-}53)$$

$$\frac{T_\delta - T_\infty}{T_i - T_\infty} = 1 - \frac{1 + \lambda}{2}\left[1 + \mathrm{erfc}(\xi)\right] \qquad (10\text{-}54)$$

Using earth model UNCON as a typical example and by assuming that $k_g \approx k_e$, λ, evaluated from Equation (10-32) is 0.123. By setting $T_i = 1500^\circ K$ and $T_\infty = 300^\circ K$, $T_i - T_s$ and $T_i - T_\delta$ can be calculated for specified values of ξ. For $\xi = 0.44$, it can be shown that by conduction heat loss to earth/rock alone, the inner surface can be cooled down to $692^\circ K$ while the outer surface is cooled down to $468^\circ K$. These may be compared with the temperatures attained at the end of the same cooldown time when only forced convective cooling is considered. In this case, the corresponding temperatures are $689^\circ K$ and $746^\circ K$. The reversed temperature drop is due to the different liner cooling methods. Clearly, these temperatures are of the same order of magnitude, suggesting that liner cooldown by conduction losses cannot be neglected. For a more realistic approximation, the cooldown times presented in Figure 10-12 should be reduced by at least a factor of 2 to account for heat loss on both sides of the liner. It should be noted that the liner temperature drop calculated on conduction losses to rock is quite moderate, i.e., only $224^\circ C$.

Since cooldown by conduction to earth/rock is shown to decrease the liner temperature somewhat faster than by forced convection alone, the cooldown time was recalculated based on the conduction heat loss equations and on the constraint that the liner outer surface temperature need to be cooled only to the maximum end use temperature. The resultant cooldown times were then reduced by a factor of 2. These results are presented in Figure 10-13. It is believed that these values should be quite realistic.

For a more accurate determination of cooldown times, more detailed and complex analyses will be needed. However, for parametric analyses and conceptual design calculations, the order of magnitude estimates provided by the theoretical models should be satisfactory.

10.5.8. Theoretical Heat Flux

It is evident that relatively long cooldown times such as those calculated here may require relatively low heat fluxes on the liner inner surface. It is important to know the magnitude of this heat flux in order to ascertain whether they are realistic. For a typical numerical example, earth model UNCON was used. At a ψ value of 0.515 and ξ value of 0.44, $T_i - T_{sp}$ of 754°C, Equation (10-46) yields

$$\phi_o = \frac{2.57}{\delta} \qquad (10\text{-}55)$$

Typical liner thicknesses required for 30 foot tunnels may range between 0.4 to 1.2 meters. In this range, the corresponding heat flux ranges between 6.42 watts/cm^2 to 2.14 watts/cm^2. The lower end of these values is compatible to the experimental value of 1.62 watts/cm^2 determined for a 75 mm consolidating penetrator operating in tuff. Since the calculated heat fluxes are higher than the experimental value, it can be concluded that forced convective cooling of the inner surface will be necessary in addition to inherent thermal radiation.

10.5.9 Theoretical Lengths of Controlled Cooldown Section

The theoretical length of controlled cooldown section required is an important

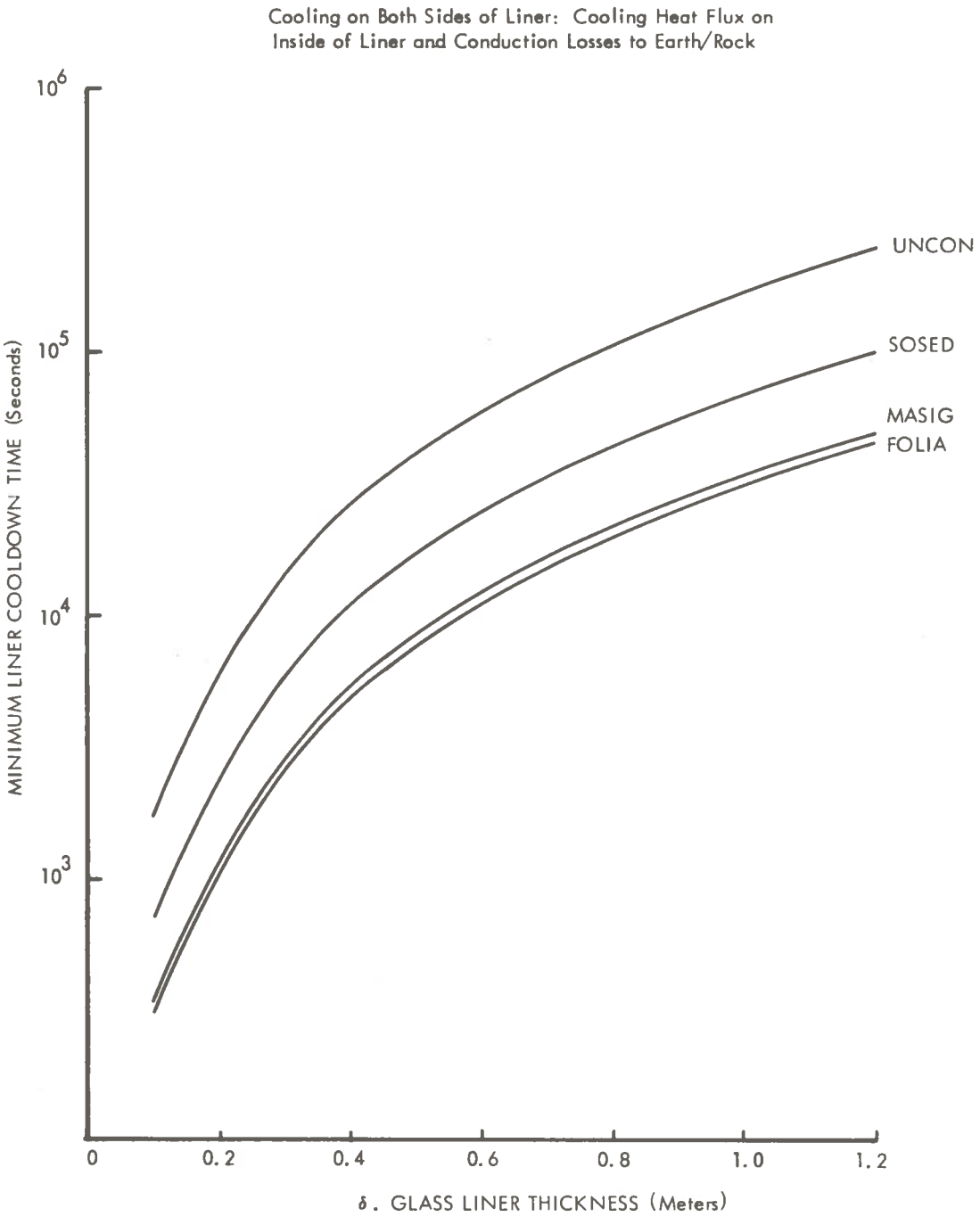

Figure 10-13. Liner Cooldown Times

parameter, for it determines the length beyond which forces can be applied to the glass wall to thrust the penetrator forward. The controlled cooldown length required can now be calculated from the cooldown times shown in Figure 10-13 by use of Equation (10-35).

$$L_c = U_\infty t_c \qquad (10\text{-}56)$$

The results of the calculation are summarized in Figure 10-14. For actual lengths, the theoretical values may be reduced by a factor of 2. It is apparent from this figure that the predicted controlled cooldown sections are relatively large for tunnel diameters (hence liner thicknesses) of interest in transportation tunnels. This is primarily due to the relatively poor thermal conductivity of glasses and the parent earth/rock materials.

10.6 CONCLUSIONS AND RECOMMENDATIONS

Based on the results of the analysis in this section, cooldown times and required length of controlled cooldown section can be estimated by the functional relations developed. Scoping calculations have shown that under conditions of interest to practical tunneling applicaations, the required lengths of controlled cooldown sections are excessive. This length establishes the distance beyond which forces can be applied to the glass wall to thrust the penetrator forward. For practical penetrator designs, the L/D ratio of the penetrator should be minimized for two reasons:

1. To minimize frictional drag, and
2. To minimize cost of construction

It is obvious that cooldown times and the length of the controlled cooldown section can be reduced only if the effective thermal conductivity of the glass liner can be increased. There are two potential means of achieving this. They are the following:

1. Implanting coolant tubes in the molten glass liner.
2. Seeding the melt with a material that will enhance thermal radiation and/or conductivity as well as improve the strength of the glass liner.

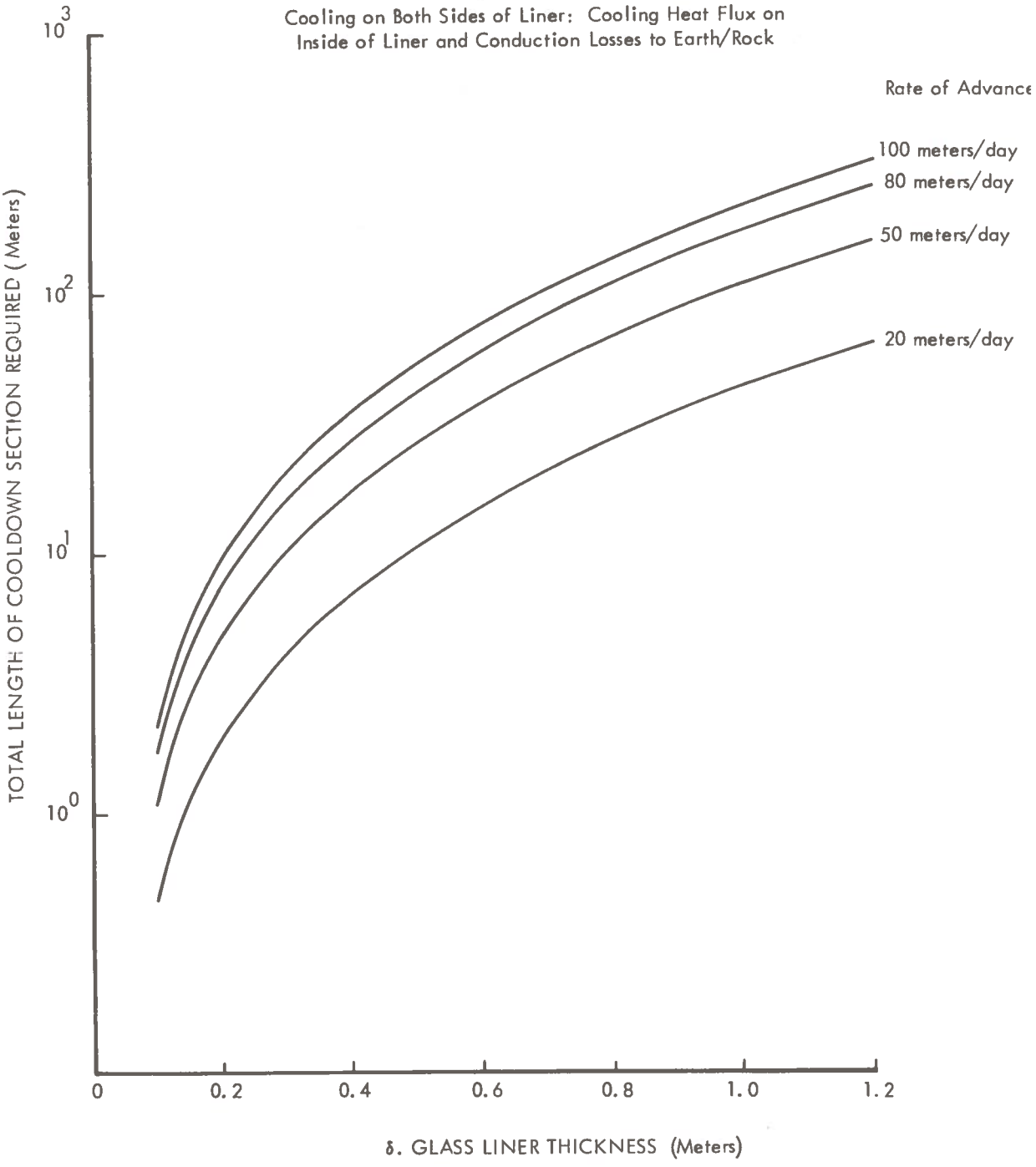

Figure 10-14. Length of Controlled Cooldown Section for Earth Model UNCON

The first method consists of implanting small diameter hollow tubes in the melt to reduce conduction path length and to accelerate cooldown. Coolant can be pumped through the tubes in a once-through process. Technically, there does not appear to be any reason why this method would not be feasible. This technique is particularly suitable to the advanced penetrator concept discussed in Section 11.0. The capabilities and limitations of this technique for reducing cooldown time can only be established by careful design analyses.

It has been established that a large contribution to heat transfer through the molten and solidified glass is due to thermal radiation. It is known that thermal radiation is affected significantly by the type of constituent materials present in the glass. However, how these materials affect the thermal radiation properties is not well understood. It is speculated that there may be certain constituent materials that can increase the strength of glass while simultaneously increasing the effective thermal conductivity. If such materials can be found and identified, it may be possible to seed the melt with such materials to permit reduced cooldown time and simultaneously increase the strength of glass. To establish the feasibility of this concept for reducing cooldown time, a thorough understanding of the thermal transport behavior of glass and its parent earth/rock material will be needed.

10.7 REFERENCES

10-1 Williams, R. E., "Development and Construction of a Modularized Mobile Rock Melting Subterrene Demonstration Unit," LA-5209-MS, March, 1973.

10-2 Churchill, R. V., Operational Mathematics, McGraw-Hill Book Co., Second Edition (1958), pp. 131-132.

10-3 Carslaw and Jaeger, Conduction of Heat in Solids, Oxford at Clarendon Press, Second Edition,

10-4 Hutchins, J. R., and R. V. Harrington, "Glass," Encyclopedia of Chemical Technology, Vol. 10, (1966), p. 581.

10-5 Gido, R., "Fifty Foot Hole Data," LASL Memo S-39, February 28, 1972.

10-6 Birch, F., Ed., "Handbook of Physical Constants," Geol. Soc. of Amer., Special Paper No. 36, January 31, 1942.

11.0 DESIGN CONSIDERATIONS

11.1 INTRODUCTION

One of the four principle objectives of this study was the identification of controlling variables and establishment of possible limits on the physical process. The analytical studies performed in this program and discussed in Sections 4.0 through 10.0 have resulted in identification of the controlling variables and obtaining a number of significant conclusions that directly affect the capability of application of this concept for large scale transportation tunneling. Most of the identified limits are relative to design constraints. There are design approaches which may be taken to accommodate most limits that could otherwise restrict desired performance.

The major conclusions of this category which affect design are noted in the following:

- The thermal power requirements and thrust levels are within practical limits for reasonable rates of advancement. (Power levels of < 50 MW(t) for full size tunnels at desired rates of advancing).
- Heat transfer limitations due to low thermal conductivity in the melt imposes requirements for excessive penetrator surface temperatures and melt superheats at desired advance rates if the melt thickness becomes significant. Melt thickness must be restricted to less than 0.5 to 1 cm for attractive advancing rates.
- Relatively thick glass liners are required, many times thicker than the permissible melt thickness if the structural support is desired (5 to 10% of the radius).
- Glass liner cooldown rates permit fast chilldown to $\sim 10^{13}$ to 10^{15} poise, but significant annealing times may be required. Because of this the required length of controlled liner cooldown section becomes excessive. However, liner designs with cracks and cooldown system designs are conceived that circumvent this restriction.

- Melt pressures and penetrator loads are relatively low and reasonable (thrust loads of $\sim 10^3$ ton for 10 m tunnel); however, local point loads and stresses may be limiting.
- Tunnel depth for non-surface disruption is of the order of one tunnel diameter, crown to surface.

These conclusions have resulted in some serious limitations in scaling up LASL's currently demonstrated hardware capabilities to the proposed concept for transportation tunneling and have posed difficult design problems. However, the problems identified have led to a number of potential solutions and design concepts that extend the capabilities of the basic concept to conditions suitable for transportation tunneling. The basic problems involved, proposed design solutions and approaches are presented and discussed in this chapter. Areas where further study and development are needed are indicated. Other areas that must be considered when designing a Subterrene type penetrator system for transportation tunneling are also discussed.

11.2 THERMAL POWER AND HEAT SOURCE

The total thermal power requirement must be estimated in order to evaluate and select a heat source for a Subterrene tunneler. The controlling variables that affect the melt power requirement and heat losses to earth/rock are well understood as a result of successful correlations of experimental and calculated data by the functional relations developed and presented in the previous section. However, for any application, it would be desirable to minimize the thermc power requirement. This section discusses factors that affect the total thermal power requirement and potential means for minimizing the total power. Considerations necessary to the selection of a heat source are also discussed. The effect of heat source geometry on the therm power is discussed in Section 11.3.

Stem Losses

It is recognized that stem losses cannot be avoided in penetrator designs because the heated portion of the penetrator must be supported by the stem to permit thrusting of the penetrator and to prevent downward drift of the penetrator (as a result of gravitational

forces). To provide this support, high strength materials and relatively large cross sections must be used. High strength materials tend to have relatively high thermal conductivities. For these reasons, stem losses are unavoidable although they may be minimized by judicious design.

Based on the experimental data obtained from the small scale penetrators, stem losses appear to be a significant fraction of the total power requirement, ranging between 40 and 60%. Stem loss data are presented in Figure 11-1 where experimental and calculated stem losses are compared. The stem losses for the 75 mm conical penetrator were calculated by correlation of the data as discussed in Section 7.0. The general trends with respect to the rate of penetration for both the experimental and calculated stem losses are identical. This gives confidence to the following conclusion. Stem losses (as a percentage of the total power required) decrease with increasing rates of penetration and increasing size of penetrator for a given penetrator design. This may or may not be the case for other penetrator designs. Detailed analyses are needed for a given penetrator design to determine the stem losses.

Control of Melting Point

From the functional relations developed in Section 6.0 for thermal power, it can be seen that sensible heat of the earth/rock (from the initial temperature up to the melting point) is the dominant contribution to the total thermal power. It becomes apparent that if the earth/rock melting point temperature can be reduced, then the thermal power requirement can be reduced correspondingly. This may be possible by the introduction of a fluxing material into the melt. In addition to the reduction of melt power, a lower melting point would also reduce the liner cooldown time and permit a thicker melt layer. The potential use of such a material is a function of the type of earth/rock through which tunneling takes place, and the economic trade-offs involved in the use of a fluxing material.

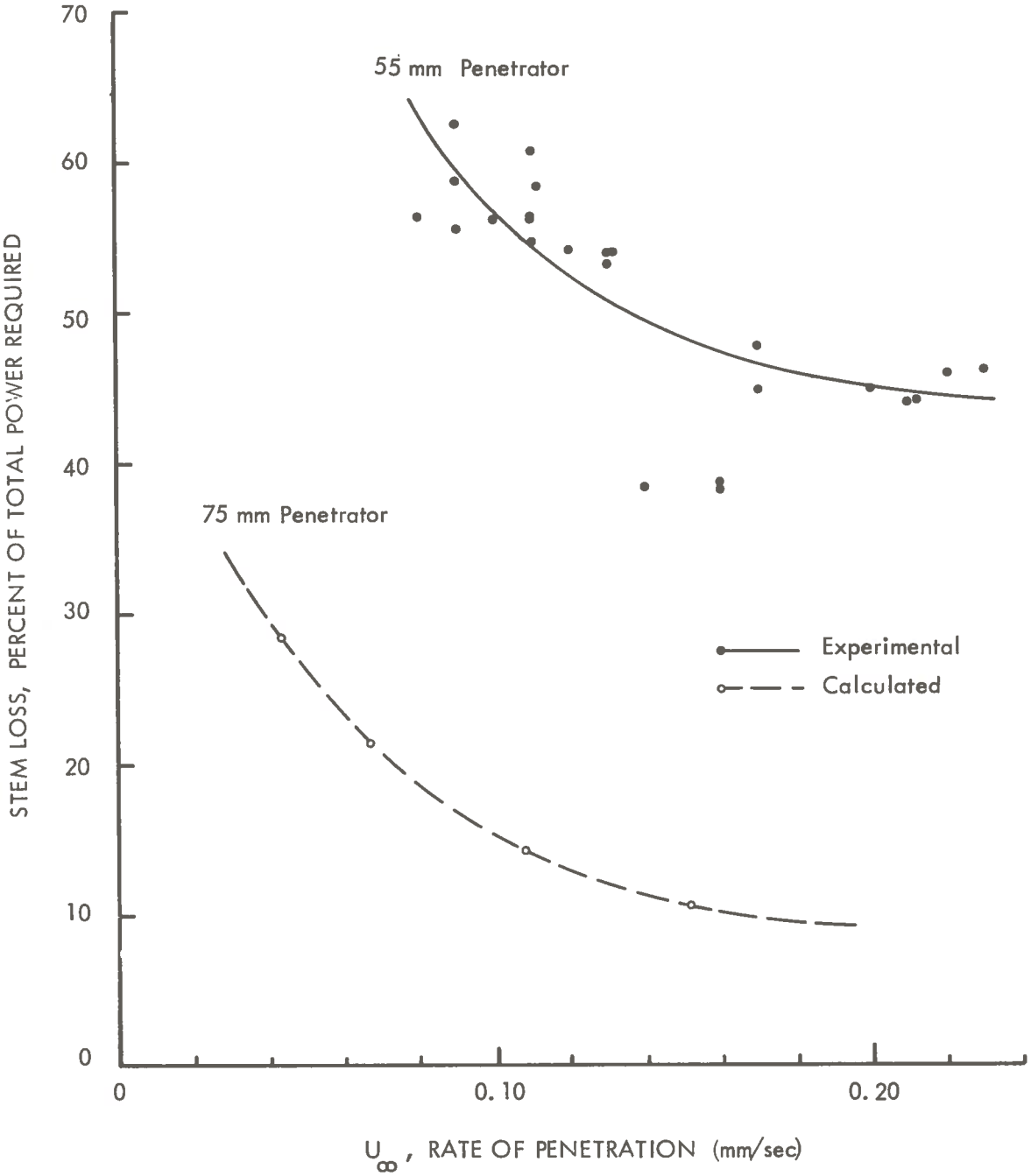

Figure 11-1. Effect of Rate of Penetration and Size of Penetrator on Stem Losses Conical Consolidators in Dried Tuff

For a given type of earth/rock, potential fluxing materials must be identified and compared Means of transporting and injecting the material into the melt must be developed. Finally, economics must determine whether fluxing materials should be used. Ideally, it would be highly desirable to select a single fluxing material:

- Reduce the melting point of earth/rock.
- Reduce the latent heat of fusion.
- Reduce the effective specific heat of the melt.
- Increase the effective thermal conductivity of the melt and the resultant glass.
- Increase the strength of the resultant glass.
- Increase the density of the resultant glass.

Heat Source Selection

The selection of a heat source for a given tunneler design depends on the amount of thermal power required and on the economics of alternate possibilities. A fossil fueled heat source can be considered for thermal power requirements as high as 50 megawatts. A nuclear powered heat source may be considered for power requirements as low as 10 megawatts. For really large power requirements, ~100 megawatts or more, only nuclear power can be seriously considered.

n addition to costs considerations, the effect of a given heat source on the design of the sub-errene must be carefully evaluated. If a fossil fueled system were considered, then a number of heat transport methods can be compared and evaluated. These include combustion and direct heating through radiation, and indirect heating through the use of heat pipes or a orced convective loop. A nuclear heat source would permit only indirect heating either hrough the use of heat pipes or a forced convective loop.

here does not appear to be any problem involved in the selection of a heat source; trade-off nd economic analyses will determine the logical heat source choice. If it is determined nat for a given application, the use of nuclear heat source should be avoided, then means ıust be sought to minimize the total thermal power requirement. Potential methods are dis-ussed in other sections of this chapter.

11.3 HEAT TRANSFER

The shape of the penetrator heat transfer surface is highly important in the design of a penetrator. It can affect a number of important design parameters.

- Amount of surface area available for heat transfer and local thermal loads
- Applied thrust loads
- Capability for tunneling through non-homogeneous media

The amount of surface area is key to the heat flux constraints and affects the melt pressure, the stress on the penetrator surface, and the maximum penetrator surface temperature. The melt pressure can determine whether surface upheaval will occur, while the last two determine the limit on the rate of penetration or the size of the tunnel that can be considered.

The selection of a penetrator shape considers a number of design factors, including:

- Size and shape of tunnel desired
- Earth/rock material through which tunneling is to take place
- Rate of penetration desired
- Glass liner thickness requirements

The size of the tunnel and the type of earth/rock material dictate selection of the mode of tunneling. For relatively large tunnels, a coring penetration is required for practical levels of thermal power and rate of penetration.

As an illustration of the power requirement, a 6 meter tunnel diameter with a 5 meter core and 0.5 meter glass liner may require 30 megawatts of power. If a full melting consolidator were used instead, the thermal power requirement would be doubled. While this increase in thermal power is not excessive for a 6 meter tunnel diameter, the difference would be much greater for larger tunnels, and the reduction in the rate of penetration would be more severe.

For the large tunnels of interest in transportation tunneling, back extrusion of the melt is a necessity for fully consolidated earth/rock materials. It may also be necessary for unconsolidated earth/rock materials, if the tunnel-to-core diameter is relatively large, or if the liner cross-sectional area required is relatively small compared to the cross-sectional area of earth/rock melted.

When back extrusion is included in the penetrator design, the melt thickness can be controlled (reduced) to allow maximization of the rate of penetration. Back extrusion requirements introduce considerable complexity into the penetrator design. Means for extrudate transport, cooldown, and handling must be provided.

Two basic design approaches are permitted for minimizing melt thickness for increased penetration rates; (1) a long conical penetrator, and (2) an extended surface penetrator. A long, thin conical penetrator shape would provide the necessary heated surface area and relatively thin layer of melt for relatively high rates of penetration. However, there are a number of problems involved in such a concept which include

- Excessive frictional drag
- Transporting and distributing the heat from a heat source to the penetrator surface
- Tunneling through non-homogeneous media

Solutions to the last two problems may be found by judicious engineering design. The frictional drag problem requires comparative analyses and trade-off studies.

The second approach utilizes a segmented, finned heater approach. The long, conical penetrator would encounter serious problems when tunneling through non-homogeneous materials. On the otherhand, a segmented heater would be considerably more complex.

One problem common to both is the frictional drag effect. Although frictional drag from melt flow over the heated portion of the penetrator has been shown to be

negligible for the relatively small penetrators that have been experimentally tested, this is not expected to be true for penetrator designs with extended surfaces. As a consequence, detailed design analyses and trade-offs are needed to produce an optimum design and optimum operating conditions.

Other design considerations include the effect of surface area on extrusion requirements. It is evident that for each heater "segment" or finned heater, a finite segment thickness must be provided in practical designs. This is necessary for the accommodation of heat transfer media such as heat pipes. For a given tunnel diameter and glass liner thickness, the required segment thickness imposes a limit on the total heater surface area allowed and this in turn limits the rate of penetration. This limit can be extended by back extruding a part of the melt, preferably with extrusion distributed along the length of the heated portions of the penetrator.

Tunneling Through Non-Homogeneous Materials

Under typical tunneling conditions, non-homogeneous materials including water, gas pockets, etc., are expected to be encountered. Such conditions will cause appreciably different local thermal environments and local thermal power requirements in the penetrator. As a result, tunneling rates can be reduced sharply and hot spots and thermal stress problems can be severe. In order to solve this problem, a penetrator must be designed to meet the following conditions:

- Variable environmental (earth/rock) temperature.
- Variable environmental (earth/rock) thermal resistance to heat transfer from the penetrator surface.
- Variable thermal power demand by the environmental earth/rock.
- Isothermal penetrator heater temperature.

It is evident that conventional penetrator designs considered in this study cannot meet these requirements. An obvious approach to this problem is the use of segmented heaters. With this approach, thermal power to the various heater segments can be varied separately to

meet changing thermal demands. Variable thermal power demands can be accommodated. Two potential methods involve the use of heat pipes. The first method incorporates inert gas controlled heat pipes in conjunction with temperature sensors and active input power control, while the second method utilizes a new type of heat pipe, called an "Isothermal Condenser, Variable Power Heat Pipe". This heat pipe was conceived specifically to solve the problem at hand.

The first method is a conventional, active control system while the latter is a passive, self-regulating control system. The latter concept consists of a heat pipe that incorporates a liquid (such as a liquid metal) enclosed within a bellows at the condenser end for thermal control rather than the conventional inert gas system. A combination of using a liquid enclosed in a bellows gives the heat pipe unique thermal control properties that meet all of the requirements listed above.

A schematic diagram of the proposed "Isothermal Condenser, Variable Power Heat Pipes" is presented in Figure .11-2 which also illustrates the principle of operation. In this invention, the control fluid is stored and enclosed in a reservoir made of bellows. In this manner, the control fluid is completely separated from the heat pipe working fluid. The condenser leg is imbedded in a block of material or component such as the segmented heater fins of a penetrator whose temperature it is desired to keep relatively constant. Heat is therefore transferred from the heat pipe condenser leg through this block of material to the earth/rock which can be any of a number of possible environments such as ambient air, water or solid materials. If the temperature or the thermal resistance of the environment changes, the heat pipe condenser temperature can be maintained relatively constant because the volume of the bellows will automatically adjust to compensate for changing thermal demands and thermal resistances.

Figure 11-2.a depicts a reference operating condition where a power output Q_1 is needed to maintain the heat block temperature at T_1. The condenser temperature is at T_{c1} which is

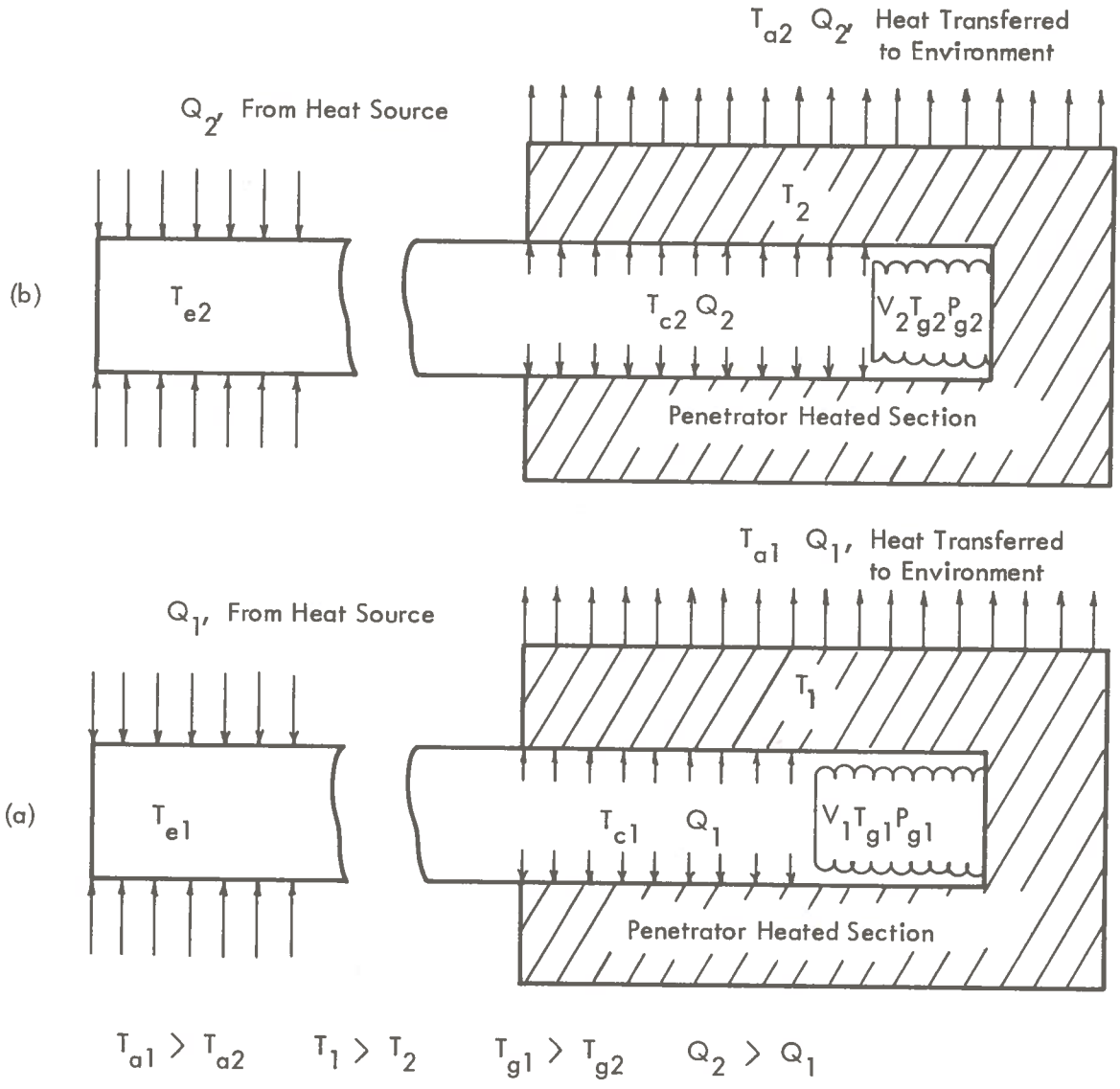

Figure 11-2. Operating Conditions of Proposed Liquid Controlled Heat Pipes

identical to T_{g1}, since the bellows is surrounded by the high thermal conductivity heat block. The thermal power Q_1 is then transferred from the heat block to the environment by conduction, convection, or radiation. Figure 11-2.b illustrates the condition when the heat receiver temperature drops below the reference condition, i.e., $T_{a2} << T_{a1}$. A slight drop in the condenser and bellows temperature causes the vapor pressure and volume in the bellows to decrease appreciably, thereby exposing a greater portion of the condenser leg to the heat pipe working fluid. A greater amount of heat is therefore transferred to and through the heat block. Conversely, if the heat receiver temperature increases or thermal resistance decreases, T_c and T_g would become slightly greater than the reference condition (T_{c1}, T_{g1}). This results in an expansion of the bellows and a reduction in heat pipe condenser area. The pressure difference between the bellows and the heat pipe condenser ($P_g - P_e$) controls the volume of the bellows. Let L_b be the length of the bellows. It may be assumed that the net force on the bellows surface area between the bellows and the condenser is proportional to the length of the bellows:

$$A\ (P_g - P_e) = k L_b \qquad (11\text{-}1)$$

or

$$A^2\ (P_g - P_e) = k V \qquad (11\text{-}2)$$

where k is a proportionality constant, and V is the volume of the bellows. From Equation (11-2), it can be readily shown that

$$V_2 = V_1 \left(\frac{P_{g2} - P_{g1}}{P_{g1} - P_e} \right) \qquad (11\text{-}3)$$

P_e, the pressure in the heat pipe, is determined by the evaporator and heat source temperatures; it is relatively unaffected by changes in the condenser temperature. P_g is determined by the vapor pressure of the fluid in the bellows and hence the temperature of the fluid in the bellows. The fluid which is selected for use is one in which the vapor pressure changes appreciably with slight changes in the temperature.

It is evident from the above discussions that the proposed heat pipes are useful whenever it is desired to maintain a component at a relatively constant temperature while ambient or heat sink temperature, thermal resistance and heat sink power demands can vary appreciably. The heat source, connected to the evaporator end of the heat pipe, can be of any type, i.e., electrical, chemical, or nuclear.

11.4 GLASS LINER CAPABILITIES

One of the attractive features of the rock melting technique for tunnel excavation is the potential for generating a self-supporting glass liner. Other capabilities that the liner should possess in order to make this potential possible are

- Capability for earth containment
- Capability to provide penetrator support, and
- Capability to provide penetrator thrust

All of these capabilities are dependent on the integrity of the glass liner. Its integrity in turn depends on the earth/rock material and environment, the thickness of the glass liner, the mechanical and physical properties of the glass formed and the liner geometry. These and other factors are discussed in this section.

Glass Liner Thickness

The liners formed from and cooled within most earth media are expected to experience stress relief cracking during the cooldown period. The medium of exception is characterized by plastic behavior approximated by very porous, water-saturated, loosely consolidated material typified by UNCON. In this environment liner stress relief cracking is less likely under controlled cooldown conditions, but here there are major tunneling disadvantages at all liner thicknesses. For a thin liner, the thrust and weight supporting capability of a liner on a plastic foundation becomes insufficient. With increasing liner thickness, the problem of water disposal by earth fissure and/or uplift becomes increasingly worse. The major advantages of a thick liner are

- Better arching capability: If the liner does contain stress relief cracks, a thicker glass liner would tend to be a more stable arch than a thin walled liner
- Better earth primary load capability: This is true for arching of a cracked liner or stability of an uncracked liner
- Less severe abrasion environment on the penetrator at the locations of increased melt thickness
- Less mucking, and
- Better thrust and weight support capability

The disadvantages associated with a thick glass liner are

- Low penetrator velocity
- More penetrator surface area required
- Larger amounts of water (in a saturated earth/rock medium) must be removed

All of these advantages and disadvantages become reversed when thin glass liners are considered.

In view of the greater number of advantages with the use of thick glass liners, the following appear to be reasonable design goals

- Design the thickness of the glass liner to withstand earth primary loads and to provide capability for penetrator support and thrusting while simultaneously meeting rate of penetration and other design goals
- Cooldown the melt consistent with requirements for penetrator length support and thrust, irrespective of liner cracking

It can be readily shown that for the magnitude of thrust loads required for large scale transportation tunneling, the pressure on the glass liner needed for thrusting is relatively small. For an illustration, consider a 10 m penetrator requiring two million pounds of thrust to move at 100 meters per day. For a coefficient of friction of 0.30 (a very conservative assumption) for thirty foot diameter grip pads, the pressure on the liner wall is given by the equation

$$P = \frac{F_t}{0.3\pi D_p L} = \frac{491}{L} \quad \text{psi} \qquad (11\text{-}4)$$

where L is given in feet. For 20 feet of grip pads, the applied pressure on the wall is 25 psi.

To support the weight of the penetrator in horizontal tunneling to prevent the downward drift of the tunneler, additional lengths of the grip pads will be needed. The additional length needed depends on the weight of the penetrator. It can be readily calculated if the weight of the penetrator is known. In view of the low pressure calculated for thrusting requirements, it is anticipated that the force required for penetrator support will be on the same order of magnitude. Consequently, the glass liner thickness is expected to be controlled by the capability to support primary loads or differential pressures.

If cracking of the glass liner cannot be prevented, then it must be resolved (through experimental testing) whether a thick cracked liner is adequative for primary support. In any case, patching, sealing or the construction of a secondary liner will be needed to seal the glass liner.

11.5 LINER COOLDOWN

Scoping calculations have shown that under tunneling conditions of interest in this study, glass liner cooldown time and the length of the controlled cooldown section are excessive for an afterbody design. These relatively long controlled cooldown sections present two major problems for any afterbody design; the impracticability of a relatively long penetrator

and the potentially large frictional drag associated with a long cooldown section. The latter may not be a problem because during cooldown, the melt must contract. Due to the greater adherency of the melt to the earth/rock, the melt tends to pull away from the penetrator. However, this fact has only minimal experimental verification for small penetrators.

In the small scale penetrators tested by the Los Alamos Scientific Laboratory, pyrolytic graphite sections were used for melt cooldown and separation. The use of this material, with the "a" direction aligned radially, serves two purposes. It permits rapid cooldown of the melt as a result of the high thermal conductivity of the graphite, and the glass has very little tendency to stick to graphite materials.

Because of the latter property, a graphite outer layer may be used in the liner cooldown section. One problem here is that graphite has very little strength. If the glass liner inner surface is irregualr or if it contains suspended material due to incomplete melting, the graphite can be abraded and eroded, thus requiring replacement.

The maximum rate of cooldown for stress relief is limited by the thickness of the glass liner, the thermal diffusivity of the glass liner and earth/rock, and the maximum forced convective cooling that can be attained. This is evident from the functional relations developed for liner cooldown temperature (Equation 10-21), where the controlling parameter is

$$\frac{\phi_o \sqrt{\alpha}}{k} \quad \text{or} \quad \frac{\phi_o}{\sqrt{k \rho C_p}} \qquad (11\text{-}5)$$

where ϕ_o is the heat flux due to thermal radiation as well as forced convective heat transport, and α is the thermal diffusivity. Glass liner cooldown can be accelerated by increasing this parameter. The heat flux can be written in terms of the liner surface temperature by

$$\phi_o = \sigma F \left[T_s^4 - T_c^4 \right] + h (T_s - T_c) \qquad (11\text{-}6)$$

where σ is the Steffan-Boltzman constant, F is a radiation interchange factor, h is the forced convective heat transfer coefficient, and T_c is the coolant or stem temperature.

At the high temperatures encountered during liner cooldown, it can be shown that the first term, for thermal radiation, is the dominant factor. Since the forced convective heat transfer coefficient is the only parameter subject to control, it becomes apparent that not much can be done to maximize the heat flux. From Equation (11-7), it becomes apparent that another approach to the reduction of cooldown time is to reduce the thermal conductivity, density and specific heat of the melt by the introduction of materials into the melt. This was suggested in Section 10. An alternate approach suggested in Section 10. 0 consists of the implantation of coolant tubes in the melt as the melt is generated. The latter approach increases heat transfer area while reducing the conduction path lengths. Both factors will accelerate glass liner cooldown. The feasibility of these concepts must first be analyzed and demonstrated before they can be seriously considered as viable design solutions.

There appears to be little alternative to the proposed concept other than direct, active control of the thermal power. Such controls would be relatively complex in comparison, because of the necessary sensors, controllers, etc.

11.6 OTHER DESIGN CONSIDERATIONS

There are two other factors which must be considered that have important consequences on the subterrene design. These are the effect of gravitational forces and the maximum heat flux discussed below.

Effect of Gravity

In the derivation of the functional relations for applied thrust loads, the effect of gravitational forces was neglected in order to arrive at closed-form analytic solutions. However, in horizontal tunneling with tunnel diameters as large as 6 to 10 meters, graviational forces would have an effect on the distribution of the melt. In addition, if the penetrator is not adequately supported by the stem and afterbody, downward drift (as a result of the weight of the penetrator) through the melt would occur. This latter phenomenon can be avoided by adequate design of the grip pads.

The effect of gravitational forces on the melt is melt slumping. This is particularly a problem with unconsolidated materials where the molten earth/rock has a higher density than the parent earth/rock material. The result of this effect is that the density and thickness of the glass formed can vary around the circumference of the tunnel. This gravitational effect can be used to advantage if a thicker glass liner is desired at the bottom of the tunnel. This would be true in general for transportation tunnels particularly if the tunnel is horse-shoe shaped. Non-uniform glass properties and glass liners can be avoided if melt extrusion is part of the mode of tunneling. In this mode of tunneling, the melt pressure around the circumference of the tunnel can be controlled by varying the rates of extrusion around the penetrator to adjust the circumferential melt pressure distribution. To do this, separate multi-extrusion ports would be needed. This does not present a problem because separate extrusion ports may be needed in any case to facilitate the transport and handling of the extrudate and to allow the handling of non-homogeneous materials.

Maximum Heat Flux

The maximum local heat flux at the penetrator can be readily evaluated from the thermal power equation developed from the planar heat source model (see Section 7.0). This heat flux is given by the equation

$$\frac{q}{A} = \rho_e U_\infty \left[C_p (T_m - T_\infty) + \overline{C}_m \overline{(T_s - T_m)} + \lambda \right] \qquad (11\text{-}7)$$

The maximum heat flux is expected at the tip of the penetrator on the tip of the heaters as in a segmented heater design. At this location, the melt thickness is a minimum and the melt superheat can be neglected. The maximum local heat flux then reduces to the equation

$$\left(\frac{q}{A}\right)_{max} = \rho_e U_\infty \left[C_p (T_m - T_\infty) + \lambda \right] \qquad (11\text{-}8)$$

It is clear from this equation that the maximum local heat flux is independent of the penetrator size or geometry. It is directly proportional to the density of the earth/rock and the rate of penetration. Heat fluxes were calculated for two earth models: UNCON and MASIG. These represent two limiting cases (except for CALCI, which has the highest melting point) and provide excellent illustrations of the magnitude of the heat flux anticipated. The results of the calculations are presented in Figure 11- 3. It can be seen from this figure that the maximum heat flux anticipated at ~100 meters/day is 282 watts/cm^2 for UNCON and 563 watts/cm^2 for MASIG. Heat fluxes of this magnitude cannot be attained readily without excessive temperatures when forced convective heat transport is considered. However, they can be readily attained by the use of heat pipes. As an illustration at the extreme sonic limit, a lithium heat pipe at 1420°K can deliver up to 24 kW/cm^2. In addition to this capability, heat pipes have a number of advantages in this application:

- They operate at relatively isothermal conditions over relatively long distances so that the heat source does not have to be located in the penetrator forebody.

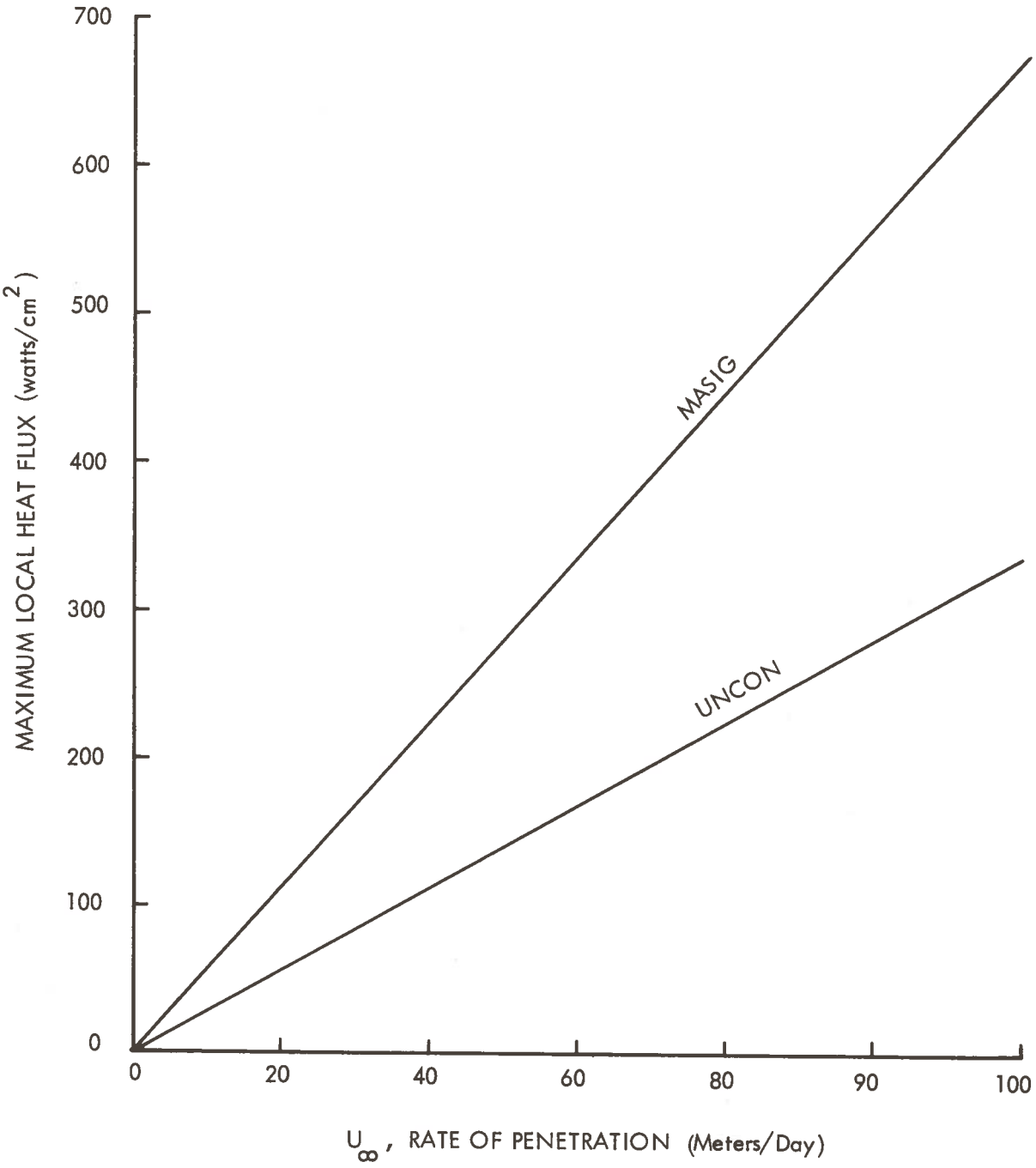

Figure 11-3. Effect of Rate of Penetration on the Maximum Local Heat Flux of Penetrator

- Heat pipes are compact and versatile. They can be designed in a variety of geometries and configurations including bent heat pipes.
- They are capable of extremely high heat fluxes, well above those needed in this application.
- The use of heat pipes permits the distribution of thermal power when coupled with a segmented heater design.
- They have capabilities for self-regulated automatic temperature and power control for tunneling through non-homogeneous materials

At the operating temperatures of interest in transportation tunneling, lithium heat pipes would be most suitable. Such heat pipes must require refractory metals such as Cb - 1Zr for construction. Both Lithium/Cb-1Zr and Lithium/ TZM heat pipes have been built and tested successfully up to 1873^{o}K . Based on these demonstrations, it is concluded that high temperature heat pipes operating at temperature ranges of interest are feasible.

11.7 MATERIALS SELECTION

For the high temperatures of operation needed by the rock melting subterrene for tunnel excavation, only refractory metals can be considered for penetrator construction. Both molybdenum and tungsten may be considered. While tungsten has appreciably higher temperature capability and hence higher rates of penetration, the cost of materials and fabrication is greater for tungsten than it is for molybdenum. Penetrators of relatively large sizes can be fabricated from tungsten with the segmented heater concept. The selection of a material for penetrator heater construction is basically an economic problem.

11.8 CONCLUSIONS AND RECOMMENDATIONS

It becomes apparent from the discussions of this chapter that all of the controlling variables affecting the design of a subterrene penetrator are directly or indirectly related. Although

the capabilities and limits of some parameters have been assessed, the actual values can only be determined through the evaluation and definition of conceptual designs for a given mission with specified design goals.

A number of problems have been identified. Potential design approach solutions to these problems have been proposed. These solutions appear to be technically feasible, but design analyses and experimental studies will be needed to establish their practicality and the limits of their capabilities.

For large scale tunnel excavations with tunnel diameters up to 10 meters and rates of penetration of ~100 meters/day, the following penetrator design features are recommended:

- Extended surface, segmented heater design to minimize penetrator surface temperatures and maximize the rate of penetration
- Extrusion of the melt to form a thick glass liner. This minimizes the melt thickness over heated portions of the penetrator and minimizes the penetrator surface temperature
- Coring and mucking capabilities to minimize thermal power and applied thrust load requirements
- Partial extrusion of melt for melt pressure control
- Generation of relatively thick glass liners to withstand primary loads and reduce logistics
- Implantation of coolant tubes in the melt to accelerate cooldown, minimize liner temperature gradients, and provide reinforcement of liner
- Use of tungsten for penetrator heater construction to maximize rates of penetration.

Some of the key proposed design features have been neither analyzed nor tested. It is therefore recommended that limited conceptual design studies be initiated to determine the

feasible capabilities and real limitations of large tunnel penetrator system with these design features. Such studies could determine whether the basic rock melting concept is really practical for large scale tunnel excavation.

Specifically, the following efforts appear highly desired and justifiable for furthering understanding:

1. Conceptual design of an extended surface, segmented penetrator for a large tunneler and evaluation of feasibility and cost.
2. Extrusion melt pressure control.
3. Conceptual design of system for implantation of coolant tubes in the glass liner.
4. Glass liner strength requirement evaluation for required thrust pad loads.
5. Cracked liner structural capability evaluation and testing.

Studies of key conceptual design and pertinent evaluations have been briefly outlined with recommended initial efforts in Appendix A.

APPENDIX A

RECOMMENDED KEY CONCEPTUAL DESIGN AND EVALUATION STUDIES

Outlines of studies of key conceptual designs and pertinent evaluations needed to verify the practicality of scaling the rock/earth melt process to large transportation tunneling are briefly presented in this Appendix.

These studies are noted by title as relating to the design problems determined in the completed work reported herein.

CONCEPTUAL DESIGN OF AN EXTENDED SURFACE SEGMENTED HEATER PENETRATOR

Problem Statement

Based on early LASL conceptual penetrator designs designated in the five "Modes" of tunneling studied in this report, it has been established that all of these are severly limited in their capabilities. Basically, the maximum allowable penetrator temperature limits the capability of the designs to relatively thin melt thicknesses, relatively small diameter penetrators, and relatively low rates of penetration.

In addition, other problems expected to be encountered in practical tunneling applications are tunneling through non-homogeneous media, and high leading edge heat flux.

Proposed Approach

Solutions to the above problems have been proposed so that large scale tunnel excavation at reasonable rates of penetration are potentially feasible. The use of extended surface segmented heaters minimizes heat flux and permits tunneling through non-homogeneous media. To reduce melt superheat and penetrator surface temperatures the penetrator is designed for thin layers of melt over the heated portions while extruding the melt into a relatively thick liner over unheated aft portions of the penetrator. Heat pipes may be used to deliver the high heat fluxes needed and to distribute unequal amounts of power to the heater segments for penetration through non-homogeneous media.

These design features are shown schematically in Figure A-1. All of these features are closely related through major parameters and the feasibility of the approaches can only be assessed through an integrated conceptual design effort.

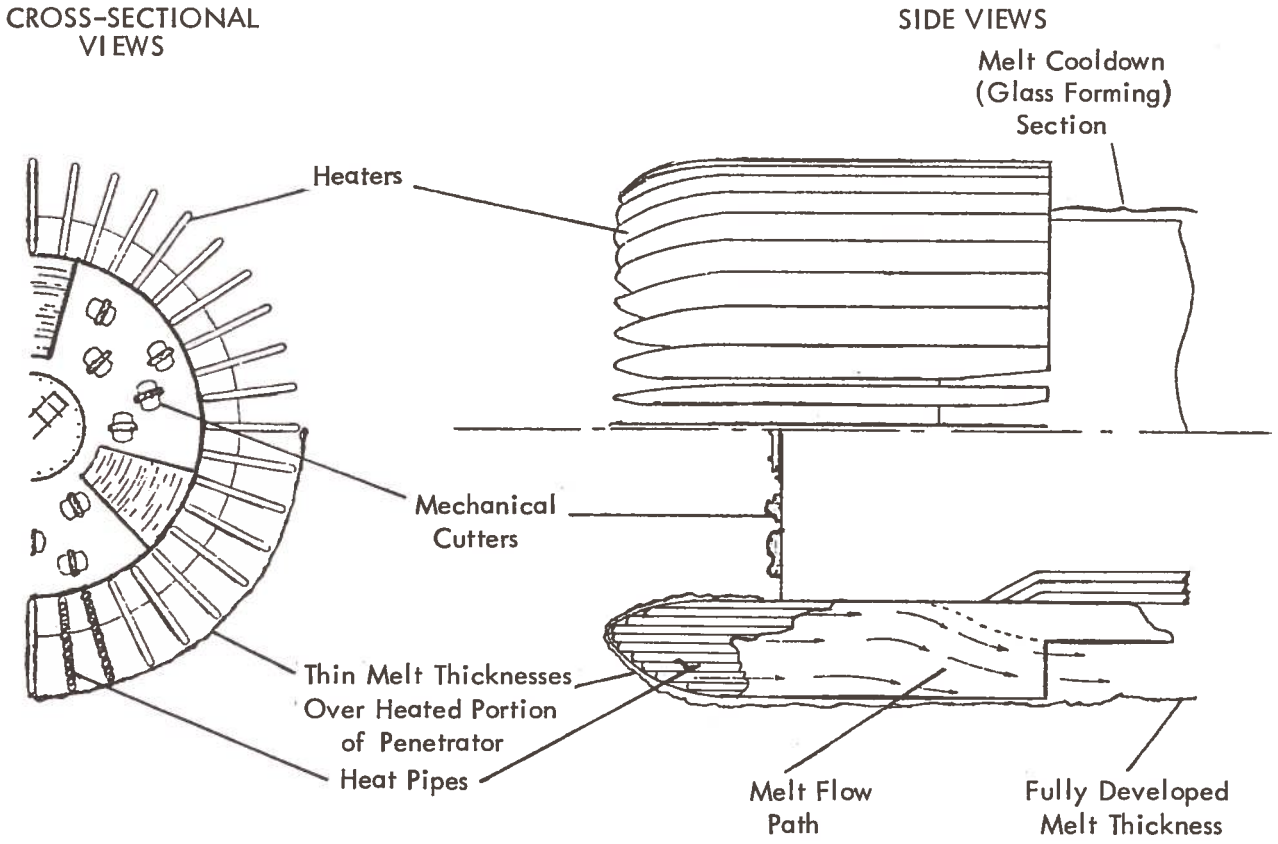

Figure A-1. Heat Pipe Concept with Extended Surface and Segmented Large Penetrator

Brief Work Statements

The conceptual design study will be carried out by the following tasks:

1. Specification of design requirements, constraints and goals
2. Concept definition
3. Technology capability evaluation
4. Concept selection
5. Preliminary design
6. Performance analyses to include:
   - Maximum rates of penetration for different earth/rock materials
   - Maximum thrust load
   - Maximum melt pressure
   - Thrust on the glass liner wall
   - Total thermal power requirement for the maximum rate of penetration
   - Controlled cooldown time
   - Lenght of controlled cooldown section needed

EXTRUDER THRUST LOADS AND MELT PRESSURE CONTROL CONCEPT

Problem Statement

Experimental data have shown that the thrust loads required for extruders are appreciably greater than those required for consolidators. Back extrusion of melt is expected to be a necessary feature for large scale penetrators. However, the data are inadequate for the verification of the functional relations developed. Because of these facts, the thrust load requirements and melt pressure for large scale penetrators cannot be predicted with a high degree of confidence. In addition, it has been determined that melt pressure control and controlled melt extrusion is necessary for horizontal tunneling to overcome gravitational affects.

Proposed Approach

For melt pressure control, one possible approach is to have multiple extrusion ports around the circumference of the penetrator. Each port is separately controlled to allow different rates of extrusion. In this way, the local extrusion rate can be varied as the material property changes.

The use of multiple extrusion ports is ideally suited to the segmented heater penetrator concept proposed above. Consequently, it is proposed that multiple extrusion ports be designed in as an integral part of the tunnel excavation penetrator. Gaseous extrusion of the melt has been successfully demonstrated by LASL and is proposed for use here. This means of extrusion is highly versatile and gas flowrates can be readily controlled to vary the rate of extrusion.

Brief Work Statements

1. Request controlled experimental testing of extruders from LASL to yield applied thrust load data for extruders.

2. Perform parametric analyses to support tasks in 1, above.

3. Based on this data, verify and/or modify the functional relations derived so that thrust loads can be predicted with a high degree of confidence.

4. Determine melt pressure distribution.

5. Conceptual study of melt pressure control system, integrated with overall penetrator design in 1, above.

6. Preliminary design of melt pressure control system.

CONCEPTUAL DESIGN OF GLASS LINER COOLANT TUBE IMPLANTING SYSTEM

Statement of Problem

The desired glass liner thickness and strength requirements make necessary a slow controlled cooldown after the penetrator and liner forming after body have passed. Low conductivity and large sensible heat storage of the glass aggravate this requirement. A means to remove evenly the heat from the liner and to provide maximum liner strength is desired.

Proposed Approach

This study would evaluate the concept of inserting a number of small cooling tubes into the glass melt during its formation into a liner. These tubes would serve not only to help in uniformly cooling the glass liner but also give structural re-inforcement to the glass. Coolant would flow from the downstream (cold) end through the glass to be cooled and into the penetrator body. In combustion heated systems, it could serve as a regenerative heat exchanger for preheating the combustion air.

The key parameters to be studied would include physical requirements of the tubes such as size and number against flow rates, heat transfer/transport requirements, and glass liner re-inforcing needs. Design concepts to be evaluated would include tube feeding mechanisms, hot end flow systems, handling of tube connections, and related problem areas. A continuous coolant tube feed system and practical design concept for key components would be defined. A basic approach is shown schematically in Figure A-2 which utilizes metal ribbon to tube formers.

Brief Work Statements

The following would be considered key efforts in this study program:

1. Determine design requirements and objectives such as maximum temperatures, flow rates, and geometry features.

2. Establish applicable technology capability and design constraints.

3. With 1 and 2, develop feasible concepts for system.

4. Conduct preliminary evaluation of concepts.

5. Select most likely concept.

6. Evaluate performance capability and limitations.

7. Provide recommendations for further evaluation if warranted.

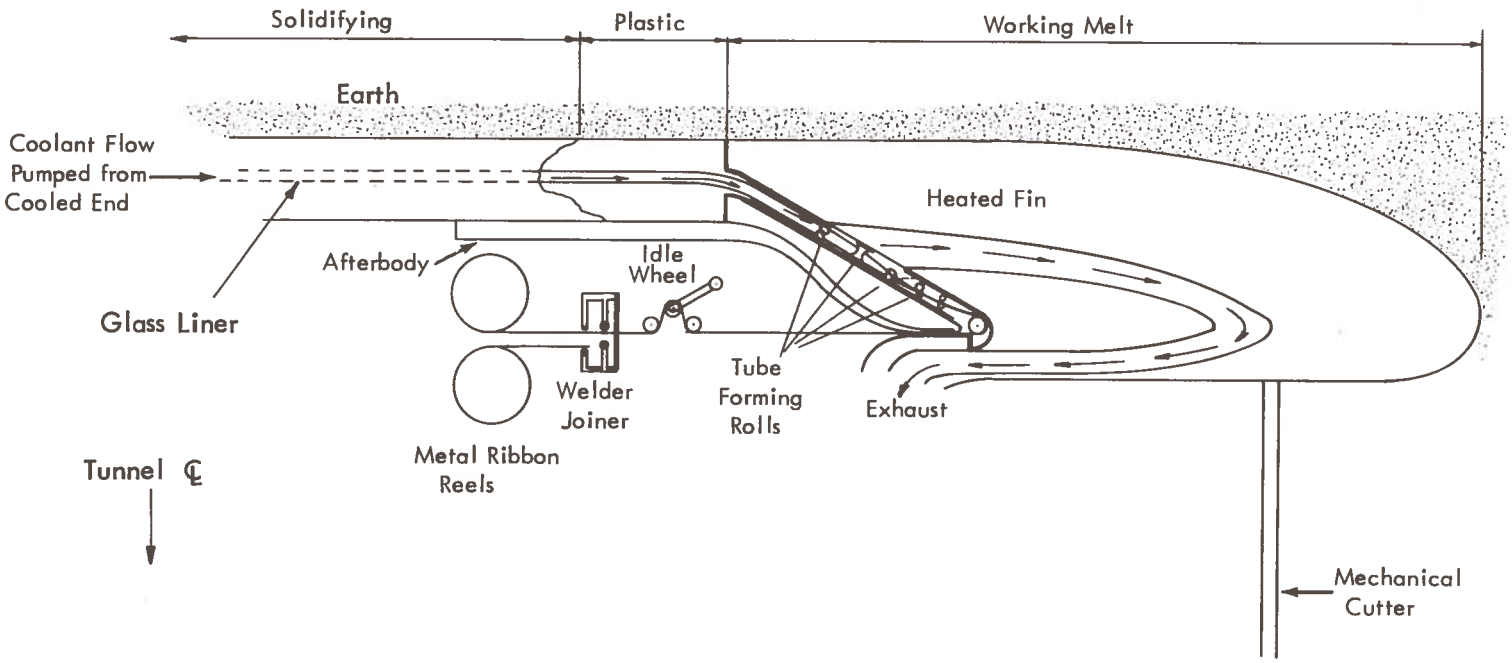

Figure A-2. Metal Ribbon - Tube Forming

GLASS LINER STABILITY EVALUATION

Problem

Thermal stress-relief cracks are expected in a glass liner formed by a heated penetrator. Therefore, the arching stability of cracked glass liners must be evaluated.

Proposal Approach

A stability evaluation of glass liner specimens filled with thermal stress cracks can be made. Liners of different thickness-to-diameter ratios can be loaded biaxially at different ratios of principal stress. These loads can be related to an overburden stress and this can be related to an elastic stability criterion for uncracked liners. Thus, a comparison can be made between arch stability crush loads and the elastic buckling loads, which are related to the liner geometry.

Brief Work Statements

1. Design a biaxial test chamber in which specimens will be loaded in soil or sand.
2. Evaluate test instrumentation requirements.
3. Acquire glass liner specimens which are formed from representative earth media after having analytically evaluated the required geometric proportions and the required number of samples.
4. Cut and polish specimens to the extent that a good qualitative description of the crack pattern is established for each specimen.
5. Evaluate the biaxial test load required to crush or partially collapse the sample glass liner.
6. Evaluate the best method of extrapolating the test results to large scale tunnel conditions.

APPENDIX B

REPORT OF INVENTIONS

Some innovative solutions to problems identified in this study have been proposed. These inventions have been described in this report and are identified in this appendix.

Title: High Performance Subterrene Thermal Tunneler

Description of this invention can be found in Section 6.4.6., pp. 6-42 to 6-48.

Title: Isothermal Condenser, Variable Power Heat Pipes

Description of this invention can be found in Section 11.3, pp. 11-9 to 11-10.

Invention disclosure of other design approaches to solving problems identified in this study may be made in the following areas:

1. A method of continuously feeding cooling tubes to the liner melt and maintaining coolant flow and control is discussed in Appendix A.
2. A method to use structural materials to reinforce the glass liner is described in Appendix A.
3. A method to provide melt pressure control to the penetrator by varying melt extrusion distribution, found in Section 11.6, p. 11-17, and described in Appendix A.